Intensified Process Technologies for the Single-Step Polycondensation of Saccharides

zur Erlangung des akademischen Grades einer
DOKTORIN DER INGENIEURWISSENSCHAFTEN (DR.-ING.)

von der KIT-Fakultät für Chemieingenieurwesen und Verfahrenstechnik des
Karlsruher Instituts für Technologie (KIT)
genehmigte

DISSERTATION

von

Dipl.-Ing. Sara Claramunt Carbonell
aus Valencia, Spanien

Tag der mündlichen Prüfung: 05.07.2023

Erstgutachter: Prof. Dr.-Ing. Roland Dittmeyer
Zweitgutachter: Prof. Dr.-Ing. Matthias Franzreb

Acknowledgements

This thesis was written as part of my work as a PhD student at the Institute for Micro Process Engineering (IMVT) of the Karlsruhe Institute of Technology (KIT). When I look back, I have a smile on my face: it was a time of hard work but also a journey of personal and professional development with plenty of great moments. I've been fortunate to have the guidance and support of numerous people along the way.

First and foremost, I am extremely grateful to Prof. Dr.-Ing. Roland Dittmeyer for the opportunity to work on this exciting topic. I appreciate his trust and support as well as his valuable feedback. I also wish to thank Prof. Dr Matthias Franzreb for taking over the second examination.

I would like to extend my deepest gratitude to my group leader, Manfred Kraut, for his enormous support, guidance and encouragement during all these years. Our countless scientific and personal discussions have helped me to grow both professionally and personally.

I would also like to extend my gratitude to our project partner Cargill Inc. for the financial support. Special thanks go to the colleagues in Krefeld and Vilvoorde, Dr. Christof Küsters, Bruno Stengel and Christa Hüser-Schwerin, for their friendly support in scientific and technical discussions and the possibility to analyze the polydextrose samples in their lab.

I would like to thank my colleagues at the IMVT for their excellent cooperation; especially the colleagues from the FAB, ADD and MAT groups, who supported me in the fabrication of my reactors as well as in the characterization of my material samples. In particular, many thanks to Cornelia Schorle and Dennis Scherhaufer for their always friendly and diligent support. I am extremely grateful to all my PhD colleagues for the amazing moments spent at the institute. I am deeply indebted to Paul Kant for his generosity in solving technical questions, as well as to Fabian Grinschek, Laura Trinkies, Dorela Dhamo and David Metzger for proofreading parts of my manuscript. I would like to express my deepest appreciation to Tabea Stadler, Jinju Zhang, Bárbara Bertin-Mente, Annette Hürter and Uta Gerhards for their warm encouragement during our time together inside and outside the institute.

During my time at IMVT, I have supervised several final year students. I am grateful for the pleasant and fruitful collaborations. I would like to especially thank Michel Bartsch, Paul

Schell and Florian Völker for their excellent work, which contributed significantly to the progress of my investigations.

Participating in KIT development programs, such as X-Ment and the Leadership Talent Academy, helped me not only to develop further but also gave me the opportunity to meet great people. I would like to thank Almuth Schwarz for her support in the final challenges of the writing phase. I also wish to thank Felicitas Müller, for the wonderful accompaniment in our development journey.

My friends from Valencia, Karlsruhe and Brilon have also been very important throughout this time. Thank you for the time together that gave me the energy to continue working. And my deepest thanks go to my family in Spain. Vull donar-li les gràcies especialment als meus pares i a la meua germana Teresa, per estar ahí sempre, perquè tot i la distància, sempre he rebut amor i un suport incondicional.

Abstract

The World Health Organization recommends reducing the daily sugar intake to a maximum of 10% of the daily energy intake. Polydextrose is a low-calorie polysaccharide that is added to a wide variety of foods as an alternative to sugar due to its properties as a bulking agent. The polycondensation reaction of glucose to form polydextrose is a reversible reaction that can be carried out at high temperatures and low residence times with a high yield in microreactors. A collaboration between Cargill Inc. (Wayzata, US) and the Institute for Micro Process Engineering of the Karlsruhe Institute of Technology (Karlsruhe, DE) led to a new way of conducting a polycondensation process to form polydextrose, in which the reaction equilibrium is shifted to higher product yields by removing water in an expansion chamber between two microchannel reactors (EP 2528950). To avoid the intermediate step of water separation and thus further simplify the process, this dissertation investigated two different routes for process intensification, targeting one single reactor stage. (1) The use of internal inserts in a double-pipe reactor, known as fluid guiding elements (FGE) and (2) the use of a membrane microchannel reactor, in which steam is separated from the reacting liquid flow through the pores of a temperature-resistant hydrophobic membrane.

The FGE used in the first route were manufactured by powder bed fusion of metals using a laser-based system. Due to the constant unsteady flow regime generated by the FGE, no thick boundary layer is formed for the heat transfer. This results in high heat transfer performance with relatively low pressure drops. Different lengths of double-pipe reactors fitted with internal inserts in the reaction and heat transfer oil side were tested. The effect of process parameters on the product yield was investigated; i.e. oil temperatures between 200°C and 235°C, pressures between 1 and 4 bar g, and feed flow rates between 2 and 3.75 $kg\,h^{-1}$. Different geometries of FGE were also compared. The results showed that the production of polydextrose in double-pipe reactors equipped with internal inserts is possible at high temperatures and over a wide range of glucose solution concentrations in the feed (i.e. product yields over 90% are obtained). With this solution, the water separation step is no longer required.

In the second route, the in situ steam removal with a hydrophobic membrane in the reactor was investigated. Since high-temperature conditions are required for the reaction to take

place, metallic membranes were considered in this study due to their robustness and temperature resistance. Their hydrophilic surface properties were modified by the application of a functional layer. In this work, two different coating methods were compared: plasma enhanced-chemical vapour deposition (PE-CVD) of silicon-doped diamond-like-carbon thin films (also known as Si-DLC) and direct immersion in a fluoroalkylsilane compound (FAS) using the dip coating technique. The fabricated coatings were qualitatively and quantitatively characterized by means of scanning electron microscopy and contact angle measurement, as well as by determination of their resistance to elevated temperatures. The results show that the coatings prepared by the method of direct immersion in a FAS solution have higher contact angles and are also more resistant to elevated temperatures than those coated with a Si-DLC layer.

The hydrophobic metallic membranes as well as commercial hydrophobic ceramic and polymeric membranes were characterized with respect to the liquid entry pressure (LEP). The LEP results of the different membrane materials were compared, being the ceramic membranes the ones with higher LEP. An investigation of the effect of higher temperatures and pressures up to 120°C and 1.5 bar g was carried out with the ceramic membranes. The findings showed that the temperature is the main factor affecting the LEP, due to its influence on the surface tension.

Separation experiments of steam were performed by means of sweeping gas membrane distillation (SGMD). The SGMD is a separation process in which only vapour molecules can penetrate a hydrophobic membrane. The sweep gas on the permeate side is in charge of extracting the separated vapour and lowering the partial pressure to enhance the driving force for the separation. A test facility was built to carry out experiments at temperatures up to 150°C and pressures up to 6 bar g. To understand the effect of different operating variables on the transmembrane flux, the process was mathematically modelled. The effect of feed parameters like mass flow rate, inlet temperature and glucose concentration, as well as the effect of sweep gas parameters like pressure and volume flow rate, were investigated. The results showed that higher temperatures lead to higher transmembrane fluxes, due to the effect of temperature on the water partial pressure. It was observed that a higher glucose content led to a decrease in transmembrane flux due to the effect on the water partial pressure in the feed. Besides, it was found that the correct choice of the sweep gas flow is crucial for a maximum transmembrane flux. However, a model-based optimization revealed that, in comparison, the pressure in the permeate compartment had the greatest influence on the transmembrane flux, and permeate pressures close to the water partial pressure at the phase boundary enhance the transmembrane flux. Experiments were also conducted on the stability of the membrane material and separation process, on the presence of two-phase flow on the feed side, and on the implementation of the coated metallic membranes. The results showed that the membranes are stable in the medium term. In addition, the two-phase

flow in the feed enhanced the transmembrane flux; the investigated metallic membranes, on the other hand, reduced the transmembrane flux. Future lines of research were suggested, such as the fabrication of metallic membranes using additive manufacturing and coating the membranes with more sustainable coatings. Recommendations were given on the scale-up of the FGE-based reactor as well as on how to conduct lab-scale experiments with a membrane microreactor.

The results presented in this dissertation allow the fabrication process of polydextrose to be simplified by the elimination of not only the water separation step but also the second microreactor stage and associated equipment in the plant. This leads to a reduction in cost and energy requirements, which results in a more energy efficient and climate-friendly production of polydextrose.

Kurzfassung

Die Weltgesundheitsorganisation empfiehlt, die tägliche Zuckeraufnahme auf maximal 10 % der täglichen Energieaufnahme zu reduzieren. Polydextrose ist ein kalorienarmes Polysaccharid, das aufgrund seiner Eigenschaften als Füllstoff einer Vielzahl von Lebensmitteln als Alternative zu Zucker zugesetzt wird. Die Polykondensationsreaktion von Glukose zu Polydextrose ist eine reversible Reaktion, die bei hohen Temperaturen und kurzen Verweilzeiten mit hoher Ausbeute in Mikroreaktoren durchgeführt werden kann. Die Zusammenarbeit zwischen Cargill Inc. (Wayzata, US) und dem Institut für Mikroverfahrenstechnik am Karlsruher Institut für Technologie (Karlsruhe, DE) führte zu einer neuen Art der Durchführung eines Polykondensationsprozesses zur Herstellung von Polydextrose, bei dem das Reaktionsgleichgewicht zu höheren Produktausbeuten verschoben wird, indem Wasser in einer Expansionskammer zwischen zwei Mikrokanalreaktoren entfernt wird (EP 2528950). Zur Vereinfachung des Verfahrens wurden in dieser Dissertation zwei verschiedene Wege zur Prozessintensivierung in einer einzigen Reaktorstufe untersucht. (1) Der Einsatz von Strömungsleitelementen (SLE) in einem Doppelrohrreaktor und (2) die Verwendung eines Membran-Mikrokanalreaktors, bei dem der Dampf über die Poren einer temperaturbeständigen hydrophoben Membran vom reaktiven Flüssigkeitsstrom getrennt wird.

SLE sind interne Einbauten, die durch pulverbettbasierten Schmelzen von Metallen mittels Laser hergestellt werden. Aufgrund der konstant instationären Strömung, die durch die SLE erzeugt wird, bildet sich keine dicke Grenzschicht für die Wärmeübertragung, was zu einer hohen Wärmeübertragungsleistung bei relativ geringen Druckverlusten führt. Es wurden verschiedene Längen von Doppelrohrreaktoren getestet, die mit internen Einsätzen auf der Reaktions- und Wärmeträgerölseite ausgestattet waren. Untersucht wurde die Auswirkung von Prozessparametern auf die Produktausbeute, d.h. Öltemperaturen zwischen 200°C und 235°C, Drücke zwischen 1 und 4 bar g und Durchflussmengen zwischen 2 und 3,75 $kg\,h^{-1}$. Außerdem wurden verschiedene Geometrien von SLE verglichen. Die Ergebnisse zeigen, dass die Herstellung von Polydextrose in Doppelrohrreaktoren mit Inneneinsätzen bei hohen Temperaturen und über einen weiten Konzentrationsbereich der Glukoselösung im Zulauf möglich ist (d. h. Produktausbeuten von über 90 % wurden erzielt). Bei dieser Lösung entfallen der Zwischenschritt der Wasserabtrennung sowie weitere Anlagenkomponenten.

Der zweite in dieser Dissertation untersuchte Lösungsweg zielt auf die in situ-Dampfentfernung mit einer hydrophoben Membran im Reaktor ab. Da für die Reaktion Hochtemperaturbedingungen erforderlich sind, werden in dieser Studie auch metallische Membranen aufgrund ihrer Robustheit und Temperaturbeständigkeit berücksichtigt. Ihre hydrophilen Oberflächeneigenschaften wurden durch das Aufbringen einer funktionellen Schicht verändert. In dieser Arbeit wurden zwei verschiedene Beschichtungsmethoden verglichen: die Plasma Enhanced Chemical Vapor Deposition (PE-CVD) von siliziumdotierten DLC-Dünnschichten (auch als Si-DLC bekannt) und die direkte Immersion in einer Fluoralkylsilanverbindung (FAS) unter Verwendung der Dip Coating Methode. Die hergestellten Beschichtungen wurden qualitativ und quantitativ mittels Rasterelektronenmikroskopie, Kontaktwinkelmessung sowie Bestimmung ihrer Beständigkeit gegenüber erhöhten Temperaturen charakterisiert. Die Ergebnisse zeigen, dass die nach der Methode der direkten Immersion in eine FAS-Lösung hergestellten Beschichtungen höhere Kontaktwinkel aufweisen und auch beständiger gegen erhöhte Temperaturen sind.

Die hydrophoben metallischen Membranen sowie kommerzielle keramischen und poylmerischen Membranen wurden hinsichtlich des Wassereintrittsdrucks (LEP-Liquid Entry Pressure) charakterisiert. Die LEP-Ergebnisse der verschiedenen Membranmaterialien wurden verglichen, wobei die Keramikmembranen den höheren LEP aufwiesen. Mit den keramischen Membranen wurden die Auswirkungen höherer Temperaturen und Drücken bis zu 120°C und 1,5 bar g untersucht. Die Ergebnisse zeigten, dass die Temperatur, aufgrund ihres Einflusses auf die Oberflächenspannung, der Haupteinflussfaktor auf die Größe des LEP ist.

Experimente zur Abtrennung von Wasserdampf wurden mit Hilfe der Sweeping Gas Membrane Distillation (SGMD) durchgeführt. Bei der SGMD handelt es sich um ein Trennverfahren, bei dem nur Dampfmoleküle eine hydrophobe Membran durchdringen können. Das Spülgas auf der Permeatseite hat die Aufgabe, den abgetrennten Dampf abzuführen und den Partialdruck zu senken, um die Triebkraft der Trennung zu erhöhen. Es wurde eine Versuchsanlage gebaut, in der Experimente bei Temperaturen bis zu 150 °C und Drücken bis zu 6 bar g durchgeführt werden können. Um die Auswirkungen verschiedener Betriebsvariablen auf den Transmembranfluss zu ermitteln und zu verstehen, wurde der Prozess mathematisch modelliert. Untersucht wurden die Auswirkungen von Feed-Parametern wie Massenstrom, Eintrittstemperatur und Glukosekonzentration, sowie die Auswirkungen von Sweepgas-Parametern wie Druck und Volumenstrom. Die Ergebnisse zeigten, dass höhere Temperaturen zu höheren Transmembranflüssen führen, was auf den Einfluss der Temperatur auf den Wasserpartialdruck zurückzuführen ist. Es wurde festgestellt, dass der Glukosegehalt aufgrund seiner Auswirkung auf den Wasserpartialdruck im Feed zu einem Abfall des Transmembranflusses führte. Außerdem wurde gezeigt, dass die richtige Wahl der Geschwindigkeit des Spülgasstroms entscheidend für einen maximalen Transmembranfluss

ist. Eine modellbasierte Optimierung zeigte jedoch, dass dass im Vergleich dazu der Druck im Permeatkompartiment den größten Einfluss auf den Transmembranfluss hat, und dass Permeatdrücke nahe dem Wasserpartialdruck an der Phasengrenze den Transmembranfluss erhöhen. Ebenfalls wurden Experimente zur Stabilität des Membranmaterials und des Trennprozesses, zum Einfluss einer Zweiphasenströmung im Feed und zum Einsatz von Metallmembranen durchgeführt. Die Ergebnisse ergaben, dass die Membranen mittelfristig stabil sind. Außerdem erhöhte die Zweiphasenströmung im Feed den Transmembranfluss. Die untersuchten Metallmembranen hingegen verringerten den Transmembranfluss, was auf die höhere Leitfähigkeit des Materials zurückzuführen sein könnte.

Es wurden zukünftige Forschungsfragen erarbeitet, wie die Herstellung von metallischen Membranen mittels additiver Fertigung und die Beschichtung der Membranen mit ökologisch nachhaltigeren Beschichtungen. Es wurde auch empfohlen, die entwickelte Lösung mit SLE zu skalieren und Experimente im Labormaßstab mit einem Membran-Mikroreaktor durchzuführen.

Die in dieser Arbeit vorgestellten Forschungsarbeiten ermöglichen eine Vereinfachung der Polydextrose-Herstellung durch den Verzicht nicht nur auf den Schritt der Wasserabscheidung, sondern auch auf weitere Geräte und Prozessschritte in der Anlage. Dies führt zu einer Verringerung der Kosten und des Energiebedarfs und damit zu einer energieeffizienteren und klimafreundlicheren Produktion von Polydextrose.

Publications

Parts of the present thesis have already been published by the author in peer-reviewed journals or presented at national and international conferences.

Publications in peer-reviewed international Journals

- S. Claramunt, P.V. Schell, M. Kraut, B. F. Stengel, C. F. Kuesters and R. Dittmeyer, Process intensification in a double-pipe reactor with additively manufactured internal inserts, ChemEngineering, vol. 6, no. 85, 2022. DOI: 10.3390/chemengineering6060085.
- S. Claramunt, F. Völker, U. Gerhards, M. Kraut, R. Dittmeyer, Membranes for the gas/liquid phase separation at elevated temperatures: Characterization of the liquid entry pressure, Membranes vol. 11, no. 907, 2021. DOI: 10.3390/membranes11120907.
- S. Claramunt, M. Khurram, W. Benzinger, M. Kraut, R. Dittmeyer, Fabrication and characterization of hydrophobic porous metallic membranes for high temperature applications, Processes, vol. 9, no. 809, 2021. DOI: 10.3390/pr9050809.

Patent applications

- B. F. Stengel, A. Hensel, S. Claramunt, M. Kraut, Polycondensation of sugars in the presence of water using a microreactor. EU Patent application 22190222.4, 2022.

Presentations at national and international conferences

- S. Claramunt, M. Kraut, R. Dittmeyer, Porous hydrophobic membranes for process intensification at elevated temperatures: Fabrication and characterization. 16th International Conference on Inorganic Membranes (ICIM), 28th-30th June 2022, Taipei (Taiwan). **Awarded: 3th prize presentation award**.
- S. Claramunt, M. Kraut, R. Dittmeyer, Characterization of porous hydrophobic membranes for high-temperature conditions. European Congress of Chemical Engineering, 20th-23rd September 2021, Berlin (Germany).

- S. Claramunt, M. Kraut, R. Dittmeyer, Membrane micro reactors for process intensification at high temperatures, Business and Innovation Event of the 14th Mediterranean Congress of Chemical Engineering, Barcelona, 16th September 2021, Barcelona (Spain). **Awarded: 2th prize Business and Innovation award**.
- S. Claramunt, F. Völker, M. Kraut, R. Dittmeyer, Membranes for the gas/liquid phase separation at elevated temperatures in micro reactors: Characterization of the liquid entry pressure. Jahrestreffen der ProcessNet-Fachgruppen Extraktion und Membrantechnik, 4th-5th February 2021, Frankfurt am Main (Germany).
- S. Claramunt, M. Kraut, R. Dittmeyer, Fabrication and characterisation of membranes for micro reactors for the intensification of condensation reactions. 14th Mediterranean Congress of Chemical Engineering, 16th– 19th November 2020, Barcelona (Spain). **Awarded: Best presentation award**.
- S. Claramunt, M. Kraut, R. Dittmeyer, Steam removal using membrane micro reactors for the concentration of sugar solutions. Jahrestreffen der ProcessNet-Fachgruppen Hochdruckverfahrenstechnik und Membrantechnik, 17th-19th February 2020, Freising (Germany). **Awarded: Best poster award**.

Supervised student's theses

During the preparation of this thesis, the author supervised several student projects. As the topics of these theses are related to the content of this dissertation, some of the findings and results of these student's theses are shown throughout the dissertation.

1. M. Bartsch. Experimentelle Untersuchung der Sweep Gas Membran Destillation zur Abtrennung von Wasserdampf aus einer Flüssigkeitsströmung. Master's Thesis, Karlsruhe Institute of Technology (KIT), Department of Chemical and Process Engineering, 2022.
2. J. Nebel. Modelling of sweep gas membrane distillation for the separation of water vapour from a liquid flow using MATLAB ©. Master's Thesis, Karlsruhe Institute of Technology (KIT), Department of Chemical and Process Engineering, 2022.
3. A. Vats. Fabrication and characterization of hydrophobic Fluor-based coatings on metallic membranes for the gas-liquid phase separation in a micro-test cell. Bachelor Thesis, Karlsruhe Institute of Technology (KIT), Department of Chemical and Process Engineering, 2022.
4. P. V. Schell. Prozessintensivierung durch 3D-gedruckte struktuierte Einbauten für die Herstellung von Polydextrose. Bachelor Thesis, Karlsruhe Institute of Technology (KIT), Department of Chemical and Process Engineering, 2021.
5. F. Völker. Charakterisierung des Wasserdurchbruchsdrucks hydrophober Membranen in einer Membrantestzelle zur gas/flüssig Phasentrennung. Bachelor Thesis, Karlsruhe Institute of Technology (KIT), Department of Chemical and Process Engineering, 2020.
6. M. Khurram. Fabrication and characterisation of hydrophobic coatings on metallic membranes for the gas/liquid phase separation at high temperatures. Master's Thesis, FH Münster, University of Applied Sciences, Material Science and Engineering, 2020.
7. L. J. Gliosca. Fabrication and characterization of hydrophobic coatings on stainless steel membranes for the gas/liquid phase separation in a microstructured device. Internship Research Report, Karlsruhe Institute of Technology (KIT), Department of Chemical and Process Engineering, 2020

Abbreviations and symbols

Abbreviations

Abbreviation	Description
AGMD	Air Gap Membrane Distillation
approx.	approximately
ASTM	American Society for Testing and Materials
CA	Contact Angle
CAD	Computer-Aided Design
CAS	Chemical Abstract Service
CAS Reg. No.	CAS Registry Number
CH	Switzerland
CVD	Chemical Vapour Deposition
DCMD	Direct Contact Membrane Distillation
DE	Germany
DI	Deionized
DIN	Deutsches Institut für Normung (German Institute for Standardisation)
DLC	Diamond-Like-Varbon layer
E	Additive accepted and processed by the European Union
EEA	European Economic Area
EDS	Energy-Dispersive Spectroscopy
EN	Europäische Norm (European Standard)
EP	European Patent
EPMA	Electron Probe Microanalysis
EU	European Union
FAS	Fluoroalkyl Silane

Abbreviation	Description
FDA	Food and Drug Administration
FGE	Fluid Guiding Elements
FGU	Fluid Guiding Units
FI	Flow Indicator
HE	Heat Exchanger
HMDSO	Hexamethyldisiloxane
HPLC	High-Performance Liquid Chromatography
IKTS	Institute for Ceramic Technologies and Systems
IMVT	Institut für Mikroverfahrenstechnik (Institute for Micro Process Engineering)
ISO	International Standardization Organization
KIT	Karlsruhe Institute of Technology
LEP	Liquid Entry Pressure
MD	Membrane Distillation
n/a	Not applicable
NCDs	Noncommunicable Diseases
NTP	Normal temperature and pressure
PBF-LB/M	Powder Bed Fusion of Metals using a Laser Based system
PDX	Polydextrose
PE	Polyethylene
PEEK	Polyether ether ketone
PE-CVD	Plasma-Enhanced Chemical Vapour Depositon
PET	Polyethylene terephthalate
PI	Pressure Indicator
P&ID	Piping and Instrumentation Diagram
PMDSO	Pentamethyldisiloxane
PMMA	Poly (methyl methacrylate)
POCS	Periodic Open Cellular Structures
PP	Prolypropylene
PTFE	Polytetrafluoroethylene
PVDF	Polyvinylidene fluoride

Abbreviation	Description
SAM	Self-Assembled Monolayer
SEM	Scanning Electron Microscopy
SGMD	Sweeping Gas Membrane Distillation
SI	International System of Units
Si-DLC	Silicon doped Diamond-Like-Carbon
SLE	Strömungsleitelemente
SLM	Selective Laser Melting
SS	Stainless Steel
STY	Space-Time Yield
TI	Temperature Indicator
TMDSO	Tetramethyldisiloxane
TMS	Tetramethylsilane
TriMS	Trimethylsilane
US	United States of America
USD	United States Dollar
VMD	Vapour Membrane Distillation
WDS	Wavelength-dispersive Spectroscopy
WHO	World Health Organization
wt.	weight

Latin symbols

Symbol	Description	Units
A	Area	m^2
B	Geometric factor	-
c	Concentration	$\mathrm{mol\,m^{-3}}$
d	Diameter	m
D	Diffusion coefficient	$\mathrm{m\,s^{-2}}$
DPn	Polymerization degree	-

Symbol	Description	Units
F	Force	N
Gz	Graetz number	-
ΔH_v	Specific molar evaporation enthalpy	$\mathrm{J\,mol^{-1}}$
i	Control variable and cell number	-
k_B	Boltzmann Constant	$\mathrm{J\,K^{-1}}$
k	Mass transfer coefficient	$\mathrm{m\,s^{-1}}$
Kn	Knudsen number	-
l	Length	m
$\tilde{M}$	Molar mass	$\mathrm{g\,mol^{-1}}$
$\dot{M}$	Mass flow rate	$\mathrm{kg\,s^{-1}}$
$\dot{N}$	Molar flow	$\mathrm{mol\,s^{-1}}$
Nu	Nusselt number	-
p	Pressure	Pa
Δp	Transmembrane pressure	Pa
Pr	Prandtl number	-
$\dot{Q}$	Heat flow	W
R	Ideal gas constant	$\mathrm{J\,mol^{-1}\,K^{-1}}$
r	Radius	m
Re	Reynolds number	-
Sa	Arithmetical mean height of the surface	µm
Sh	Sherwood number	-
Sq	Root mean square height of the surface	µm
STY	Space Time Yield	$\mathrm{kg\,m^{-3}\,s^{-1}}$
Sz	Maximum height of the surface	µm
T	Temperature	K
t	Time	s
$\dot{V}$	Volume flow rate	$\mathrm{m^3\,s^{-1}}$
V	Volume	$\mathrm{m^3}$
x	Mass fraction in the liquid phase	-
$\tilde{x}$	Molar fraction in the liquid phase	-
y	Mass fraction in the gas phase	-
$\tilde{y}$	Molar fraction in the gas phase	-

Symbol	Description	Units
X	Conversion	-
Y	Mass-related loading	-

Greek symbols

Symbol	Description	Units
α	Heat transfer coefficient	$\mathrm{W\,m^{-2}\,K^{-1}}$
β	Local mass transfer coefficient	$\mathrm{m\,s^{-1}}$
δ	Thickness	m
Δ	Difference	-
ε	Porosity	-
η	Dynamic viscosity	$\mathrm{Pa\,s}$
γ	Surface energy	$\mathrm{N\,m}$
λ	Thermal conductivity	$\mathrm{W\,m^{-1}\,K^{-1}}$
Λ	Mean free path	m
ν	Diffusion volume	$\mathrm{m^3}$
φ	Relative humidity	$\%$
ρ	Density	$\mathrm{kg\,m^{-3}}$
$\tilde{\rho}$	Density	$\mathrm{mol\,m^{-3}}$
σ	Molecule diameter	m
τ	Tortuosity	-
θ	Contact angle	$^\circ$
ζ	Factor for the calculation of the Nu-number in the turbulent regime	-

Indices

Index	Description
A	Active layer
50	Average (referred to pore size)

Index	Description
*	Saturation state
c	Critical
ch.	Characteristic
cond.	Conduction
eff.	Effective
evap.	Evaporation
f	Feed
fm	Feed-membrane interface
g	Glucose
h	Hydraulic
in	Inlet
Kn	Knudsen diffusion
lam.	Laminar
LV	Liquid-Vapour
m	Membrane
max.	Maximum
Molec.	Molecular diffusion
mp	Membrane-permeate interface
out	Outlet
p	Permeate
PDX	Polydextrose
pore	Pore
R	Reactor
S	Support
SL	Solid-Liquid
SV	Solid-Vapour
Tr.	Transition region between Knudsen and Molecular diffusion
turb.	Turbulent
w	Water

Contents

1 Introduction

1.1 Motivation

For a healthy diet and to prevent noncommunicable diseases (NCDs), such as diabetes, heart disease, stroke or cancer, the World Health Organization (WHO) recommends the population to reduce the daily energy intake from sugar to a maximum of 10 % [1, 2] and ideally, a daily intake less than 5 % [2]. Sugar has two functions in food preparations: sweetness and texture [3]. Sweetness can be replaced by sweeteners, like stevia or xylitol, but these do not bring texture. To give the necessary consistency to foods, a bulking agent needs to be added. In addition, a healthy diet should also contain dietary fibre, which has a positive effect on the intestinal flora. Both functions can be achieved with polydextrose [4]. Polydextrose is a polysaccharide low in calories, i.e. 1-2 kcal g^{-1} compared to the 4 kcal g^{-1} of D-glucose (dextrose) and sucrose [5]. Polydextrose is added to a variety of foods, such as sugar-free confectionery, dairy products, baked goods and beverages [6]. Polydextrose is approved in the European Economic Area (EEA) in the composition according to Annex A.1 as the additive E1200 [7]; similar regulations apply in the United States [8].

Chemically, polydextrose (CAS Reg. No. 68424-04-4, abbreviated as PDX) is a randomly linked polymer of D-glucose (cf. Figure 1.1) in which the individual units $\alpha-$ or β-(1,2)-, -(1,3)-, -(1,4)-, but predominantly -(1,6)- are glycosidically linked [9].

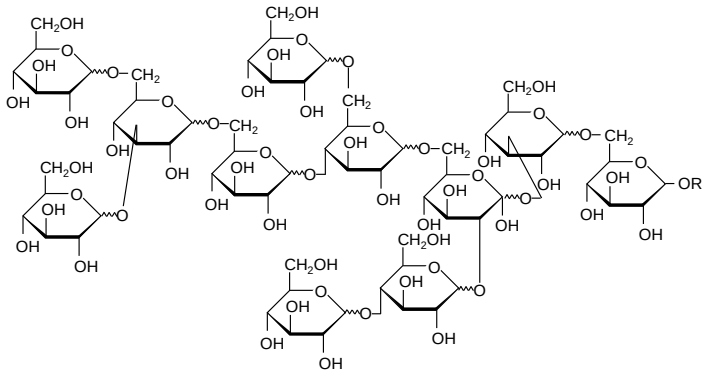

Figure 1.1.: Polydextrose molecule, predominantly with -(1,4)- and -(1,6)- glycosidic linkages, based on [6].

The molar mass of polydextrose is subject to distribution from dimers to 20,000 g mol^{-1} [10, 11], whereas it shows an average degree of polymerization of DPn = 12 [9, 10].

The polycondensation reaction to form polydextrose is a step-growth polymerization. In step-growth polymerizations, as opposed to chain growth polymerizations, any monomer or oligomer can react with any other monomer or oligomer, so that the chain length grows rather slowly. Consequently, the polymer size strongly depends on the conversion; only at very high conversions (> 85%), the required degree of polymerization is achieved.

Polydextrose is produced by thermal polymerization of glucose and sorbitol with an acid as a catalyst, e.g. citric acid [12]. During the polycondensation reaction of dextrose to form polydextrose, water is released when monomers combine [13]. Since the establishment of the process for the production of polydextrose as a batch process in a stirred tank with several hours of reaction time [13], attempts have been made to develop a continuous (and more productive) process [14–16].

Process intensification is defined as any chemical engineering development that leads to a step-change improvement towards safer, more compact, environmentally friendlier and more energy-efficient technologies and processes [17]. Micro process engineering is a powerful tool for process intensification through excellent heat transfer, fast mixing and continuous process control.

Within a technology transfer project, the Institute for Micro Process Engineering of the Karlsruhe Institute of Technology, KIT (Karlsruhe, DE) and the company Cargill Inc. (Wayzata, US) jointly started in 2010 an investigation of the production of polydextrose using micro process engineering, which led to a patented process EP 2528950 [18]. Herewith, polydextrose can be continuously produced with a relatively high yield, by using microchannel reactors at high temperatures and short residence times. In the patent EP 2528950, a solution

is presented which leads to the maximization of reaction yields: i.e. an expansion chamber for the removal of water in an intermediate step between two microreactors is established. Following Le Chatelier-Braun principle, when water (byproduct of the polycondensation) is removed from the reaction mixture, the equilibrium of the reaction is shifted to the products, leading to a maximization of the product yield.

Table 1.1 shows a comparison between the main processes for production of polydextrose. It gives an insight into the most relevant conditions and characteristics of the process, such as the pressure range, the reaction temperature, the residence time and the polydextrose yield. The last column shows the estimated specific productivity or space-time yield (STY). The calculations of the STY are shown in Annex A.2. When comparing the processes, it is remarkable that the obtained polydextrose yield for the microreactor solution is the lowest, however, its STY is much higher than for the other solutions.

Table 1.1.: Comparison of different processes for the production of polydextrose.

Process	Pressure range	Reaction temperature	Residence time	PDX fraction	STY
Batch [13]	< 0.4 bar	140-180 °C	3-24 h	97 wt.%	32 kg m^{-3} h^{-1}
CSTR [13]	< 0.4 bar	160-295 °C	3-10 min	97 wt.%	n/a
Extruder [14]	> 1 bar	160-200 °C	n/a	94 wt.%	163 kg m^{-3} h^{-1}
Microreactor [18]	< 1 bar or > 1 bar	150-250 °C	70 s	80 wt.%	1122 kg m^{-3} h^{-1}

There is still potential to improve the process design with microreactors proposed in the patent EP 2528950. Besides, the polydextrose market volume is expected to increase from USD 210 million (2021) to USD 319.9 million (2032) [19]. Both of these facts provide a reasonable basis to consider optimization measures; e.g. the simplification of the current process through process intensification, leading to the elimination of the intermediate water separation step. This would lead to:

1. a more compact design by saving process steps and their infrastructure,
2. the reduction of investment and corresponding energy costs in operation,
3. a more environmentally friendly production of polydextrose by minimizing the energy demand, and consequently, the reduction of the CO_2 footprint.

The polydextrose reaction in microstructured reactors described in the patent EP 2528950 takes place at temperatures above 200 °C. Due to the miniaturization of the flow geometry, the operation of the process comes along with a high pressure drop. As a consequence, higher pressures and a liquid state of the reacting mixture can be expected in the entrance region of the reactor. If evaporation is hindered by a limited heat transport into the reacting fluid, a **single-phase reacting fluid** may be observed through the reactor. Alternatively, if the evaporation of the produced water happens inside the reactor, a **two-phase reacting fluid** must be taken into account. Consequently, two scenarios, and therefore, two possible routes can be considered for process intensification:

- **Two-phase reacting fluid in the reactor**

  When evaporation is enabled, water can be eliminated from the liquid reacting glucose solution. The two-phase effect can be achieved when the heat is optimally transferred to the reacting fluid. Fluid guiding elements (FGE) [20], a special form of reactor inserts, exhibit very good heat transfer characteristics at low pressure drops when inserted in the inner tube and annular gap of a double-pipe heat exchanger [21]. FGE are additively manufactured by powder bed fusion of metals using a laser-based system (PBF-LB/M). The optimized heat transfer capacity achieved by the FGE can improve the evaporation in the reactor and therefore the removal of water from the reacting liquid solution.

- **Single-phase reacting fluid in the reactor**

  Membrane reactors are a compact solution for in situ removal of water. If the reaction is carried out in microchannel reactors with high pressure drops, the resulting higher inlet pressures may not enable the evaporation of water and therefore the reaction may take place in the liquid state. Pervaporation or vapour permeation are membrane processes for the separation of liquid mixtures. Examples of water removal, for the intensification of e.g. esterification reactions, are reported in the literature [22]. These processes, where the separation is based on the relative solubility and diffusivity of each component in the membrane material, require mainly dense and selective membranes [23]. Membrane distillation (MD) is another separation process used for the removal of water from an aqueous solution. The feed remains in the liquid phase and the separation is caused by a partial pressure gradient between the feed and permeate. To block the passage of the target product (reactive solution), while allowing water in vapour state to enter the pores, the membrane should be hydrophobic. Mainly, hydrophobic porous polymeric membranes are used for MD processes, since the process has only been investigated at temperatures below 80 °C and atmospheric pressures. In the polycondensation of polydextrose in microchannel reactors, however, higher temperatures are required (i.e. 200 °C). Performing membrane distillation at

such high temperatures may enhance the water separation potential of the application exponentially since the driving force for the separation is the partial pressure difference across the membrane. Nevertheless, such high temperatures imply several challenges, like a hydrophobic membrane stable in the temperature range up to about 250 °C. Further, an appropriate characterization method of the membrane at those reaction conditions is required as well as the development of suitable surface properties in the membrane to prevent the reaction product from entering into the pores [24].

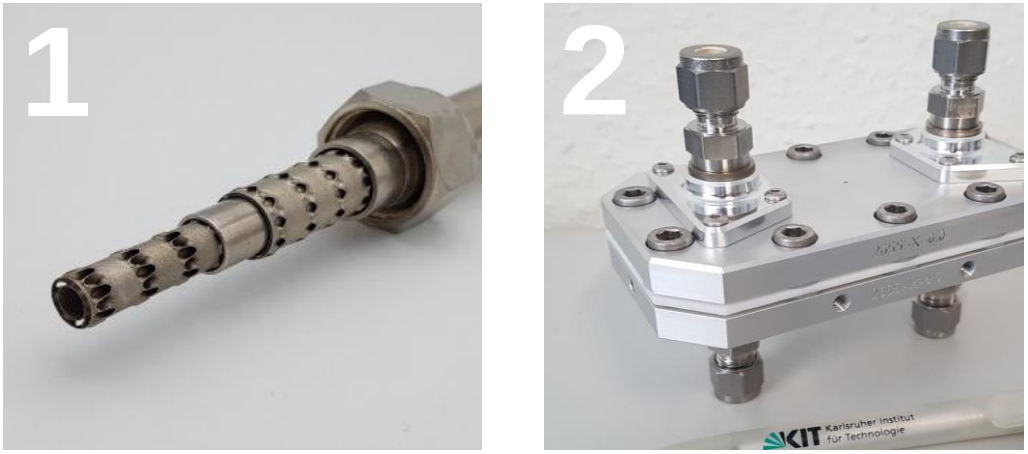

Figure 1.2.: Overview of the two investigated routes: Route 1 employs additively manufactured internal inserts with a two-phase fluid in the reactor. Route 2 uses a membrane reactor with microchannels, operating with a single-phase fluid.

1.2 Objectives and structure of this dissertation

Within the above-described scope, the aim of this dissertation is the intensification of the polycondensation of glucose to form polydextrose, i.e. the increase of the reaction yield. To simplify the process and eliminate the intermediate water separation step, the reaction should be carried out in one step. The following tasks are derived for the two different routes:

- **Two-phase reacting fluid in the reactor** - use of double-tube reactor with internal inserts.

  ➥ Experimental investigation of the effect of process parameters like temperature, pressure, feed concentration, residence time i.a. on the polydextrose yield.

- **Single-phase reacting fluid in the reactor** - use of a membrane reactor with microchannels.
  - ➥ Identification and/or development of hydrophobic membrane materials and coatings resistant to process conditions which act as a barrier to avoid the penetration of glucose solutions into the pores.
  - ➥ Identification and/or development of characterization methods of the coatings and membranes (namely, liquid entry pressure) at high temperatures and increased pressures.
  - ➥ Experimental and theoretical investigation of the removal of water using membrane distillation at high temperatures. Identification of the main phenomena and main impacting process parameters.

Within this context, the structure of this dissertation can be briefly summarized as follows: Chapter 2 provides the theoretical background and the state of the art concerning additively manufactured internal inserts for process intensification. Besides, the membrane distillation process for the removal of water from a single-phase liquid is described, with a special focus on different operation types and main occurring physical phenomena. The experimental investigation of the polycondensation reaction operated in FGE-based double-pipe reactors is presented in Chapter 3, and the fabrication and characterization of coatings for metallic membranes are described in Chapter 4. Moreover, the experimental results regarding the characterization of the liquid entry pressure of membranes at higher temperatures are outlined in Chapter 5. The experimental and theoretical investigation of sweeping gas membrane distillation at higher temperatures is considered in Chapter 6, and Chapter 7 introduces the challenges of a potential microstructured membrane reactor. Finally, in Chapter 8 the principal outcomes and findings of this work are summarized and an outlook for future studies is provided.

Remark about the units used in this dissertation

Physical quantities in the equations of this work are expressed in the units of the International System of Units (SI). However, especially experimental results are often given in practical units, e.g. nm instead of m for pore size or mm for membrane thickness for a better overview. In addition, operating parameters, like temperature and pressure, are given in °C and bar g, as these are common in chemical and process engineering. Normal temperature and pressure conditions are defined in this work as 20°C and 1 atm.

2

Theoretical background

This chapter sets the theoretical principles to address the objective of intensifying the polycondensation reaction to form polydextrose. First, the basics regarding the 3D printed structured internals are given. Next, the principles for the characterization of hydrophobic membranes are introduced, particularly the wetting of their surfaces as well as the liquid entry pressure (LEP). Finally, the basics of membrane distillation are explained, with a particular focus on the sweeping gas membrane distillation process. The heat and mass transfer steps during the membrane distillation process are also elucidated.

2.1 3D printed structured internals to improve heat transfer

The use of more efficient heat transfer equipment can reduce the size of a heat exchanger, resulting in a decrease in the associated material and investment costs. Several methods for heat transfer enhancement can be found in the literature, namely [25, 26]:

- Active methods. External forces, such as vibrating or moving walls are applied, which require an external activator.

- Passive methods. Use of internal inserts to modify the surface or geometry of the flow channel.

Among the passive methods for simple tubular heat exchangers, the implementation of inserts in simple geometric shapes, such as "twisted tape inserts" or "wire coil inserts", has long been a well-known method [27, 28]. A recent type with more complex geometry are metal foams [29, 30]. The emergence of additive manufacturing processes, also for metals (cf. Frazier [31] or Gibson et al. [32]), is associated with several advantages over long-established traditional manufacturing technologies, such as [33–37]:

- Complex shapes and patterns can be made with low labour input.
- Cost-effective production of individual parts or small series.
- Simulation-based optimization of devices is possible before fabrication since design and fabrication are fully digital.
- A variety of material compositions such as metals, alloys, ceramics, polymers, etc. can be used for fabrication.
- Customized devices with multiple functionalities can be produced very quickly.
- Lighter and more modular reactors can be manufactured.
- The design of the devices can be automated.

In chemical engineering, additive manufacturing presents a huge potential for process intensification applications by means of materials, equipment, and process innovations [38]. It can enable efficient heat and mass transfer, a significant reduction of the manufacturing and processing footprint, as well the mitigation of the associated environmental pollution [39, 40]. Additive manufacturing is used in chemical engineering in separation applications [41, 42], reaction engineering[43, 44] and heat transfer [45–48], among others.

At the Institute for Micro Process Engineering of the Karlsruhe Institute of Technology, additively manufactured inserts, named fluid guiding elements (FGE) were designed and patented by Hansjosten et al. [20] and tested in numerical simulation and experiments [21]. The FGE are made of repeating units, the fluid guiding units (FGU), which can be lined up in all 3 spatial directions. The FGU, shown in Figure 2.1, are responsible for the division of a flow into partial flows which get in contact with the heat-transferring wall, alternately.

The geometry of the FGU, based on free-form surfaces (B-splines), avoids an abrupt change in flow direction and rather guides the flow along the designed flow paths. The geometry of the FGU in combination with the low thickness of its walls results in low resistance for the flow. Due to the unsteady flow regime generated by the FGE, no thick boundary layer is formed at the walls in contact with the fluid, which results in high heat transfer performance at a relatively low pressure drop in the laminar flow regime [49]. To enable the use of FGE

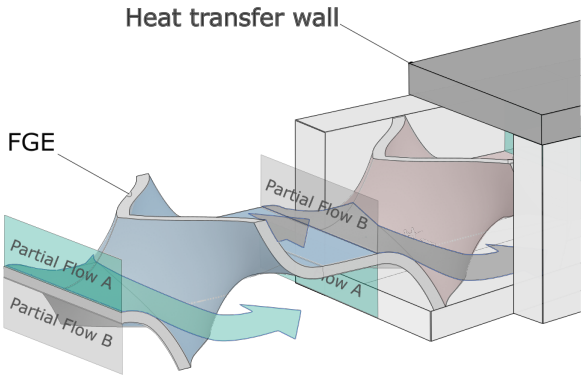

Figure 2.1.: Partial flows in the FGE system, adapted from Trinkies et al. [49].

in pipes and annular gaps, the geometry was transformed into a round shape that fills a pipe or an annular gap (Figure 2.2). Using a double-tube heat exchanger with FGE in the inner tube and annular gap, it was shown that a significant increase in heat transfer (up to over twice the power) compared to an empty tube could be achieved by the FGEs at low pressure drop [21].

In fact, other types of structured inserts like open-cell foams which show high thermal performance are associated with relatively high pressure drop [50]. Alternatively to the FGE, turbulence promoters like twisted-tape inserts disturb the flow instead of guiding it, which are also associated with a higher pressure loss [51]. Additively manufactured periodic open cellular structures (POCS) [43, 45, 52] are a competitive option for several applications, combining a large surface area and a low-pressure drop. The comparison of the thermal performance of the FGE with other inserts, like designed porous media in tubes [30] and POCS [45], showed that FGE outperform, representing an optimized compromise which combines high thermal transmittance with relatively high thermal effectivity [21].

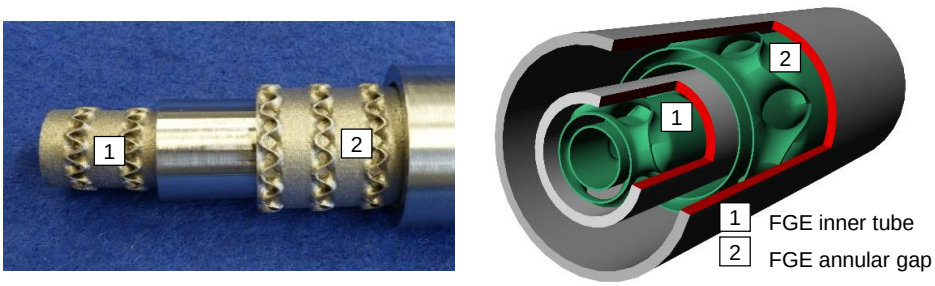

Figure 2.2.: Double-pipe configuration fitted with FGE in both internal tube and annular gap, adapted from [21].

The fabrication of the FGE is performed by powder bed fusion of metals using a laser-based system (PBF-LB/M), according to the standard ISO/ASTM 52900 [53]. PBF-LB/M is a commercially available, additive manufacturing process, also known as selective laser melting (SLM). PBF-LB uses a laser as a high-energy power source to selectively melt metallic powder [54]. The PBF process starts with the creation of a 3D CAD model, which is then numerically divided into individual layers, also known as 'slices'. For each layer, the laser trajectory vectors are calculated and then transferred to the printer. In the first process step, a thin powder layer is uniformly spread over the build platform with a re-coating blade [54]. The optimal thickness of each layer of metal powder depends on the processing conditions and the powder material, however values of 25 - 100 µm are common [32]. A laser beam melts and thermally fuses the powder layer according to the trajectory vectors to form the slice cross section [32, 55]. After completing a layer, the build platform is lowered by one layer thickness and a new layer of fresh metal powder is laid at the top of the previously built surface and levelled using the re-coating tool. Subsequently, the laser beam scans the next slice cross-section. The process is repeated layer by layer until the part is complete [32]. The build chamber is filled with inert gas, in most cases, argon, to prevent oxidation of the metal during melting and re-solidification [54]. The metal parts fabricated with PBF-LB/M are almost completely dense (e.g., 99.9 % for stainless steel [41, 56]) and require no significant post-processing. The mechanical properties of the parts are equivalent or even better than those of rolled metal sheet [57].

Recent applications of FGE-based structures are found in rectification apparatuses [41, 55], in UV-C treatment of food for microorganism deactivation [58, 59] as well as catalyst supports, e.g. for direct synthesis of H_2O_2 [49] and CO_2 methanation [60].

2.2 Hydrophobic membranes

Hydrophobic membranes used in membrane separation processes are mostly made of polymers. i.e. polytetrafluoroethylene (PTFE), polypropylene (PP), polyethylene (PE), and polyvinylidene fluoride (PVDF) [61]. However, the thermal stability of these materials is limited. Therefore, ceramic membranes are also applied [62]. They are usually made of metal oxides like TiO_2 or Al_2O_3 and coated with a hydrophobic agent [63]. Ceramic membranes exhibit higher thermal resistances than polymeric ones, however, they are brittle and may not withstand rapid temperature changes and tension. This can lead to the cracking of the membrane when high transmembrane pressures are required.

Metallic membranes exhibit high thermal resistance and high tenacity but also high surface energy, i.e. hydrophilic behaviour [64], which facilitates the wetting of the pores. For their application as hydrophobic membranes, metallic membranes should be coated with a hydrophobic layer.

Hydrophobic membranes are distinguished not only by a non-wetting surface, but also by their ability to prevent liquid from penetrating into the pores under operating conditions. The latter is characterized by the liquid entry pressure. Both concepts are described in the following sections.

2.2.1 Wetting

Wetting is caused by the contact of a liquid phase on a solid surface within a gas environment and the resulting intermolecular interactions [65]. These interactions determine the wetting and therefore the contact angle that is formed at the three-phase point, between the solid, liquid and gaseous phases.

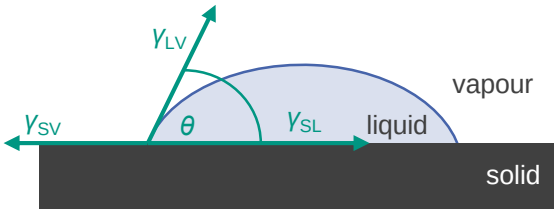

Figure 2.3.: Profile of a drop on a surface, showing the surface energies between the liquid and the vapour (γ_{LV}), the surface tension between the solid and the liquid (γ_{SL}) and the surface energy of the solid with the vapour or gas (γ_{SV}). The contact angle of the liquid on the surface θ is represented as the angle between γ_{LV} and γ_{SL}.

As shown in Figure 2.3, the contact angle is the angle between the interface of the solid-liquid phase (SL) and the tangent of the drop interface to the surroundings (LV). The three-phase point reflects the state of minimum energy and it is characterized by the equilibrium between the interfacial tensions that emerge due to the contact between the phases: surface energy of the liquid (γ_{LV}), which is also simplified as surface tension, the surface energy between the solid and the liquid (γ_{SL}) and the surface energy of the solid with the vapour or gas (γ_{SV}) [66]. The contact angle, θ can be therefore determined by a balance of forces at the three-phase point as per the Young equation:

$$cos(\theta) = \frac{\gamma_{\mathrm{SV}} - \gamma_{\mathrm{SL}}}{\gamma_{\mathrm{LV}}} \tag{2.1}$$

Depending on the value of the contact angle, surfaces can be divided into hydrophilic ($\theta < 90\,°$), hydrophobic ($\theta > 90\,°$) and superhydrophobic ($\theta > 150\,°$) [67], as depicted in Figure 2.4.

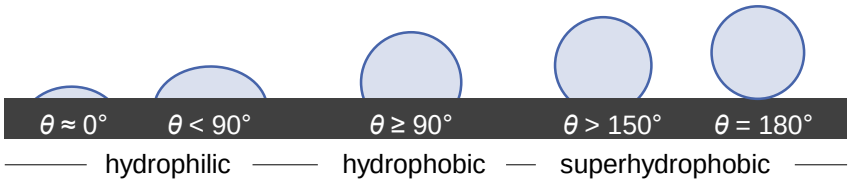

Figure 2.4.: Wetting states of a liquid on a surface, from hydrophilic $\theta \approx 0°$ up to superhydrophobic state, $\theta = 180°$.

The contact angle can be experimentally determined by employing a contact angle goniometer using e.g. the sessile drop method. Contact angle goniometers can be operated manually (the operator is in charge to set a tangent to the drop at the three-phase point) or automatically (image processing software) [65]. The contact angle measured in a static condition is referred to as static contact angle, and the contact angle measured under the condition that the three-phase contact line is moving with respect to the surface (in the course of wetting or dewetting) is referred to as dynamic contact angle [68]. The dynamic contact angle provides information about the surface heterogeneity [69]. The measurements in this work are focused on the static contact angle.

Hydrophobic membranes are commonly prepared by increasing the surface roughness and/or by chemical modification [63, 70]. Surface roughness may either lead to the so-called Wenzel or Cassie–Baxter wettability state (see Figure 2.5), which refers to a modification of the contact angle in comparison to a perfectly flat surface [71]. In the Wenzel state [72], the wetting liquid penetrates the roughness grooves or pores. For pore geometries where gas is trapped, i.e. in the Cassie-Baxter state [73], the contact area between the liquid and the solid surface is reduced, thus leading to an enhancement of the contact angle. An intermediate state, where the liquid partially wets the surface is also commonly encountered [74].

The process operating conditions, as well as the concentration of the solutes in the fluid in contact with the surface, may have a certain impact on the surface tension and, as a consequence, on the contact angle [75]. Only few works deal with the effect of temperature on the contact angle. Ge et al. [76] studied the influence of temperature by measuring the contact angle at 55 °C and 77 °C. Mettu et al. [77] measured the contact angle at 22 °C and 95 °C. Both observed a general decrease in the contact angle with the temperature. Mettu et al. [77], however, identified a coated polymeric material where an increase in contact angle with the temperature occurred. The reason here was the change in morphology of the solid surface when heated to 95 °C, which led to a rougher surface that hindered wetting.

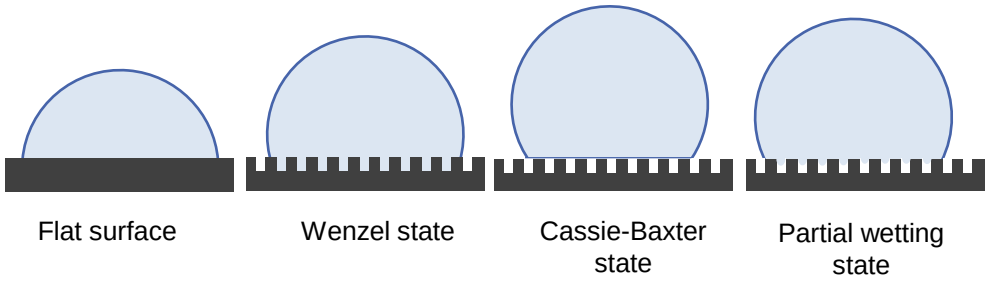

Figure 2.5.: Wettability states in flat and rough (porous) substrates.

2.2.2 Liquid entry pressure

For the efficient operation of hydrophobic membranes, it is required to avoid liquid from entering the membrane pores, as it causes the reduction of flux and quality of the permeate [78].

The liquid entry pressure (LEP) is an essential parameter for the operation of porous hydrophobic membranes: it is defined as the highest applied transmembrane hydrostatic pressure before the liquid in the feed penetrates the largest pores and thus migrates through the hydrophobic membrane [79]. When the transmembrane pressure is kept below the LEP, the liquid in the feed does not penetrate even the largest pores and the liquid-vapour interface is formed at the pore entrance so that only the diffusion of the vapour phase takes place through the pores [80].

Theoretical principles

The liquid entry pressure can be calculated based on the force balance of the Young-Laplace equation [79] for the capillary pressure of a pore. The force exerted on the pore surface by the pressure difference is in equilibrium with the force at the liquid-vapour interface.

$$F_{\text{pressure}} = F_{\text{surface tension}} \tag{2.2}$$

where F_{pressure} refers to the force exerted by the liquid pressure and $F_{\text{surface tension}}$ is the surface tension force. For a circular area, this results in:

$$\pi \frac{d^2}{4} \Delta p = \pi \, d_{\text{pore}} \, \gamma_{\text{LV}} \, cos(\theta) \tag{2.3}$$

where d_{pore} is the pore diameter, γ_{LV} is the surface tension of the liquid and θ is the contact angle of the liquid at the pore entrance. The transmembrane pressure results therefore in Equation 2.4:

$$\Delta p = \frac{4}{d_{\text{pore}}} \gamma_{\text{LV}} \, cos(\theta) \tag{2.4}$$

In the calculation of the LEP in Equation 2.5 LEP as the highest transmembrane pressure before the liquid enters into the pores, $d_{\text{pore.max}}$ corresponds to the largest pore size. Besides, the calculation of the LEP considers deviations of the pore geometry from a circular cross-section with the geometric factor, B. The geometric factor, B is an adjustable parameter which is determined by comparison with experimental data. The equation for the LEP is given in Equation 2.5 (cf. Figure 2.6 for an overview of the main parameters):

$$LEP = \Delta p = \frac{-4\,B\,\gamma_{\text{LV}}\,cos(\theta)}{d_{\text{pore.max}}} \tag{2.5}$$

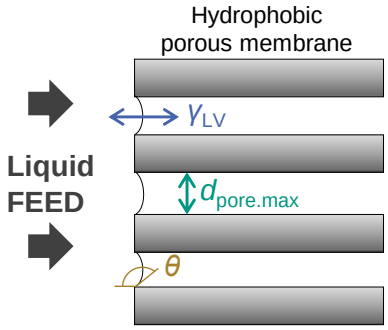

Figure 2.6.: Parameters influencing the Young-Laplace equation in a membrane with cylindrical pores: the surface tension in the pore entrance, γ_{LV}, the maximum pore size, $d_{\text{pore.max}}$, and the contact angle at the pore entrance, θ.

The liquid surface tension in Equation 2.5 represents the capillary force responsible for forming a convex meniscus in the membrane pore and preventing liquid breakthrough [81]. An increase in temperature, and therefore, in molecular thermal activity, results in the decrease of the surface tension, as the cohesive interaction between the phases falls with the temperature [82, 83]. Preventing wetting at higher temperatures is, therefore, a difficult task [81]. For proper operation of hydrophobic membranes, a contact angle of around 130 ° is recommended in the literature [75]. The largest pore size of the membrane plays a crucial role to avoid liquid crossover; therefore, a maximum pore size of 0.6 µm [84] with a uniform pore size distribution is recommended in the literature. The dimensionless parameter B considers the geometry of the pores. For $B = 1$, pores are assumed to be cylindrical. For B values between 0 and 1, non-cylindrical pores are considered [85]. However, since the pores of a real membrane may neither be cylindrical nor parallel, but rather have diverse geometries and be cross-linked [86], there exists no simple correlation between the shape and the value of B. Furthermore, the variation of shapes in a real membrane may also play a role in the determination of the value B. The factor B, therefore, acts as an adaptable parameter. For example, for PTFE membranes, the B factor takes values between 0.4 and 0.6 [87]. Special attention has been paid over the years to the proper modelling of pore geometry, length, and size in the determination of the liquid entry pressure. A complete

review of the models can be found in the works of Rezaei [81] and Chamani [78]. However, models considering the effect of temperature on the LEP are still missing.

Experimental determination

Despite the availability of models in the literature, no single model was found to exhibit good predictability for all membrane types [87–89]. The models do not consider real factors, such as defects in the geometry or in the hydrophobic coating or the existence of larger pores than expected. This may result in an overprediction of the LEP. Hence, the modelling of the LEP serves only as a guideline for the operation of the membrane, but the experimental investigation under plant operating conditions [90] remains unavoidable. The four main experimental methods are shown in Table 2.1.

State of the art of LEP measurement at elevated temperatures

Only a few studies have investigated the influence of temperature and system pressure on the liquid entry pressure: Garcia-Payo et al. [91] and Guillen-Burrieza et al. [92] experimentally investigated the liquid entry pressure of PVDF and PTFE membranes up to 60 °C, Saffarini et al. [86] until 70 °C and Varela-Corredor et al. [93] characterized the LEP of titania-based tubular membranes up to 105 °C. They also measured a liquid entry temperature of nearly 130 °C by establishing a very low constant transmembrane pressure.

Table 2.1.: Overview of experimental methods to determine the liquid entry pressure in the literature.

Method	Measurement principle	Studies	Advantages	Disadvantages
➥ Visual	Pressure at which the first water drop can be visually detected on the back side of the membrane	[75, 86, 87, 89, 91, 92, 94–102]	• Simple setup • Frequent use	• Subjective method • The membrane needs to be visually accessible • Experiments at higher temperatures and pressures are challenging
➥ Conductivity	Detection of an increase in conductivity on the permeate side	[75, 92, 103–106]	• Fast detection of liquid breakthrough	• Only suitable for electrically conducting solutions
➥ Pressure Step	The gradient $\frac{dp_f}{dt}$ becomes negative during the increase of the feed pressure	[107]	• Fast detection of liquid breakthrough • Independent on the feed composition	• Very accurate and rapid pressure sensors are required
➥Flow curve (hysteresis)	Pressure at which the flow rate vs. transmembrane pressure reaches a threshold value	[75, 80, 91, 93, 108, 109]	• Potential detection of defects in the membrane • Accurate detection of breakthrough when membrane parameters are known	• Very accurate pressure and flow sensors are required • The threshold value should be specified • Previous accurate pore characteristics (tortuosity, pore size distribution, porosity) determination required

2.3 Membrane distillation

Membrane distillation (MD) is a thermally driven separation process [84] in which only vapour molecules can pass through a hydrophobic membrane [110]. Figure 2.7 schematically shows the hot feed side of the membrane. It can be seen that the liquid feed does not penetrate the pores. A vapour-liquid equilibrium is formed at the pore entrance [110], which is determined by thermodynamics. Then, the vapour molecules diffuse through the membrane to the other side where they are extracted or condensed, depending on the MD configuration [100]. The driving force of this process is the transmembrane partial pressure difference of the component to be separated, so that the transmembrane (evaporation) flux can be expressed as:

$$\dot{N}_\mathrm{w} = A_\mathrm{m} k_\mathrm{m} \, \Delta p_\mathrm{w} = A_\mathrm{m} k_\mathrm{m} \, \left(p^*_\mathrm{w} \left(T_\mathrm{f} \right) - p_\mathrm{w.p} \right) \tag{2.6}$$

In Equation 2.6, $\dot{N}_\mathrm{w}$ is the molar transmembrane flow, A_m is the membrane area, k_m is the mass transfer coefficient, $p^*_\mathrm{w} \left(T_\mathrm{f} \right)$ is the vapour pressure of water at feed temperature T_f, and $p_\mathrm{w.p}$ is the partial pressure of water in the permeate side of the membrane.

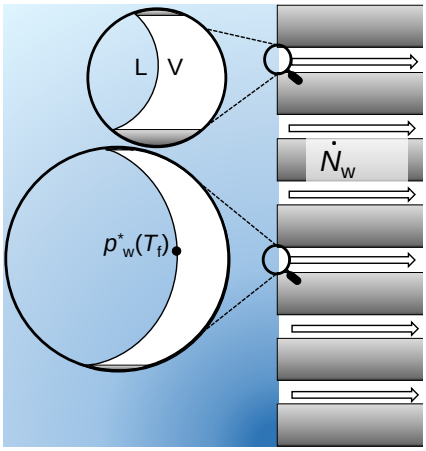

Figure 2.7.: Vapour-liquid equilibrium in the pore entrance (meniscus). The driving force caused by the partial pressure gradient between feed and permeate results in a transmembrane molar flow, $\dot{N}_w$.

In membrane distillation, the membrane does not have any selective function, but it acts as a barrier between feed and permeate [100], so that the vapour-liquid equilibrium is established. The membrane must fulfil some requirements for an optimum application. These include a hydrophobic surface, a small wall thickness, small pore size (between 100 nm and 1 µm) [110] and narrow pore size distribution as well as high porosity and low tortuosity [111].

In contrast to other thermal separation processes (e.g. conventional distillation), MD is carried out below the boiling temperature of the feed [111]. Compared to pressure-driven processes (e.g. reverse osmosis), the hydrodynamic pressure difference in MD can be set to a minimum [111]. Thus, it is possible to use membrane materials with a lower mechanical load capacity (e.g. ceramic membranes [61, 112]). MD has been mostly applied for desalination and production of pure water [113–117] as well as in the chemical and food industry for the concentration of species like alcohols [118], acids [119–121], fruit juices [122–125] and wastewater treatment [102, 126, 127]. A good overview of MD applications is given by El-Bourawi et al. [110]. The application of MD to further processes is limited due to some challenges when compared to other separation methods. These challenges are: a lower specific permeate flow, the additional mass transport resistance due to the presence of an inert gas inside the pores and the high heat losses [84].

Membrane distillation can be operated in various configurations, which are shown in Figure 2.8. In direct contact membrane distillation (DCMD) and air gap membrane distillation (AGMD), the condensation of the steam takes place within the membrane module. In DCMD, the vapour condenses in a cold liquid, whereas in AGMD the vapour condenses on a cold wall that is separated from the membrane by air. In contrast, in sweeping gas membrane distillation (SGMD) and vacuum membrane distillation (VMD), condensation takes place externally. The steam is discharged via a carrier (sweep) gas or vacuum out of the module[110].

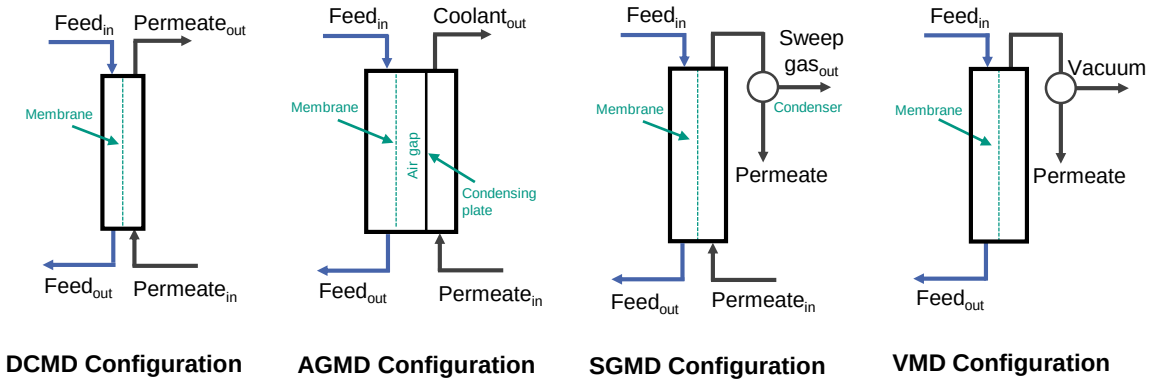

Figure 2.8.: Different types of membrane distillation configurations, based on [110]. From left to right: direct contact membrane distillation (DCMD), air gap membrane distillation (AGMD), sweeping gas membrane distillation (SGMD) and vacuum membrane distillation (VMD).

2.3.1 Sweeping gas membrane distillation

In sweeping gas membrane distillation (SGMD), an inert cold gas is in charge of two tasks:

- extracting the vapour permeate out of the module,
- lowering the partial pressure in the permeate side to generate and further increase a partial pressure difference across the membrane which enhances the driving force of the separation [126, 128, 129].

The SGMD configuration is considered to have great perspectives for the future, because of its advantages compared to other MD processes [111]. In comparison to DCMD, heat losses are lower since the sweep gas flowing on the permeate side has lower thermal conductivity and heat capacity than a liquid [130]. This leads to a higher evaporation efficiency [131–133]. Unlike air gap membrane distillation (AGMD), the gas in the SGMD is not stationary and sweeps the membrane. This leads to a reduction in the boundary layer thickness and thus, to an improved mass transfer [110, 129] and higher permeate fluxes (e.g. Khayet et al. [133] reported 1.4 times higher transmembrane flux). SGMD is mostly used for desalination [133] or separation of organic mixtures [118, 134]. SGMD has not yet been extended to other applications due to some challenges related to the high sweep gas flow required in relation to the transmembrane flow, i.e. gas transport costs [110], use of large condensers [84] and challenging recovery of heat [110, 127, 129, 135].

The works in the literature about SGMD use a maximum feed temperature lower than 80 °C and permeate pressures around atmospheric conditions. In all the works, the transmembrane flux gets maximized when increasing the feed temperature or the sweep gas flow rate and when lowering the sweep gas temperature, or the membrane thickness. Table 2.2 gives an overview of the effects of the operating parameters on the transmembrane flux in SGMD. Shukla, in his dissertation (cf. Table I.2 in [136]) or Khayet and Matsuura (cf. Table 11.1 in [111]) give good overviews of the works in the literature regarding SGMD.

For temperatures higher than 80 °C, however, no works on SGMD can be found in the literature. The expected positive effects of further increasing the feed temperature on the transmembrane flux and thermal efficiency of membrane distillation have been already published [90, 137]. The exponential relationship between vapour pressure and temperature leads to larger partial pressure gradients when the temperature is increased [84]. Only for the case of DCMD, first works at temperatures higher than 80 °C and therefore, permeate pressures higher than atmospheric can be found in literature. Singh and Sirkar [116, 138] verified experimentally the basic feasibility of successful operation at temperatures of 80 °C-130 °C, and Luo and Lior [90] performed a simulative study of DCMD at temperatures between 80 °C and 180 °C.

Table 2.2.: Effect of operating parameters on the transmembrane flux in SGMD.

Parameter	Effect on transmembrane flux
Feed temperature ↑	+
Sweep gas flow rate ↑	+
Sweep gas temperature ↑	-
Membrane thickness ↑	-

2.3.2 Heat and mass transfer

Phenomenological description

In MD processes, mass transfer and heat transfer occur simultaneously, cf. Figure 2.9. The mass transfer through the membrane in SGMD for an aqueous solution in the feed (non-volatile solute dissolved in water) consists of five consecutive steps [136, 139]:

1. Mass transfer from the bulk feed side towards the membrane surface. A concentration gradient of the non-volatile solute is formed in the feed side, which poses further mass transfer resistance for water to diffuse towards the membrane. This phenomenon is known as concentration polarization [140].
2. Evaporation of water at the liquid-vapour interface, i.e. pore entrance at thermodynamic equilibrium. This location is labelled in the variable in Figure 2.9 as the feed-membrane (fm) interface and here it applies $p_{\mathrm{w.fm}}$=$p^{*}_{\mathrm{w}}(T_{\mathrm{f}})$.
3. Mass transport of water vapour through the membrane pores due to the aforementioned partial pressure difference. The membrane pores represent a mass transfer resistance for the transport of vapour, and therefore the partial pressure of water decreases over the thickness of the membrane up to $p_{\mathrm{w.mp}}$, which is the partial pressure of water at the membrane surface on the permeate side.
4. Mass transfer from the membrane surface on the permeate side $p_{\mathrm{w.mp}}$, to the bulk permeate phase $p_{\mathrm{w.p}}$. The water vapour is carried away from the permeate channel using a sweep gas. Here, a second boundary layer is formed.
5. Permeate condensation in an outside condenser (not depicted in Figure 2.9)

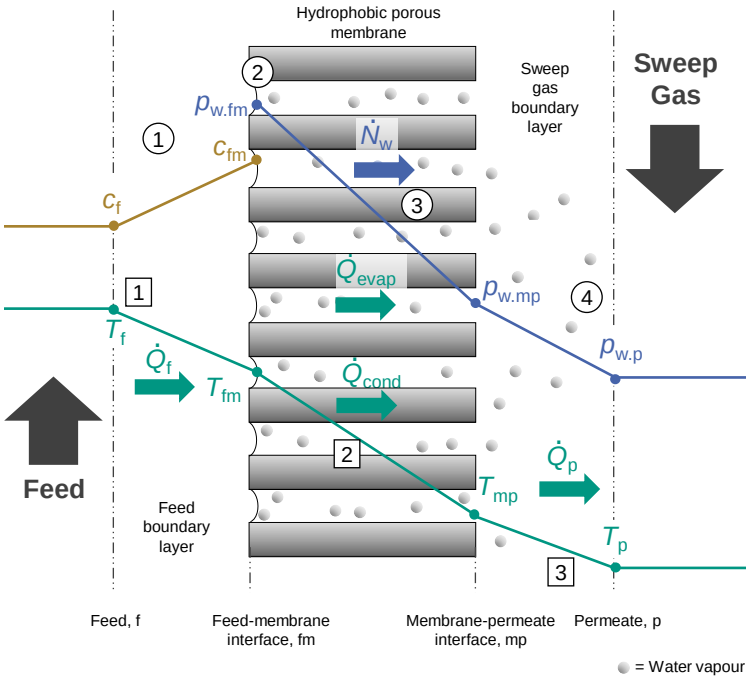

Figure 2.9.: Water partial pressure profile, temperature profile, as well as the non-volatile solute concentration profile in feed, (c_f to c_{fm}) in a membrane cell for sweeping gas membrane distillation in a counter-current configuration in steady state. Representation of the mass transfer steps (○) and heat transfer steps (□).

The heat transfer takes place in three steps [136]:

1. Heat convection in the feed compartment, $\dot{Q}_f$, from the bulk feed side T_f towards the membrane surface T_{fm}. The temperature at the membrane surface is lower than at the bulk phase due to the required heat of evaporation [141]. This phenomenon is called temperature polarization. Due to the lower temperature at the phase boundary, there is a lower vapour pressure, so that the driving force of the SGMD and therefore, the associated transmembrane flux is less than expected from T_f.
2. Evaporation of water at the prevailing feed temperature at the pore entrance (vapour-liquid interface). Here the enthalpy of evaporation of water at the given temperature applies. In addition to the latent heat, heat is also transferred through the membrane by heat conduction $\dot{Q}_{cond}$ to the membrane surface on the permeate side T_{mp}. The lower the fraction of heat conduction, the more effectively the transferred heat is used [142].
3. Heat convection from the membrane to the permeate bulk, $\dot{Q}_p$, where the sweep gas is flowing at a temperature T_p.

Mass transfer

Mass transfer through the membrane

The mass transfer coefficient of the membrane depends on the membrane geometry (thickness, tortuosity, porosity) as well as on the operating parameters (e.g. temperature and pressure) [110, 143]. This leads to different vapour transport mechanisms through the membrane pores. The prevailing transport mechanism can be determined using the Knudsen number (Kn). The Knudsen number is defined as the ratio between the mean free path (Λ) of water vapour molecules to the membrane pore diameter (d_{pore}) [111, 144, 145], cf. Equation 2.7. Since the membranes present a pore size distribution [110], several mechanisms might take place simultaneously.

$$Kn = \frac{\Lambda}{d_{\mathrm{pore}}} \tag{2.7}$$

The mean free path Λ is defined as the average distance in which a molecule travels before it collides with another molecule or a wall. It can be expressed as:

$$\Lambda = \frac{k_{\mathrm{B}} \cdot T_{\mathrm{m}}}{\sqrt{2}\pi p_{\mathrm{m}} \sigma^2} \tag{2.8}$$

where σ is the collision diameter (0.2641 nm for water vapour), k_{B} is the Boltzmann constant, p_{m} is the mean pressure within the membrane pores and T_{m} is the membrane temperature.

Based on the Knudsen number and the mean free path, there are five main mass transfer mechanisms [145, 146]. The mechanisms listed below are also depicted in Figure 2.10:

- **Knudsen diffusion** ($\Lambda > d_{\mathrm{pore}}$ or $Kn > 10$). The mean free path of the water molecules is greater than the membrane pore diameter [144], so that the water vapour molecules are more likely to collide with the pore walls.
- **Molecular diffusion**. Gas molecules present in the membrane pores hinder vapour transport along the pores. The membrane pore diameter, in this case, is larger than the mean free path of the vapour molecules ($100\,\Lambda < d_{\mathrm{pore}}$ or $Kn < 0.1$), so mostly there are collisions between water vapour molecules [111] and the gas molecules.
- **Transition region between Knudsen and molecular diffusion** ($\Lambda < d_{\mathrm{pore}} < 100\Lambda$ or $0.1 < Kn < 10$). Here, collisions occur between water vapour molecules and also between walls of membrane pores and vapour molecules [147]. The membrane is partly degassed.

- **Poiseuille or viscous flow**. The membrane pore size is larger than the mean free path ($\Lambda < d_{\mathrm{pore}}$). The collisions between the vapour molecules prevail over the collisions with the wall. In this case, the gas behaves as a continuous fluid driven by a pressure gradient.

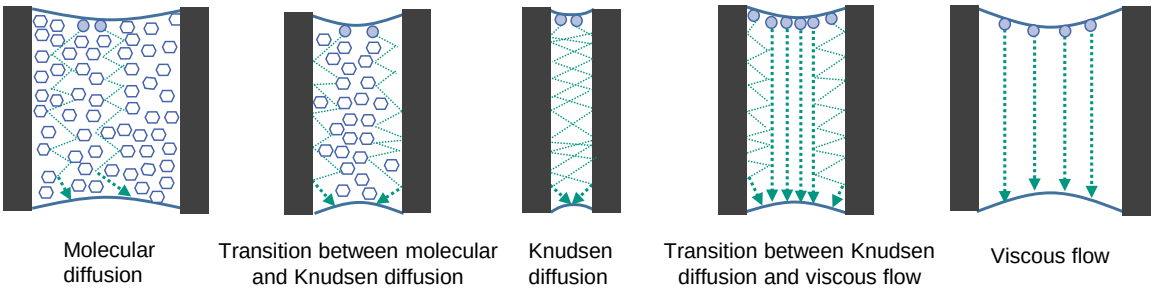

Figure 2.10.: Transport mechanisms of the water vapour molecules (symbol: ○) in pores of different diameters and air (symbol: ⬭) content, adapted from [142]

If the total pressure on both sides of the membrane is similar, the viscous (i.e. Poiseuille) type of flow is negligible [111]. For SGMD, previous investigations [148] have shown that the vapour transport across the membrane takes place via a combined Knudsen/Molecular diffusion mechanism. The diffusion coefficient for the molecular diffusion, $D_{\mathrm{w.Molec}}$ can be calculated considering the interaction of the vapour molecules with the sweep gas molecules and can be estimated according to the Fuller-Schettler-Giddings Equation [149], see Annex A.4. The diffusion coefficient for the Knudsen regime can be calculated following the approach of the kinetic gas theory from the average velocity of the particles according to Maxwell [142, 150]. The calculation of the diffusion coefficients is summarized in Table 2.3.

Table 2.3.: Diffusion coefficients based on the prevailing diffusion mechanism.

Molecular	Knudsen	Transition
$D_{\mathrm{w.Molec}}$, Fuller-Schettler-Giddings equation, see Annex A.4	$D_{\mathrm{w.Kn}} = \frac{d_{\mathrm{pore}}}{3}\sqrt{\frac{8RT}{\pi\tilde{M}}}$ (2.9)	$D_{\mathrm{w.Tr}} = \frac{1}{\frac{1}{D_{\mathrm{w.Kn}}} + \frac{1}{D_{\mathrm{w.Molec}}}}$ (2.10)

The mass transport coefficient of the membrane for vapour pressure-driven separations to be used in Equation 2.6 [151] is, therefore:

$$k_{\mathrm{m}} = \frac{\varepsilon}{\tau} \underbrace{\frac{D_{\mathrm{w}}}{\delta_{\mathrm{m}}}}_{\beta_{\mathrm{m}}} \frac{1}{RT_{\mathrm{m}}} \tag{2.11}$$

where ε represents the porosity of the membrane and τ is the pore tortuosity. The expression is divided by RT_{m} to be applied in Equation 2.6, where the driving force is the transmembrane vapour pressure difference. The convective mass transfer rate in the membrane, β_{m} is related to the diffusion coefficient, D_{w} and the membrane thickness, δ_{m}. The diffusion coefficient, D_{w} can be calculated according to the prevailing diffusion mechanism, see Table 2.3. The mass transfer rate, β_{m} can be calculated using the Sherwood number, as defined in the Equation 2.12:

$$Sh = \frac{\beta_{\mathrm{m}}\, l_{\mathrm{ch.}}}{D_{\mathrm{w}}} \tag{2.12}$$

The characteristic length of the diffusion, $l_{\mathrm{ch.}}$ is in this case the pore length, i.e. membrane thickness δ_{m}. The Sherwood number can be estimated based on the analogy between heat and mass transfer [144] and using Nusselt correlations [152, 153] (see Annex A.3).

Mass transfer in the buk phases

The mass transfer of water from the bulk feed to the feed-membrane interface, as well as from the membrane surface on the permeate side to the bulk permeate phase can be described by Fick's first law of diffusion. The diffusion through the sweep gas in the permeate compartment is:

$$\dot{N}_{\mathrm{w}} = A_{\mathrm{p}} \underbrace{\frac{D_{\mathrm{w}}}{\delta_{\mathrm{p}}}}_{\beta_{\mathrm{p}}} \frac{1}{RT_{\mathrm{p}}} (p_{\mathrm{w.mp}} - p_{\mathrm{w.p}}) \tag{2.13}$$

here the driving force is represented as the water partial difference between the membrane-permeate location and the bulk permeate, $(p_{\mathrm{w.mp}} - p_{\mathrm{w.p}})$. A_{p} is the mass transfer area in the permeate side, which, depending on the geometrical characteristics of the membrane module corresponds to or differs from the membrane area. The binary diffusion coefficient of gas (evaporated water) in gas (sweep gas) can be calculated by the Fuller-Schettler-Giddings Equation (see Annex A.4). The thickness δ_{p} is the diffusion length, which corresponds to the height of the permeate compartment.

In case a solute is present on the feed side, the mass transfer through the bulk phase towards the membrane also takes place by diffusion and can be expressed as:

$$\dot{N}_{\mathrm{w}} = A_{\mathrm{f}} \underbrace{\frac{D_{\mathrm{w}}}{\delta_{\mathrm{f}}}}_{\beta_{\mathrm{f}}} \left(c_{\mathrm{w.f}} - c_{\mathrm{w.fm}}\right) = A_{\mathrm{f}}\, \beta_{\mathrm{f}}\, \tilde{\rho}_{\mathrm{f}} \left(\tilde{x}_{\mathrm{w.f}} - \tilde{x}_{\mathrm{w.fm}}\right) \tag{2.14}$$

here A_{f} represents the transfer area related to the feed compartment, δ_{f} is the diffusive length and can be replaced by the height of the feed compartment, depending on the module geometry. The driving force is here represented as the difference in molar concentration of water between feed, $c_{\mathrm{w.f}}$ and the interface feed-membrane, $c_{\mathrm{w.fm}}$ or as the difference in molar fraction, $\tilde{x}_{\mathrm{w.f}} - \tilde{x}_{\mathrm{w.fm}}$. In the last case, the molar density is represented by $\tilde{\rho}_{\mathrm{f}}$ in Equation 2.14. For the calculation of the binary diffusion coefficient in liquids, and assuming an ideally diluted solution, the Stokes-Einstein equation can be used (see Annex A.4). The Sherwood number can be estimated employing an analogy between heat and mass transfer [153] and therefore using Nusselt correlations given in Annex A.3.

Heat transfer

The heat transfer description can be divided into heat transfer through the membrane and heat transfer across the bulk phases.

Transmembrane heat transfer

The transmembrane heat flux $\dot{Q}_{\mathrm{m}}$ is a combination of the heat transferred by convection due to the transmembrane (evaporation) flux $\dot{Q}_{\mathrm{evap}}$ and the heat transferred by conduction $\dot{Q}_{\mathrm{cond}}$ as follows [111]:

$$\dot{Q}_{\mathrm{m}} = \dot{Q}_{\mathrm{evap}} + \dot{Q}_{\mathrm{cond}} = \dot{N}_{\mathrm{w}}\, \Delta H_{\mathrm{v}} + A_{\mathrm{m}}\, \frac{\lambda_{\mathrm{m}}}{\delta_{\mathrm{m}}} \left(T_{\mathrm{fm}} - T_{\mathrm{mp}}\right) \tag{2.15}$$

Where $\dot{N}_{\mathrm{w}}$ is the transmembrane molar flow, A_{m} is the area of the membrane, ΔH_{v} is the evaporation enthalpy of water, λ_{m} is the thermal conductivity of the membrane material, δ_{m} is the membrane thickness (i.e. pore length for cylindrical pores), T_{fm} is the temperature on the membrane surface in the feed and T_{mp} is the temperature on the membrane surface in the gas channel. The effective thermal conductivity of the membrane, λ_{m} can be described by the isostrain model as follows[154]:

$$\lambda_{\mathrm{m}} = \left(\frac{\varepsilon}{\lambda_{\mathrm{p}}} + \left(\frac{1-\varepsilon}{\lambda_{\mathrm{m}}}\right)\right)^{-1} \tag{2.16}$$

Where ε is the porosity of the membrane, λ_p is the thermal conductivity of the gas mixture of water vapour and nitrogen in the permeate compartment, and λ_m is the thermal conductivity of the membrane material.

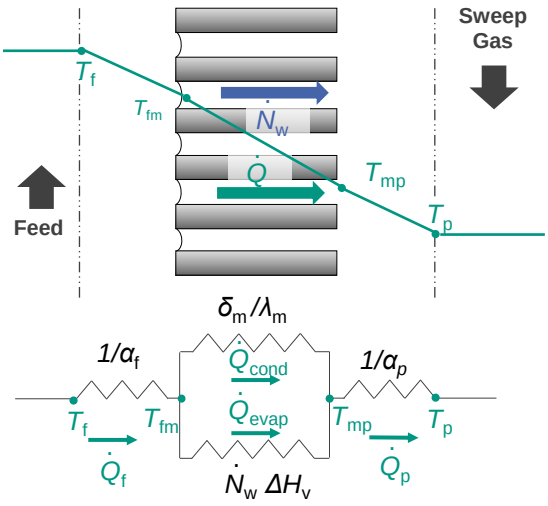

Figure 2.11.: Heat transfer resistances in sweeping gas membrane distillation.

Heat transfer in the bulk phases

Since water evaporation is an endothermic process, the temperature at the pore entrance (liquid feed-membrane interface) decreases. A thermal boundary layer is formed from the bulk temperature of the feed up to the membrane surface, which results in a resistance to mass transfer [136]. This thermal effect is called temperature polarization, and reduces the transmembrane flux and therefore the efficiency of the separation process [141]. The same phenomenon can be found in the boundary layer from the membrane surface to the bulk permeate side.

The heat transfer by convection across the feed ($\dot{Q}_f$) and permeate ($\dot{Q}_p$) boundary layer can be calculated as:

$$\dot{Q}_f = A_f \alpha_f \left(T_f - T_{fm}\right) \tag{2.17}$$

$$\dot{Q}_p = A_p \alpha_p \left(T_p - T_{mp}\right) \tag{2.18}$$

where α_f and α_p are the heat transfer coefficient of the feed and permeate side boundary layer, respectively. The temperatures on the feed side are represented by T_f (temperature of the bulk feed) and T_{fm} (the temperature at the interface feed-membrane). On the permeate side, T_p is the temperature of the bulk permeate and T_{mp} is the temperature at the interface

membrane-permeate. The heat transfer coefficients of the feed and permeate side can be calculated from the Nusselt number as follows:

$$\alpha = \frac{Nu\ \lambda}{d_{\mathrm{h}}} \tag{2.19}$$

Where λ is the thermal conductivity of the fluid and d_{h} is the hydraulic diameter of the channel. Nusselt correlations for microchannels and narrow slits can be found in Annex A.3.

In steady state, without heat loss:

$$\dot{Q}_{\mathrm{f}} = \dot{Q}_{\mathrm{p}} = \dot{Q}_{\mathrm{m}} \tag{2.20}$$

applies [146].

3

Intensification of the polycondensation reaction in a double-pipe heat exchanger with internal inserts

As already mentioned, the characteristics of the FGE [21] inserted in a double-pipe reactor are expected to enhance the heat transfer performance under low pressure drop. In this chapter, the effect of several operating parameters and reactor settings on the polysaccharide yield is investigated. Therefore, the double-pipe reactors fitted with internal inserts as well as the experimental set-up used for the polycondensation reaction are described. Moreover, the results regarding the effect of process parameters like temperature, pressure, feed concentration and residence time on the polysaccharide yield, when internal inserts based on the FGE geometry are implemented in the reactor, are outlined in this chapter. Finally, different FGE geometries are compared in terms of yielded polydextrose. Parts of this chapter are based on the publication of Claramunt et al. [155].

3.1 Experimental methodology

3.1.1 Double-pipe heated reactor with internal inserts

Table 3.1 shows the most significant dimensions of the heat exchangers. In the inner pipe (inner diameter: 10 mm), as well as in the 3 mm annular gap formed between the inner and outer tubes, FGE manufactured according to [20, 21] were used. Heat transfer oil flowed into the annular gap while the reactive glucose solution flowed in counter-current in the inner pipe. Three reactors with different lengths were used. The length designation of 30, 40 and 50 cm refers to the approximate contact length between the heat transfer oil with the inner pipe.

Table 3.1.: Common dimensions of the internal and external pipes of the different reactors used in this study. HE-01 with two heat exchangers connected in series (30 + 40 cm) and HE-02 with 50 cm.

Tube	Outer diameter	Inner diameter	Wall thickness	Contact length
Inner	12 mm	10 mm	1 mm	30 + 40 cm / 50 cm
Outer	18 mm	15 mm	1.5 mm	

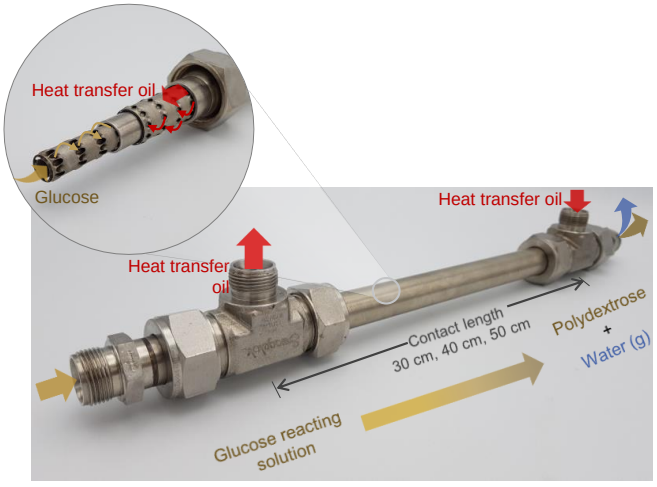

Figure 3.1.: Double-pipe reactor with the glucose reacting solution in the inner pipe, and the heat transfer oil in the annular gap. The glucose solution reacts to form polydextrose and water. The latter is in vapour state under reaction conditions. A detailed picture shows the system inside the reactor: FGE in the inner pipe distributes the flow of glucose, while annular FGE in the space between the two concentric tubes distributes the flow of the heat transfer oil.

Three different FGE geometries were tested in the inner pipe (reaction side), while the FGE geometry for the annular gap (oil side) was kept unmodified. For the design of the different FGE geometries, the repetition length as well as the length between the blades were varied, so that different shapes and lengths of the repeating units (i.e. fluid guiding units, FGU) were obtained. Different FGU lengths for the given common FGE length (55 mm) resulted in a different amount of FGU for the different FGE types. The geometrical characteristics of the three different FGE in the inner pipe are detailed in Table 3.2 and depicted in Figure 3.2. The starting geometry of the experiments was type A (left in Figure 3.2), which had a repetition length of 9 mm (black bar in Figure 3.2). This geometry was selected for having already high performance in other applications [21]. In type B (middle), the repetition length was reduced from 9 to 6 mm so that the partial flows alternate more frequently over the same length, aiming at a more unsteady flow that could increase heat transfer. In type C, the number of partial flows was reduced to two, which alternate constantly, so that there are no longer straight pipe sections. The repetition length is 9 mm, as in type A, so that the contact length for the partial streams remains the same, but the layer thickness is significantly greater. This design was expected to provide more space for the evaporation of water and thus reduce its concentration in the liquid co-existing phase. The internal inserts have been manufactured using stainless steel powder (316 L) with a particle size between 5 and 45 µm, using the PBF-LB/M-System Realizer SLM125 (DMG Mori, DE).

Table 3.2.: Geometry parameters of the different FGE types.

Type	Number of partial streams	Repetition length (FGU)	Number of FGU	Void fraction	Length of a FGE
A	3	9 mm	6	89 %	
B	3	6 mm	9	88 %	55 mm
C	2	9 mm	6	91 %	

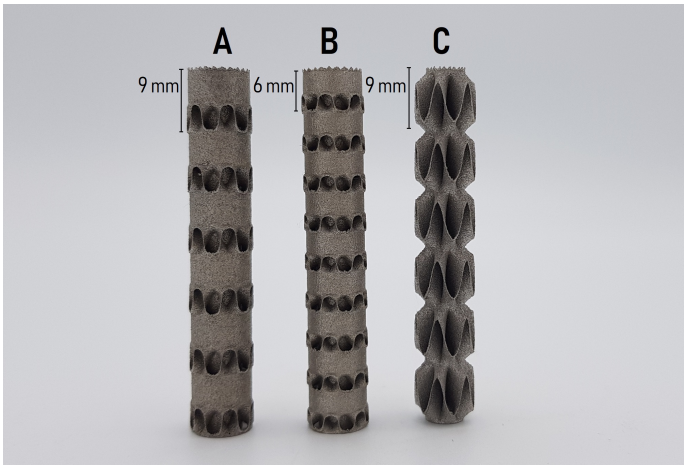

Figure 3.2.: FGE types used in this study. From left to right: A - B - C.

3.1.2 Experimental set-up

For the production of polydextrose in lab-scale, the experimental set-up depicted in Figure 3.3 was used. Details about the equipment used can be found in Annex A.5. In the experimental set-up, the reacting solution and rinsing water were stored in two double-jacketed tanks (Storage tank 1 and storage tank 2 in Figure 3.3) and heated by a thermostat each. The temperature was maintained in the supply line from the tanks to the reactor by heating cords. An eccentric screw pump (P-01) supplied the solution into the plant. The pump flow was measured by a Coriolis flow meter (FI 01).

Double-pipe heat exchangers of different lengths were available as reactors (see Table 3.1). They could be arranged in any order. The two configurations investigated more thoroughly in this work (HE 01 and HE 02) are indicated in Figure 3.3 by boxes with a dash-dotted frame, i.e. the 30 cm long reactor followed by the 40 cm long reactor (70 cm, HE 01 configuration) or the 50 cm reactor (HE 02 configuration) used as a stand-alone reactor. Pressure and temperature were measured upstream and downstream of each reactor.

A back pressure regulator (VC 01) was installed downstream of the reactors to adjust the pressure in the system. The adjoining pipes were also heated externally by heating cords. This configuration led to 9 cm of bare pipe and 14 cm of insulated length between the reactor outlet and the pressure regulator. The reactors themselves were heated in counter-current with heat transfer oil using a thermostat. The temperature of the oil was measured at each reactor, both at the inlet and the outlet (TI 09 to TI 14). The mass flow rate of the heat transfer oil was controlled by a needle valve (V3). To measure the mass flow, the oil coming from the thermostat was led through a Coriolis flow meter (FI 02) before it entered the heat exchanger. The product of the reaction was collected at ambient pressure in a stirred water

bath, placed after the back pressure regulator. Samples of the product were taken at the outlet of the pipe before the product ended in the water bath.

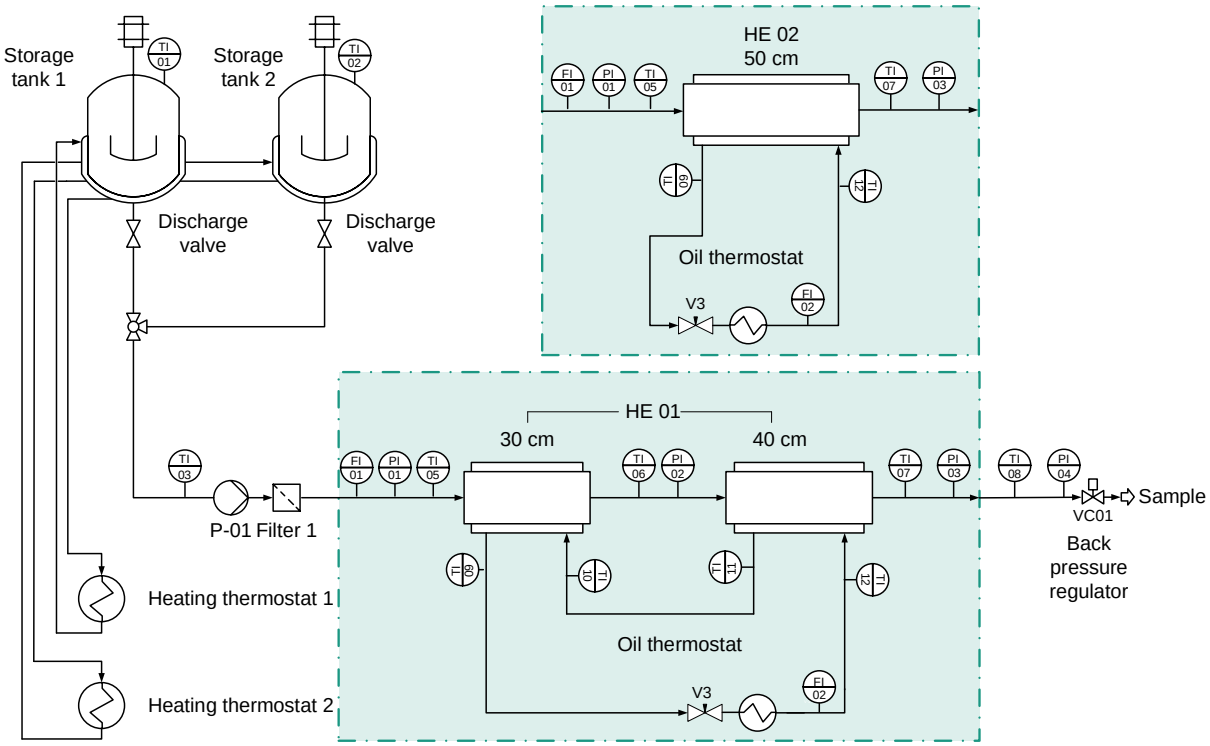

Figure 3.3.: P&ID of the experimental plant for the production of polydextrose in double-pipe reactors fitted with internal inserts.

3.1.3 Experimental procedure

To investigate the impact of internal inserts on the polysaccharide yield in the double-pipe reactor configuration, the experiments were conducted according to the procedure described hereafter and depicted in Figure 3.4:

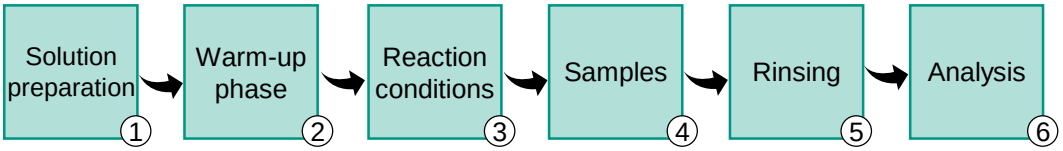

Figure 3.4.: Overview of the steps conducted during the experimental investigation of the polycondensation reaction in a double-pipe reactor.

1. **Solution preparation.** The first step consists of preparing the feed solution with glucose and deionized (DI) water. For each experiment, the solutions were prepared in storage tank 1 and heated to 80 °C to increase solubility. At the highest glucose concentration (i.e. 80 wt. %), 90 °C were required for the glucose to be soluble in water.
2. **Warm-up phase**. Thirty minutes before the start of the experiments, the heating cords and the oil thermostat were switched on to ensure that the reactors and surrounding pipes were brought to the target temperature. At the same time, heated DI water from the storage tank 2 was pumped through the system at a pressure of at least 3 bar g and a set temperature of the oil thermostat of 120 °C, to increase the temperature of the reactor pipe material. When the set temperature was reached, 1 wt. % of catalyst (citric acid) was added to the storage tank 1. The pump feed was then switched from storage tank 2 (DI water) to storage tank 1 (reacting glucose solution).
3. **Reaction conditions**. Different experiments were conducted to determine the effect of the glucose concentration in the feed (50-80 wt.%). In addition, the reactor setting was varied, using two reactors lengths: 70 cm or 50 cm. The influence of the type of inserts was also investigated, as well as the effect of using no inserts (type 0) in the reactor. The oil set temperature was varied between 180 and 235 °C, the system pressure was set between 1 and 3 bar g, and the pump was adjusted to deliver feed mass flow rates between 1.5 and 2.5 kg h^{-1}. A summary of the operating conditions is given in Table 3.3.
4. **Samples**. Each operating point was held between 15-25 min to reach a steady state. When sampling, the product was mixed with cold DI water and neutralized with sodium hydroxide up to a pH value > 5 to prevent further reaction.

Table 3.3.: Operating conditions during the experiments for the production of polydextrose.

Set glucose solution /wt. %	Reactor setting /cm	Type of inserts	Oil set temperature / °C	Pressure /bar g	Feed mass flow rate /kg h^{-1}
50, 60, 70, 80	70, 50	A, B, C, 0	200, 210, 220, 230, 235	1.5, 2, 2.5, 3, 4	2, 3.15, 3.50, 3.75

5. **Rinsing**. After completion of each experiment, the reactors were rinsed with water and cooled down. Proper flushing of the set-up is very important to avoid blockages in the reactors or the piping due to glucose precipitation. For this purpose, the feed was switched back to the DI water from storage tank 2, the inlet pressure was increased

above 3 bar g to ensure the liquid state of the rinsing water, and the pump speed was increased. The oil thermostat was switched off and the residual heat was used to flush the reactor at temperatures above 150 °C.

6. **Analysis**. The samples were analyzed externally by the project partner using HPLC according to an established method [156]. The polysaccharide yield was determined as the total of oligomers having a degree of polymerisation DPn ≥ 2 (polymerized glucose). The amount of the byproducts in the final product was also determined, i.e. 6-anhydroglucose, hydroxymethylfurfural, and furfural, as well as non-reacted glucose.

It has to be mentioned that the density of the reaction medium, the glucose solution, is not constant along the reaction path because of the evaporation of water in the reactor. For an accurate determination of the residence time, the course of the density of the reaction mixture over the reactor length should be known. Nevertheless, the kinetics of evaporation in the reactor are difficult to determine. Therefore, in order to have a reference value to evaluate the experimental results, the residence time was calculated as the formal hydrodynamic residence time of liquid water at NTP conditions.

3.2 Results and discussion

The results regarding the effect of several operating parameters and reactor settings on the polysaccharide yield are shown and discussed. The European Commission regulates the composition of the polydextrose [7], see Annex A.1. 90 % of oligomers with a degree of polymerisation DPn≥2 is required to comply with these regulations. For this reason, a polysaccharide yield of 90 % is labelled in the graphs of the present chapter as the target yield. The visual product characteristics are also elucidated at the end of the chapter.

3.2.1 Effect of temperature and pressure

To determine the influence of temperature and pressure on the polysaccharide yield, the oil temperature was increased in steps of 5 °and 10 °C from 200 °C up to as high as 225 °C in the 70 cm reactor configuration. At each temperature level, samples were taken at pressures between 2 and 3 bar g. Figure 3.5 shows the effect of the temperature and pressure on the polysaccharide yield for a constant mass flow rate of 3.15 $kg\,h^{-1}$ ± 0.1 $kg\,h^{-1}$, which

corresponds to a formal hydrodynamic residence time of 89 s ± 2 s. In Figure 3.5 (a), the polysaccharide yield is plotted against the average temperature at the reactor outlet (measured by the thermocouple at the reactor outlet, TI 07). This temperature was always the highest temperature measured in the reactor. The point clusters confirm that higher temperatures lead to higher polysaccharide yields. Besides, it can be observed, that the higher the polysaccharide yield, the smaller the scatter in the y-direction becomes. From this observation, it can be concluded, that small differences in temperature and residence time have less influence on the polysaccharide yield, the closer the reaction is to the equilibrium. In Figure 3.5 (b), the polysaccharide yield is plotted against the pressure at the reactor outlet. Comparing the points at the same oil set point temperature, it can be seen that lower pressures lead to higher polysaccharide yields. The reason for this is probably the increased water evaporation at lower pressures. The glucose is only in the liquid phase and the reaction, thus, only takes place in the liquid phase. As the pressure is reduced, more water evaporates, which leads to lower water concentrations in the liquid phase. At higher temperatures, the equilibrium lies already at higher polysaccharide yields anyway, so that the pressure effect is less pronounced.

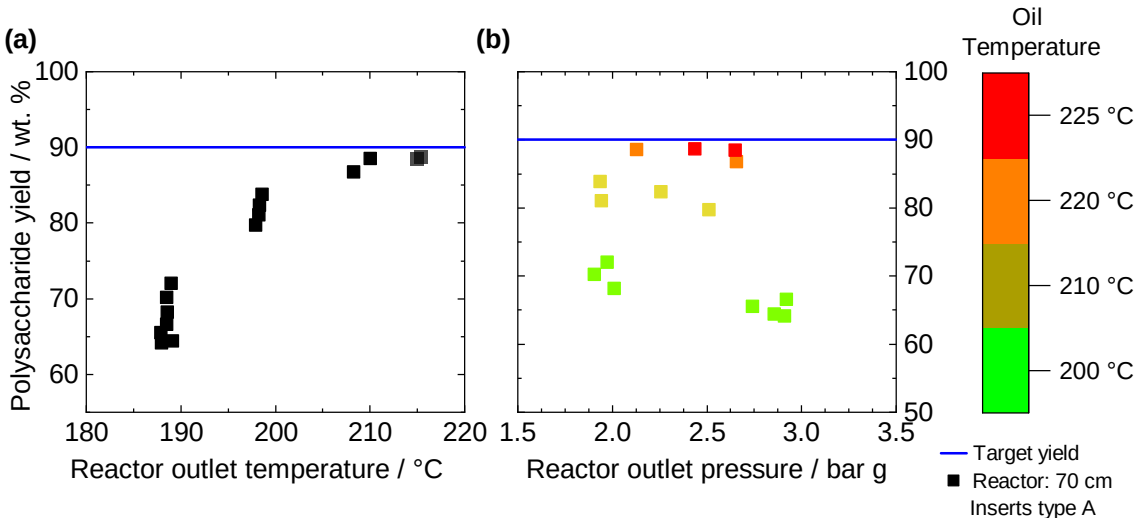

Figure 3.5.: Polysaccharide yield for **(a)** different reaction temperatures and **(b)** different pressures at the reactor outlet with mass flow rates of 3.15 kg h^{-1} ± 0.1 kg h^{-1}. The colour scale refers to the oil set temperature.

3.2.2 Effect of glucose concentration in the feed

Considering the previous studies in a microreactor with microchannels which led to the patent EP 2528950 [18], it was expected that higher mass fractions of glucose in the feed would have a positive effect on the polysaccharide yield. More water in the feed should influence the reaction equilibrium in such a way that less glucose can react. However, in the current study, the mass fraction of glucose in the feed was found to have almost no effect on the polysaccharide yield and thus on the local reaction equilibrium. Figure 3.6 displays the polysaccharide yield as a function of the glucose concentration in the feed (% in mass) for different oil temperatures. For instance, as shown in Figure 3.6, at an oil temperature of 220 °C, polysaccharide yields of 85 wt. % are reached at a glucose concentration in the feed of 60 wt. %, while at 80 wt. % of glucose concentration in the feed, 88 wt. % of the product is yielded. In the set of experiments shown in Figure 3.6, the same pump speed was always set. This means that higher feed concentrations and thus higher densities lead to an increase in the mass flow rate. Consequently, this fact leads to shorter residence times for higher feed concentrations. This could be one of the reasons for the similar polysaccharide yield values at different feed concentrations.

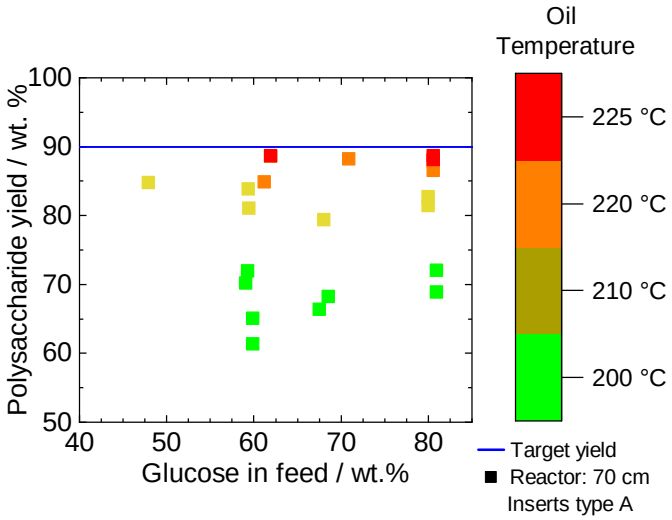

Figure 3.6.: Polysaccharide yield for different glucose concentrations in feed. Only samples for p_{out}=2 ± 0.4 bar g in the 70 cm reactor are shown. The colour scale refers to the oil set temperature.

At the prevailing inlet temperatures and pressures in the current study, the water is probably already evaporated only a few pipe diameters after the reactor inlet. Assuming that water no longer plays a decisive role in reaching the equilibrium due to its immediate evaporation, other hypotheses may emerge regarding the influence of the glucose concentration in the feed:

- On the one hand, it can be considered that the two phases (water vapour and reacting glucose) do not separate so that the phase velocities are dependent one on the other, e.g. in the case of foam formation. Under those circumstances, lower water contents in the feed should lead to higher residence times, because the volume of water is lower. Due to longer residence times (and less water in the reaction mixture), the polysaccharide yield should therefore rise with increasing glucose concentration.
- On the other hand, assuming the flow velocity of the two phases to be almost independent (e.g. with the formation of an annular flow), an increase in glucose concentration could possibly be accompanied by a higher residence time of the reacting phase, due to the increase in mass flow rate.

However, none of these cases could be observed.

The residual content of unreacted glucose was 9 wt. % for the case of 50 wt. % glucose in the feed and 2 wt. % for the case of 80 wt. % glucose in feed. The content of 1,6-anhydroglucose shows no trend with the amount of glucose in the feed. In all cases, the amount of 1,6-anhydroglucose remains below the limits given by the regulations. A diagram about the effect of the glucose content in the feed on the amount of 1,6-anhydroglucose in the final product can be found in Annex A.6.

3.2.3 Effect of residence time

The influence of the residence time on the polysaccharide yield was also investigated. Experiments were conducted at the same mass flow rate for two different glucose concentrations with reactors of different lengths. Figures 3.7 (a) and (b) display the polysaccharide yield obtained with the 70 cm reactor setup (squares) and with the 50 cm reactor (crosses) against the temperature at the reactor outlet. Figure 3.7 (a) shows the results for a feed concentration of 80 wt. % and a common mass flow rate of 3.70 $kg\,h^{-1} \pm 0.05\ kg\,h^{-1}$, while Figure 3.7 (b) illustrates the polysaccharide yield for a glucose concentration of 60 wt. % and a common mass flow rate of 3.10 $kg\,h^{-1} \pm 0.05\ kg\,h^{-1}$. In both cases, only results obtained at a reactor outlet pressure of 2 ± 0.5 bar g are shown. As expected, for a given feed concentration, i.e. 80 wt. %, and a common mass flow rate, i.e. 3.7 $kg\,h^{-1} \pm 0.05\ kg\,h^{-1}$, the polysaccharide yield is higher with the longer set-up (70 cm), which is due to the longer residence time that a larger reactor volume is expected to provide. Note that this difference in polysaccharide yield between the reactors is more pronounced at lower temperatures. This can be seen, for example, in Figure 3.7 (a), where the difference in polysaccharide yield between both reactor lengths is much higher at an oil set temperature of 200 °C (difference in polysaccharide yield of 18 wt. %) than at 220 °C (difference of 4 wt. %). In fact, it can be concluded that at

higher temperatures, the impact of the reactor length, and thus, the formal hydrodynamic residence time, is less dominant at set points closer to the reaction equilibrium location (i.e. at higher temperatures), because the conversion is already limited by the equilibrium. It can be seen that the same oil set temperature always results in almost 5 °C higher reactor outlet temperature in the larger reactor (70 cm). However, since the difference of the outlet temperatures between both reactors remains almost constant (even at higher temperatures) this can not be considered a plausible reason for the residence time independence of the yield at higher temperatures. Figures 3.7 (c) and (d) compare both reactors for different formal hydrodynamic residence times (between 50 s and 150 s).

From Figures 3.7 (c) and (d) it is clear that higher formal hydrodynamic residence times lead to higher polysaccharide yields at a constant temperature. However, considering also the impact of the reaction temperature, it is clear that the latter has a dominant impact on the desired yield. If the reaction rate increases strongly with temperature, it is conceivable that only the residence time within the zone with the highest temperature is responsible for most of the glucose conversion. The effect on the polysaccharide yield visible in Figures 3.7 (c) and (d) is thus a superposition of the effects of the residence time and the reaction temperature, which itself depends on the residence time of the mixture in the reactor.

As a comparative value, the literature results of the polysaccharide yield achieved with a single microchannel reactor (µchannels, 1-stage reactor) as used in Example 2 in the patent EP 2528950 [18], are given and marked with a star in Figures 3.7 (a) and (c). In that case, a polysaccharide yield of 54.7 wt. % was obtained for a glucose concentration in the feed of 80 wt. %. The hydrodynamic residence time was given as 70 seconds, which is only about 5 seconds shorter than in the comparable experiments of the current study. This corresponds to approximately 5 % deviation. Furthermore, the patent describes the example of a two-stage reactor process. In this case, the stream is circulated through an expansion chamber before entering the second reactor. In the chamber, the water is partly evaporated and removed to increase the degree of polymerization of polydextrose in the second reactor. Despite these additional steps, the final polysaccharide yield reported in the patent (Example 3 in the patent EP 2528950 [18]) is only 80 wt. % (µchannels, 2-stage reactor in Figure 3.7(a) and (c), marked with stars), and thus clearly below the values achieved in this work.

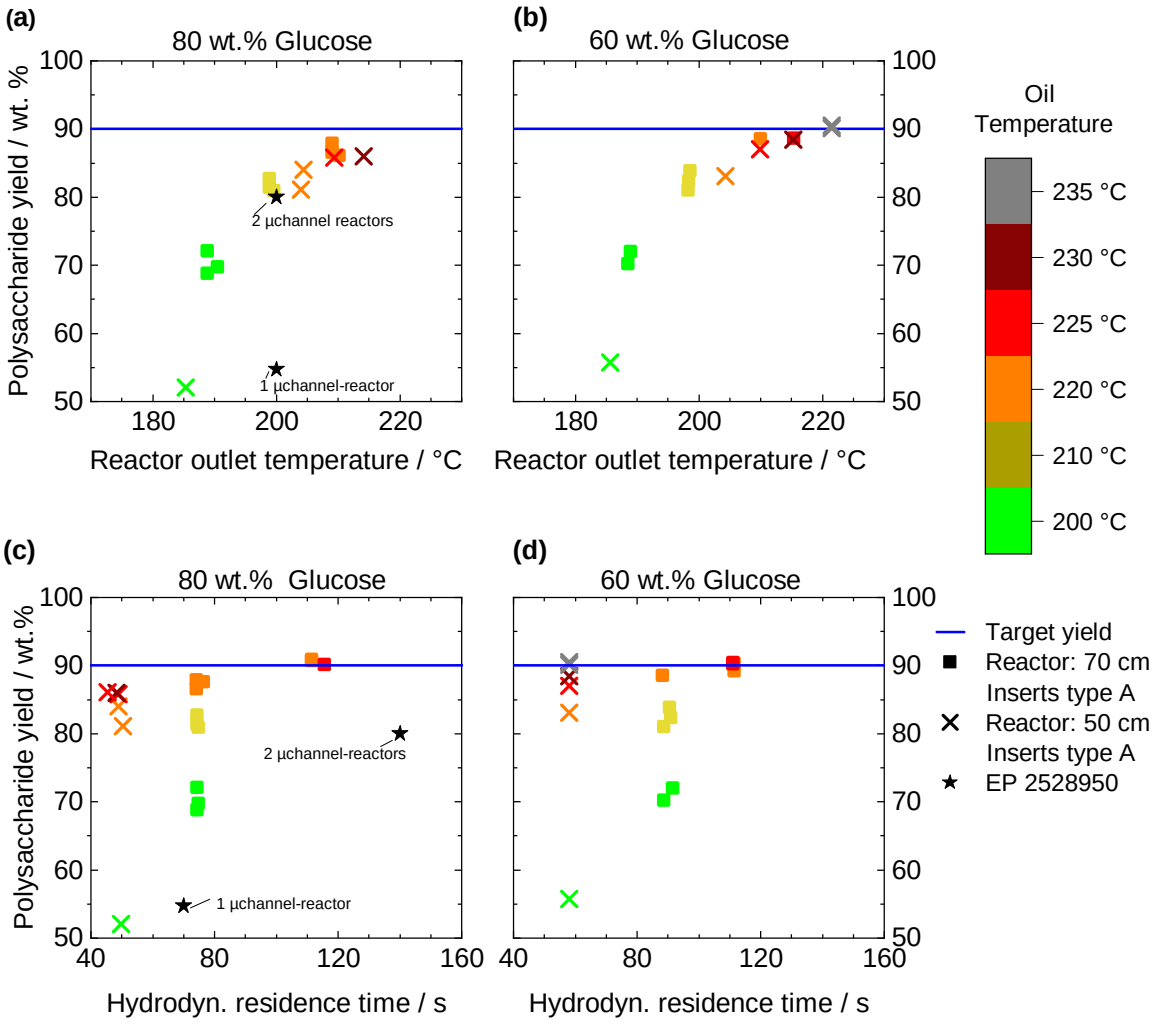

Figure 3.7.: Polysaccharide yield vs. outlet temperature for **(a)** 80 wt. % glucose solution in the feed and **(b)** 60 wt. % glucose solution in the feed. Polysaccharide yield vs. hydrodynamic residence time for **(c)** 80 wt. % glucose solution in the feed and **(d)** 60 wt. % glucose solution in the feed. The results in a 70 cm reactor are compared with the results in a 50 cm reactor. The pressure was 2 ± 0.5 bar g and the mass flow rate 3.70 kg h^{-1} ± 0.05 kg h^{-1} (80 wt. % glucose) and 3.10 kg h^{-1} ± 0.05 kg h^{-1} (60 wt. % glucose). Literature values according to the EP 2528950 [18] are given for comparison.

3.2.4 Effect of internal insert geometry

In Figure 3.8, an empty 50 cm reactor is compared with a 50 cm reactor filled with internal inserts of type A. Here, the polysaccharide yield is shown as a function of the temperature at the reactor outlet, for a 60 wt. % glucose solution in the feed and the same mass flow rate, i.e. 3.15 kg h^{-1}. Since the set oil temperatures were the same, it can be seen in Figure 3.8

that the internal inserts contribute to the intensification of the process and therefore to the increase of the polysaccharide yield.

The values obtained with an empty reactor at 235 °C (grey circle in Figure 3.8(a)) are close to those obtained with the reactor fitted with internal inserts at 220 °C oil temperature (orange crosses). Moreover, in Figure 3.8 (a), the enhancing effect of the internal inserts on the heat transfer can be seen. Without internal inserts, the reaction temperature (reactor outlet temperature) at an oil set temperature of 235 °C is only 200 °C (grey circle), while the temperature reached at the reactor exit at the same oil set temperature is approx. 220 °C when the reactor is fitted with inserts (grey crosses). Hence, the inserts clearly contribute to the enhancement of heat transfer. Figure 3.8 (b) shows that higher hydrodynamic residence times (in the empty reactor) do not necessarily lead to higher polysaccharide yields; at a reactor outlet temperature of 200 °C, the equilibrium might already have been reached. Therefore, the earlier conclusion that temperature is the most important influencing factor in this process is once again confirmed.

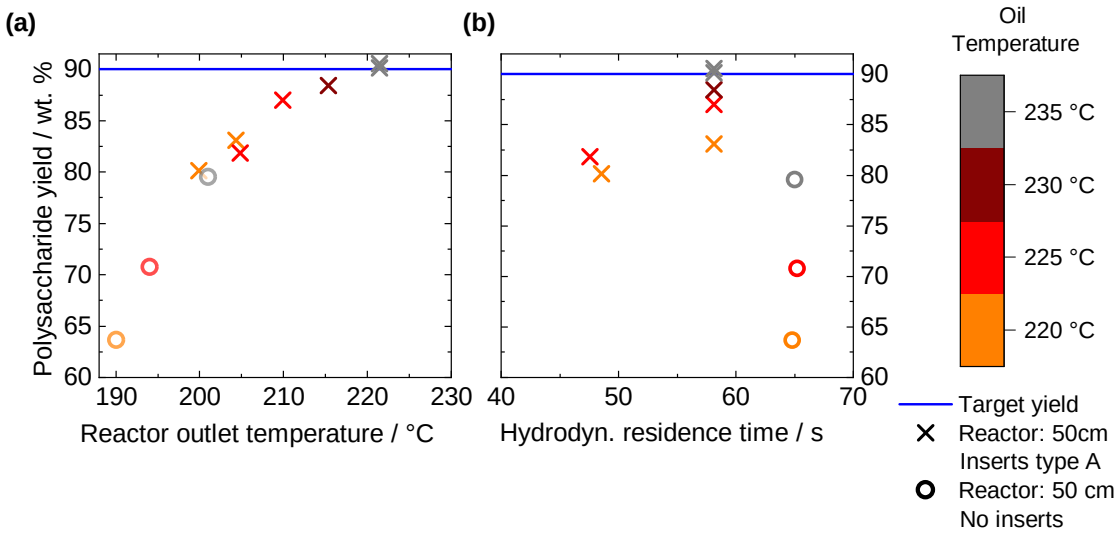

Figure 3.8.: Comparison of the polysaccharide yield versus **(a)** temperature at the reactor outlet and **(b)** hydrodynamic residence time using inserts type A and no inserts (empty reactor) in a 50 cm reactor, for 60 wt. % glucose in the feed, with a mass flow rate of 3.15 kg h^{-1} ± 0.5 kg h^{-1} and pressure in the range of 2± 0.3 bar. The colour scale represents oil set temperatures.

Three different FGE geometries were manufactured (see Figure 3.2 and Table 3.2). Comparing the geometry of type B with type A, the partial flows alternate more frequently over the same length. More frequent alternation means more frequent renewal of the inflow effect so it was expected that the heat transfer would be better for type B. In type C, the contact lengths for the partial streams remain the same as in type A, but the layer thickness is considerably larger. Therefore, a reduction in heat transfer was expected in this case.

Considering the total volume of the 50 cm reactor and taking into account the void fraction of each FGE geometry mentioned in Table 3.2, the volume decreases by 1.3 % for the inserts of type B and increases by 1.0 % for the inserts of type C, compared to the reactor equipped with type A inserts. Therefore, it seems justified to assume that the effect on the polysaccharide yield due to the use of the different types of internals is primarily due to the differences in geometry and not to the differences in hydrodynamic residence time caused by the variation of the void fraction. Figure 3.9 illustrates the glucose conversion determined experimentally in a 50 cm reactor fitted with inserts of the three different geometries as a function of the temperature at the reactor outlet (feed: 60 wt. % glucose solution, mass flow rate: 3.15kg h^{-1} ± 0.5kg h^{-1}).

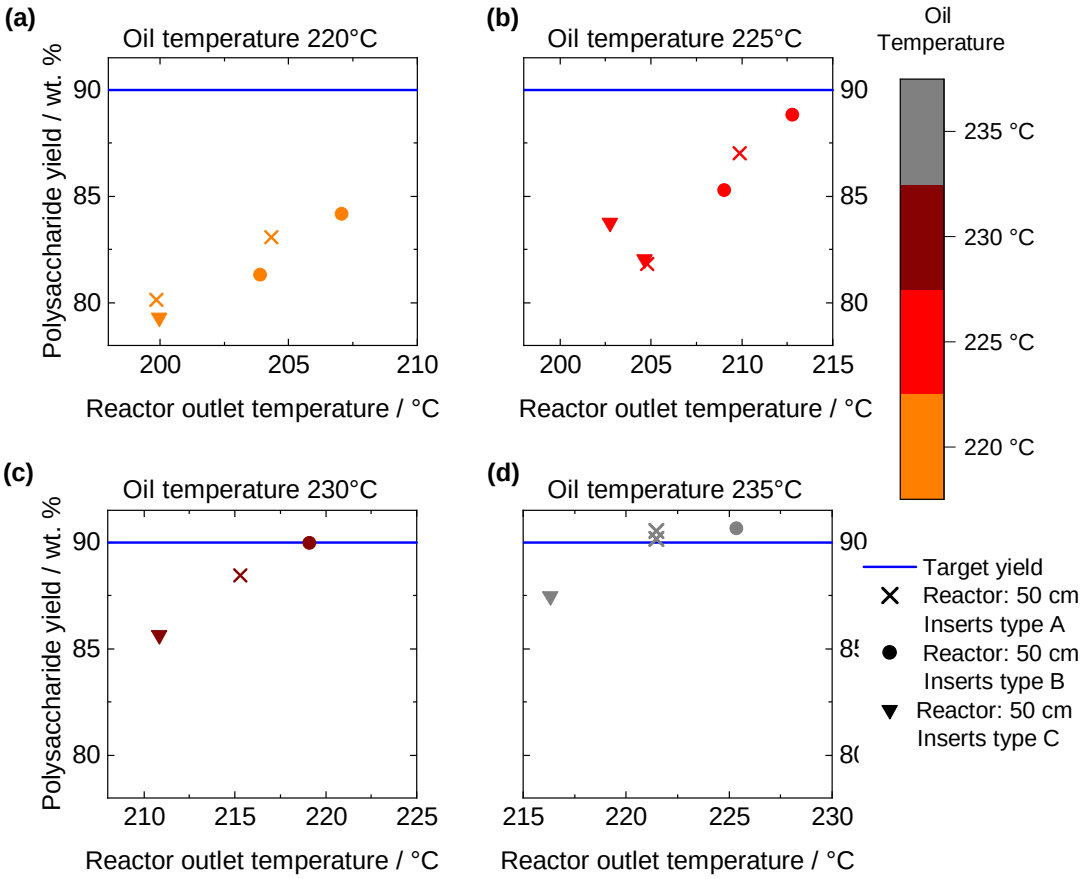

Figure 3.9.: Comparison of the polydextrose yield over **(a)** the temperature in the reactor and **(b)** the hydrodynamic residence time for three different types of internal inserts in the reactor. All values were obtained with the 50 cm reactor, the pressure at the outlet, p_{out} was 2 ± 0.3 bar g, the mass flow rate was 3.15 kg h^{-1} ± 0.5 kg h^{-1} and the glucose concentration in the feed was 60 wt. %.The colour scale refers to the set oil temperature.

At the same oil set temperatures, it is noteworthy (Figure 3.9) that outlet temperatures of the reaction mixture vary consistently in the same order (B>A>C). It is known that these systems provide an improvement in heat transfer at the expense of pressure drop. Actually, at the same mass flow rate, a pressure drop of 0.45 bar was measured for the reactor with FGE type B, 0.25 bar for the reactor fitted with FGE type A, and a pressure drop of 0.12 bar was recorded for type C. These values are significantly lower than the pressure drop values measured for the device used in the previous patent [18], which were in the range of about 2 bar.

3.2.5 Product characteristics

As the temperature rises, the properties of the product change significantly. This section is intended to give an insight into the properties of the product as it leaves the reactor. The temperatures mentioned refer to the oil set temperatures unless otherwise stated. Initially, at 200 °C, the properties of the molten glucose predominate: droplets can be seen at the reactor outlet, which are carried by the gas flow. As the temperature increases, the droplets become more viscous, so that from 220 °C on they become elongated and are partly connected by filaments. The product appearance changes from transparent to milky. This is an indication that foam is being formed (see Figure 3.10). Up to this point, the product was almost colourless, but at temperatures above 220 °C, a typical caramel-brown colour increasingly develops (cf. Figure 3.11).

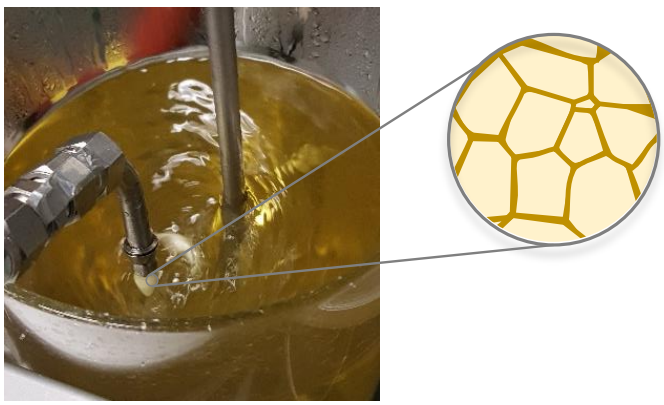

Figure 3.10.: Product appearance at the reactor outlet before being discharged in the stirred water bath. The product has a foam-like appearance due to the water evaporating inside the reactor. The detail in the image depicts a sketch of a foam-like structure.

Above 220 °C, the foam usually looks popcorn-like or puffed, with the product usually forming a continuous filament from the end of the tube to the product vessel. Unlike the compact drops from the beginning, which take a long time to dissolve, the foam acquires a porous structure in contact with water, so that it dissolves much more easily. At 230 °C or 235 °C, a smooth shell of condensed product forms around a foamy core; drops of up to about 3 cm in diameter are formed, which are connected by thin threads. When hot, the product is flexible and can form very long thin threads. When cooled down, it is hard and brittle.

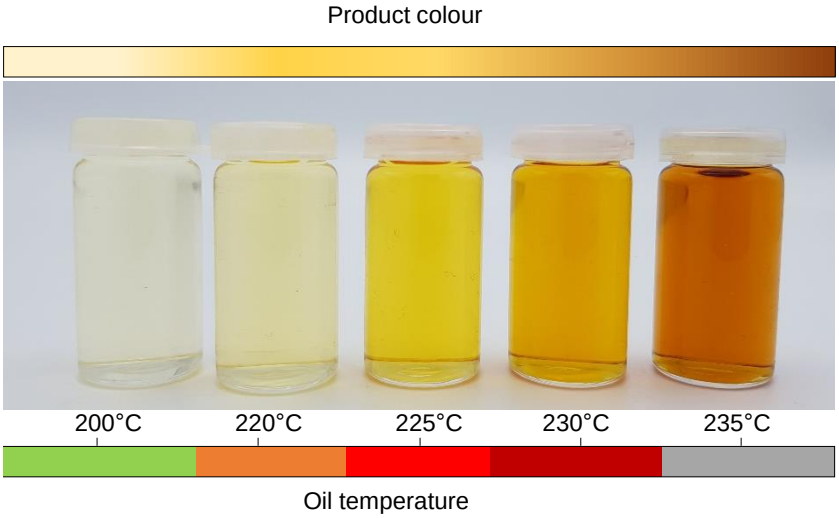

Figure 3.11.: Product samples for increasing oil set temperature and therefore reaction temperature from left to right. Higher reaction temperatures led to a browner colour.

3.3 Summary of Chapter 3

In this chapter, the performance of PBF-LB/M-manufactured regularly structured inserts, known as FGE, was studied. Two double-pipe reactor configurations with lengths of 70 cm and 50 cm were equipped with these inserts to investigate their suitability for the production of polydextrose. First, the impact of the overall process conditions on the polysaccharide yield achieved in a reactor with a given geometry of FGE (type A) was investigated. From the results, it could be confirmed that higher temperatures and lower pressures led to higher polysaccharide yields. Besides, the increase in residence time and reaction temperature had a clear positive influence on the polysaccharide yield. Higher polysaccharide yields were only possible at higher reaction temperatures, or more precisely: to achieve polysaccharide

yields of more than 90 wt. %, reaction temperatures of at least 220 °C were required. A possible cause for this observation is an equilibrium limitation. The obtained polysaccharide yield was almost independent of the mass fraction of glucose in the feed in the range of 50 wt. % to 80 wt. %. The comparison of different insert geometries showed that when a more fine-structured geometry was used for the inserts (type B), the temperature of the reaction mixture at the reactor outlet got increased, which led to higher polysaccharide yields.

4

Fabrication and characterization of hydrophobic coatings on metallic membranes

The naturally hydrophilic surface properties of metallic membranes can be modified by the application of a functional layer. In this work, the fabrication of high-temperature-resistant hydrophobic coatings on metallic membranes has been investigated by means of two different methods: the plasma enhanced-chemical vapour deposition (PE-CVD) of silicon-doped diamond-like-carbon thin films (also known as Si-DLC) and the direct immersion in a fluoroalkyl silane compound (FAS) using the dip coating technique. Figure 4.1 displays an overview of the methods used for the fabrication of these hydrophobic coatings. The coatings were characterized qualitatively and quantitatively in terms of resulting contact angle, resistance to elevated temperatures, and liquid entry pressure. The coating techniques and the experimental characterization of the resulting thin films are described in more detail in this chapter. Parts of this chapter are based on a publication of Claramunt et al. [24].

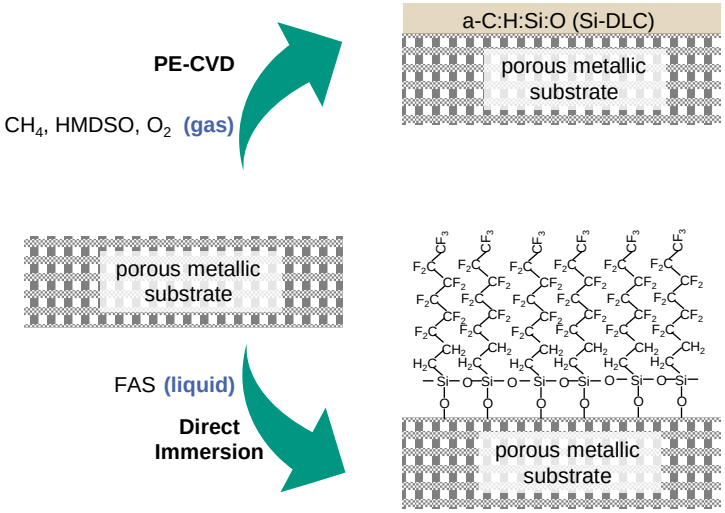

Figure 4.1.: Overview of the coating methods investigated in this dissertation.

4.1 Experimental methodology

4.1.1 Plasma enhanced - chemical vapour deposition (PE-CVD) of thin films

General description

Chemical vapour deposition (CVD) is a deposition process for the fabrication of thin films (thickness < 1 µm) [157] on a substrate by chemical reaction of vapour-phase precursors, usually initiated by heat [158]. First, these reactions in the gas phase produce reactive intermediates and byproducts which are then adsorbed on the substrate surface. These species further react with the substrate surface leading to nucleation and film growth [159] and to byproducts, which subsequently desorb. At lower temperatures, the growth rate is controlled by the kinetics of the chemical reactions (according to Arrhenius) and uniform thicknesses can be achieved [159]. One way of reducing the required temperature for sufficiently fast growth is by providing the energy through plasma, i.e. plasma enhanced - chemical vapour deposition (PE-CVD). In the PE-CVD, a high-frequency voltage field is used for the generation of high-energy ions and radicals. These chemically active species react further to form a layer on the substrate [158].

PE-CVD can be employed for the fabrication of hydrophobic metallic membranes when organosilicon compounds are deposited on them [160]. Si-DLC layers (a-C:H:Si:O) are amorphous carbon layers exhibiting: (1) diamond-like properties [161] due to a large amount

of sp^3 hybridized C atoms and (2) hydrophobic surface properties [89, 162–166] due to the presence of organosiloxane compounds like hexamethyldisiloxane (HMDSO) in the PE-CVD process [160, 167].

Coating process

In all the steps during the fabrication of a Si-DLC layer by PE-CVD, argon was used as a diluent and carrier gas. Hydrogen was used to clean the substrates via ion bombardment before the coating. Oxygen was responsible for plasma oxidation, so that reactive hydroxyl groups were present on the substrate surface. Methane was used as a precursor for the DLC layer, together with the HMDSO which is responsible for the Si-doping of the DLC to form the Si-DLC layer. Table 4.1 summarizes the precursors and carrier gases used during the process.

Table 4.1.: Materials used in the PE-CVD process, including purity and company.

Chemical	Formula	Purity grade	Company
Argon	Ar	6.0	Air Liquide
Hydrogen	H_2	6.0	Air Liquide
Oxygen	O_2	4.8	Air Liquide
Nitrogen	N_2	6.0	Air Liquide
Methane	CH_4	4.5	Basi Schoeberl
HMDSO	$C_6H_{18}OSi_2$	1.8	Merck KGaA

The Si-DLC layer was deposited using a combined PE-CVD/Magnetron-sputtering system (STARON 60-60, PT&B Silcor). The system is composed of a stainless steel vacuum chamber with a capacity of 170 L. The evacuation is carried out with three vacuum pumps which operate in cascade mode: a rotary vane pump (TRIVAV D65B), a rotary lobe pump (RUVAC WSU 501 H) which starts operation below 60 mbar, and finally a turbopump (TURBOVAC T1600) working up to 0.5 mbar. A throttle valve with a range (0.003 to 2 Pa) is used to control the recipient pressure.

The plasma generation source (Trumpf TRUPlasma DC 3002) with a specified power range between 0 and 300 W, is located in the front of the door chamber. The process was operated

using a radiofrequency power of the plasma source of 100 W. Samples are placed with the help of sample holders, which can be fixed on the existing rotating table inside the chamber. Mass flow controllers (0-200 $Ncm^3\ min^{-1}$) are used to separately control the flow of process gases. The system is controlled by an industrial automation system (SIMTIC IPC427C) from Siemens.

Table 4.2.: Parameters during the PE-CVD process.

Parameter	Value
Plasma power source	100 W
Temperature	180 °C
Pressure	1.5 Pa
Flowrate Ar	40 $Ncm^3\ min^{-1}$
Flowrate CH_4	150 $Ncm^3\ min^{-1}$
Flowrate HMDSO	4 $Ncm^3\ min^{-1}$
Coating duration	60 min

The process consists of four main steps:

1. Heating and evacuation of the chamber up to the required vacuum level (1.5 Pa) and temperature of 180 °C for at least 60 min.
2. Cleaning of the substrates with hydrogen and argon plasma by ion bombardment for 2 minutes.
3. Plasma oxidation of the surface (argon and oxygen).
4. After the evacuation of all residual gases of the previous steps, the actual coating [167] starts with HMDSO, argon, and methane as precursors under plasma conditions. The coating duration was 1 h.

The recipe is based on the previous work of Dyrda et al [167], where the samples were rotated (4 rpm) during coating to obtain a homogeneous coating thickness. The main process parameters are summarized in Table 4.2

Reaction mechanism

The description of the reaction mechanisms during the PE-CVD processes is very challenging due to the notable complexity of the simultaneous processes occurring [158]. The exact mechanism for the formation of the Si-DLC layers has not yet been elucidated and is therefore not found in the literature. Figure 4.2 shows a simplified mechanism to understand the reactions taking place during PE-CVD with the HMDSO deposition mechanism. The plasma chemical conversion of HMDSO can lead, on the one side, to the subsequent formation of pentamethlydisoloxane (PMDSO) and tetramethlydisiloxane (TMDSO), which can be split into radicals that are adsorbed on the substrate surface. On the other hand, plasma can break the Si-O bond of the HMDSO molecule and form subsequently tetramethylsilane (TMS) and trimethylsilane (TriMS). Their radicals and the radical of the trimethylsilyl ether can likewise be adsorbed on the substrate surface.

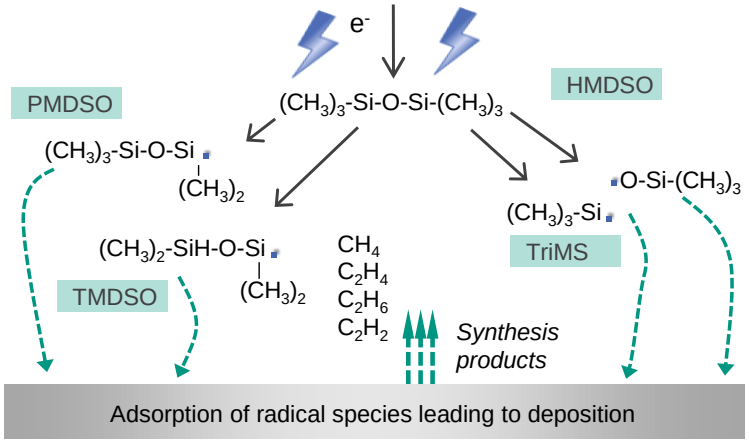

Figure 4.2.: Scheme of the mechanism of PE-CVD of HMDSO, adapted from [168].

4.1.2 Direct immersion in FAS solution

General description

Contrary to the CVD process, immersion grafting is a wet method. Hydrophobic thin layers can be fabricated through direct immersion in a coating solution [169]. A simple, reliable and reproducible method [61, 170, 171] for the deposition of a wet film by immersion of a substrate into a solution is the dip coating technique. Within the dip coating technique, the immersion time and withdrawal speed remain constant [172].

Fluoralkyl silanes (FAS) are commonly used as precursor molecules in a reactive immersion solution for hydrophobization purposes [63] via dip coating. This reactive solution is previously prepared by hydrolyzing the organosilane compound in solvents such as water or alcohol [173] under an acidic environment [174]. Therefore, in this case, the FAS molecules are not deposited onto the membrane but undergo a sequential process of hydrolysis, chemisorption and condensation onto the membrane surface. These reactions lead to the formation of a covalent bond (grafting) with other molecules of the substrate [169, 175]. For the chemical bond to form, hydroxyl groups need to be available on the surface. The layer is then formed by condensation of the silane groups with these hydroxyl groups on the substrate surface [169]. The resulting surface hydrophobicity depends now not only on the surface structure but also on the surface properties of the hydrophobic agent (in this case FAS). Dip coating in FAS solution often results in highly organized needle-like structures, also known as self-assembled monolayers (SAM) [169].

Coating materials

The reactive solution contained ethanol as a solvent, hydrochloric acid and threefold molar excess of water for the 1H,1H,2H,2H-perfluorooctyltriethoxysilane (FAS-13) to undergo hydrolyzation. The solution was prepared using the chemicals and amounts given in Table 4.3. The solution was stirred for 5 h and held for 24 h at ambient temperature before being used for coating. The curing process enhanced the coating's stability [174].

Table 4.3.: Materials used in the direct immersion process, including purity, amount and company.

Chemical	Formula	Purity / wt.%	Amount / wt.%	Company
Ethanol	C_2H_5OH	99.9	97.49	Merck KGaA
Water	H_2O	100	0.2	–
Hydrochloric acid	HCl	32	0.65	Merck KGaA
FAS-13	$C_{14}H_{19}F_{13}O_3Si$	98	1.66	Sigma Aldrich

Reaction mechanism

In the beginning, the FAS-13 undergoes a hydrolysis reaction in the presence of hydrochloric acid. This reaction takes place in a threefold molar excess of water over the acid to form the hydronium form (H_3O^+), see Figure 4.3 (a). Products of the hydrolysis of the FAS molecule are a silanol and three molecules of ethanol. The silanol molecules form condensated products. In Figure 4.3 (b) the example of the condensation of three silanol molecules is given, where two molecules of water are released. Subsequently, hydrogen bonds form between the oxygen and hydrogen molecules of the silanol molecules and those of the hydroxyl groups in the membrane metal surface, cf. Figure 4.3 (c). Covalent bonds between the FAS and the metal surface are then formed when the coated surface is exposed to heat, see Figure 4.3 (d). The perfluoroalkyl groups $-(CF_2)_2\ -CF_3$ are exposed on the surface of the stainless steel (SS) membrane, so that the fluor content contributes to the hydrophobic properties of the membrane [174].

The process is very sensitive to the process conditions (e.g., concentration, temperature, time) [169] and not always results in well-organized Self Assembled Monolayers but in covalent attachments or vertical polymerization [176].

Coating process

The direct immersion of the substrates was performed by the dip coating technique (dip coater with motorized actuator–AZ Series, Software MEXE02) in the FAS-13 solution. For this, the substrates were completely immersed in the FAS solution in the vertical direction using the dip coater technique with 3 mm min^{-1} withdrawal speed and 30 s coating immersion time at room temperature. The coated membranes were then dried for 2 h at 70 °C in a drying chamber (Series KMF, Binder GmbH). After this step, the samples were transferred to a muffle furnace (Heraeus Thermo Scientific, Waltham, MA US), heated from room temperature up to 200 °C with a heating rate of 0.5 °C min^{-1}. The samples were kept at 200 °C for 6 h to allow the grafting (formation of the covalent bond).

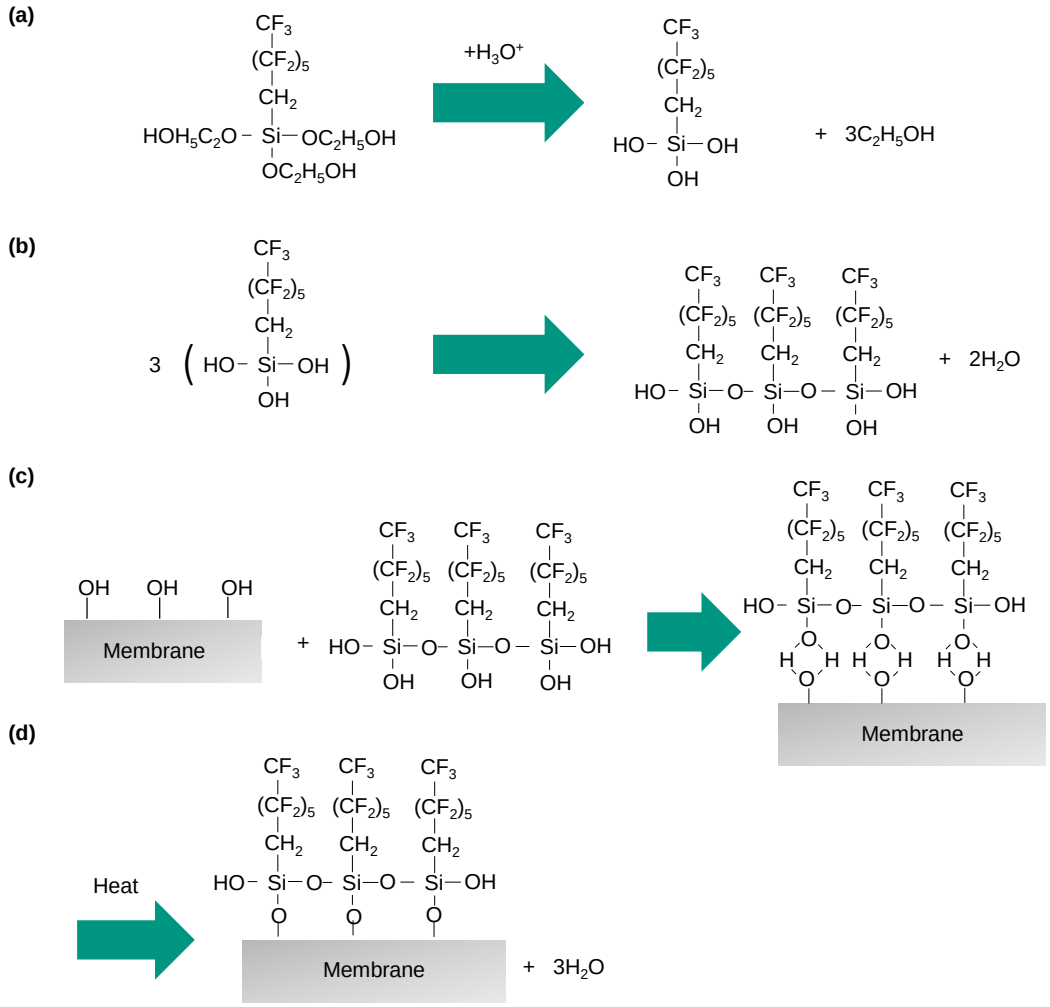

Figure 4.3.: Mechanism of bonding between the FAS molecule and the metallic membrane, adapted from [174]. The process consists of **(a)** hydrolysis of the FAS molecule, **(b)** condensation of the silanols, **(c)** adsorption on the surface through hydrogen bonding, and **(d)** covalent bonding (or grafting) after the annealing step.

4.1.3 Substrates

For a better characterization of the coating process and to avoid the influence of the substrate surface characteristics, the coating was first investigated on non-permeable surfaces. For this purpose, silicon wafers with (100) crystal orientation (Siegert Wafer GmbH, Aachen, DE) and non-permeable SS plates, see Figure 4.4 (a), were coated. Further, the coatings were tested on permeable sintered stainless steel substrates (GKN Sinter Metals Filters GmbH, Radervormwald, DE) with different porosities. Figures 4.4 (b)–(d) depict different SEM images of the cross-section of the permeable stainless steel substrates. The total thickness

of the substrates is given in Table 4.4. The permeable (fine porous) substrate, cf. Figure 4.4 (d), is an asymmetric porous metal membrane. The membrane is fabricated using two consecutive sintering processes with different metal powder particle sizes. The last sintering process results in a 140 –170 µm thick top layer of sintered fine metal powder. For the characterization of the coatings, a standard size of 10 × 20 mm for all substrates was used.

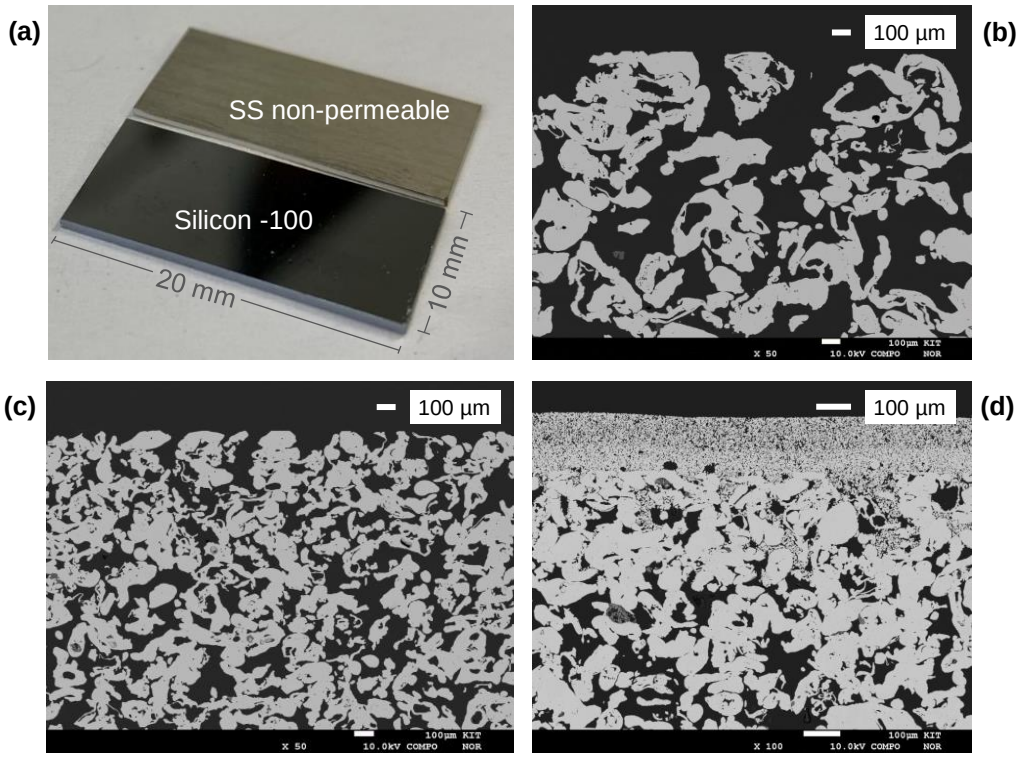

Figure 4.4.: Overview of the used substrates. **(a)** silicon and stainless steel (SS) non-permeable substrates; SEM Images of a cross-section of : **(b)** permeable SS substrate (52% porosity); **(c)** permeable SS substrate (40% porosity); and **(d)** permeable (fine porous) multi-layer SS substrate.

4.1.4 Pre-processing

Organic contaminants on the metal substrates were cleaned in an ultrasonic bath (Elba X-tra 70H) in the presence of acetone, isopropanol and water for 30 minutes each successively [177] and finally dried at 70 °C during 5 min in a drying chamber (Series KMF, Binder GmbH, DE):

Table 4.4.: Metallic substrates used in this study.

Material	Surface	Total thickness	Commercial name
Silicon (wafer)	non-permeable	0.5 mm	Siegert Wafer
Stainless steel	non-permeable	0.3 mm	–
Stainless steel	permeable	2 mm	Sika R-100 (52% porosity)
Stainless steel	permeable	2 mm	Sika R-15 (40% porosity)
Stainless steel	permeable	3 mm	Sika R-AS

To improve the probability for the FAS molecules to react and bond with the membrane surface [61], SS substrates were immersed in a pickling solution consisting of 1:1 in volume dilution of HCl (Merck, 32%) and water for 5 min at room temperature, rinsed with deionized water, and dried with compressed air [177]. Through pickling, the former oxide layer is removed and replaced by new hydroxyl groups [174].

Another way to increase the hydrophilic properties of the surface (number of –OH groups) before coating is to provide the substrate with a SiO_2 layer. Depending on the thickness of the SiO_2 layer, this step can also help to reduce the pore size and therefore increase some membrane parameters like the LEP (see Equation 2.5 in Chapter 2). For this purpose, SS substrates were coated with a 1.4 µm thick layer of SiO_2 using PE-CVD, before the dip coating process. The resulting coating layer is shown in Figure 4.5.

4.1.5 Coating characterization

Coating characteristics

The coating characteristics as well as the roughness of the substrates before and after coating were analyzed by optical profilometry (SensoFar S neox, Sensofar-Tech). To compare the coated and uncoated region of each sample after the completion of the surface modification process, one side of the sample was covered with Kapton® tape before coating. The

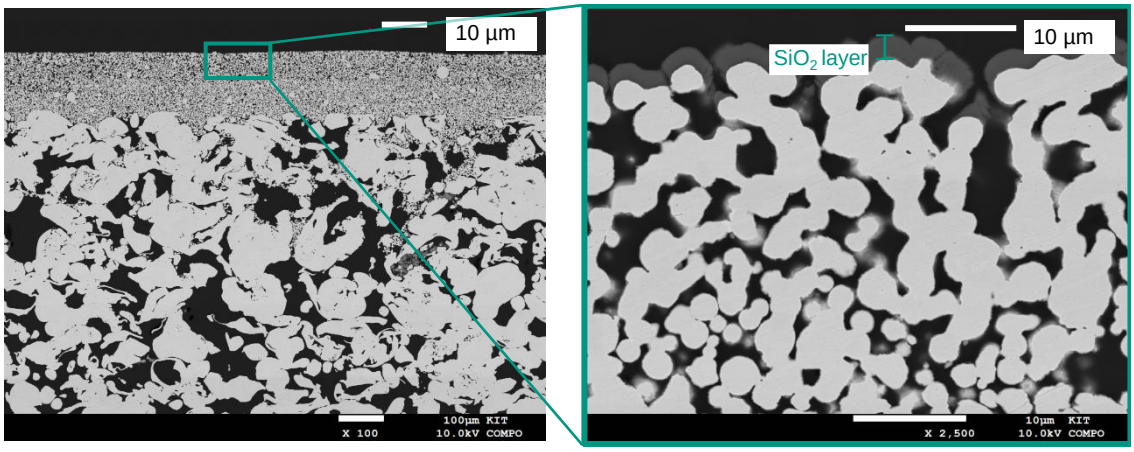

Figure 4.5.: Permeable SS substrate (fine porous) with the pre-coated SiO_2.

roughness measurements were performed according to the standard DIN EN ISO 25178-2 [178] and the roughness parameters were measured at five different points on the surface of the sample. Besides, scanning electron microscopy (SEM) and electron probe microanalysis (EPMA) with a field emission electron probe microanalyzer (JXA-8530F, JEOL Ltd.) were also used for further investigation. Before the characterization of cross-sectional images by SEM, samples were embedded in epoxy resin, ground, polished, and finally sputtered with a conductive layer of platinum to avoid charging. Due to the low thickness of the layer, only qualitative analysis was possible. Energy-dispersive spectroscopy (EDS) and wavelength-dispersive spectroscopy (WDS) were therefore employed to determine qualitatively the presence of certain elements in the coating.

Wetting

The contact angle (CA) formed by sessile drops of deionized water was measured at ambient conditions with a contact angle goniometer (OCA 5, Data physics, Filderstadt, DE) before and after the coating according to the standards [179] at room temperature and a drop volume between 2 and 6 µL. For each case, the right and left contact angles of at least three droplets were measured.

Thermal stability

The coated samples were heated to different target temperatures to characterize the hydrophobic behaviour after exposure to high temperatures. The heating tests were performed

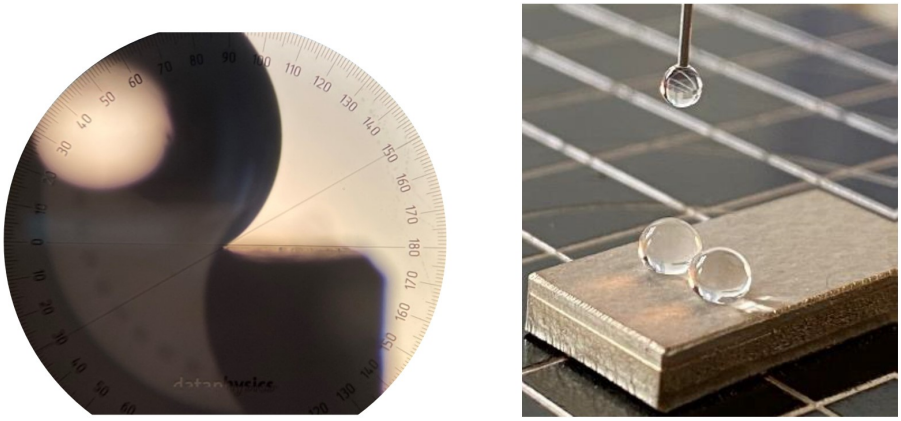

Figure 4.6.: Hydrophobic behaviour of water droplets on FAS-coated fine porous stainless steel substrates.

in the muffle furnace (Heraeus Thermo Scientific, Waltham, MA US) for different holding times and a common heating rate of 2 K min^{-1} under air.

Liquid entry pressure

As already mentioned in Section 2.2.2, the liquid entry pressure (LEP) is an essential parameter for the operation of porous hydrophobic membranes. Therefore, LEP tests were performed to characterize whether the coated membranes can be used as hydrophobic membranes for the separation process or not; i.e. the fabricated membranes have a sufficiently high LEP that prevents liquid from entering the pores during operation. The visual method (cf. Table 2.1) was employed to determine at which pressure level the first water drop arises in the membrane backside. For the tests, a set-up [167] consisting of two poly (methyl methacrylate)-PMMA plates was used. The membrane samples, with a common area of 10x20 mm^2, were clamped in the PMMA test cell, see Figure 4.7.

Depending on the membrane thickness, a spacer with a thickness between 1 to 2 mm was necessary on the permeate side to ensure tightness. One silicon flat gasket specially optimized for the membranes was used to seal the feed side of the membrane. The gasket allowed for a testing area of 5 mm^2, which corresponded to a 5 mm long and 1 mm wide slot. The transparency of the test cell material was advantageous for water breakthrough detection.

Figure 4.8 schematically shows the test rig. To conduct the feed liquid towards the membrane, and precisely set the pressure in the feed chamber, a manually operated SITEC manual screw press (SITEC-Sieber Engineering AG, Maur, CH) was used. The pressure was increased in steps of 0.1 bar and held for 30 s. The pressure at which a water droplet was visible

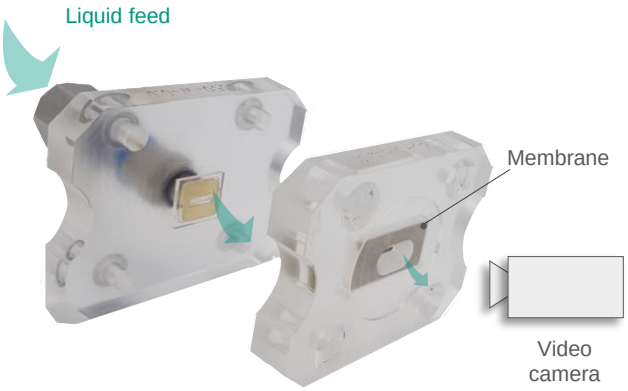

Figure 4.7.: Exploded view of the PMMA test cell with the liquid feed entering the cell. The LEP is determined visually when the first drop leaves the cell and can be detected through the video camera.

through a USB digital microscope on the back side of the membrane was recorded using a pressure sensor (Model P-31, accuracy 0.005 bar, WIKA Alexander Wiegand SE & Co. KG, Klingenberg, DE). A three-way valve ensured the elimination of possible air bubbles in the system. The remaining air pockets could be detected through a transparent inlet channel. To characterize the stainless steel membranes, measurements were carried out three times with DI water.

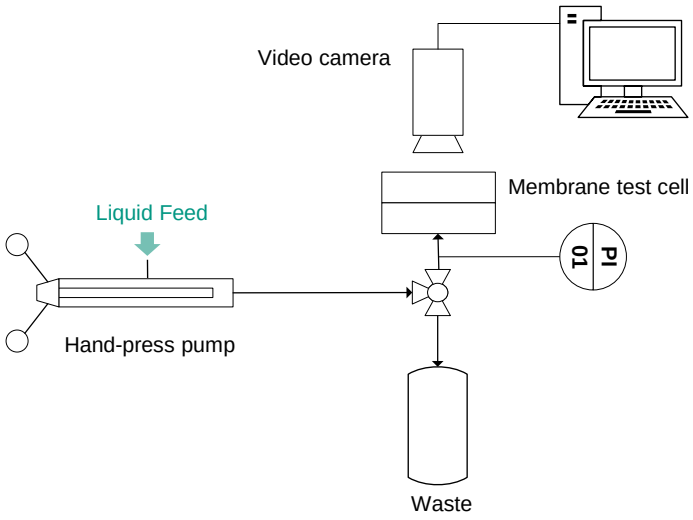

Figure 4.8.: Overview of the experimental set-up used to measure the LEP using the visual method.

4.2 Results and discussion

The relevant results on the fabrication and characterisation of hydrophobic coatings are presented and discussed in this chapter. First, the coating characteristics and wetting behaviour are presented. Subsequently, the suitability of the coatings for the application as a membrane in the investigated scenario conditions is discussed based on the results of the thermal stability of the coatings up to the application temperature and the LEP of the resulting hydrophobic membrane.

4.2.1 Coating characteristics

The results regarding the coating characteristics (thickness, morphology, and quality of the surface) after the PE-CVD process and the dip coating technique are shown and discussed separately.

- Silicon doped DLC (PE-CVD)

  In Figure 4.9, the top view of the Si-DLC coatings on a silicon wafer (a), the non-permeable SS (b), and the permeable SS substrate (c) and (d) can be observed. The images show a homogeneous coating on the left-hand side. The right-hand side was covered with Kapton® during coating, so a bare surface is shown. The thickness of the coatings was measured by profilometry and revealed an average thickness of 440 nm after 1 h coating. Besides, the PE-CVD Si-DLC coated surfaces show thin homogeneous films without apparent defects or cracks.

  The cross-section of the Si-DLC coatings on (a) a silicon wafer and (b) a fine porous SS substrate is displayed in Figure 4.10. For better observation of the coating, the process was set to 3 h, delivering an average thickness of 1.4 µm. In Figure 4.10 (b), it can be seen that the pore inner side, close to the external surface of the sample, got coated and that the pores get narrower, which both should prevent the entrance of water into the pores. Besides, Figure 4.10 also reveals that the coating thickness decreases in the perpendicular direction of the plasma source and only penetrates partially the membrane pores so that the coating does not block the pores. This fact shall allow the permeation of steam. White arrows in Figure 4.10 (b) indicate these spots.

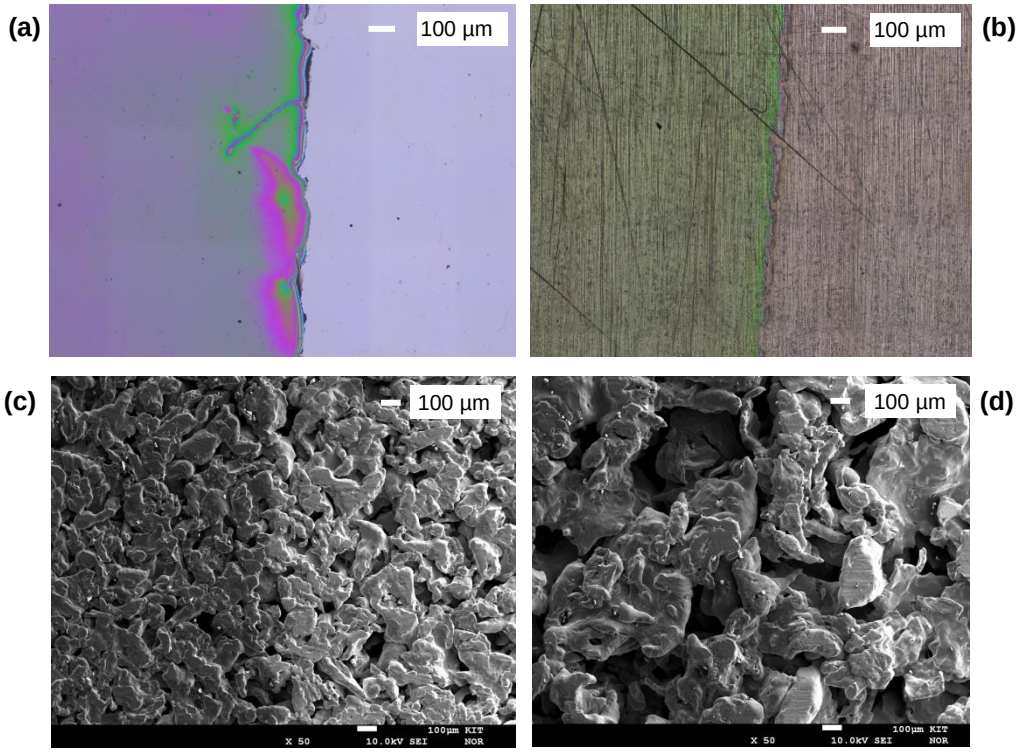

Figure 4.9.: Top view of the coatings on different substrates (left-hand side: coated; right-hand side: uncoated. **(a)** Si–DLC on silicon substrate–optical profilometry 10x; **(b)** Si–DLC on permeable SS substrate–optical profilometry 10x; **(c)** Si-DLC on permeable SS substrate (40% porosity)-SEM; **(d)** Si–DLC on permeable SS substrate (52% porosity) –SEM.

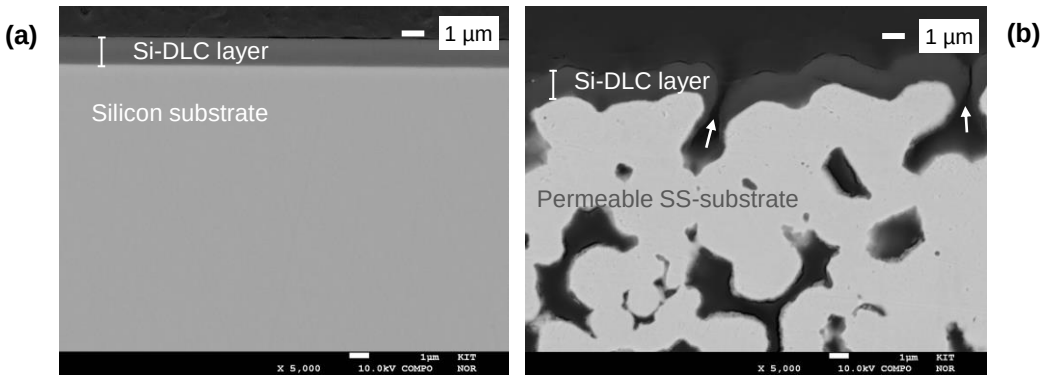

Figure 4.10.: SEM Image of the cross-section of the Si-DLC coating on **(a)** a silicon substrate and **(b)** a permeable SS substrate.

The development of a homogeneous a-C:H:Si:O layer on the metallic substrates could also be confirmed by an EDS analysis. The EDS results confirmed the presence of C, O, and Si, see Annex A.7.

- FAS self-assembled monolayer (Dip coating)

  Figure 4.11 displays the top view of the FAS coating on a silicon wafer (a) and a non-permeable SS substrate, (b) and (c). Figure 4.11 (a), reveals that the FAS coating is transparent. All SS substrates were pickled with HCl before the immersion in the FAS solution. HCl pickling [180] – removal of most external layers (surface contamination and surface oxide) – has a great effect on the fabrication of hydrophobic coatings, by increasing the polar component of the surface energy and nano roughness [181]. This effect can be seen in the cavities between the grains in Figure 4.11 (b), and with greater detail in Figure 4.11 (c). The darker colour in the coated part of the substrate in Figure 4.11 (b) might be the different emission of the secondary electrons in the coated part during SEM analyses.

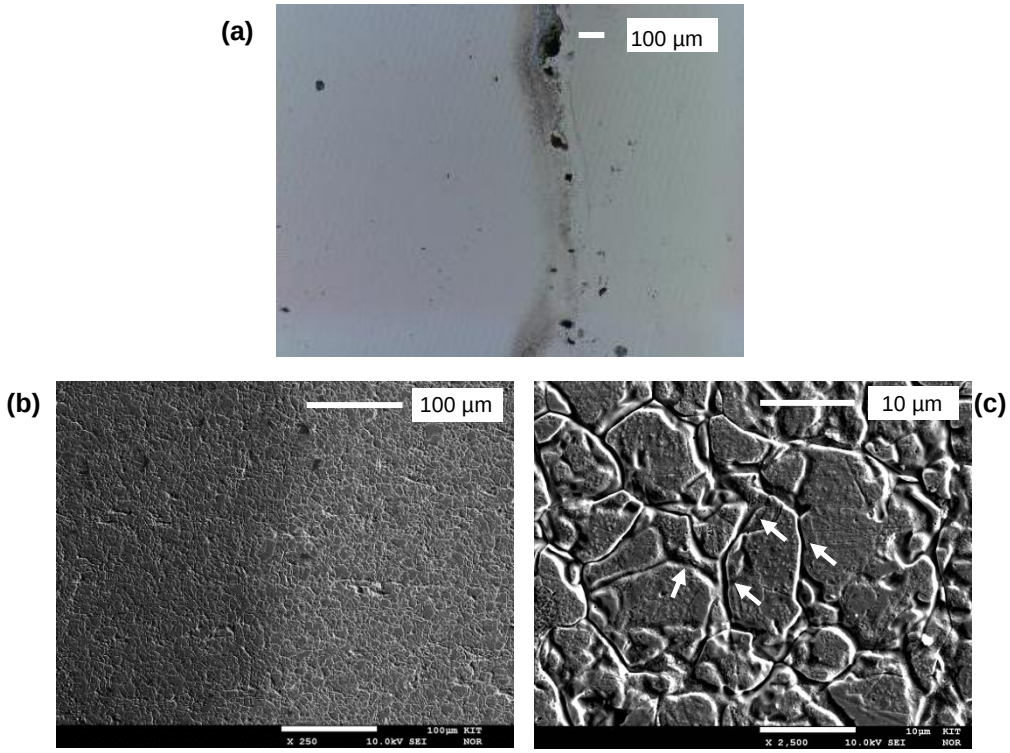

Figure 4.11.: Top view of the coatings on different substrates (left–hand side: coated; right–hand side: uncoated. **(a)** FAS on silicon substrate–optical profilometry 10x; **(b)** FAS on non-permeable SS substrate –SEM; **(c)** FAS on non-permeable SS substrate: detail of the coated part on the non-permeable SS substrate where the effect of pickling pre-processing can be seen in the grain boundaries (white arrows).

Since the coating was transparent and had a very low thickness (molecular thickness), no profilometric measurements were possible. The cross-sectional analysis performed by SEM did not display any layer. However, the presence of C, F, and Si all over the surface could be confirmed by EDS and WDS analysis of the coating top side (see

Annex A.7). This indicated the development of the hydrophobic layer on the metallic substrate. Figure 4.12 displays a SEM picture of the coating on a silicon substrate, which reveals spot-wise agglomerations. EDS analyses showed a higher concentration of the coating elements in the spots. No cracks were visible on the surface. The agglomeration (dots in Figure 4.12) might be a consequence of the polycondensation reaction among the reactive organosilane molecules, which leads to the formation of an uneven thickness [63].

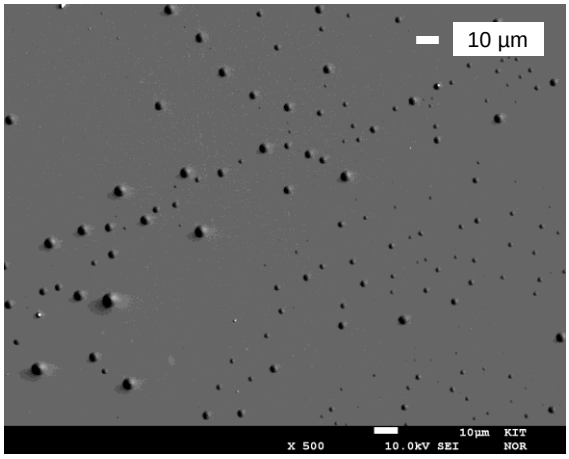

Figure 4.12.: SEM image of the top view of the FAS coating on a silicon substrate. The spots on the surface are locations with a higher concentration of the coating elements. This was confirmed by EDS analyses.

4.2.2 Wetting

Contact angle measurements with DI water were performed for the characterization of the resulting wetting properties of the coated substrates. Figure 4.13 displays the contact angle results before and after each coating for the different substrates.

Before the coating process, the substrates displayed a lower contact angle as a consequence of the highly hydrophilic nature of the metallic surfaces due to the high density of the –OH groups (natural oxide layer) on the surface. Silicon wafers exhibit the highest surface energy, and as a result, the lowest contact angle ($57\,^{\circ} \pm 7\,^{\circ}$). This low value is caused not only by the presence of a natural oxide layer but also by the polished finish of the surface, which leads to low surface roughness, and therefore low contact angles. According to Figure 4.13, the contact angle values before the coating process increase from the non-permeable substrates to the permeable substrates, as the surface roughness of the materials also does (See Annex A.8). The fine porous substrates displayed the highest contact angles

(101 °± 8 °). The wetting in the case of the porous substrates may follow the Cassie–Baxter state [73] behaviour, see section 2.2.1.

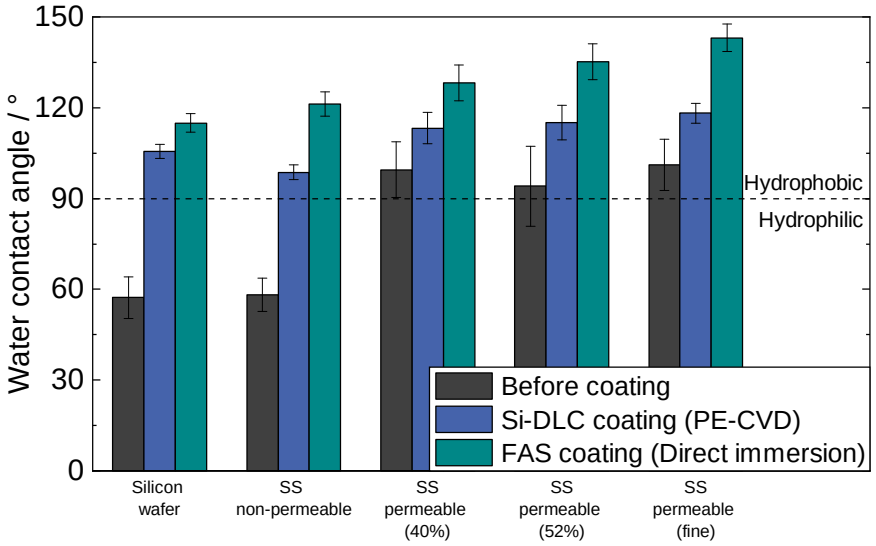

Figure 4.13.: Contact angle (average) for different substrates: before coating (grey), after Si-DLC coating (blue) and after FAS coating (green).

In the case of the Si–DLC coatings, all substrate surfaces became hydrophobic. The resulting contact angle on the silicon substrate, (105 °± 2 °) agrees with the values found in the literature [162, 166, 167]. In the case of permeable stainless steel substrates, slightly lower contact angles were achieved (99 °± 2 °). Coated permeable stainless steel exhibited higher contact angle values, as was expected, because of topological hydrophobicity. For example, a value of 118 °± 3 °was measured on the coated fine porous substrates.

Direct immersion in the FAS solution by dip coating provided even higher contact angles. The reason for that might be the presence of the CF_3 topmost group in the chain when the fluoroalkyl chains are well assembled and vertically aligned [169]. The CF_3 group exhibits a water contact angle of 120 ° [182]. However, when the fluoroalkyl chains are collapsed, disordered monolayers are formed and the CF_2 or CH_2 groups are mainly exposed [169]. The fine porous substrate exhibited almost superhydrophobic surface properties (CA 143 °± 5 °).

Considering these results, it can be concluded that the direct immersion in the FAS solution appears to be a very straightforward coating technique which leads to higher contact angles compared to the Si-DLC coatings. For better visualization, Figure 4.6 illustrates the hydrophobic behaviour of water droplets on the FAS-coated fine porous stainless steel substrates.

4.2.3 Thermal stability

The effects of temperature on the hydrophobic coatings were characterized to determine the resistance of the coatings to successive heating to relatively high temperatures and subsequent cooling. Coated samples were heated with a heating rate of 2 °C min^{-1}. The temperature was held at different target temperatures for 2 h. The contact angle was characterized at room temperature after the samples had cooled down. To analyze how the samples were responding to a repeated heat application, the same sample was again heated and then held at the next target temperature. Figure 4.14 illustrates the water contact angle values after each heating test for silicon substrates coated by the two different coatings.

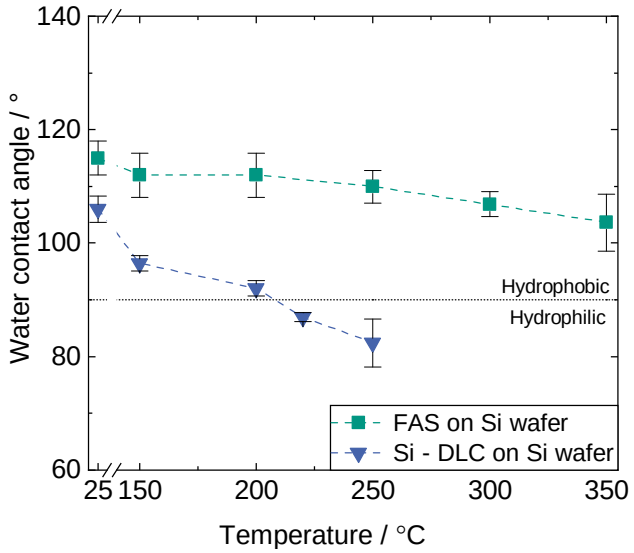

Figure 4.14.: Comparison of the thermal resistance of the different coatings on a silicon substrate.

Figure 4.14 reveals that higher temperatures lead to a degradation of the Si-DLC coating on the surface of the samples. When the samples were heated to temperatures higher than 220 °C, the hydrophobic behaviour disappeared completely. The contact angle, in that case, resulted to be 87 °± 1 °. For FAS-coated silicon wafer substrates, samples remained hydrophobic even after heating to 350 °C. Nevertheless, Figure 4.14 shows that the FAS coating experiences a certain degradation above 300 °C. Figure 4.15 depicts the results of the temperature stability test for different substrates coated with the FAS layer. Compared to the coatings on the silicon substrates, the coatings on the non-permeable SS samples lose their hydrophobicity at lower temperatures (around 270 °C).

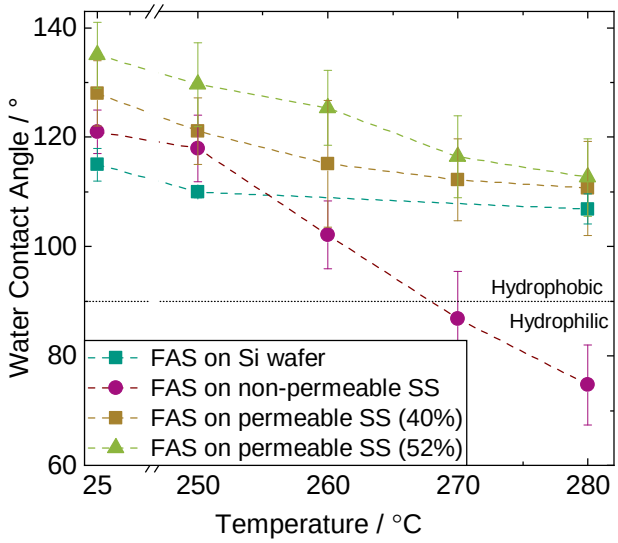

Figure 4.15.: Results of the thermal resistance test for the FAS coating on different substrates.

WDS analyses (see Figure A.4 and Figure A.5 in the Annex) still show the presence of fluor atoms on the surface after the last heating to 280 °C. In particular, the coated non-permeable SS substrates developed a blue heat tint on the surface. This effect might be an indication of the growth of the intermediate oxide layer [183–185], which leads to an increase in the surface energy and therefore, a reduction of the contact angle.

During the polycondensation reaction of glucose, temperatures up to 250 °C can be reached in the reactor. To test the adequacy of the coatings for the real application, the coatings were tested at this temperature for 2 h. After each heating (and cooling) cycle, the contact angle was again measured to determine after how many cycles at constant temperature the samples lose their hydrophobic properties. Figure 4.16 shows that the FAS coatings on silicon and permeable SS substrates are still hydrophobic after at least 4 heating cycles, even if there is a reduction of contact angle after the first cycle. For these cases, it was proven by WDS analyses (Figures A.8 and A.9 in the Annex) that F is still present in the layer. The fall in contact angle might be again caused by the growth of the intermediate oxide layer. In this case, the coating on permeable SS substrates degraded not so fast as on the non-permeable SS substrates. These results give an insight into the short-term thermal resistance of the coatings. However, for pilot plant or industrial application of the hydrophobic membranes, longer heating times and a higher number of heating cycles should be applied in order to draw conclusions closer to reality.

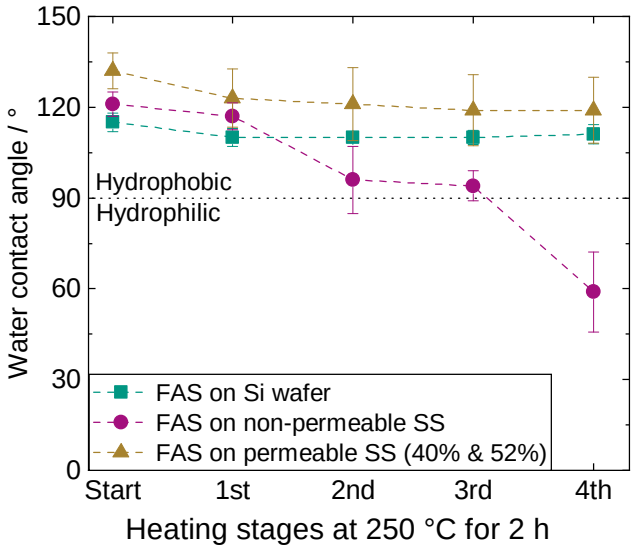

Figure 4.16.: Results of the thermal resistance test for the FAS coating on different substrates for 4 heating cycles at 250 °C.

4.2.4 Liquid entry pressure

The FAS coatings presented higher contact angles and thermal resistance to elevated temperatures in comparison to the Si-DLC coatings. Therefore, FAS-coated permeable substrates were further characterized according to their applicability as hydrophobic membranes. For this purpose, the liquid entry pressure (LEP) gives a good indication up to which transmembrane pressure level water still does not penetrate the pores of the membranes. Since the LEP is inversely proportional to the membrane pore size, see Equation 2.5, membranes with larger pores present lower LEP, even if their surfaces show higher contact angles. This is the case for the (rough) permeable SS substrates with 52 % and 40 % porosity, whose surfaces present a high contact angle in the order of 130 ° but due to their larger pore size, water breakthrough through the pores occurs at a very low-pressure level (almost no differential pressure). The permeable substrates sintered from finer particles have smaller pore sizes, which results in an enhancement of the LEP. Figure 4.17 compares the measured LEP of the FAS-coated fine porous substrates with different pre-treatments, i.e., without pickling before coating, with pickling before coating, and with a SiO_2 layer before coating.

It is remarkable from Figure 4.17, the high value of the pickled membranes (3.1 bar) in comparison with the not pickled membranes (1.3 bar). The reason here may be the pickling step itself. When the HCl is not correctly removed, a thicker oxide layer is formed (see Figure 4.18). This may lead to pore blockage, and probably to a lower permeation during the membrane distillation process. The membranes with the SiO_2 pre-coating show a higher

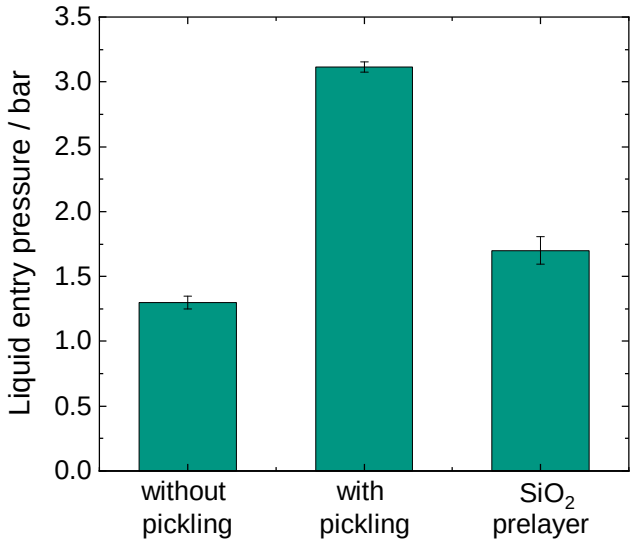

Figure 4.17.: Liquid entry pressure measurements for the hydrophobic membranes with different pretreatment; from left to right: without pickling, with pickling and with a SiO_2 prelayer.

LEP than the non-pickled ones (1.7 bar). The LEP increment can be attributed to the pore reduction due to the presence of the SiO_2 intermediate layer.

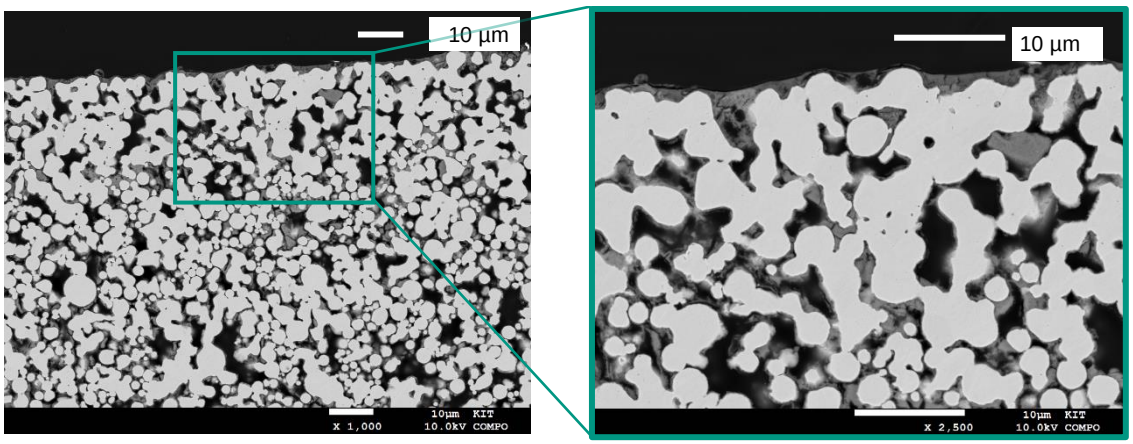

Figure 4.18.: SEM picture of the coated membrane (coating process: pickling + FAS coating + annealing) after the LEP measurement. Accumulation of material between the sintered particles is visible, which reduces the pore size and therefore results in a higher LEP for the given membrane.

4.3 Summary of Chapter 4

The surface of metallic non-permeable and permeable substrates could be hydrophobized using PE-CVD of a Si-DLC layer and, alternatively, by direct immersion in a FAS solution. The pore's inner surface could be coated as the SEM images revealed. Comparing the different metallic substrates used before coating, higher contact angles were obtained in the permeable samples as a result of their surface roughness. After coating, the FAS-coated samples displayed a higher contact angle than the Si-DLC-coated samples (i.e., 143° vs. 118° for the fine porous substrates). The thermal resistance of the coatings was also investigated. The FAS-coated substrates showed better resistance in the short-term to higher temperatures and to repeated heating up to 250 °C, without losing the hydrophobic properties. The LEP experimental results at ambient conditions ranging between 1.3 and 3.1 bar indicated that FAS-coated fine porous stainless steel substrates have a chance to be applied as hydrophobic membranes for steam separation. For industrial applications, however, tests with longer heating times and cycles are required.

5

Characterization of the liquid entry pressure at elevated temperatures

For the efficient operation of membrane distillation, the transmembrane pressure should not exceed the liquid entry pressure (LEP). Since this dissertation aims at the separation of water by means of membrane distillation at elevated temperatures, it is required to characterize the LEP of the membranes at high temperatures. Besides, in order to maintain the feed in the liquid state at such temperature conditions, pressure should be applied at both feed and permeate sides. Consequently, an understanding of the behaviour of the LEP at elevated pressures is also required. This chapter describes the experimental methodology for the determination of the LEP at higher temperatures and pressures by means of the pressure step method. In order to be able to perform experiments under these conditions, a multi-purpose membrane testing unit was designed and fabricated. Here, not only polymeric but also ceramic and metallic membranes can be characterized. Within this scope, this chapter shows the results regarding a morphological study of polymeric and ceramic membranes. Besides, the LEP of several membrane materials was characterized at ambient conditions by means of the visual method described in Chapter 4 and compared with the results of the pressure step method. Finally, the results regarding the characterization of the LEP obtained at higher temperatures and pressures are also shown and discussed. To the knowledge of the author, there are no works in the literature at comparable temperature and pressure conditions. Parts of this chapter are based on a publication of Claramunt et al. [186].

5.1 Experimental methodology

5.1.1 Membranes

In this work, different commercial types of flat sheet hydrophobic membranes were characterized. The most important parameters of the membranes are given in Table 5.1 and Table 5.2. The pore sizes reported are values provided by the respective manufacturer.

Polymeric membranes

- PEEK membranes, with an average pore size of $d_{\text{pore.50}} = 100\,\text{nm}$ (active layer) were purchased from Novamem Ltd. (Schlieren, CH).
- Versapor acryl copolymer membranes were supplied by Pall GmbH (Dreieich, DE) with an average pore size of $d_{\text{pore.50}} = 200\,\text{nm}$ and a Nylon support.
- PTFE membranes were provided by Parker Hannifin GmbH (Kaarst, DE). On the one hand, Aspire-QP955 and Aspire-QP944C with PET support and pore sizes of $d_{\text{pore.50}} = 100\,\text{nm}$ and $d_{\text{pore.50}} = 200\,\text{nm}$, respectively. On the other hand, the Aspire QL217 membrane with a pore size of $d_{\text{pore.50}} = 200\,\text{nm}$ and a PP support.

Table 5.1.: Parameters of the polymeric membranes given by the manufacturers.

Membrane name	Material	Support	Pore size / nm	Total thickness /mm	LEP /bar
PEEK100	PEEK	PEEK	100	0.03–0.04	-
Versapor®200-R	Acrylcopolymer	Nylon	200	0.15–0.20	1.79
Aspire®-QP955	PTFE	PET	100	0.15–0.25	>4.5
Aspire®-QP944C	PTFE	PET	200	0.08–0.18	>2.3
Aspire®-QL217	PTFE	PP	200	0.15–0.25	>1.0

Ceramic membranes

The ceramic membranes were acquired from Fraunhofer-IKTS (Hermsdorf, DE). These ceramic membranes are made of Alumina $\alpha-Al_2O_3$ and are asymmetrically built: a porous support with a mean pore size of $d_{pore.50} = 2.5$ µm and the active layer, with pore sizes of $d_{pore.50} = 100$, 200, and 400 nm respectively. The active layer was modified by the manufacturer with a hydrophobic agent resistant to operating temperatures of, at least, 230 °C.

Table 5.2.: Parameters of the ceramic membranes given by the manufacturers.

Membrane name	Material	Support	Pore size / nm	Total thickness /mm	LEP /bar
IKTS-100	Hydrophobic $\alpha-Al_2O_3$	Alumina	100	2	-
IKTS-200	Hydrophobic $\alpha-Al_2O_3$	Alumina	200	2	-
IKTS-400	Hydrophobic $\alpha-Al_2O_3$	Alumina	400	2	-

5.1.2 Membrane testing unit

To carry out LEP measurements at higher temperatures and pressures, a multi-purpose membrane testing unit made of aluminium was used, see the exploded view drawing in Figure 5.1. A design based on the microchannel reactor used in previous experiments for the polycondensation [18] was used, i.e., straight microchannels in the feed side. The membrane testing unit consists of two base plates made of aluminium, with engraved microchannels. The base plate consists of 24 channels with a cross-section of 0.5 mm x 0.5 mm. The cover plate for the sweep gas side has 12 channels with a cross-section of 1.5 mm x 1 mm (see Figure 5.2). Two Swagelok® fittings on the outside of the base plates connect the microchannels to the piping of the experimental set-up to allow the fluid to flow in and out of the channels.

The design of the membrane unit allows the characterization of membranes of different thicknesses and materials as well as the performance of not only LEP measurements but also permeation experiments. The test of different membrane thicknesses is possible with

membrane holders made of PTFE with different thicknesses, depending on the membrane used. The membrane (flat sheet membrane, size 31 mm x 87 mm) is clamped between the base and cover plates. Flat gaskets made of silicon or Viton® on each side ensure tightness. To test the polymeric membranes, a metallic grid support was used to ensure mechanical stability. For the ceramic (or metallic) membranes, the PTFE membrane holders were available.

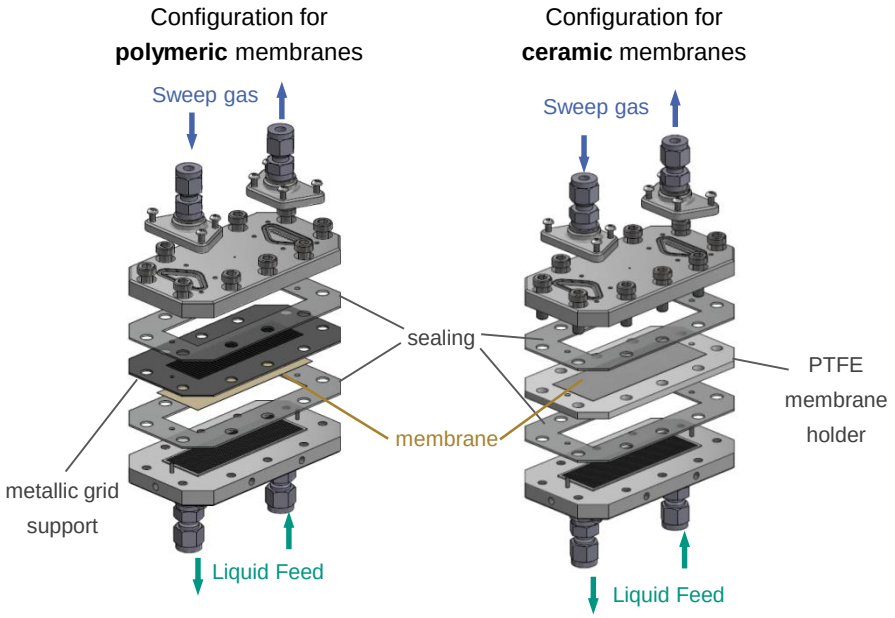

Figure 5.1.: Membrane testing unit made of aluminium used for the LEP pressurized tests. Left: configuration for polymeric membranes. Right: configuration for ceramic membranes.

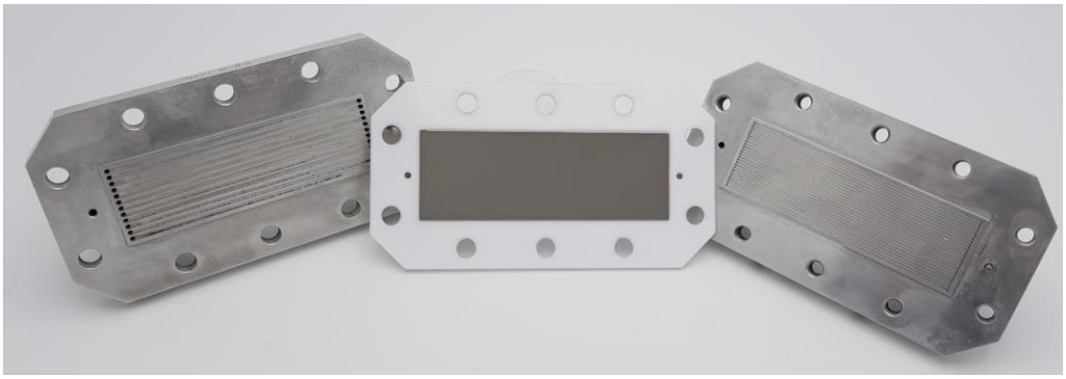

Figure 5.2.: Membrane testing unit in the configuration for ceramic and metallic membranes. From left to right: cover plate for the sweep gas side with 1.5 mm x 1mm channels, PTFE membrane holder with a metallic membrane and base plate with 0.5 mm x 0.5 mm channels.

5.1.3 Experimental set-up for the characterization of the LEP of hydrophobic membranes at elevated temperatures

A schematic flow diagram of the experimental set-up for characterizing the LEP at elevated temperatures is shown in Figure 5.3. Details about the equipment used can be found in Annex A.9. The pressure on the feed side was built up statically by closing the feed outlet valve and compressing the liquid with a manual screw press. Pressurized nitrogen in counter-current was used to build up pressure on the permeate side. Heating cords at the inlet and outlet lines of the testing unit as well as inside the unit (marked in red in Figure 5.3) were used to heat the fluid and keep the temperature of the liquid in the testing unit constant. Enough time for heating up the fluid and the unit was given to reach thermal equilibrium and ensure near isothermal conditions before performing the tests. The temperature was monitored with several thermocouples placed at the inlet and outlet of the gas (TI 04 and TI 05) and liquid side (TI 02 and TI 08), as well as in the upper and lower plate of the unit (TI 06 and TI 07).

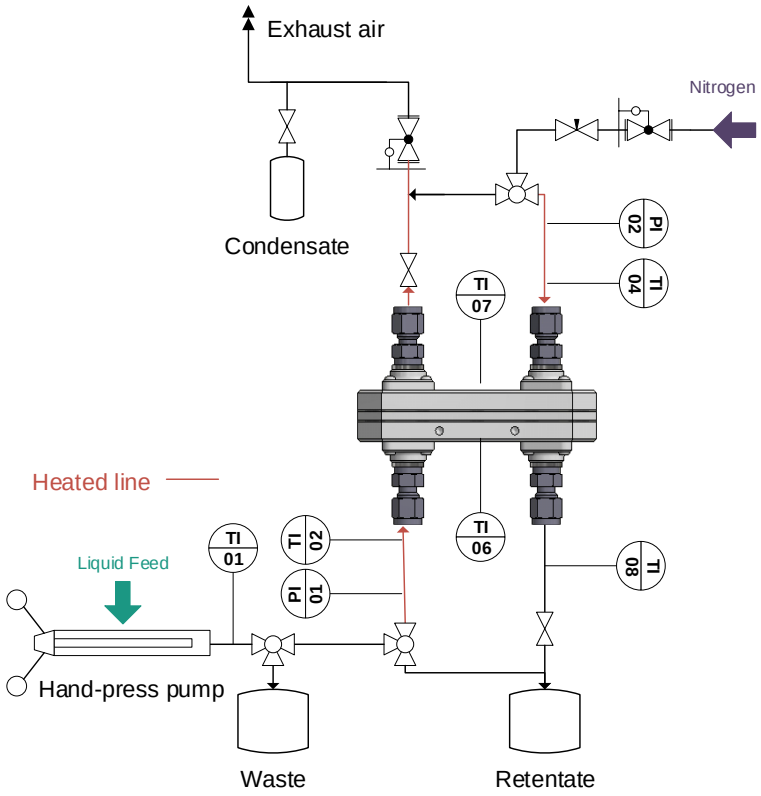

Figure 5.3.: Experimental set-up to measure the LEP using the pressure step method.

Since the membrane testing unit is not optically accessible, the visual method was not suitable to determine the LEP. Instead, the pressure step method was used to detect the LEP. This is an adapted version based on the work of Warsinger et al. [107], where the LEP is determined by the rate of change of pressure during the pauses between pressurization steps. When wetting occurs, the pressure on the feed side decreases, while without wetting, the pressure remains relatively constant. The LEP was determined from the pressure difference detected by two pressure sensors: PI 01 on the feed side and PI 02 on the permeate side. Therewith, the detection of the LEP was possible when pressurized experiments were carried out with nitrogen on the permeate side. Before each measurement, water was pumped through the system to flush out the air trapped when installing the unit into the set-up. The pressure was increased in 0.1 bar steps and then held for 12 s. A decrease of the pressure-time gradient higher than 0.05 bar s^{-1} during the holding phases indicated the attainment of the water breakthrough pressure.

5.2 Results and discussion

The membranes were examined under the microscope to characterize their pore morphology. To investigate the behaviour of the LEP of the different membranes in different conditions, experiments were first performed using the visual method at ambient conditions. These results were compared with the pressure step method. Subsequently, the influence of increased pressures and temperatures was studied. Within this framework, LEP experiments were conducted at room temperature and pressurized conditions as well as tests at ambient pressure at an elevated temperature range ($< 80\,^{\circ}C$). Finally, experiments were conducted under a higher temperature range ($> 80\,^{\circ}C$) and increased pressure conditions.

5.2.1 Morphological observations

All the membranes were examined by scanning electron microscopy as received. A JXA-8530 F field emission electron probe microanalyzer (JEOL Ltd., Tokyo, Japan) operating at 5 keV was used for the characterization of the internal morphology. The samples were attached with conductive carbon pads and additionally coated with a conductive carbon layer. Figure 5.4 shows SEM images of the front and/or back surfaces of the membranes investigated. Figure 5.4 (a) and (b) display the front and back sides of the PEEK membrane respectively. A sponge-like structure with cavities at the interconnection of pores can be distinguished, with a flat front membrane surface and a rough back membrane surface.

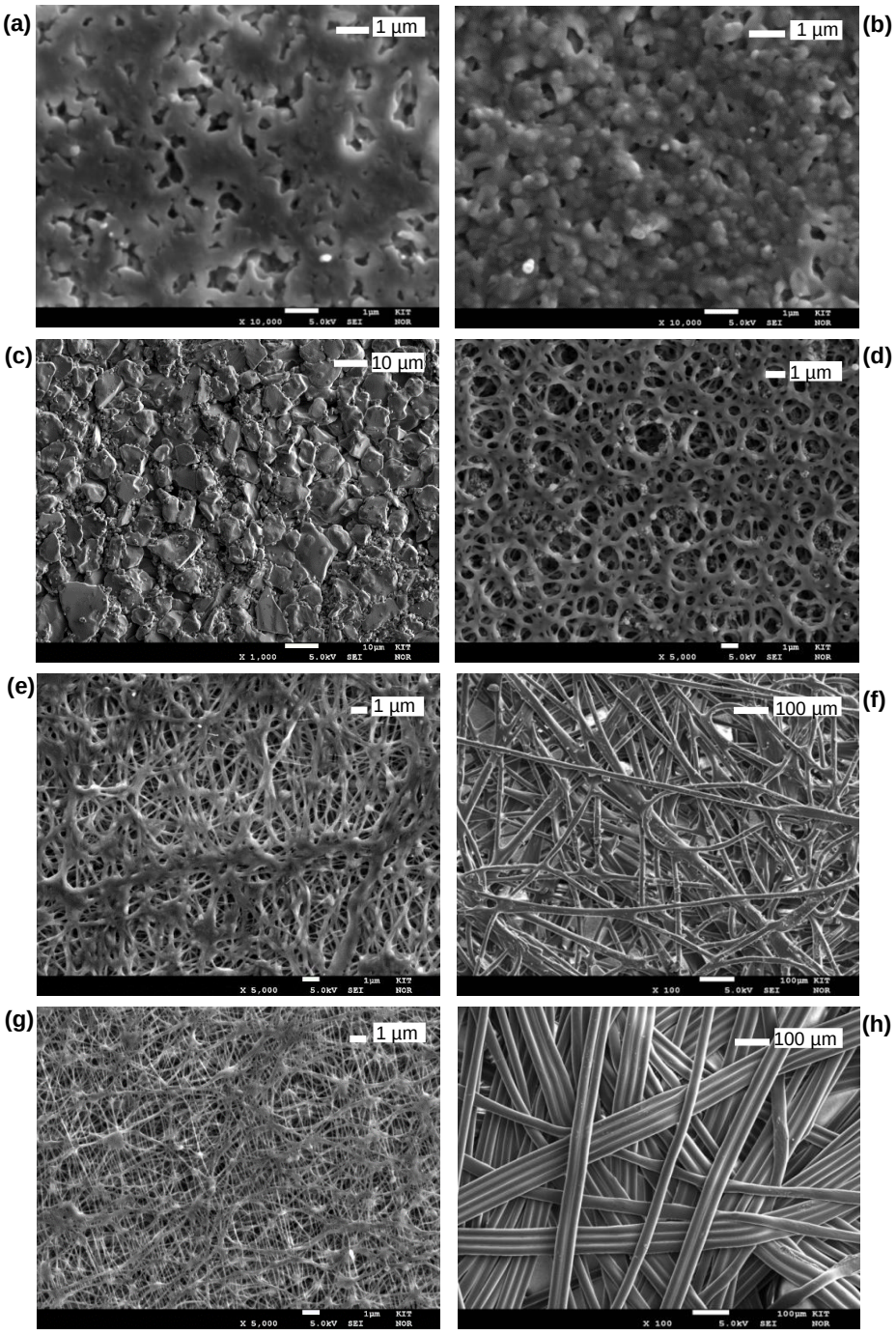

Figure 5.4.: SEM Pictures of various membranes. **(a)** front side of the PEEK membrane **(b)** back side of the PEEK membrane **(c)** front side of the ceramic 200 **(d)** front side of the acrylic copolymer membrane 200 **(e)** front side of the PTFE (PET) membrane **(f)** back side of the PTFE (PET) membrane **(g)** front side of the PTFE (PP) membrane **(h)** back side of the PTFE (PP) membrane.

In the case of ceramic membranes, see Figure 5.4 (c), the pores are the result of the voids between the sintered alumina grains. In this case, the front membrane surface is impreg-

nated with a hydrophobic agent. The support displays larger hollow volumes. The Versapor® membrane (acrylic copolymer) displays a trabecular-like meshwork with the same pore morphology and size on both sides, cf. the front side in Figure 5.4 (d). For the PTFE membranes, the selective layer (top layer) has a reticular structure with interconnected, continuous threads linked by junctions of variable size and morphology, cf. Figure 5.4 (f) and (e). The support layer, however, is a non-woven support, with a much more open structure than the top layer. The difference in the supports can be shown in Figure 5.4 (g) (PET Support) and Figure 5.4 (h) (PP support), respectively.

As can be observed from Figure 5.4, the pore geometry varies depending on the membrane material and design. Even for the same membrane materials, as shown in Figure 5.4 (e) and (g) for the PTFE membranes, the top layer is made up of a random orientation of very thin fibres. This leads to very different pore geometries for the same membrane material so that the applicability of a shape factor for the geometrical parameter B (cf. Equation 2.5 in Section 2.2.2) falls short. It is clear that the real pore geometry is very far from the assumed circular pore cross-sections and the value of such a shape factor should be far below 1.

5.2.2 LEP at ambient conditions

Figure 5.5 shows the experimental results of the LEP measurement for the membranes presented in Section 5.1.1. The LEP was measured using the experimental set-up for the visual method explained in Section 4.1.5. Figure 5.5 also includes the measured values of the static contact angle measured with deionized water. Static contact angle measurements were carried out manually with deionized water in an optical contact angle measurement system (OCA5, DataPhysics Instruments GmbH, Filderstadt, DE).

The values shown in Figure 5.5 are the average values of at least three consecutive measurements. As shown in Figure 5.5, the strong dependence of the LEP on the characteristic pore size can be confirmed. In this case, the characteristic pore size is taken as the mean pore size given by the manufacturer, since the largest pore size could not be determined in the present study. It can be observed that membranes with higher characteristic pore size, like the Alumina-400, present the lowest LEP which is in line with what the Young-Laplace equation describes, cf. Equation 2.5. It is noteworthy that porous PEEK membranes, advertised by the manufacturer as suitable for membrane distillation, display a contact angle of 80 ° and still a LEP value of 0.82 bar.

The results in Figure 5.5 reveal that ceramic membranes present a higher LEP than PTFE membranes for the same characteristic pore size. For example, in the case of the 100 nm membranes, the ceramic membrane shows a LEP of 8.2 bar (± 0.5 bar) and the PET-supported PTFE membrane shows 5.3 bar (± 0.08 bar). The reason for this difference is

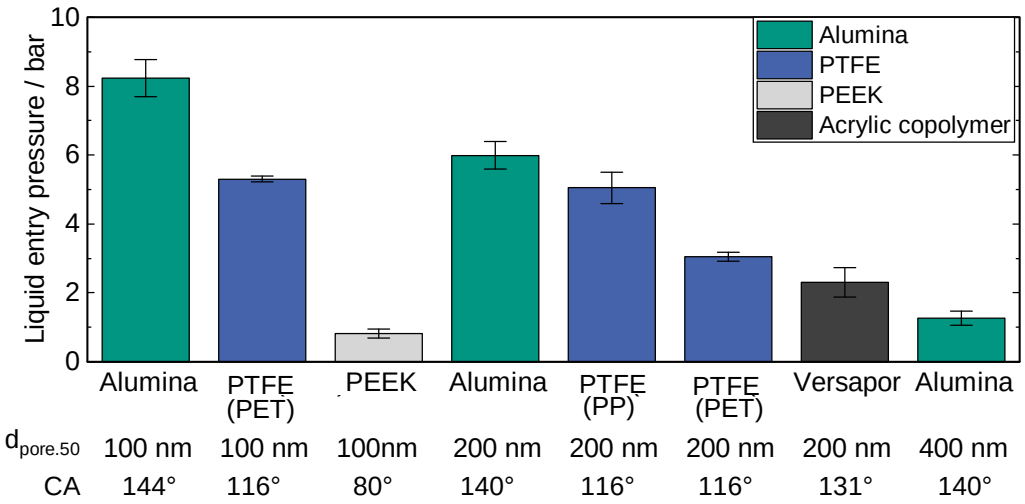

Figure 5.5.: Results of LEP measured by the visual method at ambient conditions T = 25 °C, p = 0 bar g together with the mean pore size of the membrane ($d_{pore.50}$) and the measured static contact angle values (CA).

not only the higher hydrophobicity of the ceramic surface - confirmed by the measured contact angle of 144 ° vs. 116 - but also the difference in internal geometry, as already seen in Figure 5.4.

The higher thickness of the tested ceramic membranes (2 mm) in comparison to the PTFE membranes (0.15 mm-0.25 mm) plays an important role, especially when the LEP is detected using the visual method. Here, a certain amount of time is required for a drop to form in the back side of the membrane that is large enough to be visible to the human eye. This positive effect of the membrane thickness on the LEP is also confirmed by the experimental and simulative observations of Guillen-Burrieza et al. [87] and Chamani et al. [187]. Moreover, the possibly narrower pore size distribution of ceramic membranes in comparison to polymeric membranes may be a strong factor contributing to this difference in performance. The same findings are seen for the 200 nm ceramic and PTFE membranes. Moreover, for the 200 nm PTFE membranes, a difference in LEP between the PP-supported PTFE membranes and the PET-supported membranes can be observed in Figure 5.5. The reason for this difference, apart from a possible different pore size distribution, might be the fact that PP is hydrophobic by nature and PET is hydrophilic. This leads to a faster formation of visible droplets in the back side of the PET-supported membrane. The morphological differences between the supports can be observed in Figure 5.4. Besides, even though the acrylic copolymeric membrane has a higher surface hydrophobicity (131 °), a lower LEP value was observed (2.3 bar ± 0.4 bar). The reason for this may also be the influence of the internal membrane morphology on the LEP value.

5.2.3 Visual method vs. pressure step method

Figure 5.6 shows the pressure course during a LEP test using the pressure step method and the visual method in the PMMA test cell (described in Section 4.1.5) for a 100 nm PTFE (PET) membrane at ambient conditions. The experiments were conducted at room temperature and atmospheric pressure.

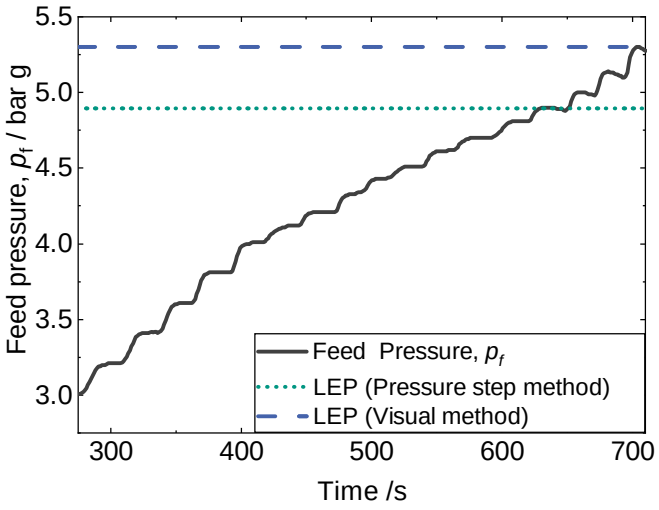

Figure 5.6.: Pressure course during LEP detection of the PTFE (PET) 100 nm membrane using pressure step method in the PMMA test cell compared to the value obtained with the visual method in the PMMA test cell. The pressure is increased step by step and held for 12 seconds. The pressure decrease at 4.8 bar g shows that the LEP has been reached.

When 4.8 bar g are reached on the feed side, a decreasing slope can be observed (negative pressure gradient), which is due to water leakage through the membrane. Comparing the value with the value obtained by the visual method (5.3 bar g), the value is approximately 10 % lower. The difference in results suggests that the pressure step method is an early detection method of the LEP compared to the visual method for the same test cell and operating conditions. In addition, Figure 5.7 shows the comparison of the LEP value obtained in the PMMA test cell via the visual method and the pressure step method as well as the results of the pressure step method in the membrane testing unit at room temperature and atmospheric pressure. Thus, without nitrogen flowing in the permeate side of the membrane testing unit. A further reduced LEP can be observed here.

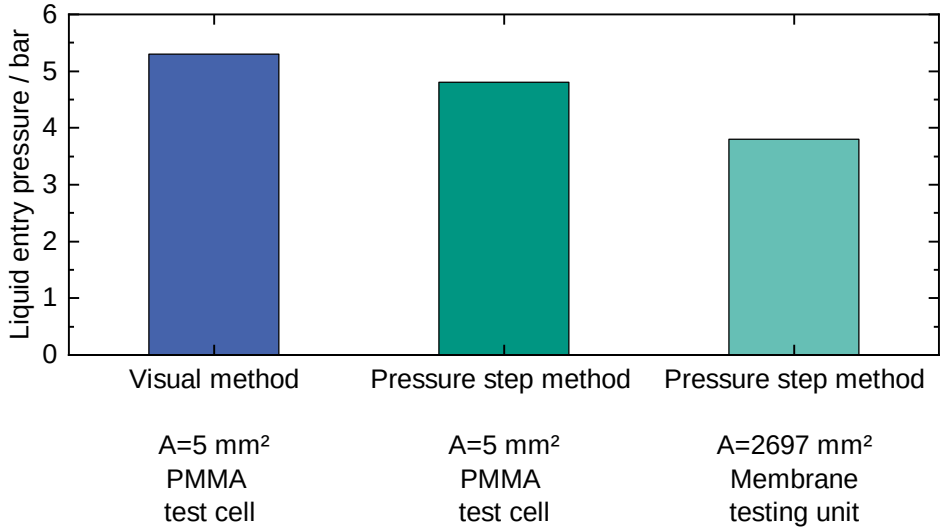

Figure 5.7.: LEP values of the PTFE (PET) 100 nm membrane using both, the visual method (left) and the pressure step method (middle) in the PMMA cell. The value obtained by means of the pressure step method in the membrane testing unit is also shown (right).

The differences in Figure 5.7 are not only due to the different detection methods, but also are influenced by the difference in the tested area. In the case of the pressure step method in the membrane testing unit, a membrane area of 2697 mm^2 is tested, instead of the 5 mm^2 test membrane area within the PMMA cell. This difference in test area may lead to a higher probability of having larger-than-average pores in the membrane testing unit, and therefore, a lower LEP value may be obtained. Overall, Figure 5.7 suggests that characterizing the LEP in the same test cell where further permeation or reaction experiments will be conducted (in this case, the membrane testing unit) leads to a more accurate characterization of the membrane for the application. These findings are consistent with the results of Warsinger [107], as well as the comparison made by Rácz [75] between dynamic and static methods [82].

5.2.4 LEP at higher pressures

To investigate the influence of increased pressure on the LEP, measurements were carried out at room temperature and pressures in the membrane testing unit up to 1.5 bar g for pure water. The permeate side was pressurized with nitrogen gas. The pressure was increased gradually to ensure that both sides of the membrane were pressurized to the same extent. In all the experiments, special care was taken to ensure that the pressure on the feed side was always slightly higher than the pressure in the permeate compartment so that no nitrogen would flow through the membrane to the feed side. When the desired pressure on both sides

of the membrane testing unit was reached, the feed pressure was further increased until the LEP could be detected.

Figure 5.8 shows the LEP results for three different membranes at room temperature: the alumina membrane-200 nm, the PTFE membrane supported by PET-100 nm, and the acrylic copolymeric membrane-200 nm. Each point is the average of two consecutive measurements. As shown in Figure 5.8, no trend can be identified when the pressure is increased; the LEP seems to remain unaffected. This behaviour can be explained by the minor effect of pressure on the surface tension in the studied range, where the intermolecular forces between the liquid molecules remain nearly unchanged [188]. Accordingly, no remarkable effect can be observed in the measured LEP. Based on [189, 190], only a 0.3 % decrease in surface tension can be expected when increasing the pressure up to 1.5 bar g [90, 191–193]. The slight differences in LEP behaviour for the different membranes may be due to secondary effects occurring during the measurement.

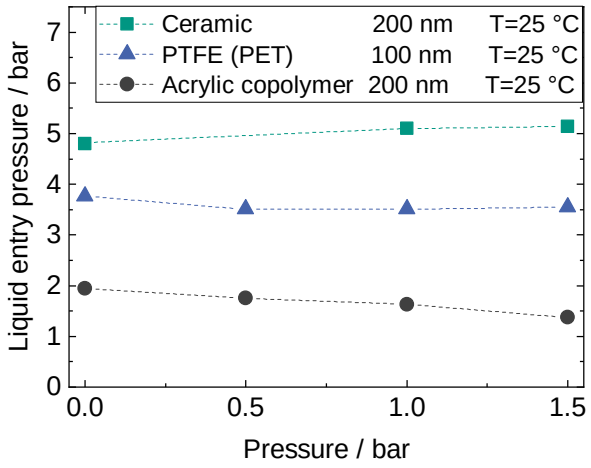

Figure 5.8.: Influence of pressures up to 1.5 bar g on LEP for a ceramic membrane 200 nm (squares), a PTFE (PET) membrane 100 nm (triangles) and an acrylic copolymeric membrane 200 nm (circles). Neither a positive nor negative trend can be clearly identified for the studied pressure range.

5.2.5 LEP at higher temperatures ($T < 80\,^{\circ}C$)

The effect of temperatures up to 80 °C at atmospheric pressure on the LEP was investigated for the ceramic membrane-200 nm and the Versapor® 200-R, both with a pore size of 200 nm. Figure 5.9 reveals a decrease in LEP of 30 % for the Versapor membranes and of 45 % for the ceramic membranes at temperatures up to 80 °C. At ambient pressure, a decrease in surface tensions of 13 % [193] is expected when the temperature is increased

up to 80 °C. The remaining LEP decrease (15-30 %) in this temperature range may be due to the change in contact angle with temperature and further secondary effects. The

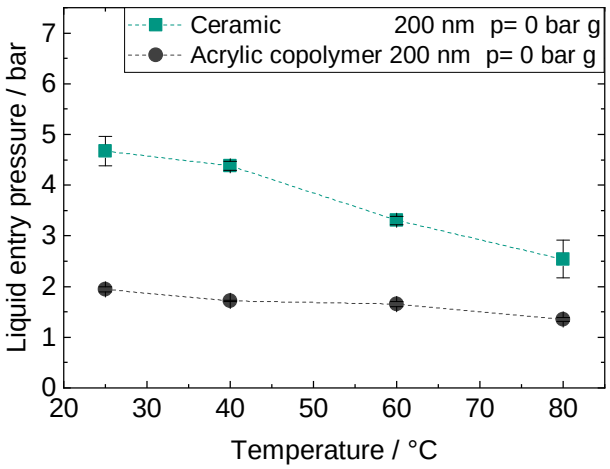

Figure 5.9.: Influence of the temperature up to 80 °C on LEP for a ceramic membrane 200 nm (squares) Versapor membrane 200 nm (circles). A decrease in the LEP can be observed, especially significant for the ceramic membranes.

decrease of LEP up to 50 °C is consistent with the LEP behaviour reported by Garcia Payo et al. [91] in the same temperature range for a PVDF membrane, i.e., a decrease of 13 % in comparison to ambient conditions. The LEP decrease up to 70 °C is 7 % larger than the LEP decrease measured by Saffarini et al. [86] in the same temperature range for PTFE membranes. Saffarini et al. attributed this decrease not only to the reduction of surface tension and contact angle but also due to the alteration of the membrane microstructure with temperature. These comparisons should be taken with care, as even if the fluid and the conditions may be equivalent, the membranes are made of different materials.

5.2.6 LEP at higher temperatures (T > 80 °C)

Measurements of LEP at temperatures between 80–120 °C were performed by raising the pressure to a value above the corresponding saturation pressure of the operating temperatures to avoid boiling. Pressure and temperature were alternately increased to avoid the boiling of water and the inflow of nitrogen into the feed chamber. A further decrease of LEP due to the temperature increase up to 120 °C can be observed in Figure 5.10 compared to Figure 5.9, where the experiments were conducted up to 80 °C.

As already confirmed in Section 5.2.4, the effect of the pressure on the surface tension is not significant within the pressure range studied; therefore, the decrease in LEP is mainly due to the increase in temperature. At 120 °C, a LEP value of 0.9 bar was measured. In the literature, a LEP of at least 2.5 bar is recommended to avoid wetting [194]. However, membranes with lower LEP values may still be applicable if the membrane module is accordingly designed so that the transmembrane pressure never exceeds the LEP. This can be achieved by considering the right pressure, volume flow rate, and hydraulic diameter of the feed and permeate side. To the best of the author's knowledge, there are no comparable values in the literature for LEP measured directly at constant temperature conditions in this higher temperature range and at elevated pressure. Varela-Corredor [93] characterized the LEP of titania-based tubular membranes up to 105 °C. He measured a liquid entry temperature of nearly 130 °C by establishing a very low constant transmembrane pressure.

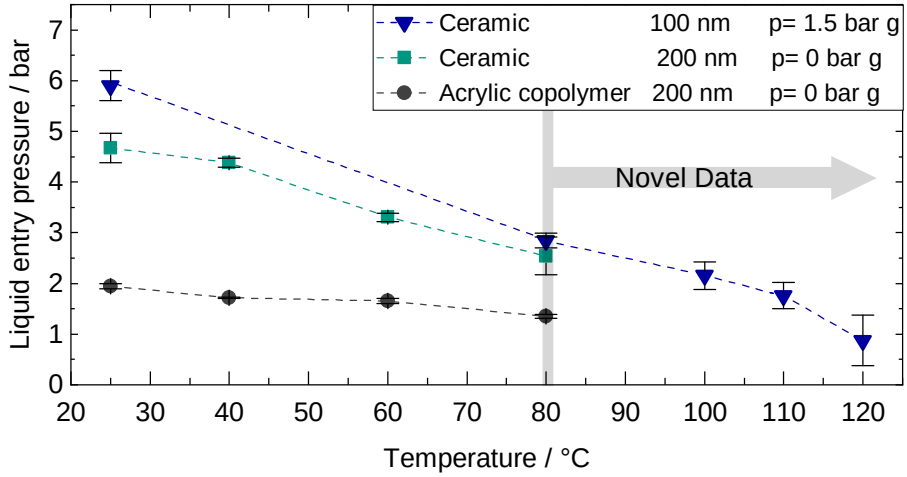

Figure 5.10.: Influence of temperatures up to 120 °C on the LEP for ceramic membrane 100 nm (triangles) at a pressure of 1.5 bar g compared to the LEP for a ceramic membrane 200 nm (squares) and a Versapor membrane 200 nm (circles) up to 80 °C. The increase of the temperature up to 120 °C results in a further increase of the LEP.

Overall, the direct measurement of LEP in the temperature range considered in this work expands the application range of hydrophobic membranes and allows the membranes to be used in unexplored fields. These results are particularly relevant for the application of these membranes for sweeping gas membrane distillation, as the operating parameters can be reproduced.

5.3 Summary of Chapter 5

The LEP of different commercial polymeric and ceramic membranes was characterized in this chapter. The visual method was used for this purpose. When comparing the different membrane materials, the influence of the membrane morphology on the value of the LEP could be identified. Thus, not only the contact angle and the pore size are relevant, but also the material and manufacturing process of the membrane have an impact on the final LEP value. The results obtained with the visual method were compared with the results obtained with the pressure step method for PTFE membranes. The results showed that the pressure step method is an early detection method for the determination of the LEP. Moreover, the LEP of several membranes was characterized at higher temperatures and pressures above atmospheric pressure using the pressure step method in the membrane testing unit. To ensure liquid conditions, pressure was applied on the feed and permeate side. The results revealed that the temperature is the main factor affecting the LEP due to its effect on the surface tension. In contrast, pressure has no significant effect on the LEP in the studied range. Novel LEP data up to 120 °C and 1.5 bar g were obtained. These findings can be used for the design of a sweeping gas membrane distillation unit and extend the application range of hydrophobic membranes.

6

Sweeping gas membrane distillation at elevated temperatures

This chapter deals with the theoretical and experimental investigation of sweeping gas membrane distillation (SGMD) at elevated temperatures. Especially at temperatures above 80 °C and pressures above atmospheric, there are no comparable works for SGMD in literature and therefore, it is particularly valuable to understand which phenomena take place. To understand the effect of different operating variables on the transmembrane flux, the process has been mathematically modelled. Thus, the theoretical principles of the modelling as well as a description of the experimental plant and procedure are given in this chapter. The results from the experiments and the mathematical modelling are presented together and discussed. The effect of feed parameters like mass flow rate, inlet temperature and glucose concentration as well as the effect of sweep gas parameters like pressure and volume flow rate are addressed.

6.1 Experimental methodology

6.1.1 Experimental set-up for water separation by means of SGMD at elevated temperatures

The experimental plant for water removal by means of sweeping gas membrane distillation at high temperatures was an extension of the plant used for the characterization of the LEP of membranes at higher temperatures (cf. Section 5.1.3). Figure 6.1 shows a schematic flow diagram of the plant. A more detailed P&ID can be found in Annex A.10. The manufacturers and type designations of all sensors and actuators can be found in Annex A.11. The membrane testing unit used for the investigation of water removal at high temperatures was the same as the one used for the LEP experiments at high temperatures and is described in Section 5.1.2. For these experiments, the ceramic membranes described in Section 5.1.1 with an average pore size of $d_{\text{pore.50}} = 100\,\text{nm}$ were used. In Figure 6.2 the SEM image of the membrane cross-section is shown.

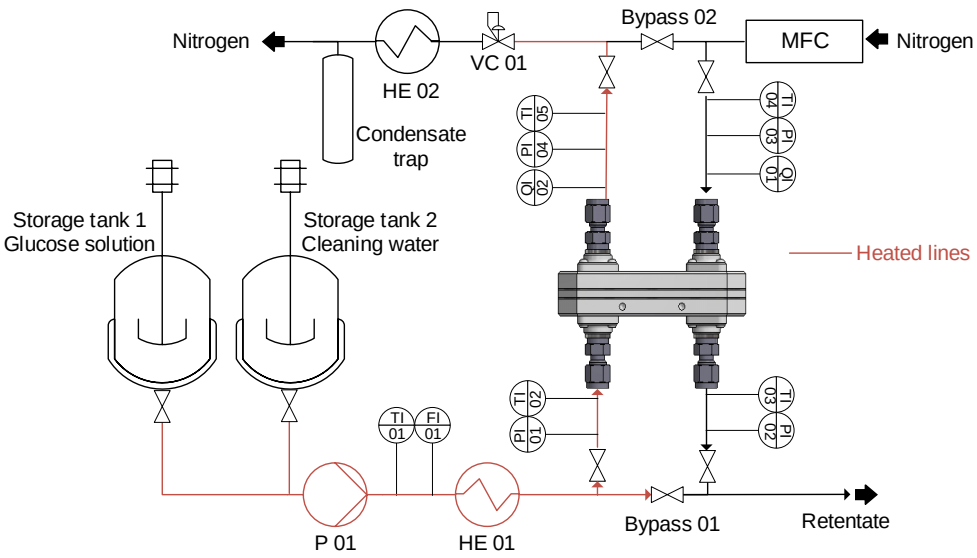

Figure 6.1.: Schematic flow diagram of the SGMD plant: membrane testing unit (in the middle), feed line (lower part) and sweep gas line (upper part). In the feed line, starting from the left, the fluid (water or glucose solution) flows towards the membrane unit. The line downstream of the membrane unit in the lower part represents the retentate stream. In the upper part, starting from the right, the nitrogen flows in counter-current into the membrane testing unit. A condenser is located at the end of the sweep gas line to separate water (permeate stream) and nitrogen.

For this investigation, the liquid solution was fed into the system via an eccentric screw pump, P 01, from the heated storage tank 01. The liquid feed was either pure water or a glucose solution with a concentration of up to 50 wt. %. In the case of experiments with glucose, the storage tank 01 was used for the feed solution, and the storage tank 02 was filled with DI water for cleaning purposes to avoid sugar from precipitating in the pipes and fittings. The feed mass flow rate was controlled manually by setting the pump speed and measured via a Coriolis flow meter, FI 01. To maintain the temperature in the feed lines, all the pipelines were fitted with electric heating coils and covered with glass wool insulation. Before entering the membrane testing unit, the feed mass flow was further heated in a microstructured cross-flow heat exchanger, HE 01. The heat exchanger was responsible for setting the temperature for the experiments. After the heat exchanger, the feed could flow via bypass 01 or through the membrane testing unit, depending on the position of the valves. This way, the liquid was flown through bypass 01 until the feed temperature stabilized and reached the target value. Afterwards, the valve position was changed, and the liquid could flow towards the membrane testing unit for the membrane distillation to start. A pressure control valve was installed downstream the membrane unit at the retentate side to adjust the pressure on the liquid side. This allowed to conduct experiments in a liquid state at pressures above the vapour pressure of water at high temperatures. The most important pressure and temperature measuring points on the feed side are shown in Figure 6.1.

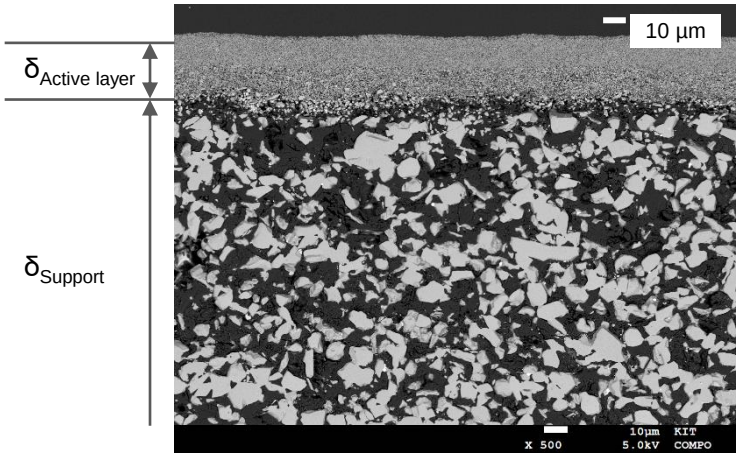

Figure 6.2.: SEM image of the cross-section of the ceramic membrane with an average pore size of $d_{\text{pore.50}} = 100\,\text{nm}$. The active layer, with a thickness of $\delta_{\text{A}} = 30\,\mu\text{m}$ and the support layer, with $\delta_{\text{S}} = 2$ mm are indicated.

On the gas side, the sweep gas (in this case, nitrogen) entered the system with a maximum pressure of 10 bar g. A control valve was used to set the upstream pressure for the mass flow controller (MFC). The sweep gas flow rate was set by the MFC nd regulated via the software LabView® (National Instruments). After the MFC, the sweep gas flowed via bypass 02 or through the membrane testing unit, depending on the position of the valves. The humidity

of the sweep gas stream was measured upstream and downstream the membrane testing unit (humidity sensors, QI 01 and QI 02). The pressure on the sweep gas side was regulated via a back pressure regulator (VC 01). Downstream of the pressure regulator, there was a microstructured cross-flow heat exchanger (HE 02) to condense the water carried by the sweep gas, which was then separated in a trap.

6.1.2 Calculation of the experimental transmembrane flux

From the measurement of the humidity upstream and downstream of the membrane testing unit (sensors QI 01 and QI 02, respectively), the molar fraction of water in the permeate stream (y_w) can be calculated. The subscripts in or out refer to the gas (permeate) flow into or out of the membrane testing unit.

$$\tilde{y}_w^{in/out} = \frac{\varphi^{in/out} \cdot 10^{-2} \cdot p_w^* \left(T_p^{in/out}\right)}{p_p} \tag{6.1}$$

here φ is the relative humidity in percent, measured at the inlet of the membrane testing unit (sensor QI 01, subscript in) or at the outlet (sensor QIR 02, subscript out). $p_w^*(T_p)$ is the water partial pressure at the temperature measured at the same location in the permeate where the relative humidity is measured, i.e. into or out of the membrane testing unit. The water partial pressure is calculated with the Wagner Equation [195]. The pressure in the permeate is represented by p_p, which remains constant along the permeate compartment (no changes along the microchannels).

From the inlet and outlet molar fraction of water, $\tilde{y}_w^{in/out}$, the inlet and outlet mass-based loading, $Y_w^{in/out}$, can be calculated with Equation 6.2:

$$Y_w^{in/out} = \frac{\tilde{M}_{N_2}}{\tilde{M}_w} \cdot \frac{\tilde{y}_w^{in/out}}{1 - \tilde{y}_w^{in/out}} \tag{6.2}$$

Where $\tilde{M}_{N_2}$ and $\tilde{M}_w$ refer to the molar mass of nitrogen and water respectively.

To determine the transmembrane flux, a mass balance is made for the entire permeate compartment of the membrane testing unit, assuming that no sweep gas flows or diffuses into the feed compartment, and therefore, the mass flow rate of sweep gas remains constant. In fact, the feed water was not degassed before entering the membrane unit, i.e., it was saturated with air. In turn, no significant diffusion of nitrogen into the feed compartment is expected. Consequently, the inlet and outlet sweep gas mass flow rates in the balance depicted in Figure 6.3 are equal, $\dot{M}_{N_2}^{in} = \dot{M}_{N_2}^{out} = \dot{M}_{N_2}$.

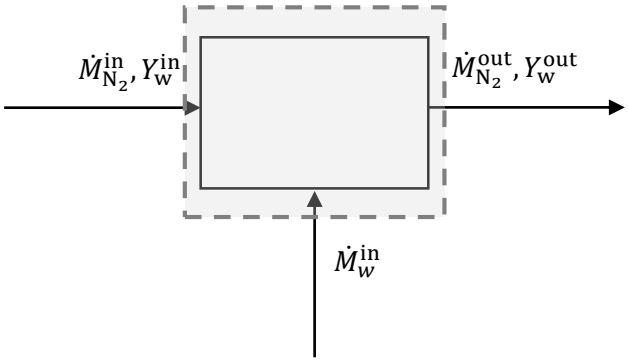

Figure 6.3.: System boundaries for the determination of the average transmembrane flux in the membrane testing unit. The control volume depicted refers to the permeate compartment. The entering streams are the mass flow of the sweep gas $\dot{M}^{in}_{N_2}$ with a given inlet loading of water Y^{in}_w and the transmembrane flow, $\dot{M}^{in}_w$. From the control volume, the outgoing flow is the mass flow of the sweep gas, $\dot{M}^{out}_{N_2}$, and the resulting loading of water, Y^{out}_w.

From the balance according to Figure 6.3 and the equation for the calculation of the water loading (Equation 6.2), the transmembrane flow of water $\dot{M}^{in}_w$ can be calculated as:

$$\dot{M}^{in}_w = \dot{M}_{N_2} \cdot (Y^{in}_w - Y^{out}_w) \tag{6.3}$$

In all experiments, for each operating point, measurements were recorded for 5 minutes after the system reached a steady state. For this period, the mean value and the standard deviation of the transmembrane water flow were calculated.

6.2 Mathematical model

The modelling of the transmembrane flux in sweeping gas membrane distillation aims to complement the understanding of the transport of water through the porous membrane as well as in the feed and permeate compartments while evaluating the experimental observations. Besides, the model seeks to determine the influence of several operating and geometrical parameters, and therefore forecast possible occurring scenarios. For this purpose, the heat transfer (heat conduction and convection) and mass transfer (mass convection and diffusion) steps across the membrane have been considered and modelled in MATLAB®. The model developed here for the transmembrane flux should serve as a basis for the future design of membrane testing units and membrane reactors.

6.2.1 Modelling approach

The membrane testing unit for SGMD has a flat configuration, cf. Figure 6.4 for a system simplification. It consists of two fluid compartments with a membrane in-between. Hot water (or hot glucose solution) flows in the 25 microchannels of the lower compartment (see section 5.1.2 for a detailed description of the geometry). The upper wall of these microchannels consists of a microporous hydrophobic membrane. Due to its hydrophobicity, only water vapour can diffuse through the membrane, whereas the liquid water (or liquid glucose solution) is retained in the feed compartment. Sweep gas (in this case, nitrogen) flows in counter-current in the 12 microchannels of the upper (permeate) side. The presence of the sweep gas on the permeate side creates a partial pressure gradient that forces the vapour to diffuse through the membrane, leading to a transmembrane flux across the membrane, and consequently also heat and mass transfer in each fluid compartment.

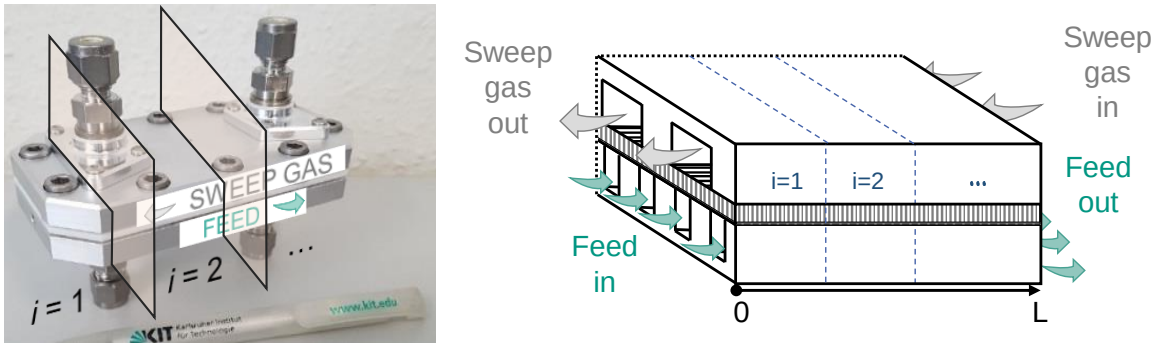

Figure 6.4.: Schematic representation of the membrane testing unit with the inlet and outlet feed streams in green and permeate (sweep gas) streams in grey.

The membrane testing unit is described mathematically with a cell model. Figure 6.5 shows schematically the picture of a 3D cell with the inlet and outlet streams, as well as the transmembrane flux from the feed channels transfer area (green) through the membrane up to the permeate channels transfer area (grey). For modelling purposes, it is simplified into a pseudo-2D model, as depicted on the right side of Figure 6.5. In each cell (i) it is assumed that the liquid phase on the feed side and the gas phase on the permeate side are, respectively, ideally mixed. The transfer area in the feed of the cell in the model is the sum of the top area of all 25 feed channels of the 3D cell. Likewise, the transfer area in the permeate of the cell in the model is the sum of the top area of all 12 permeate channels in the 3D cell.

In the experiments, the membrane testing unit was heated to compensate for the evaporative cooling in the feed. The decrease in temperature in the feed compartment due to the evaporative cooling in case of a feed flow rate of 1.8 kg h^{-1} with an inlet temperature of 50°C

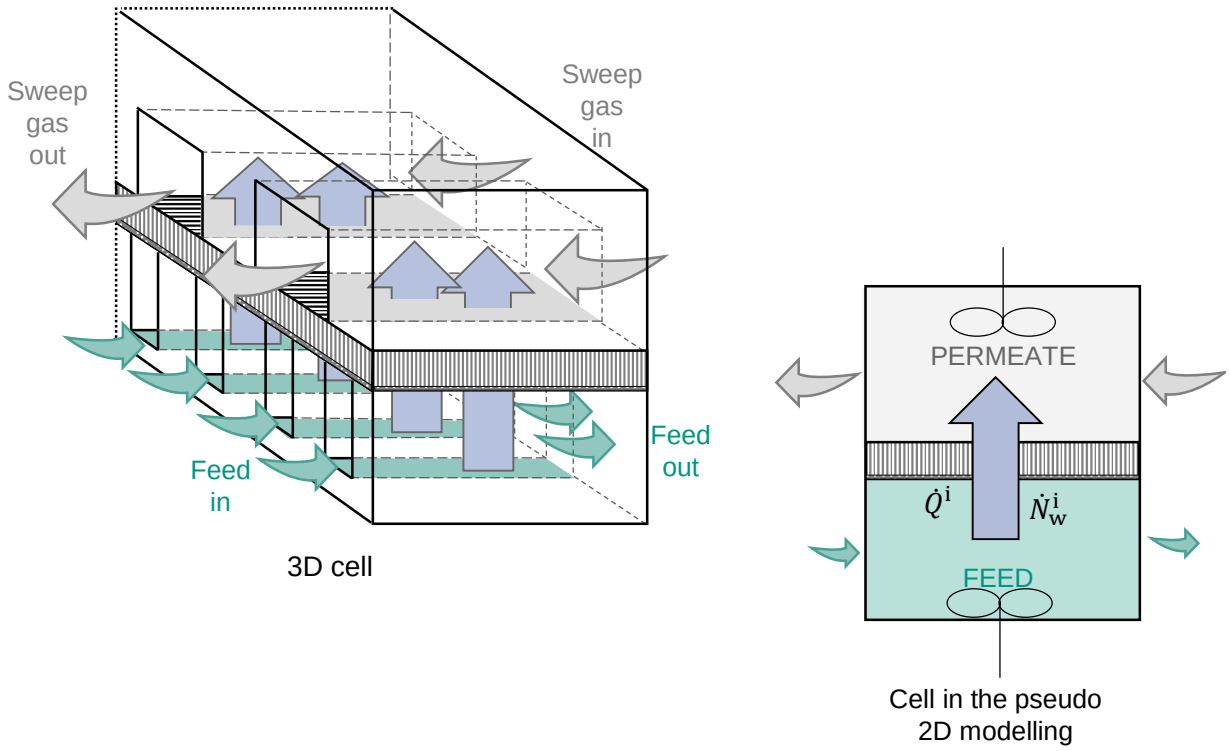

Figure 6.5.: Schematic representation of one 3D cell into which the membrane testing unit is divided as well as a simplification to a pseudo-2D system for modelling purposes. Green arrows represent the feed inlet and outlet streams and grey arrows represent the sweep gas inlet and outlet streams. The blue arrow refers to the transmembrane water flow, involving mass ($\dot{N}_{w}^{i}$) and heat ($\dot{Q}^{i}$) transfer across the membrane. No heat loss from the testing unit to the environment is considered.

and a sweep gas flow rate of 30 NL min^{-1} with an inlet temperature of 25°C was estimated to be 0.2°C. In case the feed flow entered with a temperature of 130°C, the temperature reduction was 3.7°C. The use of heating cords around the testing unit largely avoided such a temperature drop during the experiments, so that the feed could be assumed to flow isothermally. Besides, since a maximum pressure loss of 20 mbar in the flow direction was measured during the experiments, the pressure loss along the channels was neglected. In the model, it is assumed that only water vapour diffuses through the membrane pores. This assumption could be confirmed by visual checks of the membrane's back side after each operation: when no water droplets were observed in the back side, the experiment was assumed to have run properly. In the experiments with glucose solution in the feed, the measurement of the brix degree in the permeate (equal to zero) also gave an indication of whether or not glucose solution flowed through the pores. Besides, no back diffusion of nitrogen into the feed compartment was considered as already stated in section 6.1.2.

Further simplifying assumptions in the model are:

- No heat loss through the membrane testing unit wall to the environment is considered due to good isolation and heating of the membrane testing unit.
- Constant membrane properties such as thickness and pore size are considered for a given membrane. Since the tortuosity of membranes is a difficult parameter to access, it is chosen as a fitting parameter, as previously V. Karanikola et al [196] and A. Mourgues et al. [141] did. The tortuosity to porosity ratio has been therefore chosen between 0.26 - 0.35, which is within the range of literature data for alumina membranes [197–200].
- The pressure and temperature conditions in the membrane testing unit ($p_{max} = 6$ bar g and T_{max}=150 °C) allow for the description of the gas phase with the ideal gas law.
- Evaporation of water at the liquid-gas interface (pore entrance, feed-membrane location) is assumed to be in thermodynamic equilibrium.
- As in the experiments, the pressure difference between feed and permeate is always set to 0.15 bar.

Mass and heat transport steps

The mass and heat transfer in the feed and permeate compartment as well as across the membrane are modelled taking the above assumptions into account. The linear Fick's approach is used to describe mass transfer. Figure 6.6 schematically shows the individual mass transport coefficients and the course of the molar fraction of water. In the system under consideration there are four mass transfer steps:

1. Mass transfer from the bulk feed to the feed-membrane interface. Mass transfer coefficient, β_f.
2. Mass transport through the active layer of the membrane. Mass transport coefficient, β_A.
3. Mass transport through the membrane support. Mass transport coefficient, β_S.
4. Mass transfer from the membrane surface on the permeate side to the bulk permeate phase. Mass transfer coefficient, β_p.

The different layers of the membrane (active layer and support) are considered separately from each other because they differ in thickness and mean pore size. As presented in the theoretical introduction in Chapter 2, for the calculation of the mass transfer coefficient of the membrane, two main diffusion mechanisms across the membrane should be considered, Knudsen diffusion and molecular diffusion [114]. The diffusion coefficient in the feed and permeate boundary layers were calculated from the equations for the molecular diffusion

in the liquid or gas phase (cf. Annex A.4). Due to the conservation of mass, the four molar flows must be identical, and can be inserted into each other resulting in Equation 6.4:

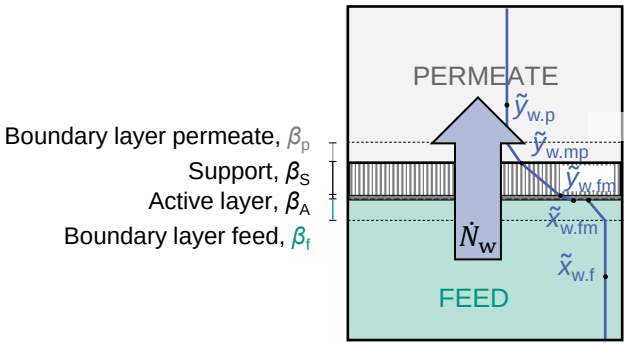

Figure 6.6.: Schematic representation of the mass transport steps with the corresponding mass transport coefficients and the course of the molar fraction of water.

$$\dot{N}_w = \frac{A_p}{\underbrace{\frac{1}{\frac{1}{\rho_p}\beta_p}}_{\text{Permeate}} + \left[\underbrace{\frac{1}{\tilde{\rho}_A\frac{\varepsilon_A}{\tau_A}\beta_A}}_{\text{Active layer}} + \underbrace{\frac{1}{\tilde{\rho}_S\frac{\varepsilon_S}{\tau_S}\beta_S}}_{\text{Support}}\right]\cdot\frac{A_p}{A_m} + \frac{A_p}{A_f}\cdot\underbrace{\frac{1}{\tilde{\rho}_f\beta_f}}_{\text{Feed}}} \cdot \left[\tilde{x}_{w.f} - \tilde{y}_{w.p}\right] \tag{6.4}$$

Specifically, in case there is no solute in the feed side, the mass transfer in the liquid bulk phase can be ignored and the expression can be written considering the water partial pressure difference between the pore entrance (feed-membrane location) and the permeate bulk phase as the driving force:

$$\dot{N}_w = \frac{A_p}{\underbrace{\frac{1}{\frac{1}{RT_p}\beta_p}}_{\text{Permeate}} + \left[\underbrace{\frac{1}{\frac{1}{RT_A}\frac{\varepsilon_A}{\tau_A}\beta_A}}_{\text{Active layer}} + \underbrace{\frac{1}{\frac{1}{RT_S}\frac{\varepsilon_S}{\tau_S}\beta_S}}_{\text{Support}}\right]\cdot\frac{A_p}{A_m}} \cdot \left[p_{w.fm} - p_{w.p}\right] \tag{6.5}$$

The different mass transport resistances are depicted in Equation 6.4 and 6.5, as well as the driving force for the separation, which is the difference in concentration expressed as the difference in the molar fraction ($\tilde{x}_{w.f} - \tilde{y}_{w.p}$, in Equation 6.4) or as the difference in partial pressures ($p_{w.fm} - p_{w.p}$, in Equation 6.5). The different transfer areas in the permeate, active layer, support, and feed, are represented by A_p, A_A, A_S and A_f, respectively while the quotient $\frac{\varepsilon}{\tau}$ represents the porosity to tortuosity ratio of the active layer and support, respectively. In Equation 6.4, $\tilde{\rho}$ is the molar density in the different locations. In Equation 6.5 T is the temperature in the different locations in Equation 6.5 and R represents the ideal gas constant.

In membrane distillation, mass and heat transfer are coupled inside the membrane. Water in the feed evaporates in the pore entrance at the prevailing temperature on the feed side. For the phase change, the evaporation enthalpy of water (ΔH_v) must be applied, which is extracted from the sensible heat of the feed flow and absorbed by the permeate flow. By taking into account the transmembrane molar flow of water resulting from Equation 6.4 (or Equation 6.5 when there is no solute in the feed), the heat associated with the phase change can be calculated. In addition to the transport of latent heat with the transmembrane flow, a portion is transferred by heat conduction through the membrane, between the feed and permeate sides of the membrane surface ($T_\mathrm{fm} - T_\mathrm{mp}$). This can be determined from the conductivity coefficient and the membrane thickness, $\left(\frac{\lambda_\mathrm{m}}{\delta_\mathrm{m}}\right)$, as well as the temperature difference. In accordance with the considerations above, the heat transport through the membrane is described as:

$$\dot{Q}_\mathrm{m} = \dot{Q}_\mathrm{evap} + \dot{Q}_\mathrm{cond} = \dot{N}_\mathrm{w} \Delta H_\mathrm{v} + \frac{\lambda_\mathrm{m}}{\delta_\mathrm{m}} \left(T_\mathrm{fm} - T_\mathrm{mp}\right) A_\mathrm{m} \tag{6.6}$$

Figure 6.7 schematically shows the individual heat transport steps and the course of the temperature. As noted above, the feed compartment is assumed to be isothermal, due to the effect of the external heating which accounts for the evaporative cooling in the feed. Thus, the temperature at the membrane surface on the feed side equals the temperature in the bulk, $T_\mathrm{fm} = T_\mathrm{f}$.

This is not the case for the permeate compartment, where Equation 6.7 applies:

$$\dot{Q}_\mathrm{p} = \alpha_\mathrm{p} A_\mathrm{p} \left(T_\mathrm{p} - T_\mathrm{mp}\right) \tag{6.7}$$

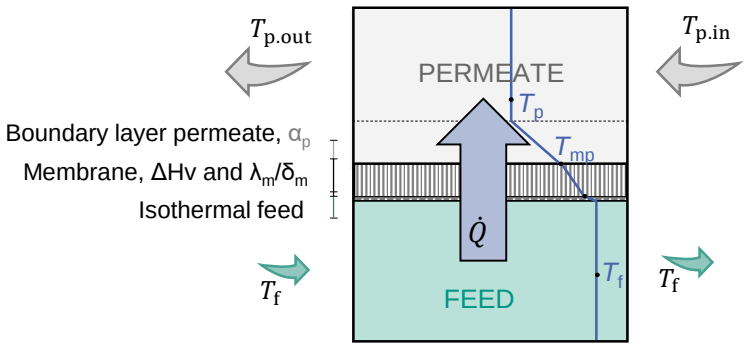

Figure 6.7.: Schematic representation of the heat transport steps with the temperature course. In the system, no heat loss to the environment as well as an isothermal feed are assumed.

Consequently, the temperature on the permeate side varies along the membrane testing unit length according to Equation 6.8:

$$\dot{Q}_\mathrm{p} = \dot{N}_\mathrm{p}\, c_\mathrm{p.p} \left(T_\mathrm{p.out} - T_\mathrm{p.in}\right) \tag{6.8}$$

The property data for water and nitrogen used in the model has been taken from the VDI-Heat Atlas [195]. The property data regarding the glucose solution used in the model is not presented in this dissertation for confidentiality reasons with the industrial project partner, Cargill Inc.

6.2.2 Material and heat balances

There are two possible flow modes of the sweep gas, i.e. co-current with the feed flow and counter-current. Figure 6.8 shows schematically both configurations for the cells i-1, i and i+1. In case the sweep gas flows in co-current mode, the calculation of the outlet temperature, $T^{\mathrm{i}}_{\mathrm{p,out}}$ and outlet molar flow rate, $\dot{N}^{\mathrm{i}}_{\mathrm{p,out}}$ in the permeate compartment of each cell is performed by solving a material and energy balance. The outlet parameters in the feed compartment are calculated following the same procedure. In case the sweep gas flows in counter-current, an initial guess for $T^{\mathrm{i}}_{\mathrm{p,out}}$ and $\dot{N}^{\mathrm{i}}_{\mathrm{p,out}}$ is generated and by means of the material and energy balance, the inlet temperature, $T^{\mathrm{i}}_{\mathrm{p,in}}$ and molar flow rate, $\dot{N}^{\mathrm{i}}_{\mathrm{p,in}}$ are solved.

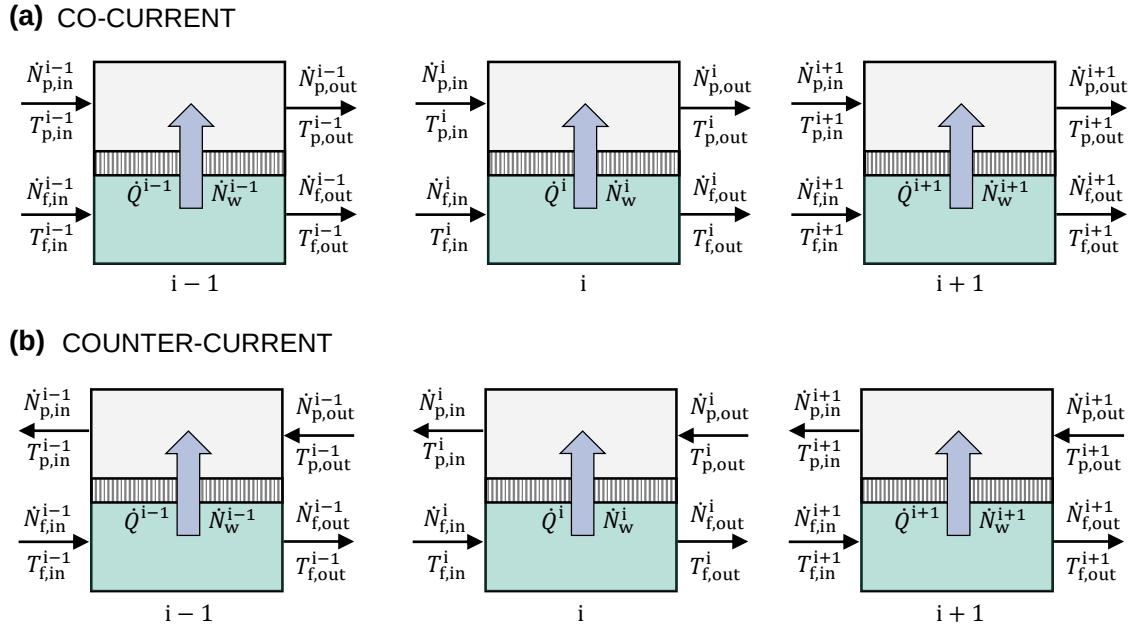

Figure 6.8.: Representation of the material and heat balances in the cells i-1, i and i+1 with the inlet (in) streams and outlet (out) streams. **(a)** Sweep gas flows in co-current and **(b)** sweep gas flows in counter-current. The heat flow through the feed and permeate compartment is determined as $\dot{N}c_{\mathrm{p}}T$ by the molar flow $\dot{N}$ (depicted), the molar heat capacity c_p and the temperature T (depicted) at the corresponding compartment (feed, f or permeate, p) and the respective cell i-1, i or i+1.

The calculation is done iteratively as to match the inlet permeate temperature, $T_{p,in}$ and molar flow rate, $\dot{N}_{p,in}$ which was set in the experiments. Further information about the generation of the initial guess and which strategy is used for the iterative update is given in section 6.2.3. In both flow modes, the calculated outlet variables are set as the inlet parameters for the next cell until the whole length of the membrane testing unit has been calculated. This means that for a given cell i, the inlet parameters correspond to the outlet parameters of the previous cell, i-1. Accordingly, Figure 6.9 applies.

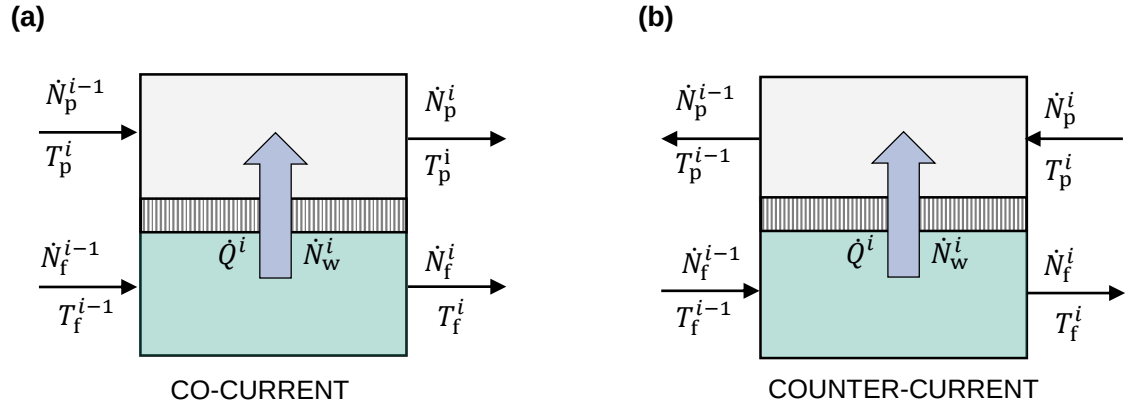

Figure 6.9.: Representation of the material and heat balances in a cell with the inlet feed stream,i-1, and outlet stream, i. **(a)** When the sweep gas flows in co-current, the permeate inlet stream is i-1 and the permeate outlet stream is i. **(b)** When the sweep gas flows in counter-current, the permeate inlet stream is i, and the permeate outlet stream is i-1.

Permeate compartment

As per Figure 6.9, depending on whether the sweep gas is flowing in counter-current or co-current, the transmembrane flow rate of water, $\dot{N}^{i}_{w}$ is added to the i-1 permeate flow, $\dot{N}^{i\text{-}1}_{p}$ or removed. This leads to Equation 6.9 for the calculation of the permeate molar flow rate $\dot{N}^{i}_{p}$, where "plus" is used for co-current flow and "minus" for counter-current flow.

$$\dot{N}^{i}_{p} = \dot{N}^{i\text{-}1}_{p} \pm \dot{N}^{i}_{w} \tag{6.9}$$

From the component balance of water, the mole fraction of water in the permeate compartment $\tilde{y}^{i}_{w}$ can be calculated in each step as follows:

$$\tilde{y}^{i}_{w.p} = \frac{\dot{N}^{i}_{w} + \dot{N}^{i\text{-}1}_{p}\,\tilde{y}^{i\text{-}1}_{w.p}}{\dot{N}^{i}_{w} \pm \dot{N}^{i\text{-}1}_{p}} \tag{6.10}$$

Here again, the "plus" symbol is used when the sweep gas flows in co-current while the "minus" symbol is used when the sweep gas flows in counter-current.

For the calculation of the temperature in the permeate, T_{p}^{i}, a heat balance is performed considering the entering sweep gas flow rate $\dot{N}_{\mathrm{p}}^{i-1}$ with the inlet temperature of the sweep gas, T_{p}^{i-1} and the corresponding heat capacity of the permeate flow $c_{\mathrm{p.p}}^{i-1}$. The heat capacity in the permeate, $c_{\mathrm{p.p}}^{i-1}$ is obtained from the molar heat capacity of the mixture nitrogen - water vapour with the water vapour molar fraction that the sweep gas is already carrying, $\tilde{y}_{\mathrm{w}}^{\mathrm{i}}$, Equation 6.10, as the weighting factor. The outlet temperature is influenced by the resulting permeate molar flow, $\dot{N}_{\mathrm{p}}^{i}$, which in turn depends on the transmembrane flow of water, $\dot{N}_{\mathrm{w}}^{i}$, as per Equation 6.9 and the heat flux resulting from the SGMD process (evaporation + conduction), $\dot{Q}^{i}$, given in Equation 6.6.

$$T_{\mathrm{p}}^{i} = T_{\mathrm{p}}^{i-1} \pm \frac{\dot{Q}^{i}}{\dot{N}_{\mathrm{p}}^{i} c_{\mathrm{p.p}}^{i}} \tag{6.11}$$

Figure 6.10 shows the resulting temperature profile in the permeate compartment for different feed temperatures. The modelled outlet temperatures in the permeate match the experimental temperatures.

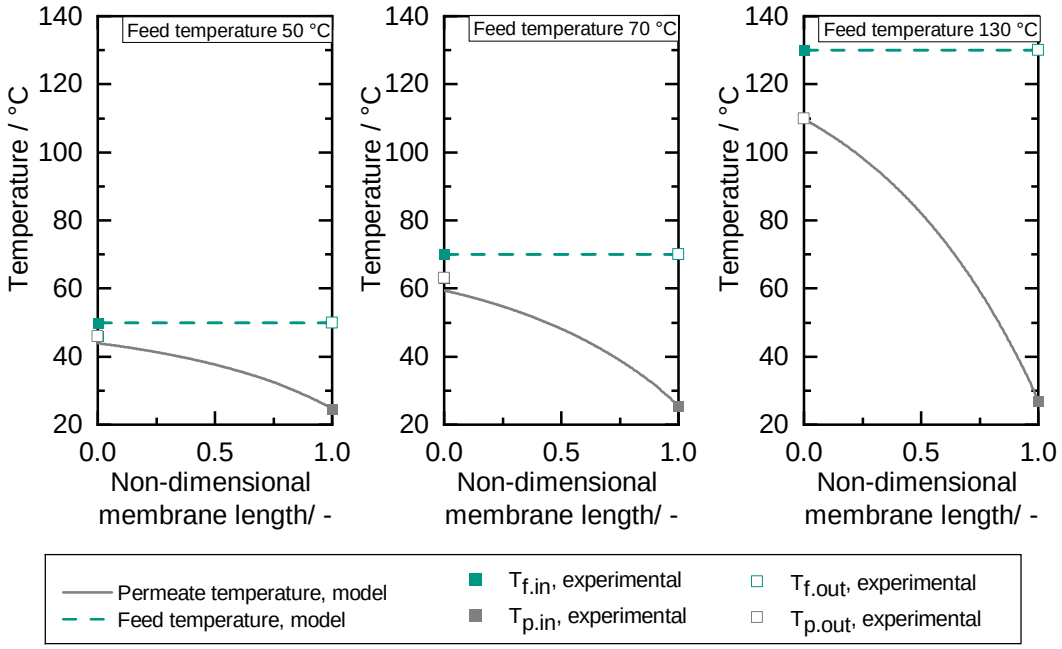

Figure 6.10.: Permeate and feed temperature profiles for a **(a)** feed temperature of 50°C, **(b)** feed temperature of 70°C and **(c)** feed temperature of 130°C.

Feed compartment

Assuming a steady state, the overall mass balance in the feed compartment of the cell depicted in Figure 6.9 can be described by:

$$\dot{N}_{\mathrm{f}}^{\mathrm{i}} = \dot{N}_{\mathrm{f}}^{\mathrm{i\text{-}1}} - \dot{N}_{\mathrm{w}}^{\mathrm{i}} \tag{6.12}$$

where $\dot{N}_{\mathrm{f}}^{\mathrm{i\text{-}1}}$ and $\dot{N}_{\mathrm{f}}^{\mathrm{i}}$ are the inlet and outlet total molar flow rate in the feed compartment of a given cell. The resulting $\dot{N}_{\mathrm{f}}^{\mathrm{i}}$ is set as the new inlet molar flow rate of the next cell in the flow direction. The component mass balance for water, $\dot{N}_{\mathrm{w}}^{\mathrm{i}}$, can be formulated as:

$$\dot{N}_{\mathrm{w}}^{\mathrm{i}} = \dot{N}_{\mathrm{f}}^{\mathrm{i\text{-}1}}\, \tilde{x}_{\mathrm{w.f}}^{\mathrm{i\text{-}1}} - \dot{N}_{\mathrm{f}}^{\mathrm{i}}\, \tilde{x}_{\mathrm{w.f}}^{\mathrm{i}} \tag{6.13}$$

where $\tilde{x}_{\mathrm{w.f}}^{\mathrm{i\text{-}1}}$ is the entering molar fraction of water in the feed compartment of the cell and for the binary mixture water-glucose corresponds to $1 - \tilde{x}_{\mathrm{g.f}}^{i-1}$, where $\tilde{x}_{\mathrm{g.f}}$ represents the molar fraction of glucose in the feed. As per the mass balance, the molar fraction of water in the feed compartment of a given cell, $\tilde{x}_{\mathrm{w.f}}^{i}$ is defined as:

$$\tilde{x}_{\mathrm{w.f}}^{i} = \frac{\dot{N}_{\mathrm{f}}^{\mathrm{i\text{-}1}}\, \tilde{x}_{\mathrm{w.f}}^{\mathrm{i\text{-}1}} - \dot{N}_{\mathrm{w}}^{\mathrm{i}}}{\dot{N}_{\mathrm{f}}^{\mathrm{i\text{-}1}} - \dot{N}_{\mathrm{w}}^{i}} \tag{6.14}$$

6.2.3 Model routine

The model can be implemented in co-current and counter-current, with regard to the sweep gas flow mode. The model routine implemented in MATLAB® follows the flow chart depicted in Figure 6.11. The simulation starts with the input parameters, i.e. the experimental inlet temperature and flow rate of the feed ($T_{\mathrm{f.in}}$ and $\dot{N}_{\mathrm{f.in}}$) and permeate ($T_{\mathrm{p.in}}$ and $\dot{N}_{\mathrm{p.in}}$) streams, as well as the geometrical parameters of the membrane and testing unit.

For each cell i, a system of five nonlinear equations using Equation 6.4 (or Equation 6.5) as well as Equation 6.6, 6.7, 6.10, and 6.14 is solved with the solver $fsolve$ to determine the transmembrane molar flow, $\dot{N}_{\mathrm{w}}$, the transmembrane heat, $\dot{Q}_{\mathrm{m}}$, the permeate temperature at the membrane surface, T_{mp}, as well as the resulting mole fraction of water in the permeate, $\tilde{y}_{\mathrm{w.p}}$ and feed side, $\tilde{x}_{\mathrm{w.f}}$. The solver $fsolve$ solves the system of equations by minimizing the sum of squares of the components. After each calculation i, the outlet permeate flow rate, $\dot{N}_{p}^{\mathrm{i}}$ and outlet permeate temperature, T_{p}^{i} are updated using Equation 6.9 and 6.11, respectively. As already mentioned, the feed temperature remains constant all over the membrane testing unit, and the outlet feed flow rate, $\dot{N}_{\mathrm{f}}^{\mathrm{i}}$ can be calculated with Equation 6.12. The calculation is repeated in a loop until the whole membrane length has been calculated (cell n). In the

case of co-current flow, the calculation is finished and the resulting $T_{\mathrm{p}}^{\mathrm{n}}$ and $\dot{N}_{\mathrm{p}}^{\mathrm{n}}$ values are the final outlet values, $T_{\mathrm{p,out}}$ and $\dot{N}_{\mathrm{p,out}}$, respectively. The transmembrane flux is calculated as the difference between the calculated permeate flow (cell n, $\dot{N}_{p}^{\mathrm{n}}$) and the initial permeate flow, $\dot{N}_{\mathrm{p,in}}$.

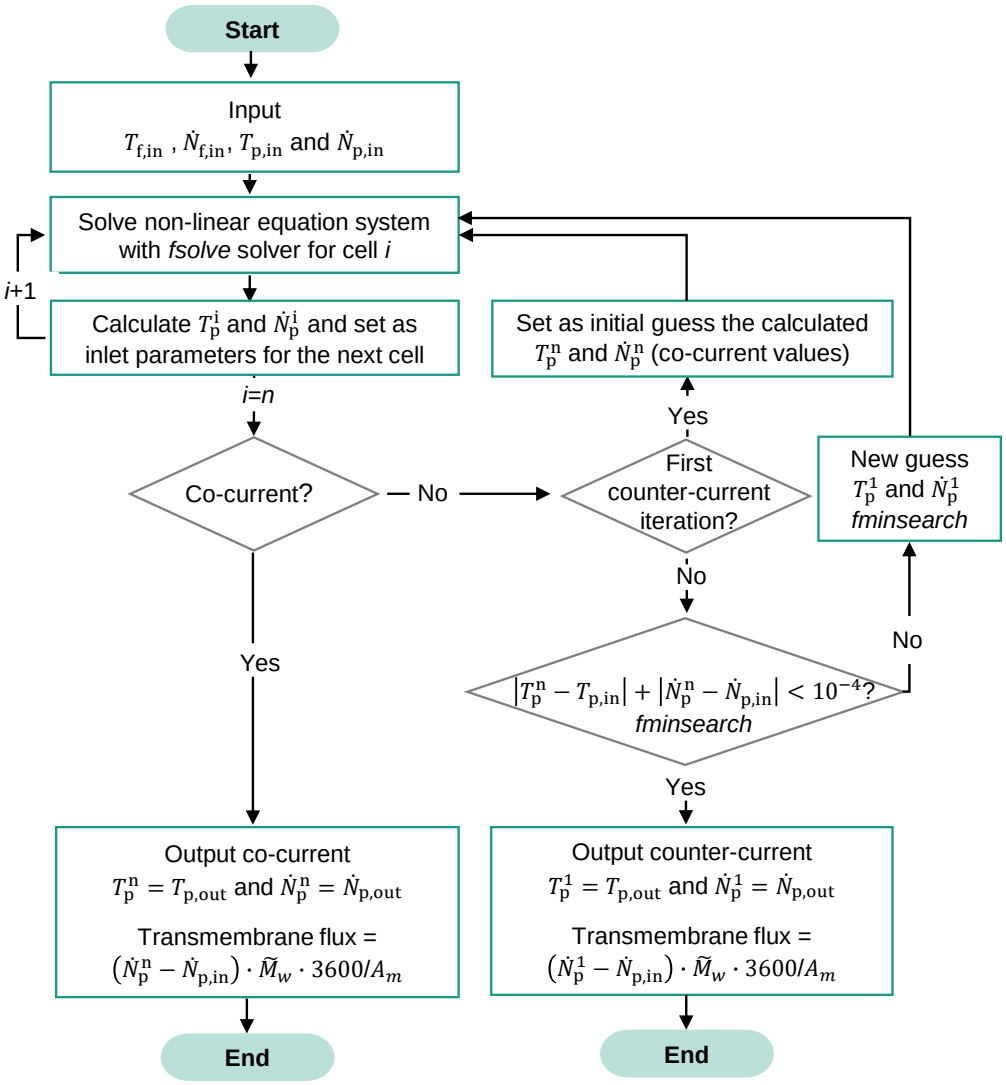

Figure 6.11.: Flow chart of the model routine.

In the case of counter-current flow, the $fsolve$ loop is embedded in a $fminsearch$ routine. Here, an initial guess for $T_{\mathrm{p,out}}$ and $\dot{N}_{\mathrm{p,out}}$ (cell i=1) is required. The initial guess for the first counter-current iteration is taken from the results of the co-current calculation. With this initial guess, the simulation is performed all over the membrane, following the same steps as for co-current. After the last cell is reached, the resulting calculated values $T_{\mathrm{p}}^{\mathrm{n}}$ and $\dot{N}_{p}^{\mathrm{n}}$ are compared with the experimental inlet values by means of the solver $fminsearch$, which

minimizes functions of several variables using the Nelder-Mead simplex algorithm [201] to find a local minimum. This solver is in charge of finding the $T_{\mathrm{p,out}}$ and $\dot{N}_{\mathrm{p,out}}$ which minimize the sum of difference between $T_{\mathrm{p}}^{\mathrm{n}}$ and $T_{\mathrm{p,in}}$, and $\dot{N}_{p}^{\mathrm{n}}$ and $\dot{N}_{\mathrm{p,in}}$. As mentioned above, the initial guess is made with the results of the calculation in co-current mode. This loop stops when the difference is minimized ($< 10^{-4}$) and the transmembrane flux is calculated as the difference between the guessed permeate flow (cell 1, $\dot{N}_{p}^{1}$) and the initial permeate flow, $\dot{N}_{\mathrm{p,in}}$.

6.2.4 Mass transport limitation

As explained in section 6.2.1, there are four mass transport steps, and accordingly four potential mass transport limitation locations: feed, active layer, support and permeate. The identification of the location where the strongest limitation exists helps to determine to which extent it is reasonable to additionally consider the concentration profiles perpendicular to the membrane in the fluid compartments. Typically this depends on the values of the different process parameters. The parameters considered are the feed temperature, the sweep gas flow rate and the pressure in the permeate compartment. Additionally, the effect of the membrane thickness is also taken into account.

Figure 6.12 shows that the membrane support is responsible for the majority of the mass transport inhibition. The reason for this is the thickness of the support, which is approx. 2 mm, whereas the active layer of the membrane is only 30 µm thick (see SEM image in Figure 6.2). In the chosen pseudo-2D modelling approach, the feed and permeate compartments in each cell are assumed to be perfectly mixed. According to the results in Figure 6.12, where it is confirmed that the largest mass transport resistance is located in the support, the chosen modelling approach is reasonable.

The mass transport resistances are determined according to Equation 6.4. The shares shown in Figure 6.12 are calculated as the ratio of the mass transport resistance in a given location to the total mass transport resistance (summation of the single mass transfer resistances) multiplied by 100. Figure 6.12 (a) shows that the shares of mass transport resistances in the gas phase and in the active layer of the membrane do not change with temperature. The share of the mass transfer resistance in the support layer of the membrane decreases with increasing feed temperature. The share of the mass transport resistance in the feed slightly increases with temperature up to a maximum of 5 %. This is due to the fact that the transmembrane flux increases with increasing temperature, resulting in an accumulation of glucose at the phase boundary. This leads to a further decrease in the vapour pressure. Figure 6.12 (b) shows the course over the nitrogen flow. It can be seen that with increasing nitrogen flow the share of the mass transport resistance in the gas phase decreases. This is

due to an increase in the Reynolds number and a reduction of the boundary layer thickness. Figure 6.12 (c) shows the influence of the permeate pressure on the shares of the different mass transport resistances. It can be seen that the share of the mass transport resistance in the feed decreases with increasing gas pressure and the one in the support layer increases. The increase in gas pressure reduces the diffusion coefficients in the gas phase (see Fuller equation, Equation A.12). This causes the transport resistance in the gas phase to increase. The pressure has no influence on the diffusion in the liquid phase. The increase in the mass transport resistance in the gas phase leads to a decreasing share of the mass transport inhibition in the feed. The influence of the membrane thickness is shown in Figure 6.12 (d). As the membrane thickness decreases, the share of the mass transport resistance in the support layer decreases due to the decrease in the diffusion distance.

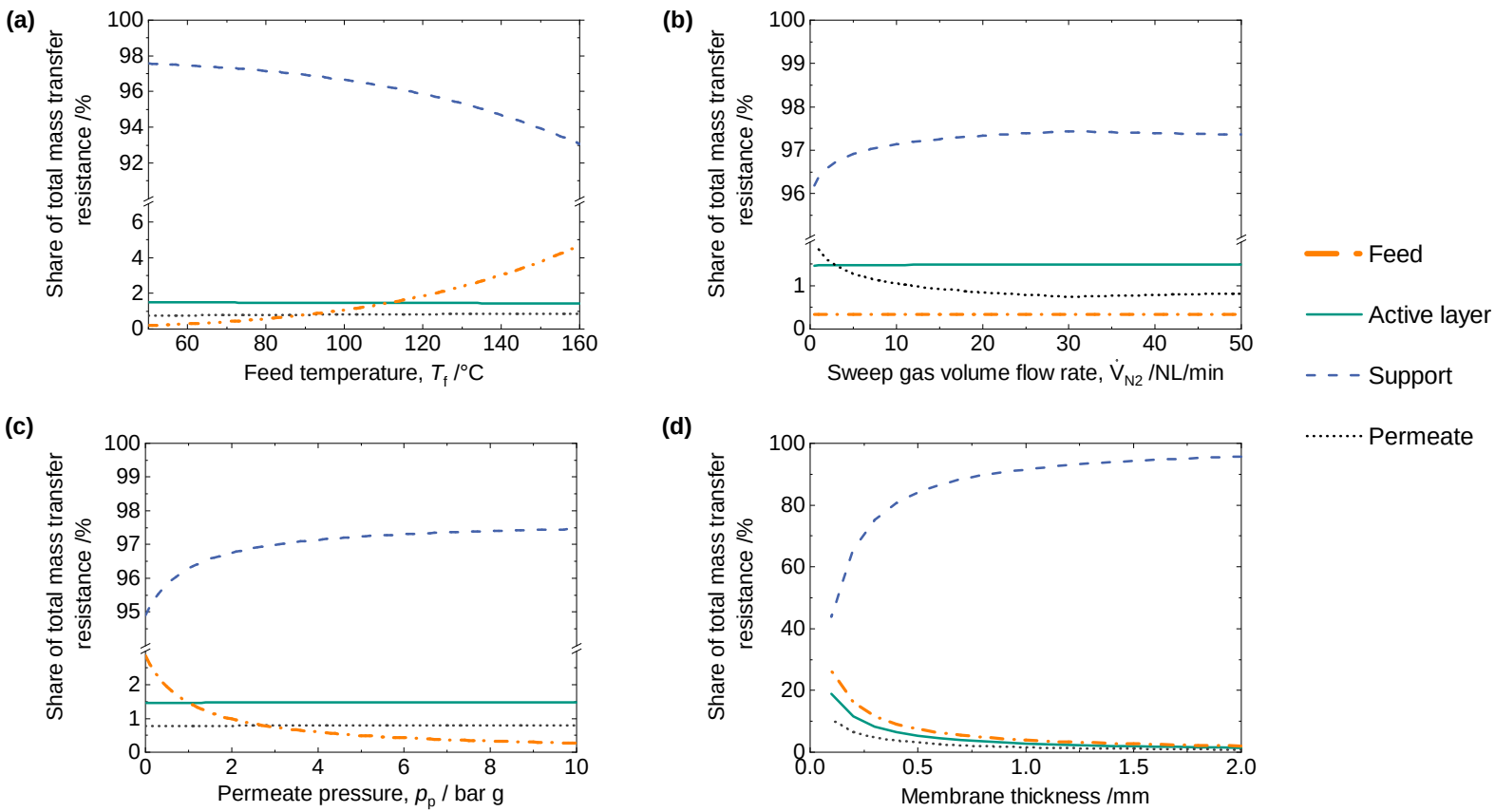

Figure 6.12.: Effect of the different process and membrane parameters on the mass transport limitations of the feed (dash dotted-orange), the active layer (solid line, green), support (dashed-blue) and sweep gas (dotted-grey). **(a)** Effect of the feed temperature for a feed pressure of $p_f = 6$ bar g, permeate pressure of $p_p = 5.85$ bar g, sweep gas flow rate of $\dot{V}_{N_2} = 30$ NL min^{-1} and a feed mass flow rate of $\dot{M}_f = 1.8$ kg h^{-1}. **(b)**Effect of the sweep gas flow rate for a feed temperature of $T_f = 50$ °C, feed pressure of $p_f = 6$ bar g, permeate pressure of $p_p = 5.85$ bar g and a feed mass flow rate of $\dot{M}_f = 1.8$ kg h^{-1}. **(c)** Effect of the permeate pressure for a feed temperature of $T_f = 50$ °C, transmembrane pressure of $\Delta p = 0.15$ bar, sweep gas flow rate of $\dot{V}_{N_2} = 30$ NL min^{-1} and feed mass flow rate of $\dot{M}_f = 1.8$ kg h^{-1}. **(d)** Effect of the membrane thickness for a feed temperature of $T_f = 50$ °C, feed pressure of $p_f = 6$ bar g, permeate pressure of $p_p = 5.85$ bar g, sweep gas flow rate of $\dot{V}_{N_2} = 30$ NL min^{-1} and feed mass flow rate of $\dot{M}_f = 1.8$ kg h^{-1}.

6.3 Results and discussion

The results from the experiments and the mathematical model are presented and discussed together in this chapter. The influence of sweep gas and feed parameters was investigated. On the feed side, the mass flow rate, inlet temperature and glucose concentration were varied. Pressure and volume flow were modified on the sweep gas side. For all the experiments, the transmembrane pressure was set to $\Delta p = 0.15$ bar. This value was definitely lower than the measured LEP (cf. Chapter 5) so that liquid penetration through the membrane pores could be avoided. Unless otherwise stated, the experiments were performed with pure water in the feed to exclude mass transfer limitation effects in the feed and better evaluate the influence of the variation of the different operating parameters. If a glucose solution was used, it is explicitly indicated in the text.

In the diagrams in this chapter, the average value of the experimental measurements is shown. This was determined from measurement data over, at least, 5 min. The standard deviation was also determined and is given as an error bar in the diagram. Due to the low standard deviation and the predominantly large range of values of the ordinate, the error bars are usually not visible in the diagrams.

6.3.1 Effect of feed flow rate

As seen in Chapter 2.3.2, boundary layers can arise on both sides of the membrane. Therefore, the fluid hydrodynamic conditions on the feed and sweep gas side may affect the mass transfer through the membrane and therefore the transmembrane flux. To study this phenomenon, experiments were carried out at three different mass flow rates: 1.8 kg h^{-1}, 2.3 kg h^{-1} and 3.3 kg h^{-1}. The feed temperature was set to $T_f = 50$ °C, the sweep gas volume flow rate to $\dot{V}_{N_2} = 2$ NL min^{-1} and the pressure in the permeate side to $p_p = 0$ bar g. The effect of the feed mass flow rate on the transmembrane flux is shown in Figure 6.13. Here, the experimentally determined transmembrane flux (black dots) is plotted over the duration of the experiment. The transmembrane flux calculated with the model in steady state is shown as a solid black line. The increase in the feed mass flow rate is shown by the different intensity of the colours at the background. When increasing the feed mass flow rate from 1.8 kg h^{-1} to 2.3 kg h^{-1}, no change in the modelled transmembrane flux can be observed. The increase of the feed mass flow rate to 3.3 kg h^{-1} leads to only a 3% enhancement of the transmembrane flux. This increase can be attributed to the increase in the inlet feed temperature from 49°C to 50°C that could be recorded, cf. secondary axis in Figure 6.13. This temperature increase is related to the mass flow rate increase which leads to higher flow

velocities and therefore an increase in heat transfer in the heat exchanger upstream of the membrane testing unit. The increase in transmembrane flux due to the temperature increase could be confirmed with the model. This increase is however not significant and therefore other authors like Charfi [202], Zhao [203] and Khayet [143, 148] neglect the influence of the feed mass flow rate on mass transfer in SGMD. For this reason, the feed mass flow rate was kept to 1.8 kg h^{-1} in the subsequent experiments of this work.

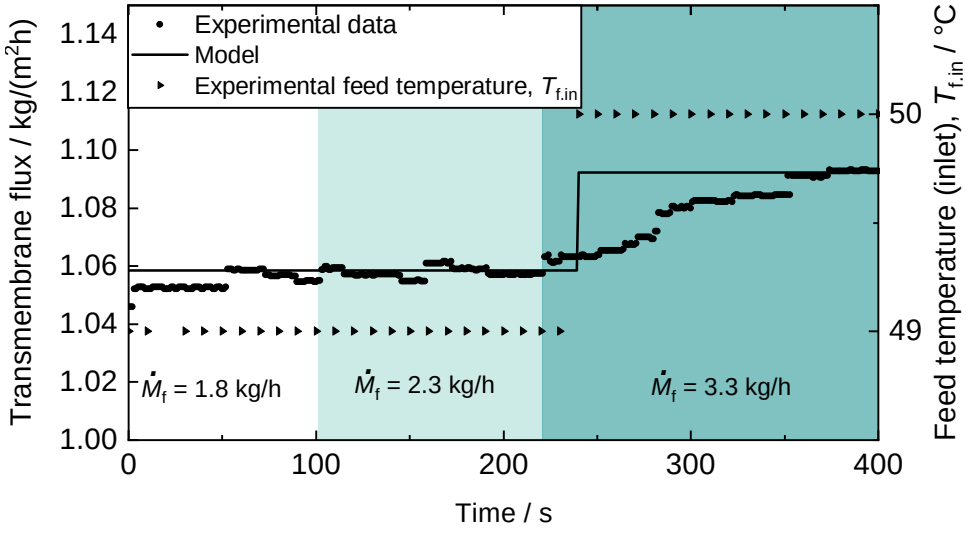

Figure 6.13.: Effect of the feed mass flow rate in the transmembrane flux for a permeate pressure of $p_p = 0$ bar g, a feed pressure of $p_f = 0.15$ bar g, a sweep gas volume flow rate of $\dot{V}_{N_2} = 2$ NL min^{-1} and a feed mass flow rate ranging between $\dot{M}_f = 1.8$ - 3.3 kg h^{-1}.

6.3.2 Effect of feed temperature

The feed temperature is directly related to the water partial pressure in the liquid interface. Since the driving force of the separation in SGMD is the difference of water partial pressure across the membrane, the feed temperature plays a decisive role in the mass transport across the membrane [203]. The ultimate goal of this study is to investigate the separation of water vapour at elevated temperatures and therefore it is crucial to understand the influence of the feed temperature on the evaporation and consequently, on the transmembrane flux. For this purpose, experiments were carried out with pure water at feed temperatures ranging between $T_f = 50$ –150 °C. In these experiments, only the feed temperature was varied; all other parameters such as volume flow rate and temperature of the sweep gas as well as the

pressure at both sides of the membrane were kept constant. To ensure liquid state on the feed side, the pressure on the feed side must be selected above the corresponding saturation pressure of the maximum feed temperature. Accordingly, the pressure on the permeate compartment was set to p_p = 5.85 bar g and thus a pressure on the feed side of $p_f = p_p + \Delta p = 6$ bar g was chosen. The sweep gas flow was selected so that the relative humidity of the sweep gas flow did not rise above 90 % during the entire experiment. This resulted in a nitrogen flow of $\dot{V}_{N_2} = 30$ NL min^{-1}.

Figure 6.14 illustrates the increase in transmembrane flux against the increase in feed temperature for membranes with an average pore size of 100 nm. In Figure 6.14, the experimental data are plotted as discrete measuring points. The error bars (fluctuation of the transmembrane flux during the measurement period of t= 5 min) are not visible due to the axis scaling. During the experiments, a minimum transmembrane flux of 0.19 kg m^{-2} h^{-1} and a maximum transmembrane flux of 11.09 kg m^{-2} h^{-1} were measured. The values calculated with the model are plotted as a continuous curve. In the diagram, the transmembrane flux for a temperature variation of ± 1.5 °C is given as a green area. This corresponds to the max. deviation of the thermocouples type K in tolerance class 1 according to IEC 60584–1 [204] used during the experiments.

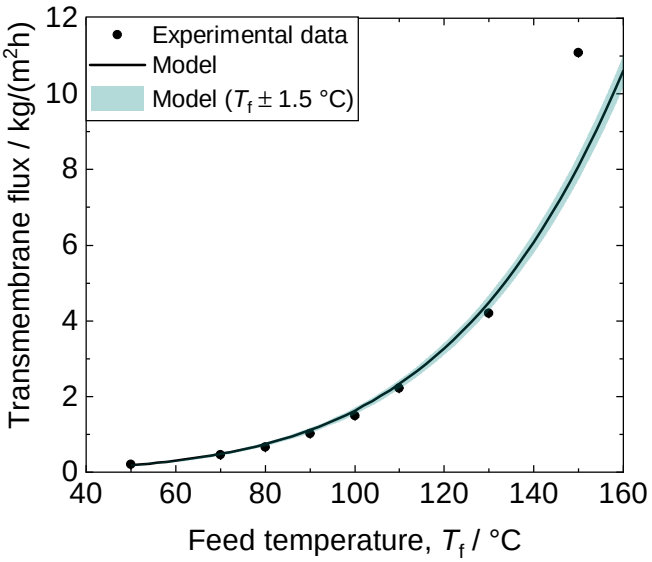

Figure 6.14.: Effect of the feed temperature on the transmembrane flux for a permeate pressure of $p_p = 5.85$ bar g, a feed pressure of $p_f = 6$ bar g, a sweep gas flow rate of $\dot{V}_{N_2} = 30$ NL min^{-1} and a feed mass flow rate of $\dot{M}_f = 1.8$ kg h^{-1}.

As expected, the transmembrane flux increases exponentially with the temperature. As shown in Figure 6.15, the increase in transmembrane flux with temperature can be attributed to two phenomena:

(a) Acceleration of the diffusive mass transport due to the temperature increase.

(b) Increase of the driving force of the SGMD due to the exponential relationship between vapour pressure in the feed and temperature, following the Wagner equation.

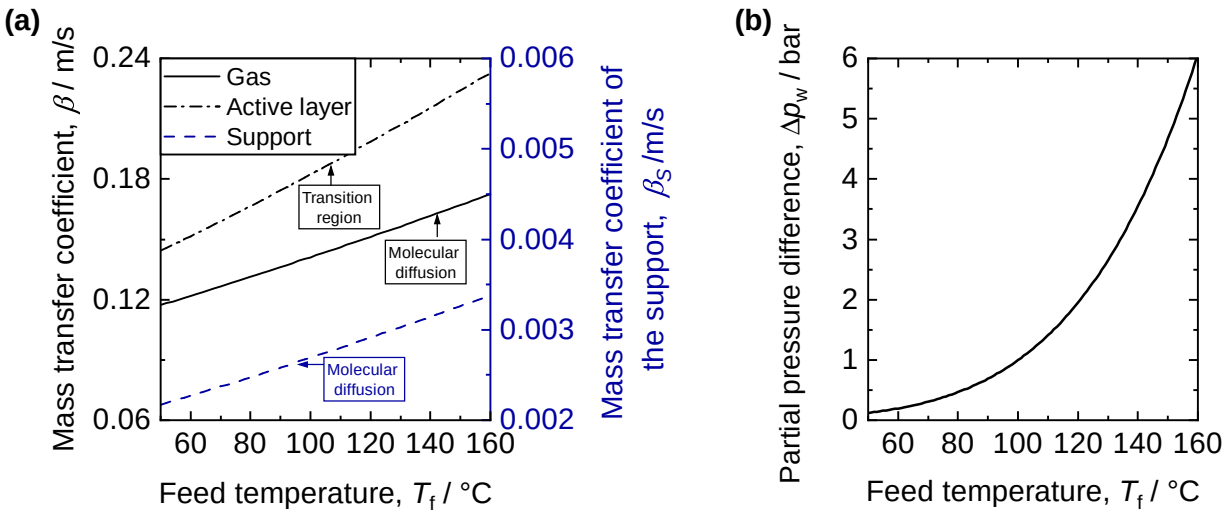

Figure 6.15.: **(a)** Effect of the feed temperature on the mass transfer coefficients through the active layer and support layer of the membrane and through the sweep gas layer. **(b)** Effect of the feed temperature on the partial pressure difference (driving force). Permeate pressure of $p_p = 5.85\,\text{bar g}$, feed pressure of $p_f = 6\,\text{bar g}$, sweep gas volume flow rate of $\dot{V}_{N_2} = 2\,\text{NL min}^{-1}$ and feed mass flow rate of $\dot{M}_f = 1.8\,\text{kg h}^{-1}$.

In Figure 6.15 (a) the course of the mass transfer coefficients through the membrane (i.e. active layer and support layer) as well as through the sweep gas, are plotted against the feed temperature. Here the values of the mass transfer coefficients in the active layer and in the gas phase are shown on the left ordinate and the mass transfer coefficient in the support is shown on the right ordinate. In Figure 6.15 (b) the course of the partial pressure difference between feed and permeate against the feed temperature is displayed. Figure 6.15 (b) illustrates how the driving force increases exponentially with temperature, as a result of the exponential relationship of the vapour pressure on the feed side of the membrane with the temperature. In contrast, all three mass transfer coefficients do not show this behaviour with the feed temperature. Figure 6.14 and Figure 6.15 therefore confirm that higher feed temperatures lead to larger transmembrane fluxes in SGMD.

6.3.3 Effect of sweep gas conditions

Influence of sweep gas pressure

Since SGMD experiments have never been performed at temperatures higher than 80-90 °C, no works in the literature could be found where the pressure in the permeate side exceeded 0 bar g. The investigation of the influence of the sweep gas pressure enables the understanding of the prevailing phenomena and broadens the application range of SGMD. An experiment was conducted in which the sweep gas pressure was the only parameter to be varied. The experiment was carried out at a temperature of 50 °C and a nitrogen flow of 5 NL min^{-1}. At this nitrogen flow rate, and due to the pressure losses in the system, the minimum inlet pressure in the permeate side resulted to be $p_p = 0.03$ bar g. The transmembrane flux determined experimentally and the modelling results vs. the sweep gas pressure are shown in Figure 6.16.

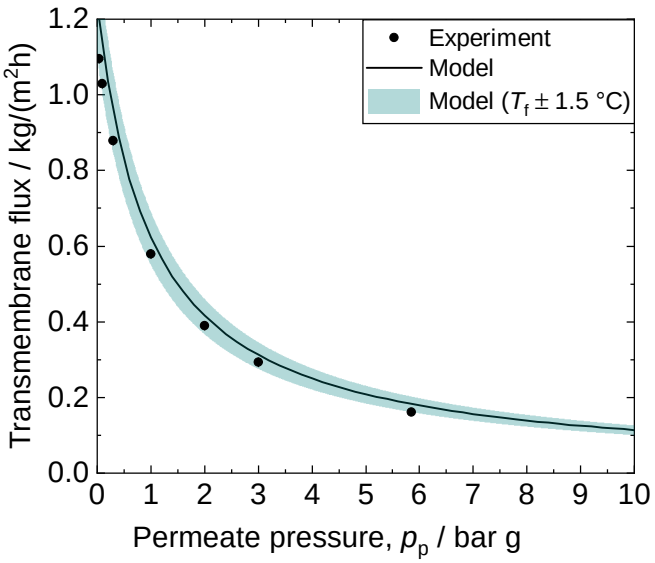

Figure 6.16.: Effect of the gas pressure on the transmembrane flux for a permeate pressure ranging between $p_p = 0$ - 3 bar g, a transmembrane pressure of $\Delta p = 0.15$ bar, a feed temperature of $T_f = 50$ °C, a sweep gas volume flow rate of $\dot{V}_{N_2} = 5$ NL min^{-1} and a mass flow rate of $\dot{M}_f = 1.8$ kg h^{-1}.

The area in which the transmembrane flux would lie if the feed temperature would deviate from the set point by ±1.5 °C is also highlighted in green. All the measured data lie within this range. It can be seen that the transmembrane flux decreases strongly at the beginning with increasing gas pressure. At higher pressures, the transmembrane flux approaches the abscissa asymptotically. The reason for the decrease of the transmembrane flux with increasing gas pressure is the decrease of the diffusion coefficient for molecular diffusion

(cf. Fuller equation, Equation A.12) and of the driving force (Δp_w). The influence of the permeate pressure on the mass transfer coefficients and the partial pressure is represented in Figure 6.17. Figure 6.17 (a) displays the course of the individual mass transfer coefficients over the pressure on the permeate side. The values of the mass transfer coefficients in the active layer and in the gas phase are shown on the left ordinate. The mass transfer coefficient in the support is shown on the right ordinate. The progression of the mass transfer coefficients over the gas pressure can be attributed to the inversely proportional relationship of the diffusion coefficients with the pressure (cf. Fuller equation, Equation A.12). Figure 6.17 (b) shows the partial pressure of water in the permeate and the resulting partial pressure difference across the membrane vs. the permeate pressure. Here, the increase in permeate pressure leads to higher water partial pressure in the permeate which in turn reduces the driving force of the separation, i.e. the partial pressure difference across the membrane.

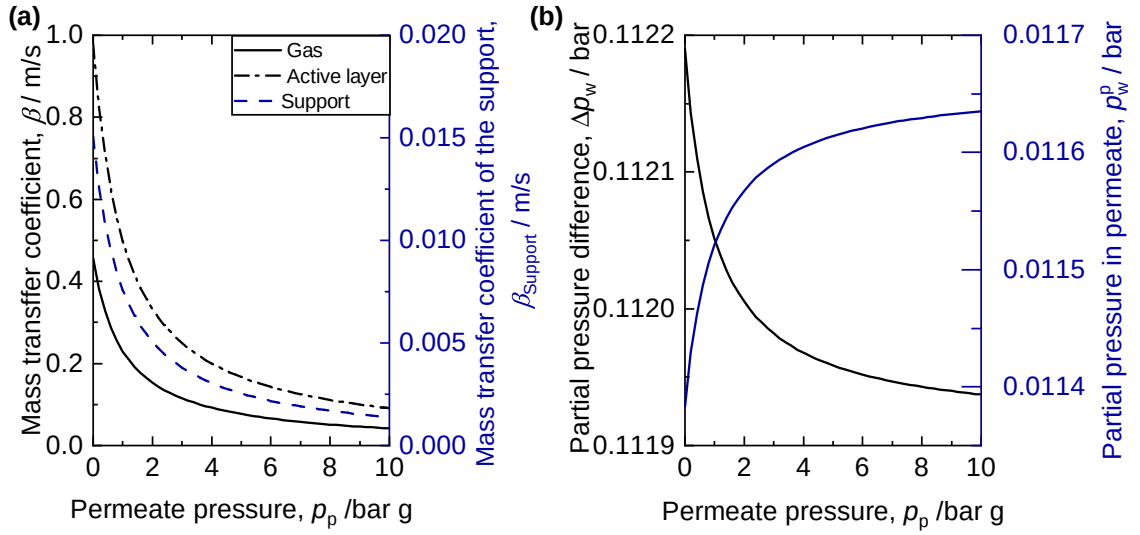

Figure 6.17.: **(a)** Effect of the permeate pressure on the mass transfer coefficients through the active layer and support layer of the membrane and through the sweep gas layer. **(b)** Effect of the permeate pressure on the partial pressure difference (driving force). Permeate pressure ranging between $p_p = 0$ - 10 bar g, feed temperature of $T_f = 50\,°C$, volume flow rate of $\dot{V}_{N_2} = 5\,NL\,min^{-1}$ and feed mass flow rate of $\dot{M}_f = 1.8\,kg\,h^{-1}$.

Influence of sweep gas volume flow rate

In contrast to the feed mass flow rate, the flow rate of the sweep gas plays an important role in the resulting transmembrane flux. The sweep gas carries the evaporated water out of the permeate chamber. Indeed, increasing the sweep gas flow rate leads to an increase in

the vapour removal capacity while reducing the partial pressure of water on the permeate side [139]. These two facts lead to an enhancement of the transmembrane flux.

When the sweep gas flow rate is increased, the pressure losses and, as a consequence, the pressure in the permeate side of the membrane testing unit, also increase. For this reason, the influence of the sweep gas flow on the transmembrane flux has been studied through two different routes:

- First, the increase of sweep gas volume flow rate with the resulting increase in permeate pressure. The gas pressure was not adjusted, which means that during the experiment the increase in the nitrogen flow rate and the increase in gas pressure could be observed simultaneously.
- In order to eliminate the effect of the increasing pressure, experiments were repeated increasing the sweep gas volume flow rate and maintaining a constant pressure on the permeate side. The gas pressure was regulated to compensate for the pressure rise when the nitrogen flow rate was increased. For this purpose, the pressure on the permeate side was set to the desired value with the back pressure regulator located downstream of the membrane testing unit, so that the pressure remained constant over the entire course of the experiment. Thus, the influence of the nitrogen flow rate could be observed independently of all other parameters.

Through the experiments, the volume flow rate of the sweep gas was not increased arbitrarily. It had to be granted that the pressure difference between the liquid feed and the gas was lower than the LEP of the membrane. Additionally, the gas pressure was always lower than the liquid pressure to avoid the gas flowing into the feed. Both conditions were necessary to prevent the wetting of the membrane [148].

The membrane testing unit was heated with heating coils so that the temperature of the feed in the testing unit remained constant. The higher the nitrogen flow, the greater the heating power required.

Increasing pressure in the permeate side

As the nitrogen flow is increased, the pressure raised on the permeate side due to more pronounced frictional losses in the entire system. The pressure on the gas side rose therefore from 0 bar g up to 0.71 bar g. To maintain the pressure difference between the feed and permeate side constant at $\Delta p = 0.15$ bar, the feed pressure was always increased accordingly. For the modelling results, in this case, the pressure has been taken from the experimental data. For this purpose, a linear fit function was defined, which describes the pressure in the permeate side as a function of the volume flow rate. The results of the transmembrane flux vs. nitrogen volume flow rate are shown in Figure 6.18.

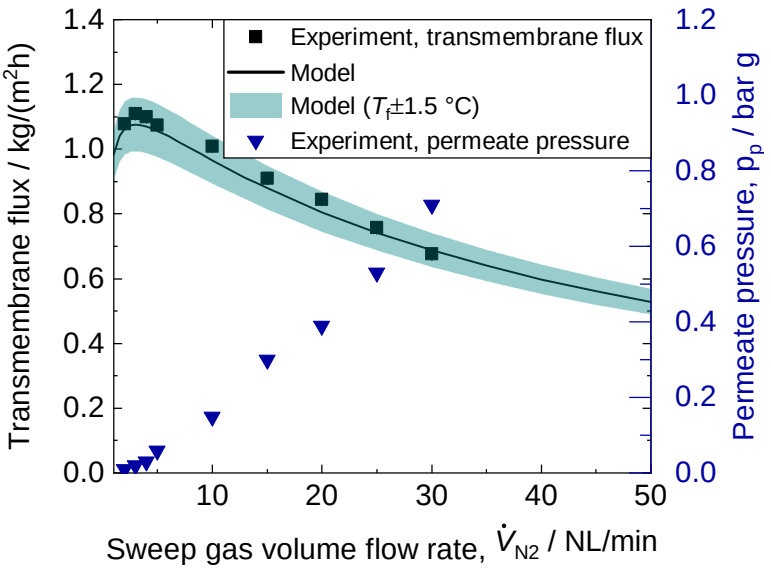

Figure 6.18.: Effect of the sweep gas flow rate on the transmembrane flux at increasing pressure in the permeate side for a transmembrane pressure of $\Delta p = 0.15$ bar, a feed temperature of $T_f = 50\,°C$ and a feed mass flow rate of $\dot{M}_f = 1.8\,kg\,h^{-1}$.

Figure 6.18 depicts how the transmembrane flux increases linearly at the beginning, reaches a maximum and then drops almost linearly. The reason for the maximum is the simultaneous variation of two parameters (volume flow rate and pressure on the permeate side) and thus several effects overlap:

- Dilution effect: The nitrogen flow increases, causing the mole fraction of water on the permeate side to decrease due to dilution. Since the gas pressure remains almost constant for volume flow rates $< 5\,NL\,min^{-1}$, the partial pressure on the permeate side decreases, leading to an increase in the partial pressure difference across the membrane, and thus in the transmembrane flux.
- Reduction of the diffusion coefficients: The pressure on the permeate side increases, which results in the reduction of the mass transfer coefficients (see Figure 6.17 (a) for increasing permeate pressures). This leads to a decrease in transmembrane flux.

The course of the mole fraction of water at the phase boundary feed-membrane ($\tilde{y}_{w.fm}$, dotted curve), in the bulk of the gas phase ($\tilde{y}_{w.p}$, dashed curve) and their difference ($\tilde{y}_{w.fm}$-$\tilde{y}_{w.p}$, solid curve) are plotted in Figure 6.19 against the sweep gas flow rate.

It can be seen in Figure 6.19 that especially for low nitrogen flows, the mole fraction of water in the bulk of the permeate compartment falls up to almost zero. This gives the resulting solid curve, which represents the course of the mole fraction difference which is related to

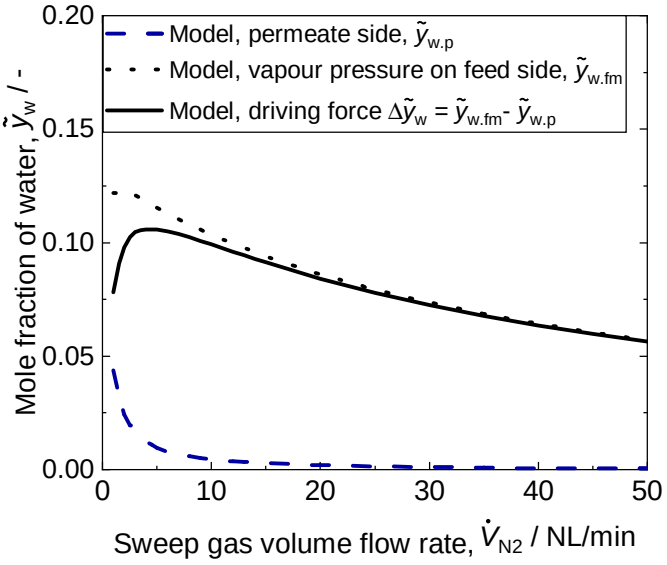

Figure 6.19.: Effect of the sweep gas flow rate on the mole fraction of water at increasing permeate pressure. Phase boundary feed-membrane surface $\tilde{y}_{w.fm}$, bulk permeate phase $\tilde{y}_{w.p}$ and difference of both mole fractions, $\Delta\tilde{y}$ at a permeate pressure ranging between $p_p = 0$ - 1.16 bar g, a transmembrane pressure of $\Delta p = 0.15$ bar, a feed temperature of $T_f = 50\,°C$ and a feed mass flow rate of $\dot{M}_f = 1.8\,kg\,h^{-1}$.

the partial pressure difference. With a further increase in the nitrogen flow, the mole fraction difference decreases. This course is also reflected in Figure 6.18.

Constant pressure on the permeate side

To eliminate the pressure effect, experiments were performed at a constant pressure level on the permeate side. Accordingly, Figure 6.20 shows the effect of the sweep gas volume flow rate in the transmembrane flux for three (constant) pressure levels in the permeate compartment of $p_p = 0.75$ bar g, 1.50 bar g and 5.85 bar g. During the experiments, the volume flow rate was varied between 2 - 50 NL min^{-1}. The experiments illustrated in Figure 6.20 were carried out at a feed temperature of $T_f = 50\,°C$. The course of the transmembrane flux over the nitrogen flow rate is very similar for all three pressure levels. At low nitrogen flows the transmembrane flux increases.

To illustrate this, Figure 6.21 (a) displays the partial pressure of water in the bulk of the gas phase (i.e. permeate side, $p_{w.p}$) for a permeate pressure of $p_p = 1.50$ bar g over the sweep gas volume flow rate and Figure 6.21 (b) shows the behaviour of the mass transfer coefficients in the membrane. Figure 6.21(a) reveals that the driving force initially sharply increases and asymptotically approaches the abscissa at higher nitrogen flows. Here, again, the strong decrease in the water partial pressure on the permeate side is caused by the dilution effect

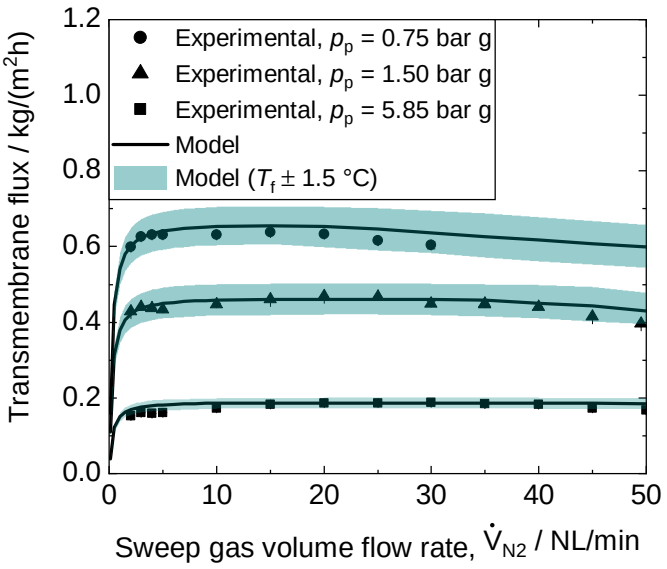

Figure 6.20.: Effect of the sweep gas flow rate on the transmembrane flux for three different permeate pressure levels of $p_p = 0.75$, 1.50, 5.85 bar g, a transmembrane pressure of $\Delta p = 0.15$ bar, a feed temperature of $T_f = 50\,°C$ and feed mass flow rate of $\dot{M}_f = 1.8\,kg\,h^{-1}$.

when the sweep gas flow is increased, which leads to higher partial pressure gradients and therefore larger transmembrane fluxes in Figure 6.20. At these lower volume flow rates, increasing the volume flow rate results in higher Reynolds numbers which leads to larger heat transfer coefficients on the permeate side. This causes a reduction of the boundary layer in the gas compartment [151]. Hence, the transmembrane flux is enhanced [128]. At these velocity conditions, the boundary layer is supposed to be thicker [139], and therefore a positive effect on the transmembrane flux can be observed in Figure 6.20 (up to $\dot{V}_{N2} \sim 4\,NL\,min^{-1}$).

With a further increase in the nitrogen flow, the course of the transmembrane flux in Figure 6.20 flattens out, reaches a maximum and slightly drops again. In fact, above a certain nitrogen flow, the dilution is at its maximum and the water partial pressure on the permeate side approaches 0, cf. Figure 6.21 (a). Here a further increase in the nitrogen flow no longer has an effect on the driving force. Under these conditions, the overall resistance to the transmembrane flux is rather governed by the membrane [141].

The moderate decrease after this maximum can be further explained by the reduction of the gas temperature in the support. The diffusion coefficient, see Figure 6.21(b), depends on the temperature in the support (cf. Fuller equation, Equation A.12). For higher flow rates of the cooler nitrogen sweep gas, the membrane may be cooled down and thus the temperature of the gas phase in the membrane may decrease with increasing nitrogen flow.

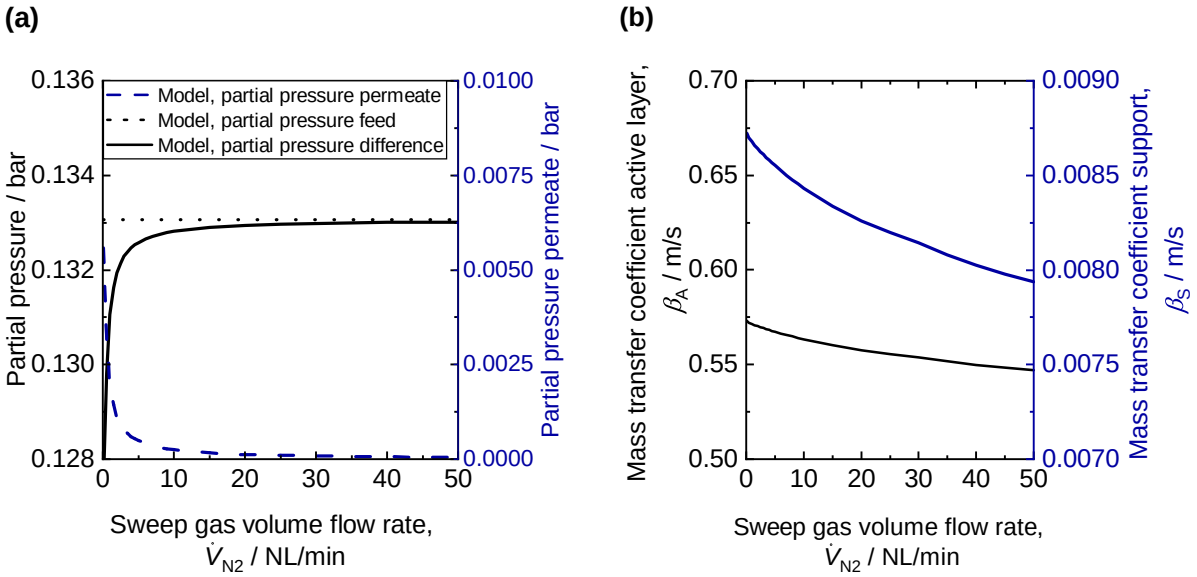

Figure 6.21.: Effect of the sweep gas flow rate on **(a)** the partial pressure of water on the permeate bulk phase and **(b)** the mass transfer coefficients at a constant pressure in the permeate compartment of $p_p = 1.50$ bar g, a transmembrane pressure of $\Delta p = 0.15$ bar, a feed temperature of $T_f = 50\,°C$ and feed mass flow rate of $\dot{M}_f = 1.8\,kg\,h^{-1}$.

For constant gas mass flow rates, a decrease in gas pressure leads to a rise in the gas volume flow and, in turn, an increase in the gas velocity. Accordingly, more heat is dissipated by the gas flow and the temperature in the support decreases even more. This results in a decrease in the diffusion coefficients in the support and thus a reduction of the transmembrane flux. The variation of the volume flow rate of nitrogen at a constant pressure in the permeate compartment has also been carried out at a temperature of $T_f = 120\,°C$ and a gas pressure of $p_p = 5.85$ bar g. The results are shown in Figure 6.22. The minimum possible nitrogen flow in the experiment was $\dot{V}_{N_2} = 15\,NL\,min^{-1}$. Otherwise, there was a risk of condensation at the downstream of the membrane testing unit, more specifically in the humidity sensor or rotameter due to the temperature drop. Comparing Figure 6.22 and the curve for $p_p = 5.85$ bar g in Figure 6.20, it can be seen that the maximum of the modelling results is located at almost the same sweep gas volume flow rate ($\dot{V}_{N2} \approx 4\,NL\,min^{-1}$). However, at a $T_f = 120\,°C$, the maximum of the curve reaches transmembrane flux values of $3.5\,kg\,m^{-2}\,h^{-1}\,m^{-2}$ while at $T_f = 50\,°C$, only approx. $0.2\,kg\ h^{-1}\ m^{-2}$ of steam is separated.

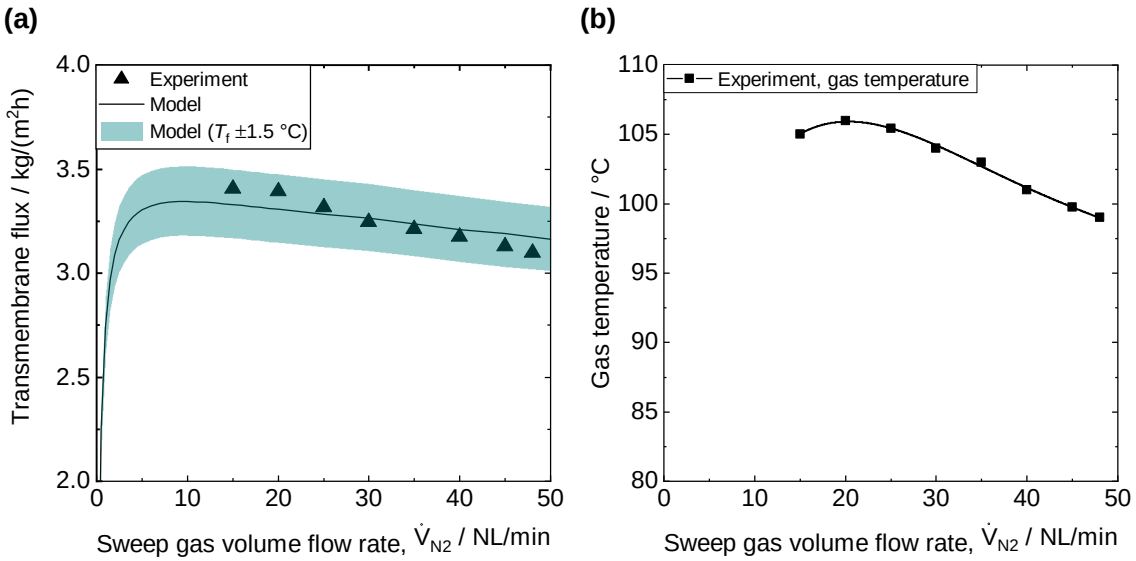

Figure 6.22.: Effect of the sweep gas flow rate on the transmembrane flux at a constant pressure in the permeate compartment of $p_p = 5.85$ bar g, transmembrane pressure of $\Delta p = 0.15$ bar, a feed temperature of $T_f = 120\,°C$ and a feed mass flow rate of $\dot{M}_f = 1.8\,kg\,h^{-1}$.

6.3.4 Effect of sugar concentration

After a systematic study on the influence of the different operating parameters affecting the SGMD for pure water, with a particular emphasis on high temperatures, the present section deals with the effects of the glucose content in the feed stream on the transmembrane flux. According to Raoult's law for ideal solutions, the addition of a non-volatile solute (in this case, glucose) to a solvent (in the present case, water), decreases the partial pressure of the resulting solution, when compared to the partial pressure of the pure solvent. Since the driving force of the SGMD is the partial pressure gradient, it is expected the transmembrane flux to also get reduced. Some works in the literature confirm this behaviour [122, 123, 128]. In fact, the partial pressure for pure water at 50 °C is 0.124 bar whereas for a feed solution with 50 wt.% glucose, the partial pressure takes a value of 0.112 bar. This, in turn, means a reduction of the transmembrane flux by 10 %. The experimental transmembrane flux values for a constant gas pressure of 5.85 bar g, and increasing glucose content up to 50 wt.% are shown in Figure 6.23.

Due to the evaporation of water at the pore entrance, there is an accumulation of glucose at the phase boundary (feed-membrane interface). This leads to higher mole fractions of glucose (subscript g) at the phase boundary than in the feed bulk ($\tilde{x}_{g.fm} > \tilde{x}_{g.f}$) and hence, the partial pressure of water at the phase boundary feed-membrane becomes even smaller. As explained in Chapter 2.3.2, this phenomenon is known in the membrane distillation literature as concentration polarization and leads to a further reduction of the transmembrane flux.

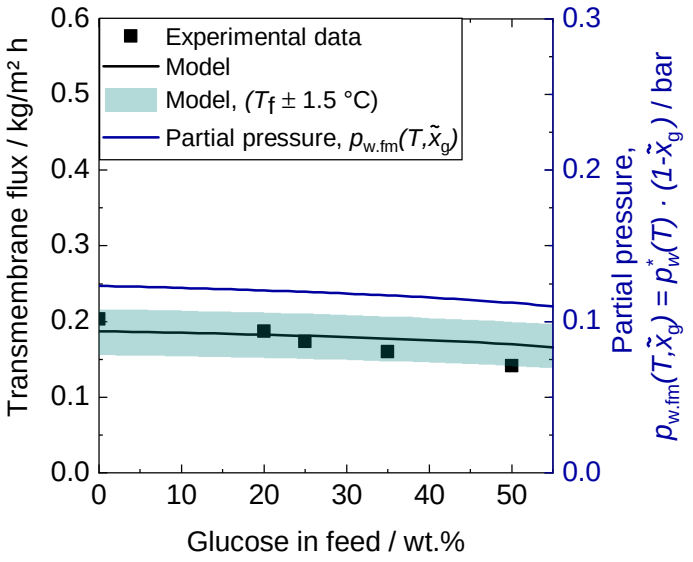

Figure 6.23.: Effect of the glucose concentration on the transmembrane flux for a feed temperature of $T_f = 50\,°C$, a permeate pressure of $p_p = 5.85\,bar\,g$, a transmembrane pressure of $\Delta p = 0.15\,bar$, a sweep gas volume flow rate of $\dot{V}_{N_2} = 30\,NL\,min^{-1}$ and feed mass flow rate of $\dot{M}_f = 1.8\,kg\,h^{-1}$.

Influence of feed temperature

In Chapter 6.3.2, it has been shown for pure water that higher temperatures lead to an increase in the driving force and therefore the transmembrane flux raises. For glucose solutions, the relationship between the transmembrane flux and the feed temperature follows likewise an exponential curve. This can be seen in Figure 6.24 for a constant gas pressure of $p_p = 5.85\,bar\,g$, a nitrogen flow $\dot{V}_{N_2} = 30\,NL\,min^{-1}$ and a feed mass flow $\dot{M}_f = 1.8\,kg\,h^{-1}$. Here, the experimental data for pure water and different glucose concentrations of 20 wt.%, 35 wt.% and 50 wt.% are given as discrete points. For a better overview, the data of the experiment and the model for 25 wt.% glucose content in the feed are not shown. The values calculated with the model are presented as solid lines.

In Figure 6.24, it can be observed that higher glucose contents do not lead to such a strong exponential increase in comparison to lower glucose contents or pure water. The difference in transmembrane flux for different glucose concentrations in the feed is higher at elevated temperatures. For instance, at a temperature of $T_f = 150\,°C$, the addition of glucose (50 wt.%) decreases the transmembrane flux by 31.3 %, in comparison to the 22.1% decrease at 50 °C. This effect can be attributed to the mass transport inhibition on the feed side, which is slightly higher at elevated temperatures.

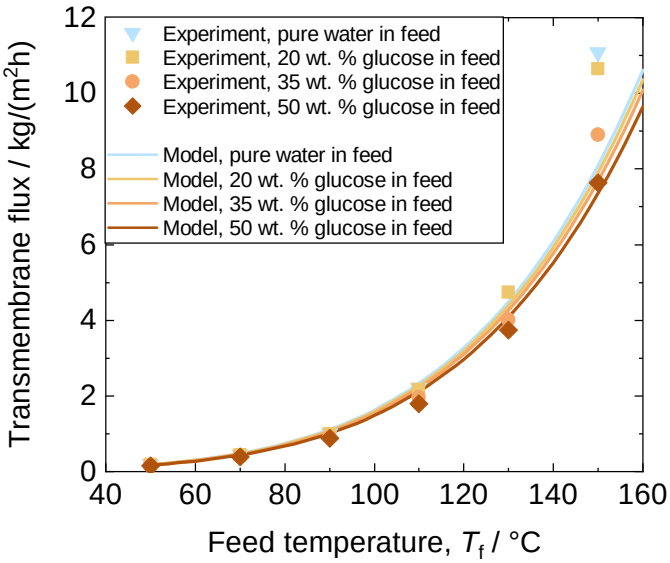

Figure 6.24.: Effect of the feed temperature and the glucose concentration on the transmembrane flux for a permeate pressure of $p_p = 5.85$ bar g, a transmembrane pressure of $\Delta p = 0.15$ bar, a volume flow rate of nitrogen of $\dot{V}_{N_2} = 30$ NL min^{-1} and a feed mass flow rate of $\dot{M}_f = 1.8$ kg h^{-1}.

In addition, the water partial pressure reduction due to the glucose content has a greater effect at high temperatures, as a consequence of the exponential behaviour of the water partial pressure with the temperature. This effect is shown in Figure 6.25 for pure water and a glucose content of 50 wt.%. At higher temperatures, the difference between the water partial pressures increases: at a temperature of 50 °C, the difference between both curves is 0.011 bar, whereas at a temperature of approx. 150 °C, the difference is 0.432 bar. Thus, the reduction of the driving force increases at elevated temperatures.

Figure 6.24 also shows that the decrease in the transmembrane flux of the experimental data is not linear with the mass fraction of glucose. At $T_f = 150$ °C, the transmembrane flux decreases by 0.45 kg m^{-2}h^{-1} between the curve for pure water and the one for 50 wt.% glucose in feed. Between the experimental points for 20 wt.% and 35 wt.% glucose in feed, the transmembrane flux decreases by 1.73 kg m^{-2} h^{-1}. The model does not reproduce this behaviour.

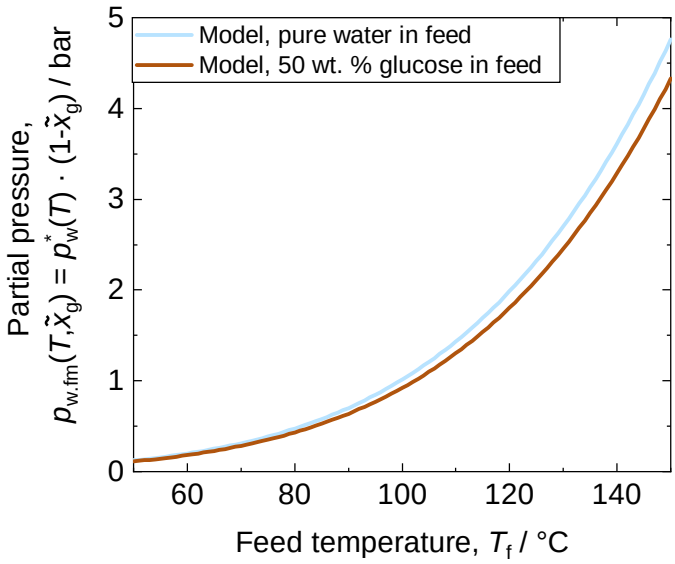

Figure 6.25.: Effect of the feed temperature on the partial pressure of water in the phase boundary for pure water and a 50 wt. % glucose solution at a permeate pressure of $p_p = 5.85$ bar g, a transmembrane pressure of $\Delta p = 0.15$ bar, a sweep gas volume flow rate of $\dot{V}_{N_2} = 30\,\mathrm{NL\,min^{-1}}$ and a feed mass flow rate of $\dot{M}_f = 1.8\,\mathrm{kg\,h^{-1}}$.

Deviations at feed temperatures above 130 °C

As shown in Figure 6.14 for pure water and Figure 6.24, it can be observed that the model reproduces the course of the experimental transmembrane flux up to a temperature of 130 °C very well, especially in the case of pure water. However, at higher temperatures, the model underestimates the transmembrane flux, in the case of water by up to a 23%.

To exclude further measurement errors for the difference between experiment and model, all relevant parameters have been varied in such a way that the transmembrane flux is maximized or minimized. The feed temperature is varied by ± 1.5 °C, the pressure on the gas side by ± 2 % (consideration of the measuring error of the pressure transducer and the possible change in ambient pressure) and the glucose concentration by ± 2 % (considering the measuring error of refractometer which displays the Brix Degree to mass concentration conversion for saccharose instead of glucose). This results in the area highlighted in green in Figure 6.26, where the case for 20 wt.% glucose in the feed is shown.

As reflected in Figure 6.26, the measurement errors in the varied parameters cannot be the reason for the difference between the model and the experiments at temperatures higher than 130 °C. Subsequently, the deviations at high temperatures must be caused by additional physical effects not considered in the model. On the one hand, these can be phenomena

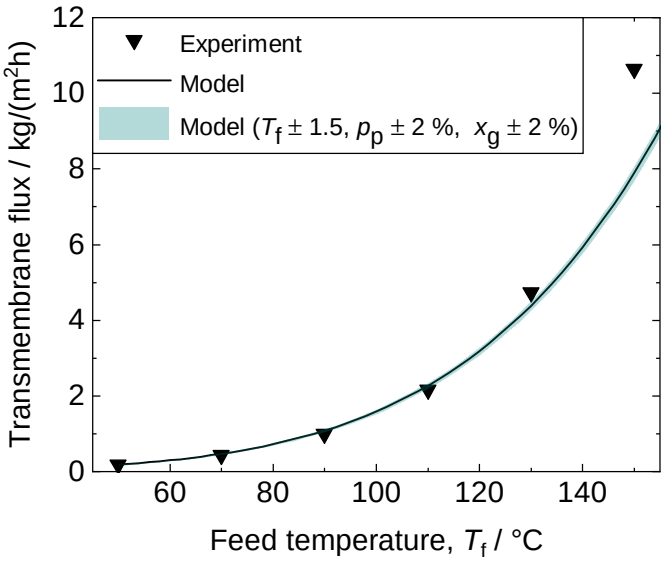

Figure 6.26.: Effect of the feed temperature to model data for a permeate pressure of $p_p = 5.85$ bar g, a transmembrane pressure of $\Delta p = 0.15$ bar, a sweep gas volume flow rate of $\dot{V}_{N_2} = 30$ NL min^{-1} and a feed mass flow rate of $\dot{M}_f = 1.8$ kg h^{-1}.

that only occur at temperatures > 130 °C or phenomena whose effect is stronger at higher temperatures. Hereafter, some hypotheses are listed:

(a) Due to the temperature increase, the surface tension of the feed is reduced. This results in the change of the contact angle at the pore entrance. This change in the contact angle leads to a change in the phase interface area and thus to a change in the free evaporation area.

(b) The linear Fick's approach is used in the model. However, this approach is valid only if the mole fraction of the diffusing component is small. At higher temperatures, this assumption may no longer be correct, which could lead to deviations between experiment and model. Accordingly, not the high temperature, but the high transmembrane flux would be responsible for the strong deviation between model and experiment.

Influence of sweep gas volume flow

The variation of the sweep gas volume flow rate for glucose solutions in the feed has a similar effect on the transmembrane flux as for pure water. Measurements were done for a 50 wt.% glucose solution, at a constant gas pressure of $p_p = 5.85$ bar and a temperature of 120 °C. Due to the high temperature, the experiments could only be started at 30 NL min^{-1} to avoid the saturation of the sweep gas at lower volume flow rates. The results for pure water

and the glucose solution 50 wt.% are shown in Figure 6.27. There are no major discrepancies between the behaviour for pure water and for the glucose-water solution. Only a decrease in the transmembrane flux due to the drop of the water partial pressure by glucose can be observed.

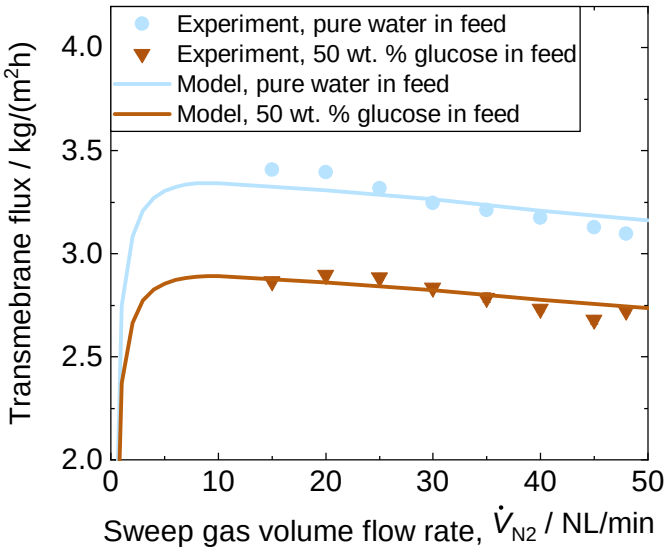

Figure 6.27.: Effect of the sweep gas flow rate and the glucose concentration on the transmembrane flux for a permeate pressure of $p_p = 5.85$ bar g, a transmembrane pressure of $\Delta p = 0.15$ bar, a feed temperature of $T_f = 120\,°C$ and a feed mass flow rate of $\dot{M}_f = 1.8\,kg\,h^{-1}$.

6.3.5 Model-based optimization of the transmembrane flux

The transmembrane flux in SGMD can be further maximized when the pressure level for the separation is accordingly chosen. Hence, a model-based optimization was performed, setting the pressure to the lowest permeate pressure for each feed temperature. Theoretically, this corresponds to the vapour pressure at the corresponding temperature and results in $p_p = p_w^*(T)$ for the gas pressure and $p_f = p_w^*(T) + 0.15$ bar for the feed pressure, being 0.15 bar the transmembrane pressure. Figure 6.28 illustrates the modelling results for pure water.

The transmembrane flux in Figure 6.28 increases linearly with temperature when the pressure in the permeate compartment is set to the corresponding saturation pressure. In contrast to what is shown in Figure 6.14 for a common permeate pressure of p_p (exponential increase with temperature), here the pressure effect is more pronounced than the temperature effect, see Table 6.1. In Figure 6.28, it can be observed that with a 40 °C increase, the transmem-

brane flux increases from $T_f = 110\,°C$ ($p_p = 0.43$ bar g) to $T_f = 150\,°C$ ($p_p = 3.76$ bar g) by only 9.3 %. However, when comparing the values obtained at a common permeate pressure of $p_p = 5.85$ bar g in Figure 6.14 for $T_f = 110\,°C$ and $T_f = 150\,°C$, a 400 % increase in transmembrane flux is obtained. When comparing the transmembrane flux for the same feed temperatures, the effect of the pressure can be observed. Thus, at $T_f = 110\,°C$, the decrease of pressure from 5.85 bar g to the vapour pressure ($p_p = 0.43$ bar g) means an increase of a 409 % while at $T_f = 110\,°C$, the adjustment of pressure from 5.85 bar g to the prevailing vapour pressure ($p_p = 3.76$ bar g) leads to a 6.4 % increase in transmembrane flux.

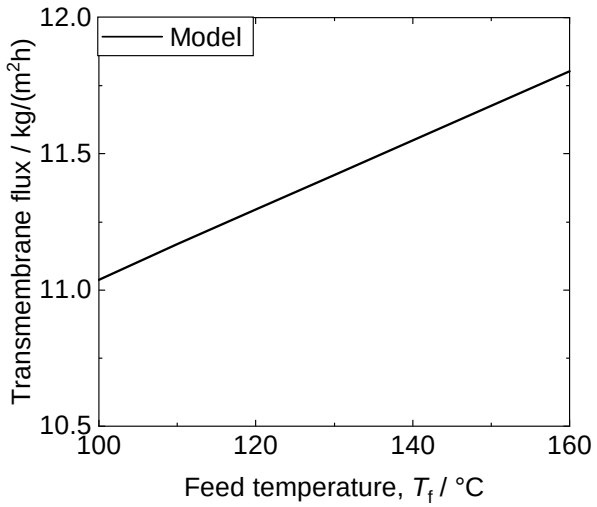

Figure 6.28.: Effect of the feed temperature on the transmembrane flux for a permeate pressure $p_p = p_w^*(T_f)$, a feed temperature ranging between $T_f = 50$ - 160 °C, a sweep gas volume flow rate of $\dot{V}_{N_2} = 30$ NL min^{-1} and a mass flow rate of $\dot{M}_f = 1.8$ kg h^{-1}.

This means that it is not only the feed temperature but the choice of a permeate pressure as close as possible to the vapour pressure which maximizes the transmembrane flux when operating SGMD separation experiments.

In the previous section, the influence of the glucose concentration at constant gas pressure in the permeate compartment was examined. It could be shown that the addition of glucose (up to 50 wt.% glucose content in feed) led to a reduction of the transmembrane flux as a result of the decrease of the driving force. Since the addition of glucose causes a reduction of the partial pressure at the phase boundary $p_w^*(T, \tilde{x}_g)$, the permeate pressure can be chosen accordingly to a lower value, like in Figure 6.28. If the pressure on the gas side is adjusted to the glucose concentration, the driving force of the SGMD does not change. The modelling results of the transmembrane flux for the adjusted permeate pressure corresponding to a feed temperature range of $T_f = 120$ - 130 °C are shown in Figure 6.29.

Table 6.1.: Comparison of the effect on transmembrane flux (in %) due to the temperature increase and the pressure adjustment to water partial pressure. Pure water only.

Results	Transmembrane flux /kg m^{-2} h^{-1}		Increase with
	$T_f = 110$ °C	$T_f = 150$ °C	temperature, T_f / %
Experiments, p_p=5.85 bar g	2.2	11	400
Model optimization, $p_p = p^*_w(T_f)$	11.2	11.7	9.3
Increase with pressure, p_p /%	409	6.4	-

It can be seen that the transmembrane flux in Figure 6.29 increases linearly with temperature and the influence of the glucose concentration is small and constant over temperature. This means that for subsequent optimizations of the transmembrane flux, the influence of the reduction of the water partial pressure due to glucose can be almost completely compensated by adjusting the gas pressure.

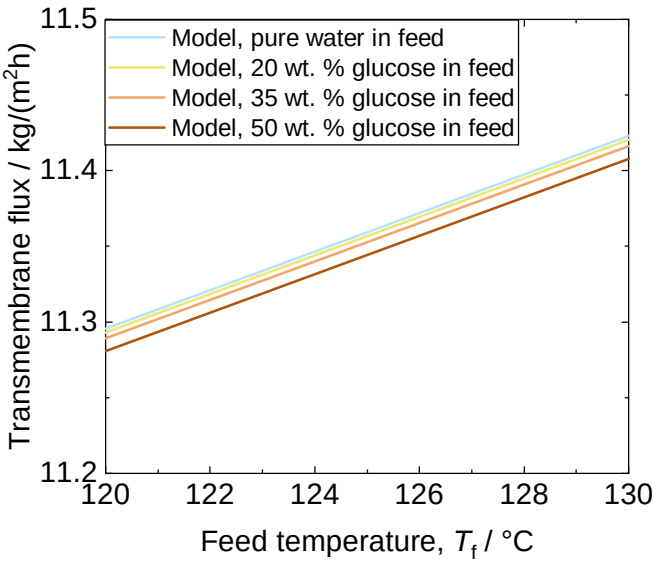

Figure 6.29.: Effect of the feed temperature and the glucose concentration on the transmembrane flux for $T_f = 120$ - 130 °C, permeate pressure of $p_p = p^*_w(T_f, \tilde{x}_g)$, feed pressure of $p_f = p^*_w(T_f, \tilde{x}_g)$ + 0.15 bar, volume flow rate of the sweep gas of $\dot{V}_{N_2} = 30$ NL min^{-1} and feed mass flow rate of $\dot{M}_f = 1.8$ kg h^{-1}.

6.4 Summary of Chapter 6

An experimental plant was built to perform experiments where the separation of water using the SGMD could be carried out. The influence of various operating parameters on the transmembrane flux was investigated, such as feed temperature, feed mass flow rate, sweep gas flow rate, permeate pressure and glucose concentration. Ceramic membranes were used for the experiments. For a better understanding of the physical phenomena and to reduce the number of experiments, a pseudo-2D cell MATLAB® model was developed, where the heat and mass transfer in the feed and permeate compartment, as well as across the membrane, were considered. Both, experiments and modelling results agree that higher temperatures lead to higher transmembrane fluxes, due to the effect of temperature on the water partial pressure. It was observed that the glucose content led to a decrease in transmembrane flux due to the decrease of the water partial pressure in the feed when glucose is present. Besides, it was seen that the right choice of the sweep gas flow is decisive for a maximum transmembrane flux. A model based-optimization revealed that when permeate pressures were chosen close to the water partial pressure at the phase boundary, the transmembrane flux got maximized. By adjusting the gas pressure in this manner, the influence of the water partial pressure reduction due to glucose could be almost completely compensated.

7

Microstructured membrane reactor: potential and challenges

For the intensification of the polycondensation process, two routes were considered: the use of FGE in a double-pipe reactor where the reacting mixture is biphasic and, on the other hand, the use of a membrane reactor, where water is removed from the (single-phase) reacting fluid by means of membrane distillation. Regarding the second route, hydrophobic coatings for metallic membranes have been developed. These membranes, as well as other membrane materials, have been characterized in terms of their hydrophobicity and LEP. Separation experiments at high temperatures for pure water and glucose solutions using SGMD have been performed. However, the design of the microstructured membrane reactor still needs to be clarified and several requirements for the process and for the membrane should be proven. This chapter investigates the influence of three different requirements (i.e. the stability over time, two-phase in the feed and application of hydrophobic metallic membranes) on the SGMD process. Therewith, conclusions are derived for the design of the membrane reactor.

The use of a membrane microreactor in comparison to the previously patented process, EP 2528950 B1 [18], with two microreactors and an expansion chamber in between for water removal could not only lead to the simplification of the system by saving equipment but also a reduction in operational costs. For example, since the expansion chamber becomes unnecessary in the membrane micro-reactor set-up, the respective pressure control equip-

ment needed to decrease the pressure for the flash and the consecutive pressure build-up for further processing in the second microreactor are also dispensable. In addition, the use of a membrane microreactor eliminates the need for a second pump and therefore the associated investment, operating and maintenance costs. The application of the membrane microreactor deals with different requirements regarding the membrane material and separation process:

- The membrane material and separation process should be stable over time. In the experiments shown in Chapter 6, each point was measured for 5 minutes, after reaching a steady state. However, longer-term experiments are required to determine the stability of the membrane in the application and to ensure the tightness of the membrane reactor.
- The reaction conditions stated in the patent EP 2528950 B1 [18] reveal that the reacting fluid is not in liquid state but it might be a two-phase mixture. In fact, keeping the feed in liquid state for the temperatures stated in the patent would require the pressure to go up to at least 12 bar g for a 80 wt. % glucose solution. The experiments in Chapter 6 for SGMD with single-phase feed, however, are still of fundamental importance to set the basis of the separation process at high temperatures and enable the understanding of the occurring phenomena. Nevertheless, reducing the pressure (with the consequence of allowing the evaporation of water and having a two-phase flow in the feed) holds the potential to lower the operating costs.
- The membrane should be resistant to temperature and pressure conditions. In Chapter 6, the investigation of the SGMD process, especially at higher temperatures, was done with commercial ceramic membranes. Metallic materials provide higher mechanical strength than ceramics. Hydrophobic metallic membranes can be therefore a good alternative, due to their excellent thermal and mechanical resistance. The question here is whether the hydrophobic properties of the membrane are lost over time.

According to the process described in the Example 3 of the patent EP 2528950 B1 [18], the reaction temperature was 200 °C and the glucose concentration in the feed, 80 wt. %. Since the experimental plant used in this work for separations at elevated temperatures was only designed up to a maximum pressure of 10 bar g, it was not possible to conduct experiments at the reaction conditions of the polycondensation process. The following explorative experiments were performed to ascertain the influence of the aforementioned requirements on the separation performance of the process; in this case, in terms of transmembrane flux.

7.1 Medium-term experiments

To determine the medium-term behaviour of the membranes, it was investigated whether the transmembrane flux at a stationary measuring point changes over time (e.g. due to the occurrence of fouling). Experiments with pure water or a glucose solution were conducted for up to 3 hours at a constant temperature and pressure using the experimental set-up described in Chapter 6. The results of the medium-term tests are shown in Figure 7.1. The tests were performed on the same day, however, they had to be paused. During this pause, the cell was not opened or cooled down, but the feed line was closed. Therefore, Figure 7.1(a) and 7.1(b) show the results of the consecutive experiments and model for pure water. In the lower two diagrams, Figure 7.1(c) and 7.1(d), the results for the consecutive experiments with a 50 wt. % glucose solution are shown. In the experiment depicted in Figure 7.1(c) and 7.1(d), first water was used and after a certain time of stationary conditions, the feed was switched to the glucose solution line. In all diagrams of Figure 7.1, the specific evaporation flux is plotted against the time of the experiment.

The medium-term experiments showed that the transmembrane flux experienced a gradual decrease over time, especially in Figure 7.1(a) and (b) as well as in Figure 7.1(c). At the beginning of the tests, the transmembrane flux dropped slightly. This observation can be attributed to the fact that the temperature in the cell and the inlet temperature were not stationary yet. As the experiment progressed, the transmembrane flux decreased much slower over time. In the experiments with the 50 wt. % glucose solution, pure DI water was used at the beginning of the experiment to reach the operating conditions. After a certain time, the feed was switched to the glucose solution (labelled in the figures). The decrease in transmembrane flux is clearly visible. In both diagrams, a brief increase in the transmembrane flux can be seen when switching to the glucose solution. This is due to the fact that switching to the glucose solution led to a brief increase in the inlet temperature of the feed by up to 3 °C, as a consequence of a slightly higher set temperature on the glucose storage tank. On dismantling the reactor after each experiment, no liquid water was visible neither in the permeate channels nor on the back side of the permeate. This was an indication that the membrane reactor was tight during the experiments. These findings together with the relatively steady behaviour of the transmembrane flux lead to the conclusion that the process and the membrane material can be considered relatively stable in the medium term. Long-term experiments are however still necessary to characterize the applicability of the membranes in the process.

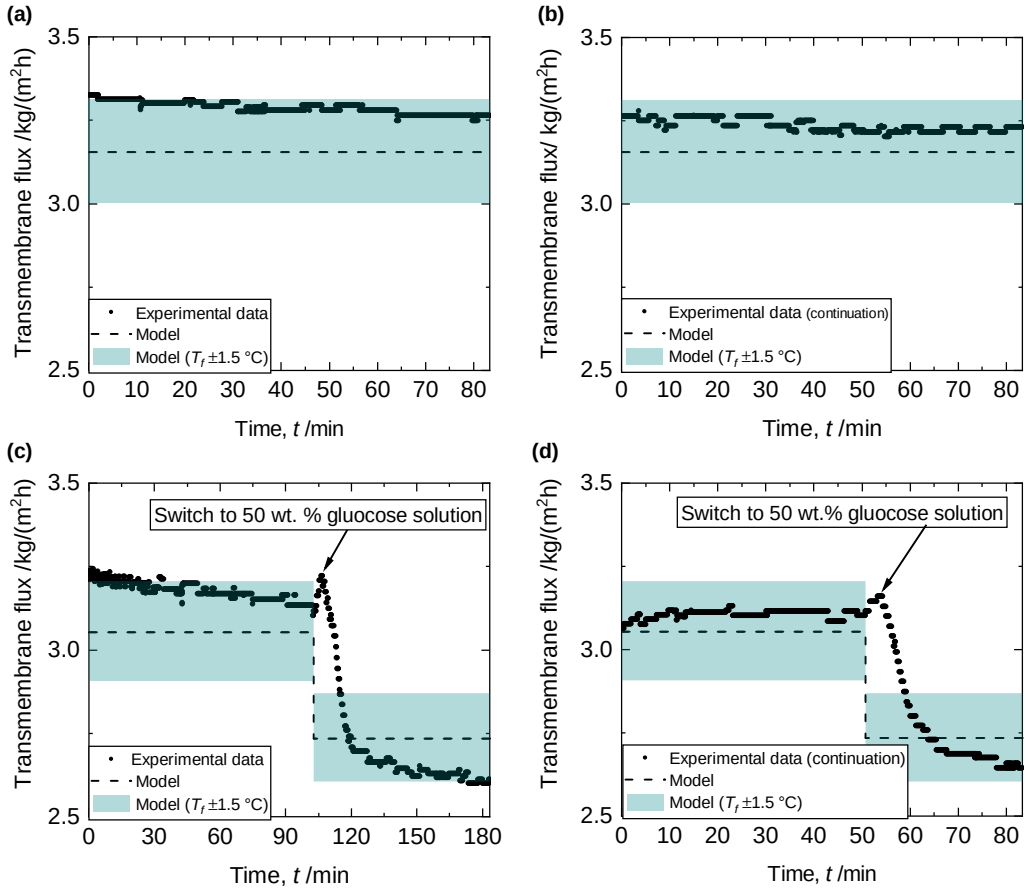

Figure 7.1.: Results of the medium-term tests regarding the stability of the measured transmembrane flux. **(a)** and **(b)** consecutive experiments (same day, without opening or cooling down the membrane reactor) for pure water. **(c)** and **(d)** consecutive experiments (same day, without opening or cooling down the membrane reactor) for a glucose content of 50 wt. %. Operating conditions: feed pressure $p_\mathrm{f} = 6$ bar g, permeate pressure $p_\mathrm{p} = 5.85$ bar g, feed temperature $T_\mathrm{f} = 120\,^\circ\mathrm{C}$, sweep gas volume flow rate $\dot{V}_{\mathrm{N}_2} = 30\,\mathrm{NL\,min^{-1}}$ and feed mass flow rate of $\dot{M}_\mathrm{f} = 1.8\,\mathrm{kg\,h^{-1}}$.

7.2 Two-phase flow experiments

In this experiment, it was investigated how the transmembrane flux behaves for a two-phase feed, i.e. the pressure was lowered to allow water to evaporate. A feed temperature of $T_\mathrm{f} = 110\,^\circ\mathrm{C}$ was chosen for the experiment. At this temperature, the vapour pressure of water is $p^*_\mathrm{w}(T_\mathrm{f}) = 1.433$ bar. Considering an ambient pressure of 1.013 bar, the feed pressure must be chosen lower than 0.42 bar g, so that the feed is a two-phase fluid. The results of the experiment are shown in Figure 7.2, where the transmembrane flux is plotted against the duration of the experiment. During the experiment, the feed pressure was varied, and

accordingly, the pressure in the permeate compartment too. The different pressure stages are indicated in Figure 7.2 by the change in the background colour.

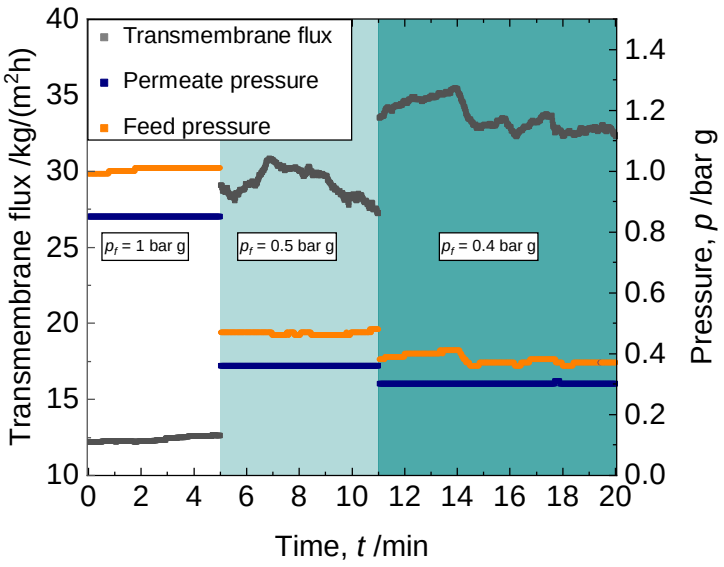

Figure 7.2.: Effect of the presence of a biphasic fluid (pure water) in the feed for a feed pressure of $p_f = 0.4$, 0.5 and 1 bar g, feed temperature of $T_f = 110\,°C$, sweep gas volume flow rate of $\dot{V}_{N_2} = 16\,NL\,min^{-1}$ and a feed flow rate of $\dot{M}_f = 1.8\,kg\,h^{-1}$.

Figure 7.2 shows that the feed is still single-phase at the first pressure level ($p_f = 1$ bar g). The observed transmembrane flux as well as the feed pressure are constant, neglecting slight fluctuations of the feed pressure at the beginning of the experiment. When decreasing the feed pressure to $p_f = 0.5$ bar g, the transmembrane flux increased to values up to approx. 30 $kg\,m^{-2}\,h^{-1}$ and fluctuated strongly over the duration of the experiment (see Figure 7.2). The feed pressure also fluctuated which is an indicator that a two-phase flow is occurring. As the pressure was lowered further to $p_f = 0.40$ bar g, the transmembrane flux further increased. Again the same behaviour as for $p_f = 0.5$ bar g can be observed: the feed pressure and the transmembrane pressure fluctuate. Figure 7.3 shows the mean values of the measured transmembrane fluxes, including their standard deviations, plotted against the feed pressure. The dashed line in Figure 7.3 marks the vapour pressure at 110 °C. It can be seen that the transmembrane flux, but also the standard deviation increase strongly as soon as the pressure is lowered towards the vapour pressure and the feed becomes two-phase.

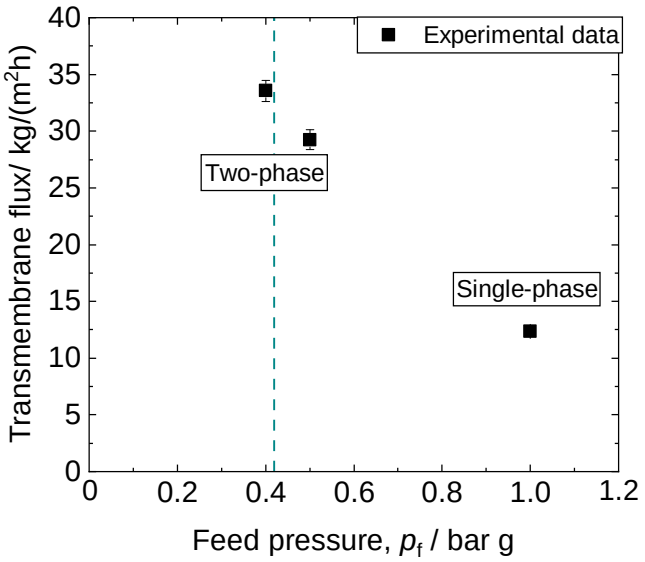

Figure 7.3.: Average value of the transmembrane flux at different feed pressures for pure water at a feed temperature of $T_f = 110\,°C$, sweep gas volume flow rate of $\dot{V}_{N_2} = 16\,NL\,min^{-1}$ and a feed flow rate of $\dot{M}_f = 1.8\,kg\,h^{-1}$.

The positive effect of two-phase (gas/liquid) flow in the feed of membrane processes has already been mentioned in the literature [205]. However, in the case of membrane distillation, only few works in the literature consider a two-phase flow in the feed [206, 207]. Due to the lower temperature used in the literature (usually temperatures lower than 80 °C), two phases occur as a result of the introduction of inert gas in the feed, e.g. N_2. The results reported show that having a two-phase flow in the feed may reduce the fouling phenomena, reduce the mass transfer inhibition in the feed boundary layer, and, therefore, enhance the transmembrane flux [206, 207]. In the present case, the gas phase in the feed is a result of evaporation due to the high temperatures, thus, all gas bubbles consist of pure steam. Even if in the above-mentioned literature cases, the gas was nitrogen or air, the same positive trend on the transmembrane flux can be observed.

7.3 Metallic membranes

To investigate the adequacy of metallic membranes in the SGMD process, experiments were performed with metallic membranes hydrophobized following the process described in Chapter 4. Specifically, the method of the direct immersion in FAS (cf. Section 4.1.2) was

used to coat the membranes, since these coatings showed the best thermal resistance. As membranes, sintered asymmetric porous steel substrates from the company GKN Sinter Metals Filters GmbH were used. A SEM image (magnification: $x50$) of the cross-section of a metallic membrane is shown in Figure 7.4.

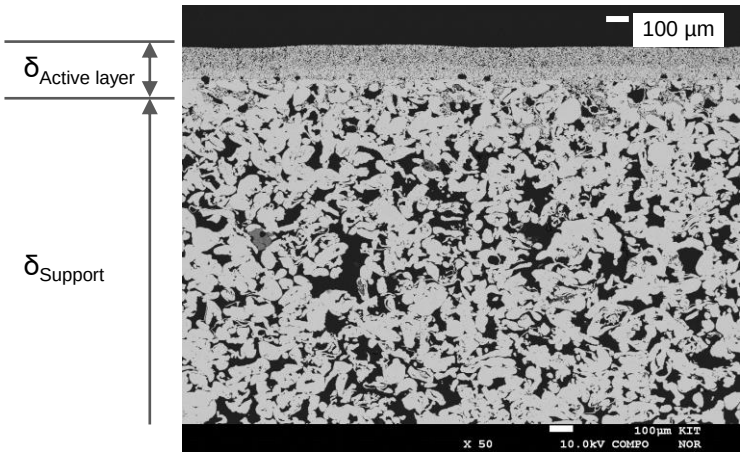

Figure 7.4.: SEM image of the cross-section of the metallic membrane. The thickness of the active layer, $\delta_A = 140\,\mu m$ and the support $\delta_S = 2\,mm$ are indicated.

To compare the performance of metallic membranes and ceramic membranes, the same conditions as in Chapter 6.3.2 were chosen, i.e. pressure in the permeate side of $p_p = 5.85\,bar\,g$, a nitrogen flow of $\dot{V}_{N_2} = 30 NL\,min^{-1}$, a feed mass flow of $\dot{M}_f = 1.8\,kg\,h^{-1}$ and pure water in the feed. The results of the experiments with metallic membranes are given in Figure 7.5 together with the results obtained under the same conditions for the ceramic membranes (cf. Figure 6.14). In Figure 7.5, the transmembrane flux is plotted against the feed temperature. The experimental data of the metallic membranes are plotted as triangles and the results obtained with the ceramic membrane are represented by circles. In contrast to the case of ceramic membranes, where at higher temperatures the model underestimates the transmembrane flux (i.e. 23.4% underestimation at 150 °C), in the case of metallic membranes, the model and experiments are consistent over the entire temperature range investigated. This behaviour confirms the hypothesis made in Chapter 6.3.4 that the reason for the deviation between model and experiment is not the high temperature, but the high transmembrane flux. The transmembrane flux with the metallic membranes is lower than with the ceramic membranes. With increasing temperature, this difference becomes more noticeable. At $T_f = 150\,°C$, the transmembrane flux with the metallic membranes is up to 73% lower when compared to the transmembrane flux with ceramic membranes.

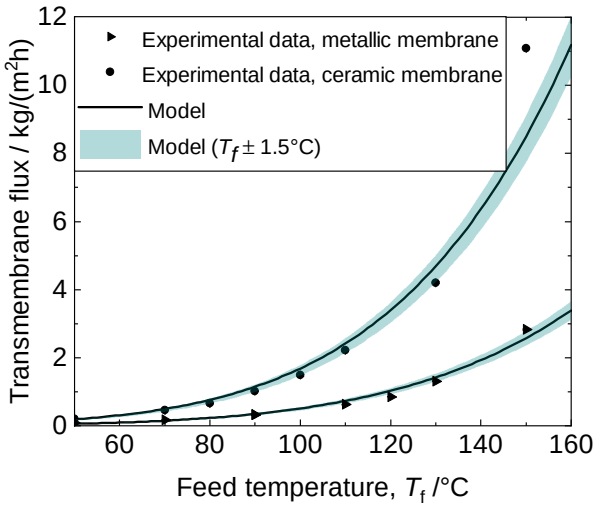

Figure 7.5.: Effect of the temperature on the transmembrane flux for metallic and ceramic membranes, at a constant permeate pressure of $p_p = 5.85$ bar g, a transmembrane of $\Delta p = 0.15$ bar, $\dot{V}_{N_2} = 30$ NL min^{-1} and $\dot{M}_f = 1.8$ kg h^{-1}.

The enhanced heat transfer leads to higher heat dissipation (namely, heat loss). Consequently, this may lead to a lower temperature at the phase boundary and consequently, a lower water partial pressure. This might lead to the reduction of the driving force of the separation [112]. In the literature, usually materials with low thermal conductivity (between 0.04 W m^{-1} K^{-1} and 0.06 W m^{-1} K^{-1}) [111] are recommended for membrane distillation, and therefore polymeric membrane made of PTFE, PVDF or PP are taken. These polymeric materials, however, do not withstand the temperature conditions of this study. One possible way to compensate for the high thermal conductivity of ceramic and metallic materials is to use membranes with higher porosity and lower thickness.

7.4 Challenges in the design of a microstructured membrane reactor

The mathematical characterization of the equilibrium displacement due to water removal through a membrane during the reaction is challenging due to different reasons:

- No reliable property data are available for glucose solutions up to 80 wt. % and up to 200 °C, which are the conditions described in Example 3 of the patent EP 2528950 B1 [18].

- The reaction itself consists of a large number of parallel as well as underlying reactions, which make the detailed modelling of the reaction kinetics a demanding task. This task was beyond the scope of this thesis. Figure 7.6 gives an insight into the individual reactions taking place in the process of the formation of polydextrose. Besides, each reaction shown can take place through two alternative paths: either 1,4 linkages or 1,6 linkages can be formed. This implies that the quantity of reactions effectively increases twofold.

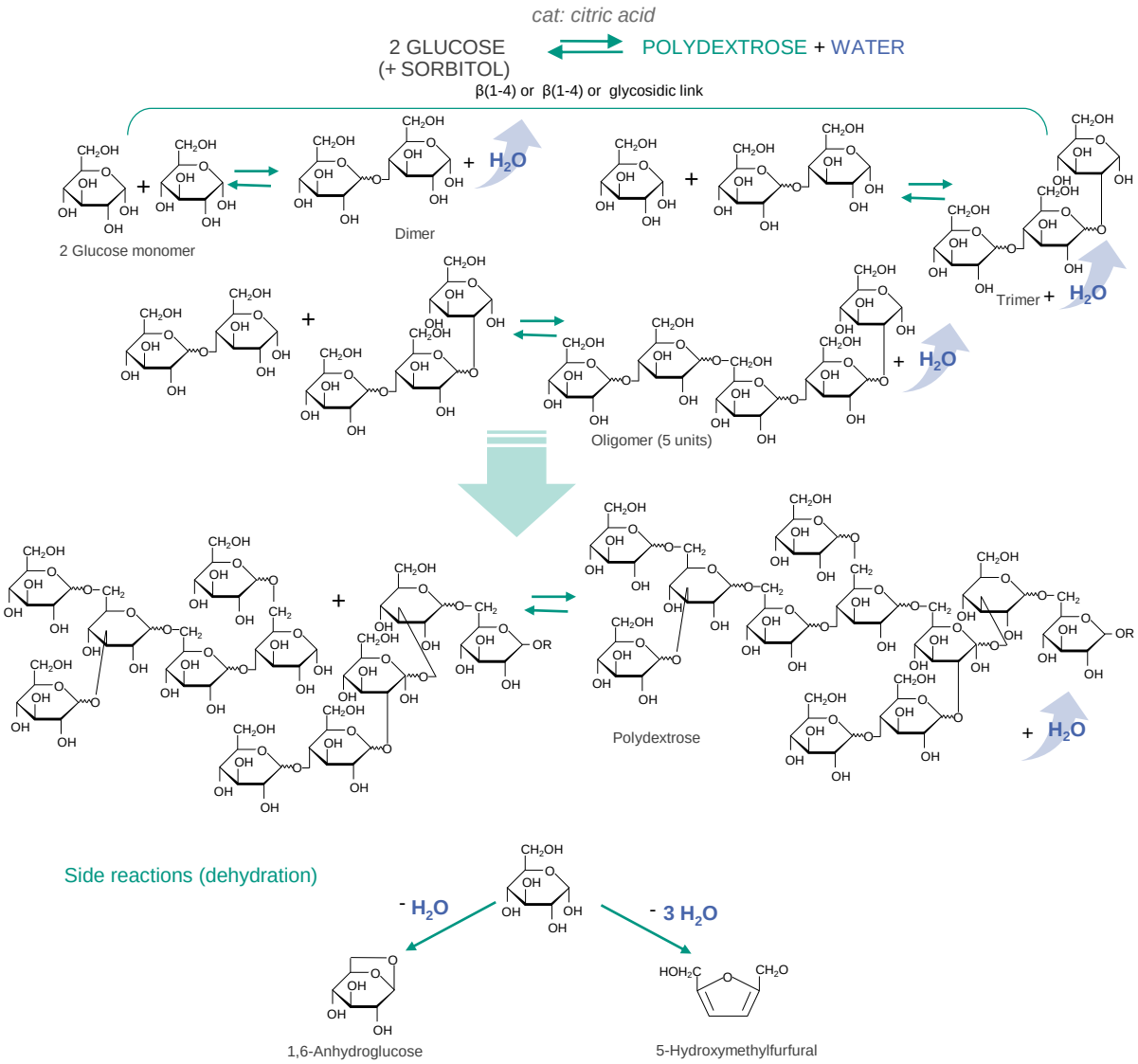

Figure 7.6.: Reactions involved in the polycondensation of polydextrose.

Because of this reason, there is a more practical definition of polydextrose, i.e. when the polymerization degree, DPn is equal to or greater than 2. The idea of carrying

out kinetic experiments under this last definition of polydextrose was also discarded because of (a) the high viscosity of the product (see discussion in Section 3.2.5) and therefore the unfeasibility of taking samples in e.g. a reactor with capillary sampling and (b) the rapid attainment of equilibrium at the beginning of the experiment makes it impractical to conduct meaningful kinetic experiments.

As a consequence of the above-mentioned facts, the determination of the suitability of the membrane separation for steam removal during the polycondensation process was carried out rather qualitatively. The determination of the transmembrane flux for a glucose content in the feed of 80 wt. % and a reaction temperature of 200 °C followed the following steps:

Step 1 Mathematical model (Chapter 6) for a glucose content of 50 wt. % and $T_f = 150$ °C. Using the model-based optimization presented in Chapter 6, and assuming the minimum pressure in the permeate side of $p_p = p^* \left(T, \tilde{x}_g\right)$, a transmembrane flux of 11.7 kg m^{-2} h^{-1} is obtained for 50 wt. % and $T_f = 150$ °C.

Step 2 Linear regression from $T_f = 150$ °C up to $T_f = 200$ °C. As observed in Figure 6.29, when the pressure in the permeate side is set equal to the saturation pressure, the transmembrane flux follows a linear behaviour for increasing temperatures. Since the property data is only validated up to 150 °C, solid line in Figure 7.7 (a), a linear regression is performed to determine the transmembrane flux at $T_f = 200$ °C, which results in 12.3 kg m^{-2} h^{-1}.

Step 3 Exponential fit from a glucose content of 50 wt. % to 80 wt. %. As observed in Section 6.3.4, the increase in glucose content, had a negative effect on the transmembrane flux, as a consequence of the reduction of the water partial pressure. The property data is only validated up to a glucose content of 50 wt.%, solid line in Figure 7.7 (b). Consequently, and following the behaviour of the water partial pressure when glucose is in the feed, the transmembrane flux for glucose contents > 50 wt.% has been estimated using an exponential regression. The exponential fit for a feed temperature of $T_f = 150$°C, cf. dashed lines in Figure 7.7 (b), shows a reduction in transmembrane flux of only 0.50 % between 50 wt. % and 80 wt. %. Applying this reduction to the transmembrane flux estimated in Step 2 with the linear regression leads to a transmembrane flux of 12.2 kg m^{-2} h^{-1} for 200 °C, i.e. the operating parameters of the polycondensation.

Considering the membrane testing unit and membrane area used throughout the experiments in this chapter as well as in Chapter 6 (A_m=0.27 m^2), and multiplying this area value by the above estimated transmembrane flux at the operating conditions of the polycondensation, a removal of 3.3 kg h^{-1} of water is estimated. The feed flow given in Example 3 of the patent is 20 ml min^{-1}, which corresponds to 0.03 kg h^{-1} for an 80 wt. % glucose content. Being the feed flow lower than the transmembrane flow capacity of the available membrane means

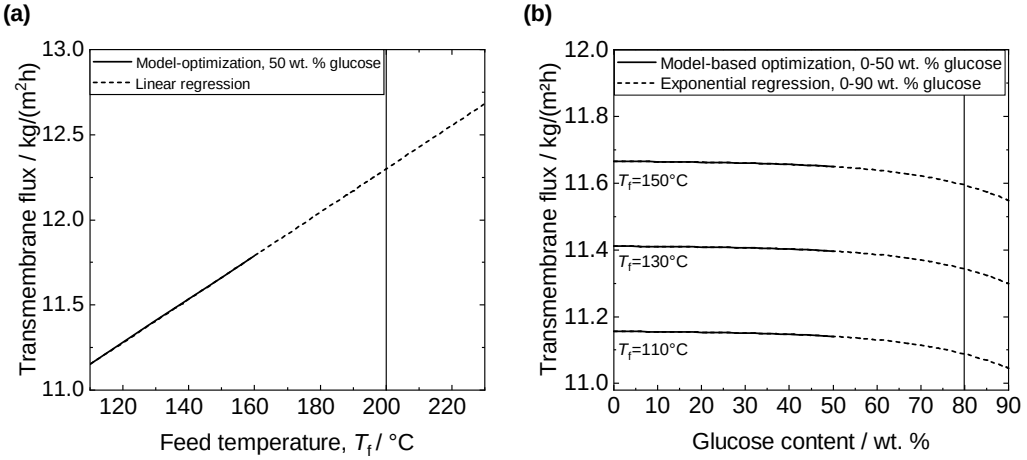

Figure 7.7.: (a) Effect of the feed temperature on the transmembrane flux for $p_p = p^*\left(T, \tilde{x}_g\right)$, feed temperature, T_f=50 - 150 °C, glucose content of 50 wt. %, feed flow rate of $\dot{M}_f = 1.8\,kg\,h^{-1}$and sweep gas volume flow rate of $\dot{V}_{N_2} = 30\,NL\,min^{-1}$. Linear regression up to 230 °C. **(b)** Effect of the glucose content in feed for $p_p = p^*\left(T, \tilde{x}_g\right)$, feed temperature, $T_f = 110°C$, 130 °C, 150 °C, glucose content of 50 wt. %, feed flow rate of$\dot{M}_f = 1.8\,kg\,h^{-1}$and sweep gas volume flow rate of $\dot{V}_{N_2} = 30\,NL\,min^{-1}$. Exponential regression up to 90 wt.%.

that the membrane is sufficiently sized to remove the existing water in the feed. In industrial applications, however, much larger feed flow rates of the order of magnitude of tone per hour are required, and therefore larger water flows should be removed. For example, for a $500\,kg\,h^{-1}$ feed flow rate, and assuming that 10 wt.% of the water content is required to be removed (i.e. $50\,kg\,h^{-1}$), a membrane area of 4 m^2 would be needed. Tubular membranes may offer a more robust, space-saving and cost-effective option when larger membrane areas are required (see Annex A.12 for an insight into the design proposal of a potential tubular membrane reactor). The use of a membrane in a microstructured reactor is, however, associated with several challenges, some of which are listed below:

- Membrane costs, since thin and defect-free membranes and/or support are required. Besides, the membrane fabrication method (scalable, with a reproducible outcome) for the hydrophobic coatings should be able to sustain wide operating conditions and possible thermal cycles, while avoiding the penetration of the liquid.
- Mass transfer inhibition in the feed and fouling. The subsequent concentration of the solute in the feed represents a further mass transfer resistance which may additionally lead to fouling; not only in the microchannels but also in the pores. Besides, the polydextrose viscous characteristics (see Section 3.2.5) in comparison to the glucose solution, intensify the problem of fouling.
- Membrane wetting and further leaking, which may lead to unprofitable operations since the separation may not be feasible and part of the product may be lost. However,

the major problem may be related to the difference in temperature between the feed (hot) and sweep gas (cold) sides. If polydextrose permeates through membrane pores or rifts, it would immediately precipitate in the back side of the membrane and start to accumulate in any part of the sweep gas passage. This situation may lead to the risk of clogging.

- Complex operation, still requiring full-time supervision, as well as the membrane limited lifetime and the consequent downtime for membrane replacement. The configuration adopted for the integration of the membrane in the reactor is also important to approach long-term operation with the highest membrane performance.

Taking into account these points, further research is needed to provide an industry and market-ready solution with membranes, which is cost-effective and can guarantee a stable operation in the long term.

7.5 Summary of Chapter 7

The fundamentals for the conception of a microstructured membrane reactor for the in situ removal of water during the polycondensation to form polydextrose were set in this chapter. Within this scope, different requirements were defined: the stability of the membrane material and separation process, the existence of two-phase flow in the feed and the implementation of metallic membranes. The results show that the membranes are stable in the medium term. Besides, the existence of a two-phase flow in the feed enhances the transmembrane flux. The investigated metallic membranes, however, reduced the transmembrane flux. Challenges in the design of the microstructured membrane reactor could be also identified, mostly related to the availability of process data and the long-term stability of the hydrophobic membrane during the polycondensation process. Further research in the area is definitely needed to provide an effective solution which includes membranes.

8

Conclusions and outlook

Following the recommendations of the WHO to reduce the daily sugar intake, alternative products such as polydextrose have emerged as sugar substitutes. The polycondensation reaction to form polydextrose is a reversible reaction that can be carried out at high temperatures and low residence times with high yields in microreactors. In 2011, the collaboration between Cargill Inc. (Wayzata, US) and the Institute for Micro Process Engineering of the KIT (Karlsruhe, DE) led to a patented solution: two microchannel reactors with an expansion chamber in between to evaporate and remove the water from the reaction mixture and thus shift the reaction equilibrium, so that a higher product yield is achieved in the second microchannel reactor. To simplify the process and minimize costs as well as the process-related CO_2 footprint, the scope of this dissertation was to investigate process intensification technologies to achieve a single-step polycondensation of dextrose, so that the intermediate water separation step could be eliminated. In this work, two scenarios, and therefore two different routes were considered: (1) The reaction is carried out in double-pipe reactors fitted with internal inserts (FGE), consequently the reacting mixture forms a two-phase flow. (2) The reaction is carried out in a membrane microchannel reactor, where steam is separated from the single-phase (liquid) feed flow through the pores of a hydrophobic membrane.

Using a double-pipe reactor with additively manufactured internal inserts, the polycondensation reaction can be carried out in one step, reaching product yields higher than 90 wt. %. With the FGE-reactor, it is possible to carry the reaction at lower pressure levels than with

the microchannel reactor, which enables the evaporationof water and thus its removal from the reacting liquid mixture. The polycondensation process carried out in the studied reactor configuration is mainly influenced by the reaction temperature and the residence time, with the reaction temperature being the most influencing factor. Heating oil temperatures of 235 ° C are enough to achieve product yields higher than 90 % and therefore meet the product specifications of the FDA and the EEA. The temperature of the reaction mixture at the reactor outlet and consequently the product yield can be increased by using internal inserts with a finer-structured geometry. Moreover, the product yield is independent of the mass fraction of glucose in the feed. These latter findings are advantageous for the industrial solution: they not only allow for the elimination of the expansion chamber and the second microchannel reactor (and thus also with the required second pumping system), but also to dispense with an upstream evaporator, which is necessary to achieve an initial feed composition of dry solids of 80 wt. %. Furthermore, a pre-heater is also no longer required for the industrial solution, because the double-pipe solution offers enough length for the necessary reaction temperature to be reached. In conclusion, using FGE in double-pipe reactors and carrying out the reaction at a reaction temperature of 220 ° C and feed concentration ranging from 60-80 wt. % leads to the achievement of the specified product yield in a simplified reactor solution that reduces equipment and energy requirements. These good results led to a patent application (European patent application no. 22190222.4) and a 4th position in the KIT Innovation Contest, Neuland in 2021.

The second route presented in this dissertation intends to continuously remove steam from the reaction using a hydrophobic membrane. Hence, it aims to investigate not only a suitable membrane separation method for high temperatures (and associated pressures) but also to develop suitable membranes and membrane characterization methods that can be used under such temperature conditions. When high-temperature conditions are required for the reaction to take place in a membrane reactor, membrane materials are needed which can withstand these temperatures. Metallic membranes are often more robust than ceramic membranes and can be joined easier with other parts of the reactor. This is advantageous for the membrane reactor development when parts are welded together in the reactor. The coating of inherently-hydrophilic metallic membranes to render their surface hydrophobic is possible. PE-CVD can be used to fabricate hydrophobic Si-DLC coatings on metallic substrates. Similarly, FAS coatings can be applied by means of direct immersion to form hydrophobic metallic membranes. Comparing both methods, FAS coatings provide stainless steel porous substrates with stronger hydrophobic characteristics (CA = 143 °) and are more resistant to elevated temperatures (up to 250 °C). The liquid entry pressure experimental results at ambient conditions ranging between 1.3 and 3.1 bar g indicate that FAS-coated

fine porous stainless steel substrates have a chance to be applied as membranes for steam separation.

It could be confirmed that the choice of the experimental method for the determination of the LEP can influence the final result. Early detection methods that don't rely on subjective observations of the operator are needed, and the pressure step method meets these requirements. It could be observed that the tested ceramic membranes have higher LEP than the polymeric ones, which can be attributed to the higher contact angles of their surface as well as larger thicknesses and narrower pore size distributions. Understanding the behaviour of LEP with pressure and temperature is particularly relevant when membranes are to be applied under high temperature and pressure conditions. It could be experimentally observed that the temperature is the main factor affecting the LEP, due to its strong influence on the surface tension. Novel data were obtained at temperatures up to 120 °C and pressures above atmospheric pressure. Overall, being able to measure LEP at the temperature region considered in the present work broadens the application range of hydrophobic membranes and enables the use of the membranes for unexplored fields.

For the first time in literature, the SGMD process at temperatures above 80 °C was investigated by means of experimental and modelling work. The main objective was to study the influence of the operating conditions on the transmembrane flux. The heat and mass transfer during the SGMD process could be mathematically modelled with very good accuracy. As from the experimental and modelling results, to maximize the transmembrane flux, it is recommended to set high temperatures in the feed and low pressure in the permeate, since these parameters maximize the water partial pressure difference between the feed and permeate side and minimize the mass transfer resistances. Furthermore, the choice of the nitrogen flow rate is decisive for a maximum transmembrane flux and it is recommended to set moderate nitrogen flows. If the nitrogen flow is selected too high, the transmembrane flux decreases due to the cooling of the support and hence, the reduction of the mass transfer coefficient. Besides, the higher required heating power for high nitrogen flows and the larger condenser surface can result in a higher cost for the final application. Finally, it was observed that the glucose content led to a decrease in the transmembrane flux. Especially in these cases, it is recommended to lower the gas pressure as close as possible to the saturation pressure in the feed to compensate for this decrease. The mathematical modelling showed that the largest mass transfer resistance was located in the membrane support. Hence, it is recommended to use membranes with the lowest possible thicknesses and highest porosity, which still guarantee the mechanical stability of the membranes.

With regard to the implementation of the membrane in the final process, the following conclusions can be drawn: (1) The SGMD process is stable for 3 h and the membrane reactor remains tight. (2) The use of coated metallic membranes for the SGMD is feasible for the separation of steam, but with lower transmembrane flux than when using ceramic

membranes. (3) Allowing two-phase flow in the feed by lowering the feed pressure has positive effects on the transmembrane flux. These outcomes can be taken into account in the design of a microstructured membrane reactor.

Comparing route 1 and route 2 from a practical point of view, the solution with the internal inserts has a better potential for the intensification of the polydextrose process. Membranes still present many challenges for their industrial application: wetting and fouling of the membrane are major drawbacks which hinder the long-term operation of the membrane processes. Besides, the membrane reactor design and operation with the sweep gas still remains complex. The solution with the FGE, on the other side, is a robust solution allowing to reach the target product yield without including sensitive parts like a membrane. Using the internal inserts in tubular reactors, allows the process to be run in one step and eliminates equipment and process steps in the plant. This leads to a reduction of costs and energy requirements and results in a more energy-efficient and climate-friendly production of polydextrose.

For future investigations, the solution with FGE in a double-pipe reactor should be further tested on a pilot scale to validate the existing results and draw conclusions for the industrial application. Regarding the membrane solution, a more sustainable strategy to hydrophobize the metallic membranes should be investigated, like the use of non-fluor-containing coatings, like stearic acid instead of FAS. Besides, for the characterization of the hydrophobic coatings at high temperatures, it is of scientific interest to determine the influence of temperature and pressure on the contact angle. Only few works in literature deal with this topic. When organic compounds are present in the feed, the LEP may be negatively affected as a result of the surface tension decrease. Further LEP characterization tests should be performed when glucose is present in the feed. In addition, to counter the effect of fouling by glucose, the in situ regeneration of the membrane should be investigated so that the longest possible service life in the industrial application can be ensured.

Additive manufacturing opens up new possibilities for the development of new membrane concepts. For instance, thickness, pore size, porosity and tortuosity could be designed to best fit the application and find the optimum parameters which lead to high mechanical stability and a high LEP, while still enabling a high transmembrane flux.

A

Annex

A.1 Regulated composition of polydextrose

Table A.1 shows the maximum or minimum concentration of the main products and byproducts involved in the polycondensation.

Table A.1.: Regulatory requirements for the composition of the dry matter of polydextrose following the authorization as a food additive in the EEA [7].

Component	Composition
Oligomer (DPn≥ 2)	>90 wt.%
Glucose + Sorbitol	< 6 wt.%
1,6-Anhydroglucose	< 4 wt.%
5-Hydroxymethyl-furfural	< 0. 1 wt.%

A.2 Calculation of the space-time yield of different reactor concepts for the production of polydextrose

The space-time yield STY, also known as specific productivity, is the quotient of the mass flow of a reaction product $\dot{M}_P$ and the volume of the reactor in which it is produced, V_R:

$$STY = \frac{\dot{M}_P}{V_R} \tag{A.1}$$

The values shown in Table 1.1 are the result of the calculations made for different types of reactors, i.e. batch, extruder and microreactor.

- **Batch process** according to the patent of Rennhard [13]:
  The volume of the reactor was 0.25 Gallons (US), which is equivalent to 0.378 m^3. The total input of reactants was:

  $$M = 212 \text{ lbs glucose} + 21 \text{ lbs sorbitol} + 7.5 \text{ lbs citric acid} = 233 \text{ lbs} \approx 109 \text{ kg} \tag{A.2}$$

  During the reaction, the reaction mass becomes lower because part of the dry substance is converted to water. It has been assumed that the product mass in the reactor corresponds to 90 wt.% of the feed mass. According to the patent of Rennhard [13], there was about 96.7 wt.% polydextrose in the product. The reaction time was given as 3.25 h. Considering the extra cleaning and preparation time, it can be assumed that the total time approximates to the time of a working shift, i.e. 8 h. The Space–Time Yield can be therefore calculated as:

  $$STY = 0.9 \cdot \frac{M}{t \cdot V_R} = 32.44 \frac{\text{kg}}{\text{m}^3\text{h}} \tag{A.3}$$

- **Extruder process** according to the work of Hwang [14]:
  The barrel diameter of the twin-screw extruder was 0.175 m and it had a length-to-diameter ratio of $l/d = 40$. As a twin-screw extruder, there were two barrels, therefore the reaction volume has been estimated as:

  $$V_R = d^2 \cdot \frac{1}{4}\pi \cdot l \cdot 2 = 0.336 \text{m}^3 \tag{A.4}$$

  The reactant input was $\dot{M} = 65 \text{ kg h}^{-1}$. With an amount of polydextrose in the product of $x_{\text{PDX}} = 0.937$, the space-time yield can be calculated as:

  $$STY = 0.9 \cdot \frac{\dot{M} \cdot x_{\text{PDX}}}{V_R} = 163.14 \frac{\text{kg}}{\text{m}^3\text{h}} \tag{A.5}$$

- **Microreactor process** according to the patent of Kuesters et al. [18]:

  The volume flow rate was $20\,\mathrm{ml\,min^{-1}}$ which is equivalent to a mass flow rate of $0.03\,\mathrm{kg\,s^{-1}}$, when the glucose content in feed is $x_g = 0.8$, as given in the patent. A product with $x_{PDX} = 0.8$ was obtained. The Space–Time –Yield is thus calculated to:

$$STY = 0.9 \cdot \frac{\dot{M} \cdot x_g \cdot x_{PDX}}{V_R} = 1122.08 \frac{\mathrm{kg}}{\mathrm{m^3 h}} \tag{A.6}$$

A.3 Nusselt correlations

The Nusselt correlations used in the modelling of the heat transfer in the microchannels were taken from the collection of Kockmann [153] and the VDI-Heat Atlas [152]. The following Nu correlations can be used also for the calculation of the Sh-number, due to the analogies between heat and mass transfer [153]. Herewith, the Pr-number will be replaced by the Sc-number.

Laminar flow (Re $<$ 2300)

$$\mathrm{Nu}_{\mathrm{lam.}} = \sqrt[3]{\mathrm{Nu}_1^3 + \mathrm{Nu}_2^3 + \mathrm{Nu}_3^3} \tag{A.7}$$

For the flow in a narrow slit or microchannel, the Nu-correlations are calculated according to Equation A.8 - A.10.

$$\mathrm{Nu}_1 = 7.54 \tag{A.8}$$

$$\mathrm{Nu}_2 = 1.849 \cdot \sqrt[3]{Gz} \tag{A.9}$$

$$\mathrm{Nu}_3 = \sqrt[6]{\frac{2}{1 + 22 \cdot \mathrm{Pr}}} \cdot \sqrt[2]{\mathrm{Gz}} \tag{A.10}$$

Turbulent flow (Re $>$ 10000)

In the turbulent regime, the pressure loss is proportional to the square of the mean velocity [153] and therefore the heat transfer can be calculated according to the expression of Gnielinski [152].

$$\mathrm{Nu}_{\mathrm{turb.}} = \frac{(\zeta/8) \cdot \mathrm{Re} \cdot \mathrm{Pr}}{1 + 12.7 \cdot (\zeta/8)^{1/2} \cdot (\mathrm{Pr}^{2/3} - 1)} \cdot \left(1 + \left(\frac{d_\mathrm{h}}{l}\right)^{2/3}\right) \tag{A.11}$$

with the coefficient $\zeta = (1.8 \log_{10} \mathrm{Re} - 1.5)^{-2}$.

A.4 Calculation of the diffusion coefficients

Diffusion coefficient in gases

For low pressures, the binary diffusion coefficient of gas 1 in gas 2 can be calculated according to the Fuller-Schettler-Giddings Equation [149]. For the input variables and the diffusion coefficient to be in SI units, the equation reads:

$$D_{1,2} = \frac{1.013 \cdot 10^4 \cdot T^{1.75} \cdot [(\tilde{M}_1 \cdot 10^3)^{-1} + (\tilde{M}_1 \cdot 10^3)^{-1}]^{\frac{1}{2}}}{p \cdot [(\sum \nu_1^{\frac{1}{3}} + (\sum \nu_2^{\frac{1}{3}}]^2} \tag{A.12}$$

Here ν corresponds to the diffusion volume; calculated as the summation of the atomic values of individuals atoms that compose the molecular structure of each gas, which can be taken from Table D-1 in [149].

Diffusion coefficient in liquids

For the calculation of diffusion coefficients in liquids, and assuming the case of an ideally diluted solution, the Stokes-Einstein equation reads [150]:

$$D_{1,2} = \frac{k_\mathrm{B} \cdot T}{3 \cdot \pi \cdot \eta_1 \cdot d_2} \tag{A.13}$$

Here $D_{1,2}$ is the diffusion coefficient of the component 1 in the component 2 for a high dilution (Higher amount of component 2). k_B is the Boltzmann constant, T the temperature, η_1 the dynamic viscosity of the component 1 and d_2 the molecular diameter of the component 2. The diffusion coefficient can be applied approximately for molar concentrations up to $10\,\%$.

A.5 Overview of the equipment in the polycondensation set-up

Table A.2.: Overview of all the equipment in the set-up for polycondensation.

Component	Manufacturer	Type/Designation	Measuring / Operating Range	Quantity
Double-jacketed tank	QVF®, DeDietrich, FR	AD 1682	10 L	1
Double-jacketed tank	QVF®, DeDietrich, FR	AD 1682	30 L	1
Thermocouple	Conatex	Sheathed thermocouple Type K	-200 - 1300 °C	12
Thermocouple	Conatex	Surface thermocouple Type K	-200 - 1300 °C	7
Pressure transducer	Wika	Type S-10	0 - 10 bar	4
Coriolis flow sensor	Rheonik	RHM015	2- 600 g min^{-1}	1
Eccentric screw pump	Seepex	MD 0005-24	0.3 - 7.2 L h^{-1}	1
Thermostat	Lauda	Proline P12	-	1
Heat transfer oil	Shell (NL)	Thermia B	up to 320°C	-
Reactor thermostat	Tool-Temp (CH)	-	-	1
Coriolis oil	Endress+Hauser, CH	Promass F	0-2000kg/h	1
Needle valve at oil thermostat	Swagelok	N series	-	1
Heating cords	Horst	HSS-450°C	up to 450 °C	7
Backpressure regulator	Swagelok	KBP	$p_{max.}$ = 34.4 bar	1

A.6 Byproducts of the polycondensation reaction

As a product of the polycondensation of glucose, several byproducts are formed which are found in the final product, i.e. 1,6-anhydroglucose and 5-hydroxymethylfurfural. The regulations (see Annex A.1) indicate limits in the concentration of these byproducts as well as the amount of unreacted glucose. Figure A.1 shows the amount of 1,6-anhydroglucose found in the final product for different glucose concentrations in feed. In all the cases, the amount lies below the limit (4 wt. %).

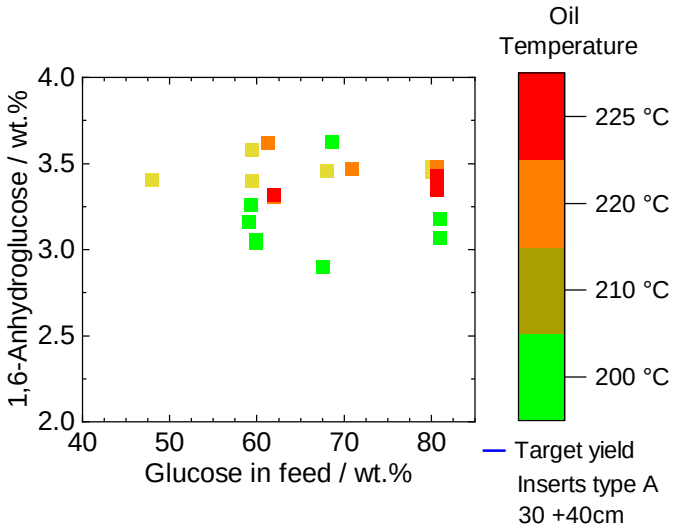

Figure A.1.: 1,6-Anhydroglucose in wt. % in the final product for different glucose concentrations in the feed. Only samples for $p_{out} = 2 \pm 0.4$ bar g in the $30 + 40$ reactor are shown. The colour scale refers to the oil set temperature.

The amount of 5-hydroxymethylfurfural in the final product was only measured in certain cases and always laid below the limit marked by the regulation (0.1 wt.%).

A.7 EDS and WDS analyses of the coated metallic substrates

Table A.3.: Average EDS Results for the Si-DLC layer on a permeable SS substrate and for a FAS coated silicon wafer (including substrate). Sample positions see Figure A.2.

Substrate material	C / wt%	O wt%	F / wt%	Si / wt%
Si-DLC coating	51.11	24.54	-	24.34
FAS homogeneous coating, 001 in Figure A.2 (b)	1.63	0.28	0.21	97.88
FAS coated, 002 in Figure A.2 (b)	7.20	0.76	1.45	90.59

For the quantitative characterization of the fluor-containing coating (FAS) by means of EDS analysis, the results on the FAS-coated silicon wafer are shown in Table A.4, to avoid the overlapping of the Fe and F peaks, when analysing an SS sample.

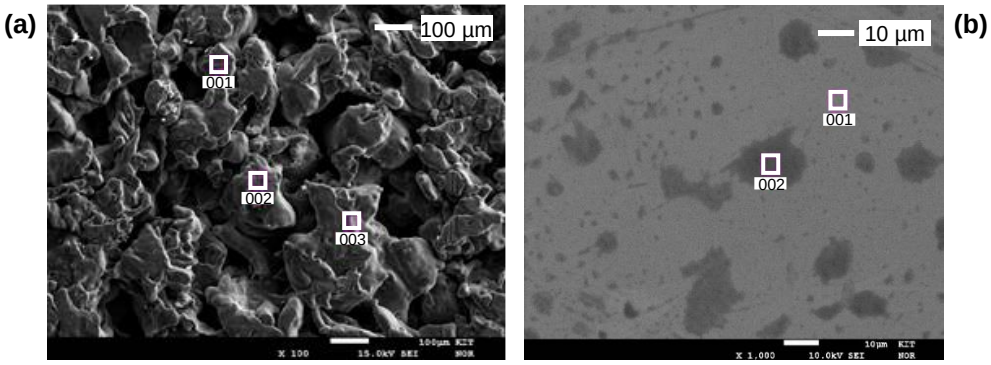

Figure A.2.: Sample positions marked for EDS analysis of **(a)** Si-DLC layer on a permeable SS sub-strate; **(b)** FAS coated silicon wafer (including substrate).

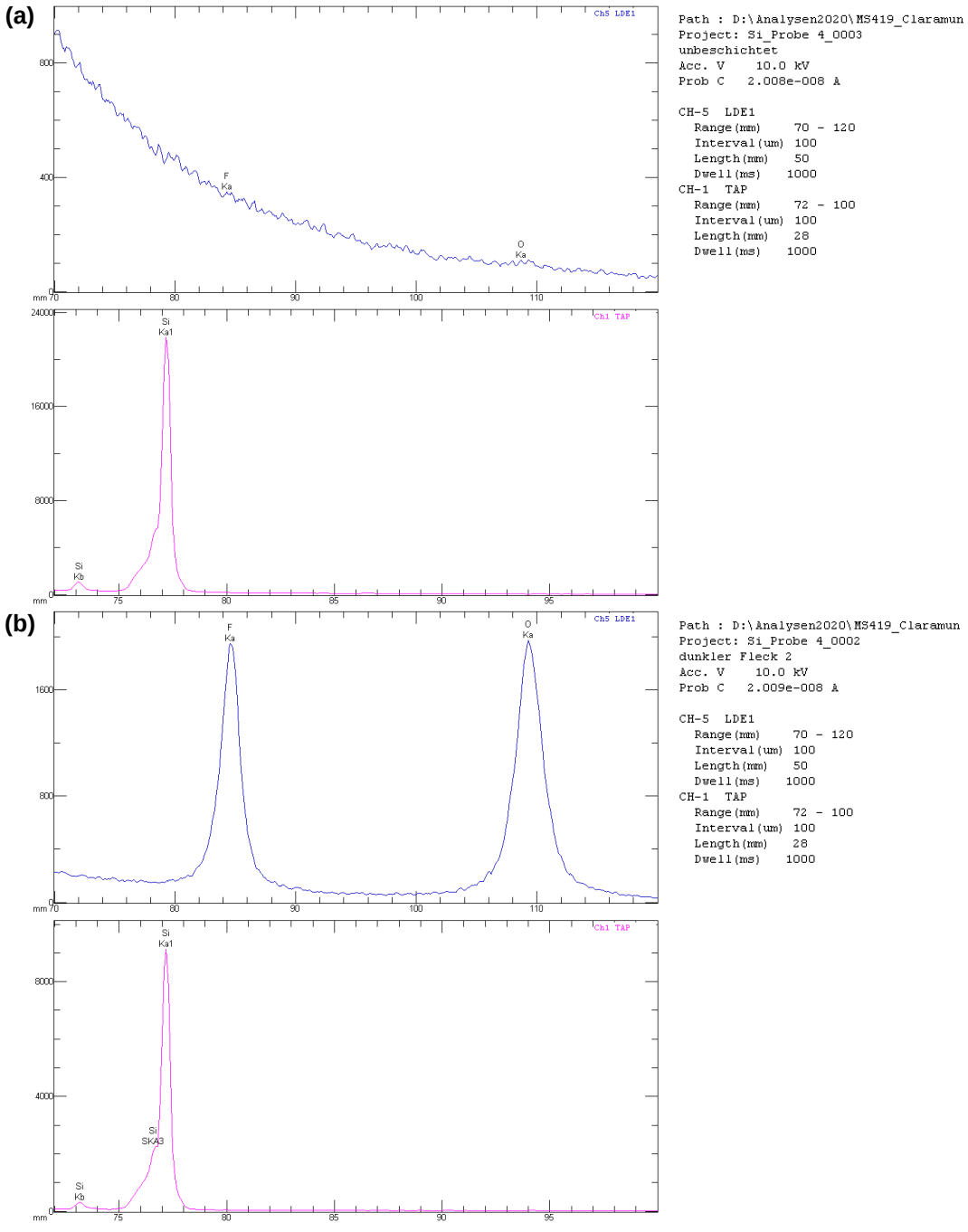

Figure A.3.: WDS analysis of **(a)** uncoated silicon wafer, showing the absence of O and F (no peaks); **(b)** FAS coated silicon wafer, showing the presence of Si, O and F in the layer, corresponding to Figure A.2.

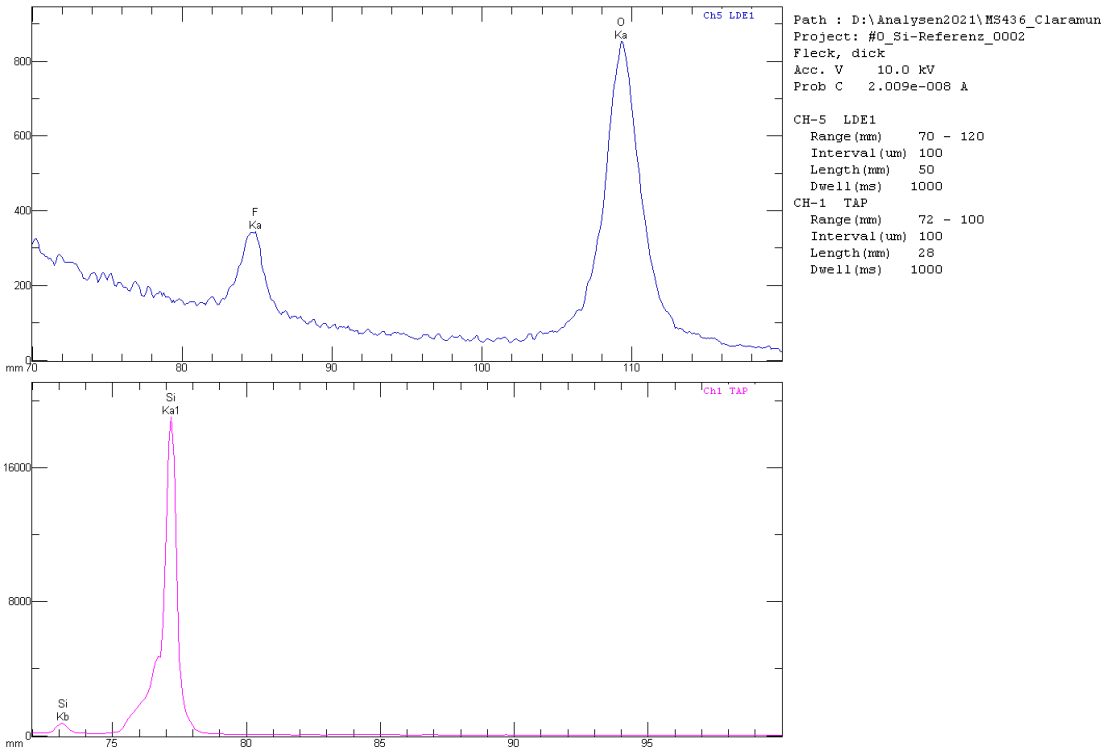

Figure A.4.: WDS analysis of the FAS coated silicon wafer after 350°C heating stage, corresponding to sample in Figure A.5.

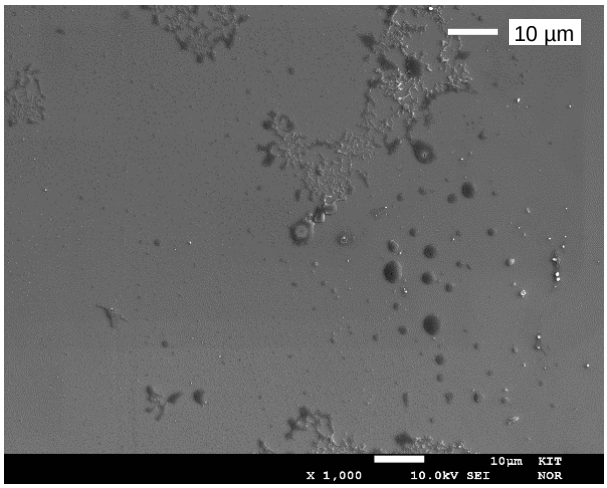

Figure A.5.: SEM picture of the FAS coated silicon wafer after 350 °C heating stage.

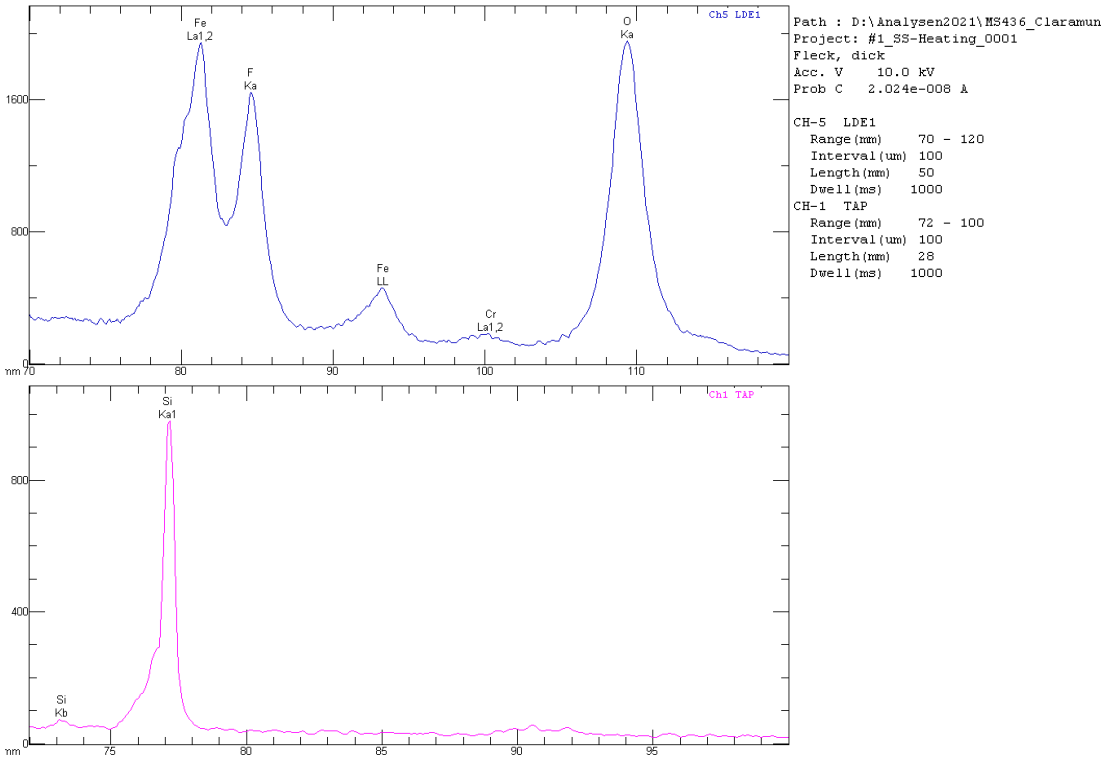

Figure A.6.: WDS analysis of the FAS coated non-permeable SS substrate after the 280°C heating stage corresponding to the sample of Figure A.7, showing still qualitatively the presence of the layer elements.

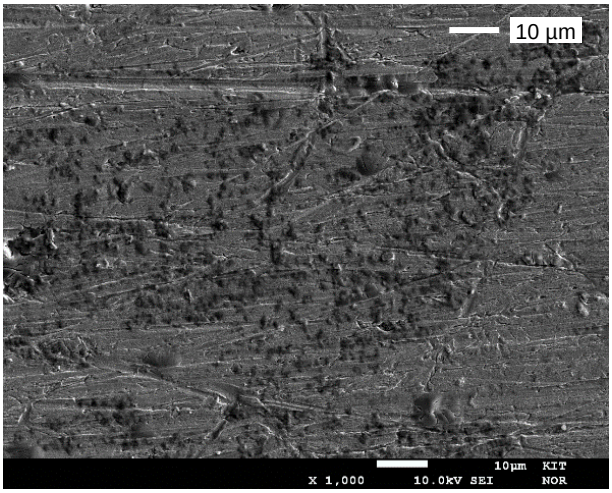

Figure A.7.: SEM picture of the FAS coated non-permeable SS substrate after the 280 °C heating stage.

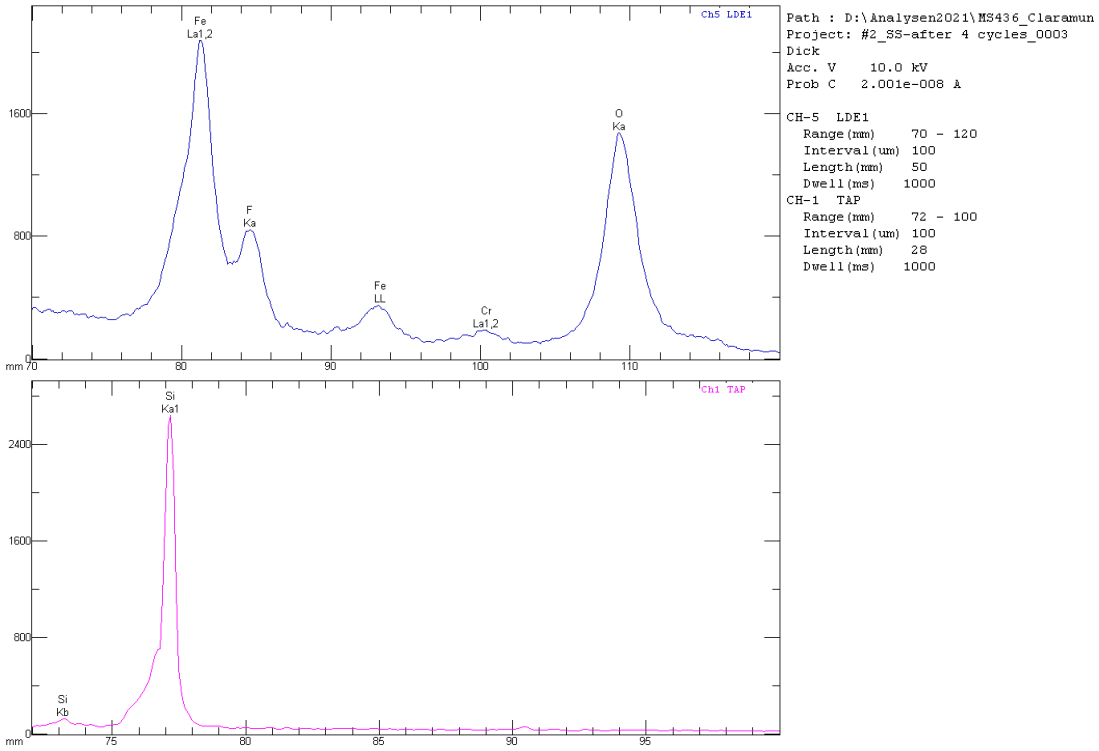

Figure A.8.: WDS analysis of the FAS coated non-permeable SS substrate after 4 heating cycles at 250°C corresponding to the sample of Figure A.9, showing the presence of the layer elements.

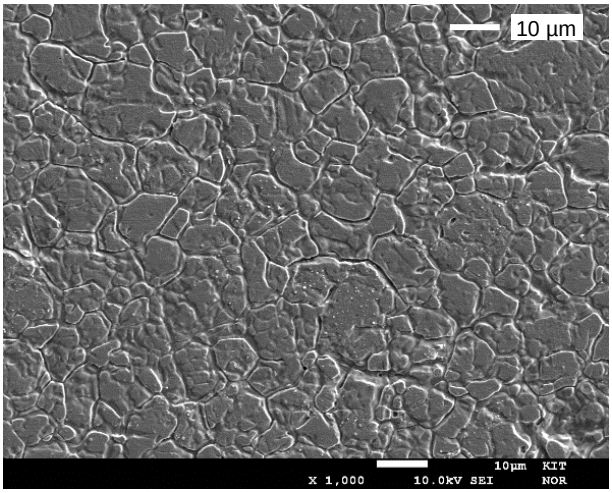

Figure A.9.: SEM picture of the FAS coated non-permeable SS substrate after 4 heating cycles at 250°C.

A.8 Surface roughness analysis of the metallic substrates

Table A.4.: Average 3D surface texture parameters according to ISO 25178[34], performed with confocal microscopy.

Substrate	Sa / µm	Sq / µm	Sz/ µm
Non-coated non-permeable SS	9.8314	11.762	113.38
Non-coated permeable SS (fine porous)	11.154	13.733	122.44

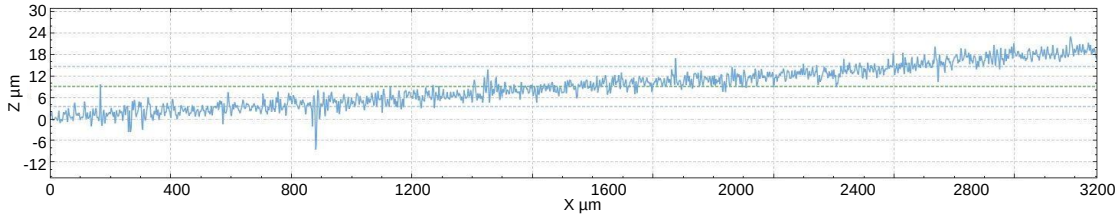

Figure A.10.: Exemplary surface height profile of the non-permeable SS substrate (non-coated).

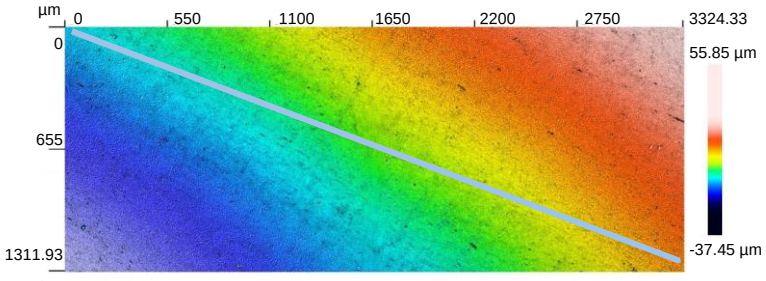

Figure A.11.: Confocal image of a flat SS substrate (non-coated) corresponding to the height profile in Figure A.10.

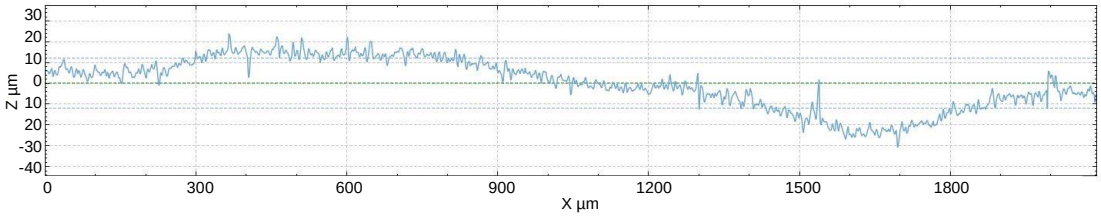

Figure A.12.: Exemplary surface height profile of the fine porous SS substrate (non-coated).

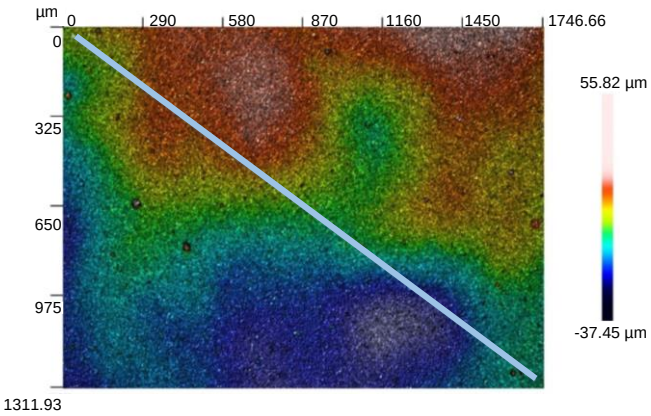

Figure A.13.: Confocal image of a fine porous SS substrate (non-coated) corresponding to the height profile in Figure A.12.

A.9 Overview of the equipment in the LEP set-up

Table A.5.: Overview of all the instrumentation in the LEP set-up.

Component	Manufacturer	Type/Designation	Measuring / Operating Range	Quantity
Thermocouple	Conatex	Sheathed thermocouple Type K	-200 - 1300 °C	7
Thermocouple	Conatex	Surface thermocouple Type K	-200 - 1300 °C	5
Pressure transducer	Wika	Type P-30	0 - 10 bar	1
Pressure transducer	Wika	Type P-31	0 - 10 bar	1
SITEC manual screw press	SITEC-Sieber Eng. AG	750.1400	0 - 400 bar	1
Heating cords	Horst	HSS-450 °C	up to 450 °C	4
Backpressure regulator feed side	Swagelok	KBP	$p_{max.}$ = 34.4 bar	1
Backpressure regulator permeate side	Swagelok	KBP	$p_{max.}$ = 36.8	1

A.10 P&ID of the SGMD set-up

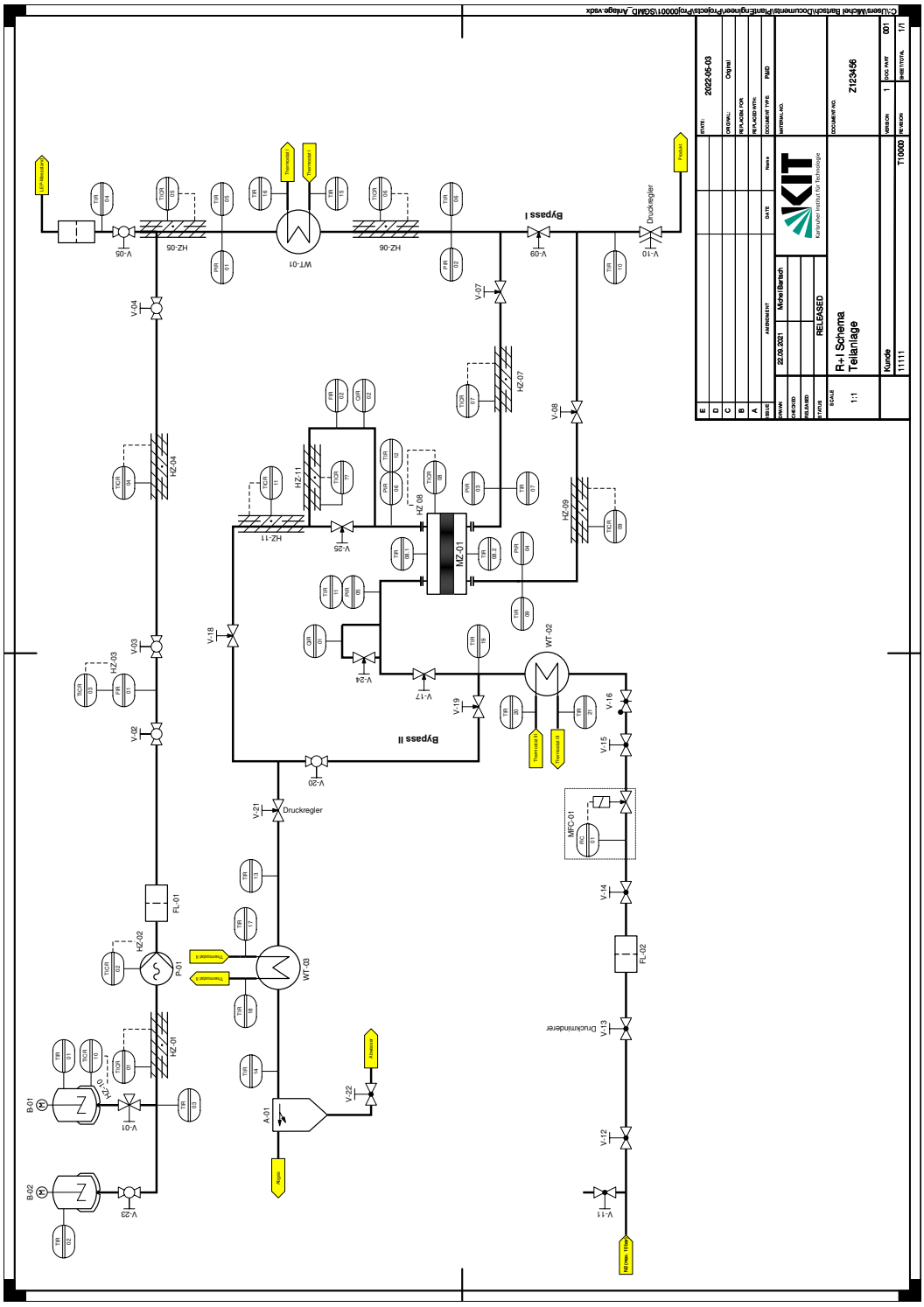

Figure A.14.: P&ID of the SGMD Plant described in Chapter 6.

A.11 Overview of the equipment in the SGMD set-up

Table A.6.: Overview of all the instrumentation in the SGMD plant.

Component	Manufacturer	Type/Designation	Measuring / Operating Range	Quantity
Thermocouple	Conatex	Sheathed thermocouple Type K	-200 - 1300 °C	17
Thermocouple	Conatex	Surface thermocouple Type K	-200 - 1300 °C	8
Pressure transducer	Wika	Type A-10	0 - 10 bar	4
Pressure transducer	Wika	Type P-31	0 - 10 bar	2
Coriolis flow sensor	Rheonik	RHM015	2- 600 g min^{-1}	1
Mass flow controller	Brooks	SLA8500	1 - 50 L min^{-1}	1
Humidity sensor	DeltaOHM	HP480	0 - 100% RH	2
Eccentric screw pump	Seepex	MD 0005-24	0.3 - 7.2 L h^{-1}	1
Thermostat	Lauda	Proline P12	-	1
Heating cords	Horst	HSS-450 C	up to 450 °C	8
Cross-flow heat exchanger (WT-01)	KIT-IMVT	2621-I-0.0	-	1
Counter-flow heat exchanger (WT-02)	KIT-IMVT	2463-I-7.0	-	1
Cross-flow heat exchanger (WT-03)	KIT-IMVT	1612-A-0.0	-	1
Backpressure regulator feed side	Swagelok	KBP1J0G4C5A20000	$p_{max.}$ = 34.4	1
Backpressure regulator permeate side	Swagelok	KBP1F0G4D5A20000	$p_{max.}$ = 36.8	1

A.12 Prototype of a microstructured membrane reactor

A prototype of a microstructured membrane reactor which uses the technology of the FGE was designed. Due to time constraints, the prototype was not tested but sets the principles of a possible advancement towards the production of polydextrose.

The prototype combines the use of the FGE - which enhances the heat transfer during the reaction- and the use of a membrane - to remove the evaporated water. The removal of water vapour from the reaction channel would modify the existing two-phase flow pattern. Less vapour in the reactor means less acceleration of the reacting mixture due to the gas bubbles. As a consequence, higher residence times for the reacting mixture are expected. Higher residence times, in turn, would mean that a shorter reactor length might be sufficient for the reaction to achieve the required product yield.

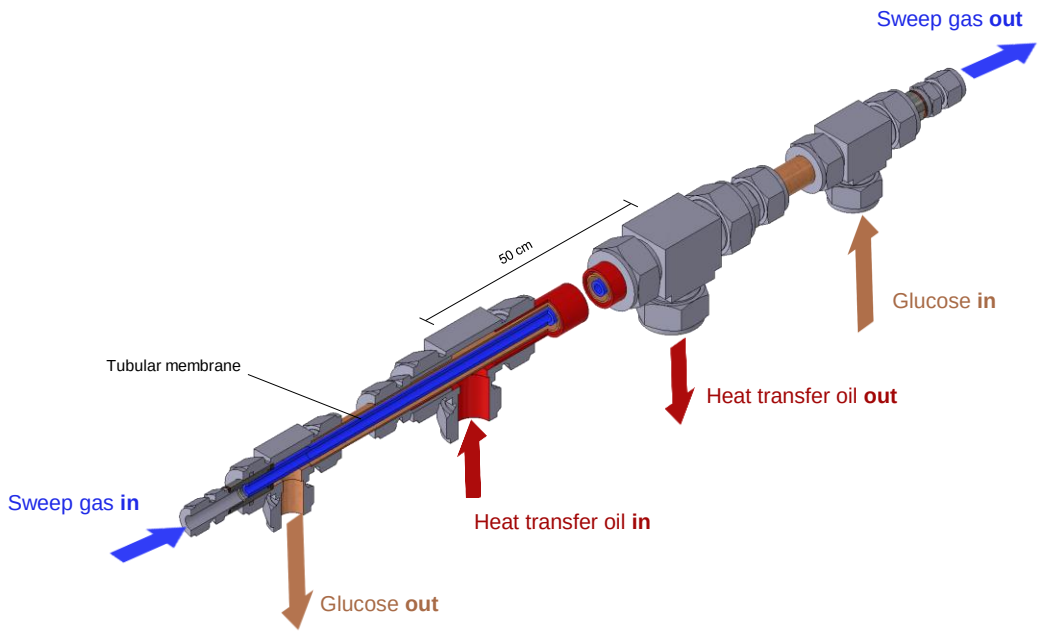

Figure A.15.: Prototype for the integrated separation in a pipe (steam removal/sweep gas) in pipe (reaction) in pipe (heating oil) reactor system.

In the proposed prototype, shown in Figure A.15, the heat transfer oil flows in the 3 mm thick outer annular gap. The glucose-reacting solution flows in counter-current in the inner annular gap. The contact length between oil and glucose is 50 cm. With the presented design and resulting assembly constraints, there is a section of 15 cm at the inlet and outlet of the glucose channel that is not heated. Due to construction-related issues, other options were

not conceivable. Therefore, in that case, heating cords at both sides are recommended to maintain the reaction temperature.

The outer and inner annular gap are fitted with FGE manufactured according to Chapter 3. The difference now is that the FGE for the reacting fluid also have an annular shape. The membrane is located in the inner pipe. Here, N_2 flows in counter-current to the glucose and sweeps the water vapour separated by the membrane out of the reactor (cf. Figure A.16).

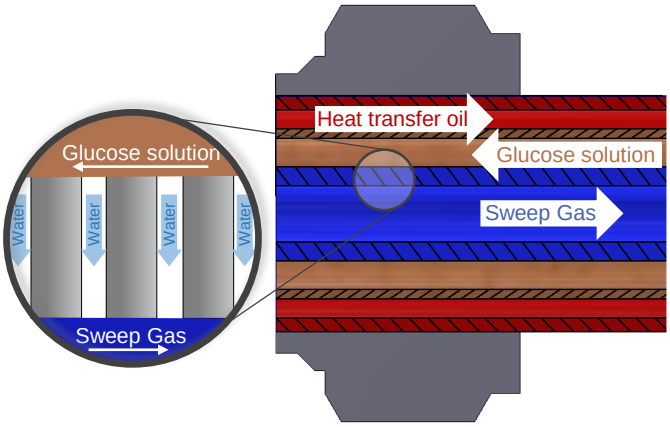

Figure A.16.: Detail of an schematic view of the cross-section of the membrane reactor with the different streams flowing in counter-current.

An alumina tubular membrane from the company Inopor® (Scheßlitz, DE) or a sintered metallic filter cartridge from the company GKN Sinter Metals Filters GmbH Radevormwald (Radevormwald, DE) - coated according to the direct immersion method in Chapter 4- could be used as the membrane. As an alternative to the configuration presented, it is also conceivable that the feed flows on the inner side of the membrane and the permeate at the outer side. Then, the heating oil would flow in the inner pipe, the reacting mixture in the inner annular gap and the outer annular gap would consist of the tubular membrane. In this case, a new design would be necessary. Moreover, it should be evaluated which flow velocities and residence times would be appropriate.

List of Figures

List of Tables

Bibliography

[1] Diet, nutrition, and the prevention of chronic diseases: Report of a Joint WHO/FAO expert consultation [Geneva, 28 January - 1 February 2002] (WHO technical report series). Geneva: World Health Organization, 2003, vol. 916, ISBN: 924120916X.

[2] WHO, Guideline: Sugars intake for adults and children (Nonserial Publications). Geneva: World Health Organization, 2015, ISBN: 9789241549028.

[3] P. Koivistoinen and L. Hyvönen, The use of sugar in foods, International Dental Journal, vol. 35, no. 3, pp. 175–179, 1985.

[4] M. H. Auerbach, S. A. Craig, J. F. Howlett, and K. C. Hayes, Caloric availability of polydextrose, Nutrition Reviews, vol. 65, no. 12, pp. 544–549, 2007. DOI: 10.1111/j.1753-4887.2007.tb00279.x.

[5] J. N. BeMiller, Carbohydrate chemistry for food scientists, Third edition. London: WP : AACC International Press, 2019, ISBN: 9780128134382.

[6] J. D. Stowell, Prebiotic potential of polydextrose, in Prebiotics and Probiotics Science and Technology, D. Charalampopoulos and R. A. Rastall, Eds., New York, NY: Springer New York, 2009, pp. 337–352, ISBN: 978-0-387-79057-2. DOI: 10.1007/978-0-387-79058-9{_}11.

[7] EU-Comission, Annexes II and III to Regulation (EC) No 1333/2008 of the European Parliament and of the Council Text with EEA relevance, 2012. [Online]. Available: https://eur-lex.europa.eu/legal-content/EN/ALL/?uri=celex%3A32012R0231 (visited on 07/18/2022).

[8] The United States Pharmacopeial Convention, Ed., Food Chemicals Codex (Food Chemicals Codex), 8. ed. Rockville, Md.: USP, 2012, vol. 8, ISBN: 9781936424054.

[9] M. Auerbach, H. Mitchell, and F. K. Moppett, Polydextrose, in O'Brien-Nabors (Ed.) 2011 – Alternative Sweeteners, pp. 489–505.

[10] S. A. S. Craig, J. F. Holden, J. P. Troup, M. H. Auerbach, and H. I. Frier, Polydextrose as soluble fiber: Physiological and analytical aspects, Cereal Foods World, vol. 43, no. 5, pp. 370–376, 1998.

[11] P. R. Murray, Polydextrose, in Low-Calorie Products, L. Birch, Ed., 1988, pp. 83–100.

[12] C. Ribeiro, J. Zimeri, E. Yildiz, and J. Kokini, Estimation of effective diffusivities and glass transition temperature of polydextrose as a function of moisture content, Carbohydrate Polymers, vol. 51, no. 3, pp. 273–280, 2003. DOI: 10.1016/S0144-8617(02)00182-0.

[13] H. H. Rennhard, Polysaccharides and their preparation, Patent US3766165 (A), 1973.

[14] J.-K. Hwang, C.-J. Kim, and C.-T. Kim, Production of glucooligosaccharides and polydextrose by extrusion reactor, Starch - Stärke, vol. 50, no. 2-3, pp. 104–107, 1998. DOI: 10.1002/(SICI)1521-379X(199803)50:2/3<104::AID-STAR104>3.0.CO;2-B.

[15] R. O. Elmore, Method of preparing a randomly-bonded polysaccharide, Patent US5051500 (A), 1991.

[16] P. S. Shah, C. S. A. Shaw, C. S. Morrill, and M. T. Wuesthoff, Polymerization of mono-and disaccharides using low levels of mineral acids, Patent WO98/41545, 1998.

[17] V. Hessel, S. Hardt, and H. Löwe, Chemical micro process engineering: Fundamentals, modelling and reactions / Volker Hessel, Steffen Hardt, Holger Löwe. Weinheim: Wiley-VCH, 2004, ISBN: 9783527307418.

[18] C. Kuesters, B. F. Stengel, W. Benzinger, and J. Brandner, Microprocessing for preparing a polycondensate, Patent EP 2528950 B1, 2011.

[19] FMI-Futer Market Insights, Polydextrose market. polydextrose market by Form (powder form, liquid form) & Region: Forecast 2022 - 2032. [Online]. Available: https://www.futuremarketinsights.com/reports/polydextrose-%20market/table-%20of-%20content (visited on 04/19/2022).

[20] A. Hensel, A. Wenka, E. Hansjosten, and W. Benzinger, Flow guide in a channel, Patent DE102015113432A1, 2017.

[21] E. Hansjosten, A. Wenka, A. Hensel, W. Benzinger, M. Klumpp, and R. Dittmeyer, Custom-designed 3D-printed metallic fluid guiding elements for enhanced heat transfer at low pressure drop, Chemical Engineering and Processing: Process Intensification, vol. 130, pp. 119–126, 2018. DOI: 10.1016/j.cep.2018.05.022.

[22] N. Diban, A. T. Aguayo, J. Bilbao, A. Urtiaga, and I. Ortiz, Membrane reactors for in situ water removal: A review of applications, Industrial & Engineering Chemistry Research, vol. 52, no. 31, pp. 10 342–10 354, 2013. DOI: 10.1021/ie3029625.

[23] M.R. Qtaishat and T. Matsuura, 13 - Modelling of pore wetting in Membrane Distillation compared with Pervaporation, in Pervaporation, Vapour permeation and Membrane distillation, ser. Woodhead Publishing Series in Energy, A. Basile, A. Figoli, and M. Khayet, Eds., Oxford: Woodhead Publishing, 2015, pp. 385–413, ISBN: 978-1-78242-246-4. DOI: 10.1016/B978-1-78242-246-4.00013-1.

[24] S. Claramunt, M. Khurram, W. Benzinger, M. Kraut, and R. Dittmeyer, Fabrication and characterization of hydrophobic porous metallic membranes for high temperature applications, Processes, vol. 9, no. 5, p. 809, 2021. DOI: 10.3390/pr9050809.

[25] M. Omidi, M. Farhadi, and M. Jafari, A comprehensive review on double pipe heat exchangers, Applied Thermal Engineering, vol. 110, pp. 1075–1090, 2017. DOI: 10.1016/j.applthermaleng.2016.09.027.

[26] S. Liu and M. Sakr, A comprehensive review on passive heat transfer enhancements in pipe exchangers, Renewable and Sustainable Energy Reviews, vol. 19, pp. 64–81, 2013. DOI: 10.1016/j.rser.2012.11.021.

[27] E. Smithberg and F. Landis, Friction and forced convection heat-transfer characteristics in tubes with twisted tape swirl generators, Journal of Heat Transfer, vol. 86, no. 1, pp. 39–48, 1964. DOI: 10.1115/1.3687060.

[28] A. Dewan, P. Mahanta, K. S. Raju, and P. S. Kumar, Review of passive heat transfer augmentation techniques, Proceedings of the Institution of Mechanical Engineers, Part A: Journal of Power and Energy, vol. 218, no. 7, pp. 509–527, 2004. DOI: 10.1243/0957650042456953.

[29] I. Ghosh, How good is open-cell metal foam as heat transfer surface?, Journal of Heat Transfer, vol. 131, no. 10, 2009. DOI: 10.1115/1.3160537.

[30] C. Hutter, D. Büchi, V. Zuber, and P. Rudolf von Rohr, Heat transfer in metal foams and designed porous media, Chemical Engineering Science, vol. 66, no. 17, 2011. DOI: 10.1016/j.ces.2011.05.005.

[31] W. E. Frazier, Metal additive manufacturing: A review, Journal of Materials Engineering and Performance volume, vol. 23, pp. 1917–1928, 2014.

[32] I. Gibson, D. W. Rosen, B. Stucker, and M. Khorasani, Additive manufacturing technologies, Third edition. Cham, Switzerland: Springer, 2021, ISBN: 978-3-030-56127-7.

[33] C. Parra-Cabrera, C. Achille, S. Kuhn, and R. Ameloot, 3D printing in chemical engineering and catalytic technology: structured catalysts, mixers and reactors, Chemical Society Reviews, vol. 47, p. 209, 2018.

[34] A. Bandyopadhyay, Y. Zhang, and S. Bose, Recent developments in metal additive manufacturing, Current Opinion in Chemical Engineering, vol. 28, pp. 96–104, 2020. DOI: 10.1016/j.coche.2020.03.001.

[35] A. K. Stark, Manufactured chemistry: Rethinking unit operation design in the age of additive manufacturing, AICHE Journal, vol. 64, pp. 1162–1173, 2018. DOI: 10.1002/AIC.16118.

[36] I. Diañez Amores, J. González-Gutiérrez, I. Martínez García, J. M. Franco, and C. Gallegos, 3d printing – present and future – a chemical engineering perspective, Chemical Engineering Research and Design, vol. 187, pp. 598–610, 2022. DOI: 10.1016/j.cherd.2022.08.049.

[37] P. Minetola, P. Priarone, and G. Ingarao, Sustainability for 3dp operations, in Managing 3D Printing, D. Eyers, Ed., Elsevier, 2020, pp. 143–174, ISBN: 978-3-030-23323-5. DOI: 10.1007/978-3-030-23323-5_7.

[38] S. Mehla, R. D. Gudi, D. Mandaliya, T. Hisatomi, K. Domen, and S. K. Bhargava, Additive manufacturing as the future of green chemical engineering, in Additive Manufacturing for Chemical Sciences and Engineering, S. K. Bhargava, S. Ramakrishna, M. Brandt, and P. Selvakannan, Eds., Springer, 2022, pp. 239–307, ISBN: 978-981-19-2292-3. DOI: 10.1007/978-981-19-2293-0_8.

[39] T. Femmer, i. Flack, and M. Wessling, Additive manufacturing in fluid process engineering, Chemie Ingenieur Technik, vol. 88, pp. 535–552, 2016. DOI: 10.1002/cite.201500086.

[40] M. Brandt and S. K. Bhargava, An introduction to the world of additive manufacturing, in Additive Manufacturing for Chemical Sciences and Engineering, S. K. Bhargava, S. Ramakrishna, M. Brandt, and P. Selvakannan, Eds., Springer, 2022, pp. 1–18, ISBN: 978-981-19-2292-3. DOI: 10.1007/978-981-19-2293-0_1.

[41] F. Grinschek, S. Dübal, C. Klahn, and R. Dittmeyer, Einfluss des additiven fertigungsverfahrens auf die gestalt einer mikrorektifikationsapparatur, Chemie Ingenieur Technik, vol. 94, no. 7, pp. 958–966, 2022. DOI: 10.1002/cite.202200011.

[42] M. A. A. Neukäufer, N. Sarajlic, H. Klein, S. Rehfeldt, H. Hallmann, S. Meinicke, J. Paschold, C. Knösche, and T. Grützner, Development of enhanced three-dimensional printed packings for scale-up of distillation columns: A successful case study, AIChE Journal, vol. e17902, 2022. DOI: doi.org/10.1002/aic.17902.

[43] M. Ambrosetti, R. Balzarotti, L. Fratalocchi, M. Bracconi, G. G., and E. Tronconi, Structured catalysts and non-conventional reactor designs for energy applications, in Heterogeneous Catalysis for Energy Applications, T. R. Reina and J. Odriozola,

Eds., Royal Society of Chemistry, 2020, pp. 361–396, ISBN: 978-1-78801-957-6. DOI: 10.1039/9781788019576-00361.

[44] A. Jastram, S. Schaack, and C. Kiener, Simulation-driven design of an additively manufactured reactor for exothermic liquid-liquid reactions, Chemie Ingenieur Technik, vol. 94, no. 7, pp. 948–957, 2022. DOI: 10.1002/cite.202200049.

[45] C. Busse, H. Freund, and W. Schwieger, Intensification of heat transfer in catalytic reactors by additively manufactured periodic open cellular structures (pocs), Chemical Engineering and Processing - Process Intensification, vol. 124, pp. 199–214, 2018. DOI: 10.1016/j.cep.2018.01.023.

[46] J. Ning, X. Wang, Y. Sun, C. Zheng, S. Zhang, X. Zhao, C. Liu, and W. Yan, Experimental and numerical investigation of additively manufactured novel compact plate-fin heat exchanger, International Journal of Heat and Mass Transfer, vol. 190, p. 122 818, 2022. DOI: 10.1016/j.ijheatmasstransfer.2022.122818.

[47] R. Tiwari, R. S. Andhare, A. Shooshtari, and M. Ohadi, Development of an additive manufacturing-enabled compact manifold microchannel heat exchanger, Applied Thermal Engineering, 2018. DOI: 10.1016/j.applthermaleng.2018.10.122.

[48] M. Fuchs, D. Heinrich, X. Luo, and S. Kabelac, Thermal performance measurement of additive manufactured high-temperature compact heat exchangers, Journal of Physics: Conference Series, vol. 2116, p. 012 095, 2021. DOI: 10.1088/1742-6596/2116/1/012095.

[49] L. L. Trinkies, A. Düll, B. J. Deschner, A. Stroh, M. Kraut, and R. Dittmeyer, Simulation of fluid flow during direct synthesis of h 2 o 2 in a microstructured membrane reactor, Chemie Ingenieur Technik, vol. 93, no. 5, pp. 789–795, 2021. DOI: 10.1002/cite.202000232.

[50] T. J. Lu, H. Stone, and M. F. Ashby, Heat transfer in open-cell metal foams, Acta Materialia, vol. 46, no. 10, pp. 3619–3635, 1998. DOI: 10.1016/S1359-6454(98)00031-7.

[51] G. Liu, C. Yang, J. Zhang, H. Zong, B. Xu, and J.-Y. Qian, Internal flow analysis of a heat transfer enhanced tube with a segmented twisted tape insert, Energies, vol. 13, no. 207, 2020. DOI: 10.3390/en13010207.

[52] M. Bracconi, M. Ambrosetti, M. Maestri, G. Groppi, and E. Tronconi, Analysis of the effective thermal conductivity of isotropic and anisotropic periodic open cellular structures for the intensification of catalytic processes, Chemical Engineering and Processing - Process Intensification, vol. 158, no. 207, 2020. DOI: 10.1016/j.cep.2020.108169.

[53] I. I. O. for Standardization, Additive manufacturing — general principles — fundamentals and vocabulary, Geneva.

[54] Y. Zhang, W. Jarosinski, Y. Jung, and J. Zhang, 2 - additive manufacturing processes and equipment, in Additive Manufacturing. Materials, Processes, Quantifications and Applications, J. Zhang and Y. Jung, Eds., Butterworth-Heinemann, 2018, pp. 39–51, ISBN: 9780128121559. DOI: 10.1016/B978-0-12-812155-9.00002-5.

[55] F. Grinschek, D. Xie, M. Klumpp, M. Kraut, E. Hansjosten, and R. Dittmeyer, Regular microstructured elements for intensification of gas–liquid contacting made by selective laser melting, Industrial & Engineering Chemistry Research, vol. 59, pp. 3736–3743, 2020.

[56] N. Ahmed, I. Barsoum, G. Haidemenopoulos, and R. Abu Al-Rub, Process parameter selection and optimization of laser powder bed fusion for 316l stainless steel: A review, Journal of Manufacturing Processes, vol. 75, pp. 415–434, 2022. DOI: 10.1016/j.jmapro.2021.12.064.

[57] N. Guo and C. L. Ming, Additive manufacturing: Technology, applications and research needs, Frontiers of Mechanical Engineering, vol. 8, no. 3, pp. 215–243, 2013. DOI: doi:10.1007/s11465-013-0248-8.

[58] S. Barut Gök, E. Vetter, L. Kromm, E. Hansjosten, A. Hensel, V. Gräf, and M. Stahl, Inactivation of e. coli and l. innocua in milk by a thin film uv-c reactor modified with flow guiding elements (fge), International journal of food microbiology, vol. 343, p. 109 105, 2021. DOI: 10.1016/j.ijfoodmicro.2021.109105.

[59] B. Hirt, E. Hansjosten, A. Hensel, V. Gräf, and M. Stahl, Improvement of an annular thin film uv-c reactor by fluid guiding elements, Innovative Food Science & Emerging Technologies, vol. 77, p. 102 988, 2022. DOI: 10.1016/j.ifset.2022.102988.

[60] M. Gonzalez-Castano, F. Baena-Moreno, J. Navarro de Miguel, K. U. M. Miah, F. Arroyo-Torralvo, R. Ossenbrink, J. A. Odriozola, W. Benzinger, A. Hensel, A. Wenka, and H. Arellano-García, 3d-printed structured catalysts for co2 methanation reaction: Advancing of gyroid-based geometries, Energy Conversion and Management, vol. 258, 2022. DOI: 10.1016/j.enconman.2022.115464.

[61] S. K. Hubadillah, Z. S. Tai, M. H. D. Othman, Z. Harun, M. R. Jamalludin, M. A. Rahman, J. Jaafar, and A. F. Ismail, Hydrophobic ceramic membrane for membrane distillation: A mini review on preparation, characterization, and applications, Separation and Purification Technology, vol. 217, pp. 71–84, 2019. DOI: 10.1016/j.seppur.2019.02.014.

[62] S. Parani and O. S. Oluwafemi, Membrane distillation: Recent configurations, membrane surface engineering, and applications, Membranes, vol. 11, no. 12, 2021. DOI: 10.3390/membranes11120934.

[63] N. A. Ahmad, C. P. Leo, A. L. Ahmad, and W. K. W. Ramli, Membranes with Great Hydrophobicity: A Review on Preparation and Characterization, Separation & Purification Reviews, vol. 44, no. 2, pp. 109–134, 2015. DOI: 10.1080/15422119.2013.848816.

[64] B. Zhu, M. Duke, L. F. Dumée, A. Merenda, E. Des Ligneris, L. Kong, P. D. Hodgson, and S. Gray, Short review on porous metal membranes-fabrication, commercial products, and applications, Membranes, vol. 8, no. 3, 2018. DOI: 10.3390/membranes8030083.

[65] K.-Y. Law and H. Zhao, Surface wetting: Characterization, contact angle, and fundamentals. Cham: Springer International Publishing AG, 2015, ISBN: 978-3-319-25214-8.

[66] H. Reiss, Warum gibt es benetzung?, Physik in unserer Zeit, vol. 23, no. 5, pp. 204–212, 1992. DOI: 10.1002/piuz.19920230507.

[67] K.-Y. Law, Definitions for hydrophilicity, hydrophobicity, and superhydrophobicity: Getting the basics right, The journal of physical chemistry letters, vol. 5, no. 4, pp. 686–688, 2014. DOI: 10.1021/jz402762h.

[68] M. Marengo and J. de Coninck, Eds., The Surface Wettability Effect on Phase Change, 1st ed. 2022. Cham: Springer International Publishing and Springer, 2022, ISBN: 978-3-030-82992-6.

[69] F. Rupp, L. Scheideler, and J. Geis-Gerstorfer, Effect of heterogenic surfaces on contact angle hysteresis: Dynamic contact angle analysis in material sciences, Chemical Engineering & Technology, vol. 25, no. 9, pp. 877–882, 2002. DOI: 10.1002/1521-4125(20020910)25:9<877::AID-CEAT877>3.0.CO;2-D.

[70] T.-Y. Kim, B. Ingmar, K. Bewilogua, K. H. Oh, and K.-R. Lee, Wetting behaviours of a-C:H:Si:O film coated nano-scale dual rough surface, Chemical Physics Letters, vol. 436, no. 1-3, pp. 199–203, 2007. DOI: 10.1016/j.cplett.2007.01.036.

[71] Y.-J. Sheng, S. Jiang, and H.-K. Tsao, Effects of geometrical characteristics of surface roughness on droplet wetting, The Journal of chemical physics, vol. 127, no. 23, p. 234 704, 2007. DOI: 10.1063/1.2804425.

[72] R. N. Wenzel, Surface roughness and contact angle, The Journal of Physical and Colloid Chemistry, vol. 53, no. 9, pp. 1466–1467, 1949. DOI: 10.1021/j150474a015.

[73] A. B. D. Cassie and S. Baxter, Wettability of porous surfaces, Transactions of the Faraday Society, vol. 40, p. 546, 1944. DOI: 10.1039/TF9444000546.

[74] G. Nagayama and D. Zhang, Intermediate wetting state at nano/microstructured surfaces, Soft matter, vol. 16, no. 14, pp. 3514–3521, 2020. DOI: 10.1039/c9sm02513h.

[75] G. Rácz, S. Kerker, Z. Kovács, G. Vatai, M. Ebrahimi, and P. Czermak, Theoretical and experimental approaches of liquid entry pressure determination in membrane distillation processes, Periodica Polytechnica Chemical Engineering, vol. 58, no. 2, pp. 81–91, 2014. DOI: 10.3311/PPch.2179.

[76] J. Ge, Y. Peng, Z. Li, P. Chen, and S. Wang, Membrane fouling and wetting in a dcmd process for ro brine concentration, Desalination, vol. 344, pp. 97–107, 2014. DOI: 10.1016/j.desal.2014.03.017.

[77] S. Mettu, M. Kanungo, and K.-Y. Law, Anomalous thermally induced pinning of a liquid drop on a solid substrate, Langmuir, vol. 29, no. 34, pp. 10 665–10 673, 2013. DOI: 10.1021/la400991y.

[78] H. Chamani, J. Woloszyn, T. Matsuura, D. Rana, and C. Q. Lan, Pore wetting in membrane distillation: A comprehensive review, Progress in Materials Science, vol. 122, p. 100 843, 2021. DOI: 10.1016/j.pmatsci.2021.100843.

[79] A. Franken, J. Nolten, M. Mulder, D. Bargeman, and C. A. Smolders, Wetting criteria for the applicability of membrane distillation, Journal of Membrane Science, vol. 33, no. 3, pp. 315–328, 1987. DOI: 10.1016/S0376-7388(00)80288-4.

[80] F. Varela-Corredor and S. Bandini, Advances in water breakthrough measurement at high temperature in macroporous hydrophobic ceramic/polymeric membranes, Journal of Membrane Science, vol. 565, pp. 72–84, 2018. DOI: 10.1016/j.memsci.2018.08.005.

[81] M. Rezaei, D. M. Warsinger, J. H. Lienhard V, M. C. Duke, T. Matsuura, and W. M. Samhaber, Wetting phenomena in membrane distillation: Mechanisms, reversal, and prevention, Water research, vol. 139, pp. 329–352, 2018. DOI: 10.1016/j.watres.2018.03.058.

[82] H. Chang, B. Liu, Z. Zhang, R. Pawar, Z. Yan, J. C. Crittenden, and R. D. Vidic, A critical review of membrane wettability in membrane distillation from the perspective of interfacial interactions, Environmental science & technology, vol. 55, no. 3, pp. 1395–1418, 2021. DOI: 10.1021/acs.est.0c05454.

[83] N. B. Vargaftik, B. N. Volkov, and L. D. Voljak, International tables of the surface tension of water, Journal of Physical and Chemical Reference Data, vol. 12, no. 3, pp. 817–820, 1983. DOI: 10.1063/1.555688.

[84] A. Alkhudhiri, N. Darwish, and N. Hilal, Membrane distillation: A comprehensive review, Desalination, vol. 287, pp. 2–18, 2012. DOI: 10.1016/j.desal.2011.08.027.

[85] M. R. Rahimpour and M. A. Esmaeilbeig, Membrane wetting in membrane distillation, in Current Trends and Future Developments on (Bio-) Membranes, A. Basile, A. Cassano, and N. Rastogi, Eds., Elsevier, 2019, pp. 143–174, ISBN: 9780128135518. DOI: 10.1016/b978-0-12-813551-8.00006-1.

[86] R. B. Saffarini, B. Mansoor, R. Thomas, and H. A. Arafat, Effect of temperature-dependent microstructure evolution on pore wetting in ptfe membranes under membrane distillation conditions, Journal of Membrane Science, vol. 429, pp. 282–294, 2013. DOI: 10.1016/j.memsci.2012.11.049.

[87] E. Guillen-Burrieza, A. Servi, B. S. Lalia, and H. A. Arafat, Membrane structure and surface morphology impact on the wetting of md membranes, Journal of Membrane Science, vol. 483, pp. 94–103, 2015. DOI: 10.1016/j.memsci.2015.02.024.

[88] F. F. Zha, A. G. Fane, C. Fell, and R. W. Schofield, Critical displacement pressure of a supported liquid membrane, Journal of Membrane Science, vol. 75, no. 1-2, pp. 69–80, 1992. DOI: 10.1016/0376-7388(92)80007-7.

[89] K. Smolders and A. Franken, Terminology for membrane distillation, Desalination, vol. 72, no. 3, pp. 249–262, 1989. DOI: 10.1016/0011-9164(89)80010-4.

[90] A. Luo and N. Lior, Study of advancement to higher temperature membrane distillation, Desalination, vol. 419, pp. 88–100, 2017. DOI: 10.1016/j.desal.2017.05.020.

[91] M. C. García-Payo, M. A. Izquierdo-Gil, and C. Fernández-Pineda, Wetting study of hydrophobic membranes via liquid entry pressure measurements with aqueous alcohol solutions, Journal of colloid and interface science, vol. 230, no. 2, pp. 420–431, 2000. DOI: 10.1006/jcis.2000.7106.

[92] E. Guillen-Burrieza, M. O. Mavukkandy, M. R. Bilad, and H. A. Arafat, Understanding wetting phenomena in membrane distillation and how operational parameters can affect it, Journal of Membrane Science, vol. 515, pp. 163–174, 2016. DOI: 10.1016/j.memsci.2016.05.051.

[93] F. Varela-Corredor and S. Bandini, Testing the applicability limits of a membrane distillation process with ceramic hydrophobized membranes: The critical wetting temperature, Separation and Purification Technology, vol. 250, p. 117 205, 2020. DOI: 10.1016/j.seppur.2020.117205.

[94] J. Zuo and T.-S. Chung, Metal–organic framework-functionalized alumina membranes for vacuum membrane distillation, Water, vol. 8, no. 12, p. 586, 2016. DOI: 10.3390/w8120586.

[95] J. Schnittger, M. Weyd, I. Voigt, and A. Lerch, Keramische membranen in der membrandestillation, Chemie Ingenieur Technik, vol. 91, no. 8, pp. 1101–1109, 2019. DOI: 10.1002/cite.201900037.

[96] J. Kujawa, W. Kujawski, S. Koter, K. Jarzynka, A. Rozicka, K. Bajda, S. Cerneaux, M. Persin, and A. Larbot, Membrane distillation properties of tio 2 ceramic membranes modified by perfluoroalkylsilanes, Desalination and Water Treatment, vol. 51, no. 7-9, pp. 1352–1361, 2013. DOI: 10.1080/19443994.2012.704976.

[97] M. Khayet and T. Matsuura, Preparation and characterization of polyvinylidene fluoride membranes for membrane distillation, Industrial & Engineering Chemistry Research, vol. 40, no. 24, pp. 5710–5718, 2001. DOI: 10.1021/ie010553y.

[98] J. Hereijgers, T. Breugelmans, and W. de Malsche, Breakthrough in a flat channel membrane microcontactor, Chemical Engineering Research and Design, vol. 94, pp. 98–104, 2015. DOI: 10.1016/j.cherd.2014.12.004.

[99] M. C. Garcıa-Payo, M. Essalhi, and M. Khayet, Effects of PVDF-HFP concentration on membrane distillation performance and structural morphology of hollow fiber membranes, Journal of Membrane Science, vol. 347, no. 1-2, pp. 209–219, 2010. DOI: 10.1016/j.memsci.2009.10.026.

[100] K. W. Lawson and D. R. Lloyd, Membrane distillation, Journal of Membrane Science, vol. 124, no. 1, pp. 1–25, 1997. DOI: 10.1016/S0376-7388(96)00236-0.

[101] W. Kujawski, S. Krajewska, M. Kujawski, L. Gazagnes, A. Larbot, and M. Persin, Pervaporation properties of fluoroalkylsilane (fas) grafted ceramic membranes, Desalination, vol. 205, no. 1-3, pp. 75–86, 2007. DOI: 10.1016/j.desal.2006.04.042.

[102] J. Cai and F. Guo, Mass transfer during membrane distillation treatment of wastewater from hot-dip galvanization, Separation and Purification Technology, vol. 235, p. 116 164, 2020. DOI: 10.1016/j.seppur.2019.116164.

[103] A. T. Servi, J. Kharraz, D. Klee, K. Notarangelo, B. Eyob, E. Guillen-Burrieza, A. Liu, H. A. Arafat, and K. K. Gleason, A systematic study of the impact of hydrophobicity on the wetting of md membranes, Journal of Membrane Science, vol. 520, pp. 850–859, 2016. DOI: 10.1016/j.memsci.2016.08.021.

[104] L. García-Fernández, M. C. Garcıa-Payo, and M. Khayet, Effects of mixed solvents on the structural morphology and membrane distillation performance of PVDF-HFP hollow fiber membranes, Journal of Membrane Science, vol. 468, pp. 324–338, 2014. DOI: 10.1016/j.memsci.2014.06.014.

[105] M. C. Duke, S. Mee, and J. C. D. da Costa, Performance of porous inorganic membranes in non-osmotic desalination, Water research, vol. 41, no. 17, pp. 3998–4004, 2007. DOI: 10.1016/j.watres.2007.05.028.

[106] K. He, H. J. Hwang, and I. S. Moon, Air gap membrane distillation on the different types of membrane, Korean Journal of Chemical Engineering, vol. 28, no. 3, pp. 770–777, 2011. DOI: 10.1007/s11814-010-0415-0.

[107] D. M. Warsinger, A. Servi, G. B. Connors, M. O. Mavukkandy, H. A. Arafat, K. K. Gleason, and J. H. Lienhard V, Reversing membrane wetting in membrane distillation: Comparing dryout to backwashing with pressurized air, Environmental Science: Water Research & Technology, vol. 3, no. 5, pp. 930–939, 2017. DOI: 10.1039/c7ew00085e.

[108] Y. Lee, J. Jeong, I. J. Youn, and W. H. Lee, Modified liquid displacement method for determination of pore size distribution in porous membranes, Journal of Membrane Science, vol. 130, no. 1-2, pp. 149–156, 1997. DOI: 10.1016/S0376-7388(97)00017-3.

[109] K. S. McGuire, K. W. Lawson, and D. R. Lloyd, Pore size distribution determination from liquid permeation through microporous membranes, Journal of Membrane Science, vol. 99, no. 2, pp. 127–137, 1995. DOI: 10.1016/0376-7388(94)00209-H.

[110] M. S. El-Bourawi, Z. Ding, R. Ma, and M. Khayet, A framework for better understanding membrane distillation separation process, Journal of Membrane Science, vol. 285, no. 1-2, pp. 4–29, 2006. DOI: 10.1016/j.memsci.2006.08.002.

[111] M. Khayet and T. Matsuura, Membrane Distillation: Principles and Applications. Amsterdam, The Netherlands: Elsevier, 2011, ISBN: 9780444531261. DOI: 10.1016/C2009-0-17487-1.

[112] J. Schnittger, J. McCutcheon, T. Hoyer, M. Weyd, G. Fischer, P. Puhlfürß, M. Halisch, I. Voigt, and A. Lerch, Hydrophobic ceramic membranes in md processes – impact of material selection and layer characteristics, Journal of Membrane Science, vol. 618, p. 118 678, 2021. DOI: 10.1016/j.memsci.2020.118678.

[113] L. Basini, G. D'Angelo, M. Gobbi, G. C. Sarti, and C. Gostoli, A desalination process through sweeping gas membrane distillation, Desalination, vol. 64, pp. 245–257, 1987. DOI: 10.1016/0011-9164(87)90100-7.

[114] A. K. Thakur, I.-M. Hsieh, M. R. Islam, B. Lin, C.-C. Chen, and M. Malmali, Performance of sweeping gas membrane distillation for treating produced water: Modeling and experiments, Desalination, vol. 492, 2020. DOI: 10.1016/j.desal.2020.114597.

[115] I. N. Floros, E. P. Kouvelos, G. I. Pilatos, E. P. Hadjigeorgiou, A. D. Gotzias, E. P. Favvas, and A. A. Sapalidis, Enhancement of flux performance in ptfe membranes for direct contact membrane distillation, Polymers, vol. 12, no. 2, 2020. DOI: 10.3390/polym12020345.

[116] D. Singh and K. K. Sirkar, Desalination of brine and produced water by direct contact membrane distillation at high temperatures and pressures, Journal of Membrane Science, vol. 389, pp. 380–388, 2012. DOI: 10.1016/j.memsci.2011.11.003.

[117] A. Khalifa, H. Ahmad, M. Antar, T. Laoui, and M. Khayet, Experimental and theoretical investigations on water desalination using direct contact membrane distillation, Desalination, vol. 404, pp. 22–34, 2017. DOI: 10.1016/j.desal.2016.10.009.

[118] C. H. Lee and W. H. Hong, Effect of operating variables on the flux and selectivity in sweep gas membrane distillation for dilute aqueous isopropanol, Journal of Membrane Science, vol. 188, no. 1, pp. 79–86, 2001. DOI: 10.1016/S0376-7388(01)00373-8.

[119] M. Tomaszewska, M. Gryta, and A. W. Morawski, Study on the concentration of acids by membrane distillation, Journal of Membrane Science, vol. 102, pp. 113–122, 1995. DOI: 10.1016/0376-7388(94)00281-3.

[120] M. Tomaszewska, Concentration and purification of fluosilicic acid by membrane distillation, Industrial & Engineering Chemistry Research, vol. 39, no. 8, pp. 3038–3041, 2000. DOI: 10.1021/ie9908534.

[121] M. Khayet, Direct contact membrane distillation of humic acid solutions, Journal of Membrane Science, vol. 240, no. 1-2, pp. 123–128, 2004. DOI: 10.1016/j.memsci.2004.04.018.

[122] M. A. Izquierdo-Gil, M. C. Garcıa-Payo, and C. Fernández-Pineda, Air gap membrane distillation of sucrose aqueous solutions, Journal of Membrane Science, vol. 155, no. 2, pp. 291–307, 1999. DOI: 10.1016/S0376-7388(98)00323-8.

[123] M. A. Izquierdo-Gil, M. C. García-Payo, and C. Fernández-Pineda, Direct contact membrane distillation of sugar aqueous solutions, Separation Science and Technology, vol. 34, no. 9, pp. 1773–1801, 1999. DOI: 10.1081/SS-100100738.

[124] S. Al-Asheh, F. Banat, M. Qtaishat, and M. Al-Khateeb, Concentration of sucrose solutions via vacuum membrane distillation, Desalination, vol. 195, no. 1-3, pp. 60–68, 2006. DOI: 10.1016/j.desal.2005.10.036.

[125] V.D. Alves and I. M. Coelhoso, Orange juice concentration by osmotic evaporation and membrane distillation: A comparative study, Journal of Food Engineering, vol. 74, no. 1, pp. 125–133, 2006. DOI: 10.1016/j.jfoodeng.2005.02.019.

[126] P. M. Duyen, P. Jacob, R. Rattanaoudom, and C. Visvanathan, Feasibility of sweeping gas membrane distillation on concentrating triethylene glycol from waste streams, Chemical Engineering and Processing: Process Intensification, vol. 110, pp. 225–234, 2016. DOI: 10.1016/j.cep.2016.10.015.

[127] M. M. A. Shirazi, A. Kargari, M. Tabatabaei, A. F. Ismail, and T. Matsuura, Concentration of glycerol from dilute glycerol wastewater using sweeping gas membrane distillation, Chemical Engineering and Processing: Process Intensification, vol. 78, pp. 58–66, 2014. DOI: 10.1016/j.cep.2014.02.002.

[128] S. Shukla, N. E. Benes, I. Vankelecom, J. P. Méricq, M. P. Belleville, N. Hengl, and J. S. Marcano, Sweep gas membrane distillation in a membrane contactor with metallic hollow-fibers, Journal of Membrane Science, vol. 493, pp. 167–178, 2015. DOI: 10.1016/j.memsci.2015.06.040.

[129] S. O. Olatunji and L. M. Camacho, Heat and mass transport in modeling membrane distillation configurations: A review, Frontiers in Energy Research, vol. 6, 2018. DOI: 10.3389/fenrg.2018.00130.

[130] B. B. Ashoor, S. Mansour, A. Giwa, V. Dufour, and S. W. Hasan, Principles and applications of direct contact membrane distillation (DCMD): A comprehensive review, Desalination, vol. 398, pp. 222–246, 2016. DOI: 10.1016/j.desal.2016.07.043.

[131] C. Rivier, Separation of binary mixtures by thermostatic sweeping gas membrane distillation i. theory and simulations, Journal of Membrane Science, vol. 201, no. 1-2, pp. 1–16, 2002. DOI: 10.1016/S0376-7388(01)00648-2.

[132] M. Garcıa-Payo, C. Rivier, I. Marison, and U. von Stockar, Separation of binary mixtures by thermostatic sweeping gas membrane distillation, Journal of Membrane Science, vol. 198, no. 2, pp. 197–210, 2002. DOI: 10.1016/S0376-7388(01)00649-4.

[133] M. Khayet, M. P. Godino, and J. I. Mengual, Theoretical and experimental studies on desalination using the sweeping gas membrane distillation method, Desalination, vol. 157, no. 1-3, pp. 297–305, 2003. DOI: 10.1016/S0011-9164(03)00409-0.

[134] C. Boi, S. Bandini, and G. C. Sarti, Pollutants removal from wastewaters through membrane distillation, Desalination, vol. 183, no. 1-3, pp. 383–394, 2005. DOI: 10.1016/j.desal.2005.03.041.

[135] M. Khayet, C. Cojocaru, and A. Baroudi, Modeling and optimization of sweeping gas membrane distillation, Desalination, vol. 287, pp. 159–166, 2012. DOI: 10.1016/j.desal.2011.04.070.

[136] S. Shukla, Membrane distillation with porous metal hollow fibers for the concentration of thermo-sensitive solutions, Ph.D. dissertation, University of Montpellier, University of Twente, KU Leuven, 2014.

[137] A. M. Alklaibi and N. Lior, Membrane-distillation desalination: Status and potential, Desalination, vol. 171, no. 2, pp. 111–131, 2005. DOI: 10.1016/j.desal.2004.03.024.

[138] D. Singh and K. K. Sirkar, High temperature direct contact membrane distillation based desalination using ptfe hollow fibers, Chemical Engineering Science, vol. 116, pp. 824–833, 2014. DOI: 10.1016/j.ces.2014.05.042.

[139] M. Boukhriss, M. B. Ben Hmida, M. A. Maatoug, K. Zarzoum, R. Marzouki, and H. Ben Bacha, The design of a unit sweeping gas membrane distillation: Experimental study on a membrane and operating parameters, Applied Water Science, vol. 10, no. 5, 2020. DOI: 10.1007/s13201-020-01194-3.

[140] L. Martınez-Dıez and M. Vázquez-González, Temperature and concentration polarization in membrane distillation of aqueous salt solutions, Journal of Membrane Science, vol. 156, no. 2, pp. 265–273, 1999. DOI: 10.1016/S0376-7388(98)00349-4.

[141] A. Mourgues, N. Hengl, M. P. Belleville, D. Paolucci-Jeanjean, and J. Sanchez, Membrane contactor with hydrophobic metallic membranes: 1. modeling of coupled mass and heat transfers in membrane evaporation, Journal of Membrane Science, vol. 355, no. 1-2, pp. 112–125, 2010. DOI: 10.1016/j.memsci.2010.02.040.

[142] K. Nikolaus, Trink- und reinstwassergewinnung mittels membrandestillation, Ph.D. dissertation, Techn. Univ. Kaiserslautern, Kaiserslautern, 2013.

[143] M. Khayet, P. Godino, and J. I. Mengual, Nature of flow on sweeping gas membrane distillation, Journal of Membrane Science, vol. 170, no. 2, pp. 243–255, 2000. DOI: 10.1016/S0376-7388(99)00369-5.

[144] Ó. Andrjesdóttir, C. L. Ong, M. Nabavi, S. Paredes, A. Khalil, B. Michel, and D. Poulikakos, An experimentally optimized model for heat and mass transfer in direct contact membrane distillation, International Journal of Heat and Mass Transfer, vol. 66, pp. 855–867, 2013. DOI: 10.1016/j.ijheatmasstransfer.2013.07.051.

[145] I. Hitsov, T. Maere, K. de Sitter, C. Dotremont, and I. Nopens, Modelling approaches in membrane distillation: A critical review, Separation and Purification Technology, vol. 142, pp. 48–64, 2015. DOI: 10.1016/j.seppur.2014.12.026.

[146] M. Khayet, Membranes and theoretical modeling of membrane distillation: A review, Advances in colloid and interface science, vol. 164, no. 1-2, pp. 56–88, 2011. DOI: 10.1016/j.cis.2010.09.005.

[147] R. Bouchrit, A. Boubakri, A. Hafiane, and S. A.-T. Bouguecha, Direct contact membrane distillation: Capability to treat hyper-saline solution, Desalination, vol. 376, pp. 117–129, 2015. DOI: 10.1016/j.desal.2015.08.014.

[148] M. Khayet, P. Godino, and J. I. Mengual, Theory and experiments on sweeping gas membrane distillation, Journal of Membrane Science, vol. 165, no. 2, pp. 261–272, 2000. DOI: 10.1016/S0376-7388(99)00236-7.

[149] E. N. Fuller, P. D. Schettler, and J. C. Giddings, New method for prediction of binary gas-phase diffusion coefficients, Industrial & Engineering Chemistry, vol. 58, no. 5, pp. 18–27, 1966. DOI: 10.1021/IE50677A007.

[150] A. Mersmann, Stoffübertragung (Wärme- und Stoffübertragung). Berlin et al.: Springer, 1986, ISBN: 3-540-15920-7.

[151] M. Khayet, M. P. Godino, and J. I. Mengual, Thermal boundary layers in sweeping gas membrane distillation processes, AIChE Journal, vol. 48, no. 7, pp. 1488–1497, 2002. DOI: 10.1002/aic.690480713.

[152] V. Gnielinski, Wärmeübertragung im konzentrischen Ringspalt und im ebenen Spalt, in VDI-Wärmeatlas, P. Stephan, S. Kabelac, M. Kind, D. Mewes, K. Schaber, and T. Wetzel, Eds., Springer Verlag Berlin, pp. 793–800, ISBN: 978-3-662-52988-1.

[153] N. Kockmann, Transport Phenomena in Micro Process Engineering. Heidelberg: Springer Verlag Berlin, 2018, ISBN: 978-3-540-74616-4. DOI: 10.1007/978-3-540-74618-8.

[154] J. Phattaranawik, R. Jiraratananon, and A. Fane, Heat transport and membrane distillation coefficients in direct contact membrane distillation, Journal of Membrane Science, vol. 212, no. 1-2, pp. 177–193, 2003. DOI: 10.1016/S0376-7388(02)00498-2.

[155] S. Claramunt, P. V. Schell, M. Kraut, B. F. Stengel, C. F. Kuesters, and R. Dittmeyer, Process intensification in a double-pipe reactor with additively manufactured internal inserts, ChemEngineering, no. (submitted), 2022.

[156] International Organization for Standardization, Starch derivatives — determination of the composition of glucose syrups, fructose syrups and hydrogenated glucose syrups: Method using high-performance liquid chromatography, 2013-09-01. [Online]. Available: https://www.iso.org/standard/50792.html.

[157] S. Kasap and P. Capper, Springer Handbook of Electronic and Photonic Materials. Cham: Springer International Publishing, 2017, ISBN: 978-3-319-48931-5. DOI: 10.1007/978-3-319-48933-9.

[158] A. C. Jones and M. L. Hitchman, Chemical vapour deposition: Precursors, processes and applications / edited by Anthony C. Jones and Michael L. Hitchman, Precursors, processes and applications ed. Cambridge: Royal Society of Chemistry, 2009, ISBN: 978-0-85404-465-8.

[159] A. C. Jones and P. O'Brien, CVD of compound semiconductors: Precursor synthesis, development and applications / Anthony C. Jones, Paul O'Brien. Weinheim and Cambridge: VCH, 1997, ISBN: 9783527292943.

[160] P. Bankovic, N. R. Demarquette, and M. da Silva, Obtention of selective membranes for water and hydrophobic liquids by plasma enhanced chemical vapor deposition on porous substrate, Materials Science and Engineering: B, vol. 112, no. 2, pp. 165–170, 2004. DOI: 10.1016/j.mseb.2004.05.026.

[161] J. Robertson, Diamond-like amorphous carbon, Materials Science and Engineering: R: Reports, vol. 37, no. 4, pp. 129–281, 2002. DOI: 10.1016/S0927-796X(02)00005-0.

[162] K. Bewilogua, I. Bialuch, H. Ruske, and K. Weigel, Preparation of a-C:H/a-C:H:Si:O and a-C:H/a-C:H:Si multilayer coatings by pacvd, Surface & Coatings Technology, vol. 206, no. 4, pp. 623–629, 2011. DOI: 10.1016/j.surfcoat.2011.02.020.

[163] R. G. Turri, R. M. Santos, E. C. Rangel, N. C. da Cruz, J. R. Bortoleto, Dias da Silva, José H., C. A. Antonio, and S. F. Durrant, Optical, mechanical and surface properties of amorphous carbonaceous thin films obtained by plasma enhanced chemical vapor deposition and plasma immersion ion implantation and deposition, Applied Surface Science, vol. 280, pp. 474–481, 2013. DOI: 10.1016/j.apsusc.2013.05.013.

[164] R. M. Santos, R. Turri, E. C. Rangel, N. C. da Cruz, W. Schreiner, C. U. Davanzo, and S. F. Durrant, Diverse amorphous carbonaceous thin films obtained by plasma enhanced chemical vapor deposition and plasma immersion ion implantation and deposition, Physics Procedia, vol. 32, pp. 48–57, 2012. DOI: 10.1016/j.phpro.2012.03.517.

[165] N. Guermat, A. Bellel, S. Sahli, Y. Segui, and P. Raynaud, Thin plasma-polymerized layers of hexamethyldisiloxane for humidity sensor development, Thin Solid Films, vol. 517, no. 15, pp. 4455–4460, 2009. DOI: 10.1016/j.tsf.2009.01.084.

[166] M. Grischke, A. Hieke, F. Morgenweck, and H. Dimigen, Variation of the wettability of dlc-coatings by network modification using silicon and oxygen, Diamond and Related Materials, vol. 7, no. 2, pp. 454–458, 1998. DOI: 10.1016/S0925-9635(97)00237-9.

[167] K. M. Dyrda, F. Grinschek, G. Rabsch, K. Haas-Santo, and R. Dittmeyer, Development of a microsieve based micro contactor for gas/liquid phase separation, Separation and Purification Technology, vol. 220, pp. 238–249, 2019. DOI: 10.1016/j.seppur.2019.03.016.

[168] A. Sonnenfeld, T. M. Tun, L. Zajíčková, K. V. Kozlov, H.-E. Wagner, J. F. Behnke, and R. Hippler, Deposition process based on organosilicon precursors in dielectric barrier discharges at atmospheric pressure. a comparison. Plasmas and Polymers, vol. 6, no. 4, pp. 237–266, 2001. DOI: 10.1023/A:1014414016164.

[169] S. A. Kulinich and M. Farzaneh, Hydrophobic properties of surfaces coated with fluoroalkylsiloxane and alkylsiloxane monolayers, Surface Science, vol. 573, no. 3, pp. 379–390, 2004. DOI: 10.1016/j.susc.2004.10.008.

[170] J. Lu, Y. Yu, J. Zhou, L. Song, X. Hu, and A. Larbot, FAS grafted superhydrophobic ceramic membrane, Applied Surface Science, vol. 255, no. 22, pp. 9092–9099, 2009. DOI: 10.1016/j.apsusc.2009.06.112.

[171] T. Schneller, Ed., Chemical solution deposition of functional oxide thin films. Wien: Springer, 2013, ISBN: 978-3-211-99311-8.

[172] M. N. Rahaman, Ceramic Processing and Sintering. CRC Press, 2017, ISBN: 9781315274126. DOI: 10.1201/9781315274126.

[173] F. Zhang, S. Chen, L. Dong, Y. Lei, T. Liu, and Y. Yin, Preparation of superhydrophobic films on titanium as effective corrosion barriers, Applied Surface Science, vol. 257, no. 7, pp. 2587–2591, 2011. DOI: 10.1016/j.apsusc.2010.10.027.

[174] S. Rasouli, N. Rezaei, H. Hamedi, S. Zendehboudi, and X. Duan, Design, fabrication, and characterization of a facile superhydrophobic and superoleophilic mesh-based membrane for selective oil-water separation, Chemical Engineering Science, vol. 236, p. 116 354, 2021. DOI: 10.1016/j.ces.2020.116354.

[175] I. Bernagozzi, C. Antonini, F. Villa, and M. Marengo, Fabricating superhydrophobic aluminum: An optimized one-step wet synthesis using fluoroalkyl silane, Colloids and Surfaces A: Physicochemical and Engineering Aspects, vol. 441, pp. 919–924, 2014. DOI: 10.1016/j.colsurfa.2013.05.042.

[176] A. Y. Fadeev and T. J. McCarthy, Self-assembly is not the only reaction possible between alkyltrichlorosilanes and surfaces: Monomolecular and oligomeric covalently attached layers of dichloro- and trichloroalkylsilanes on silicon, Langmuir, vol. 16, no. 18, pp. 7268–7274, 2000. DOI: 10.1021/la000471z.

[177] Y. W. Hu, H. R. He, and Y. M. Ma, Preparation of superhydrophobic SiO_2 coating on stainless steel substrate, Key Engineering Materials, vol. 512-515, pp. 1028–1031, 2012. DOI: 10.4028/www.scientific.net/kem.512-515.1028.

[178] ISO International Organization for Standardization, Geometrical product specifications (GPS) — Surface texture: Areal: Part 2: Terms, definitions and surface texture parameters, Geneva, 2021.

[179] ISO International Organization for Standardization, Paints and varnishes -Wettability: Part 2: determination of surface free energy of solid surfaces by measurement of contact angle, Geneva, 2017.

[180] P. Shi, H. Shi, C. Liu, and M. Jiang, Effect of pickling process on removal of oxide layer on the surface of ferritic stainless steel, Canadian Metallurgical Quarterly, vol. 57, no. 2, pp. 168–175, 2018. DOI: 10.1080/00084433.2017.1405540.

[181] M. Pantoja, F. Velasco, J. Abenojar, and M. A. Martinez, Development of superhydrophobic coatings on AISI 304 austenitic stainless steel with different surface pretreatments, Thin Solid Films, vol. 671, pp. 22–30, 2019. DOI: 10.1016/j.tsf.2018.12.016.

[182] E. L. Decker and S. Garoff, Contact line structure and dynamics on surfaces with contact angle hysteresis, Langmuir, vol. 13, no. 23, pp. 6321–6332, 1997. DOI: 10.1021/la970528q.

[183] I. Esih, V. Alar, and I. Juraga, Influence of thermal oxides on pitting corrosion of stainless steel in chloride solutions, Corrosion Engineering, Science and Technology, vol. 40, no. 2, pp. 110–120, 2005. DOI: 10.1179/174327805x46977.

[184] R. L. Higginson, C. P. Jackson, E. L. Murrell, P. A. Z. Exworthy, R. J. Mortimer, D. R. Worrall, and G. D. Wilcox, Effect of thermally grown oxides on colour development of stainless steel, Materials at High Temperatures, vol. 32, no. 1-2, pp. 113–117, 2015. DOI: 10.1179/0960340914Z.00000000083.

[185] L. Li, V. Breedveld, and D. W. Hess, Creation of superhydrophobic stainless steel surfaces by acid treatments and hydrophobic film deposition, ACS applied materials & interfaces, vol. 4, no. 9, pp. 4549–4556, 2012. DOI: 10.1021/am301666c.

[186] S. Claramunt, F. Völker, U. Gerhards, M. Kraut, and R. Dittmeyer, Membranes for the gas/liquid phase separation at elevated temperatures: Characterization of the liquid entry pressure, Membranes, vol. 11, no. 12, 2021. DOI: 10.3390/membranes11120907.

[187] H. Chamani, P. Yazgan-Birgi, T. Matsuura, D. Rana, M. I. Hassan Ali, H. A. Arafat, and C. Q. Lan, CFD-based genetic programming model for liquid entry pressure estimation of hydrophobic membranes, Desalination, vol. 476, p. 114 231, 2020. DOI: 10.1016/j.desal.2019.114231.

[188] J. D. Bernardin, I. Mudawar, C. B. Walsh, and E. I. Franses, Contact angle temperature dependence for water droplets on practical aluminum surfaces, International Journal of Heat and Mass Transfer, vol. 40, no. 5, pp. 1017–1033, 1997. DOI: 10.1016/0017-9310(96)00184-6.

[189] F. Petke and B. Ray, Temperature dependence of contact angles of liquids on polymeric solids, Journal of Colloid and Interface Science, vol. 31, no. 2, pp. 216–227, 1969. DOI: 10.1016/0021-9797(69)90329-4.

[190] R. Massoudi and A. D. King, Effect of pressure on the surface tension of water. adsorption of low molecular weight gases on water at 25.deg, The Journal of Physical and Colloid Chemistry, vol. 78, no. 22, pp. 2262–2266, 1974. DOI: 10.1021/j100615a017.

[191] J.-W. Song, M.-C. Ma, and L.-W. Fan, Understanding the temperature dependence of contact angles of water on a smooth hydrophobic surface under pressurized conditions: An experimental study, Langmuir: the ACS journal of surfaces and colloids, vol. 36, no. 32, pp. 9586–9595, 2020. DOI: 10.1021/acs.langmuir.0c01671.

[192] J.-W. Song, D.-L. Zeng, and L.-W. Fan, Temperature dependence of contact angles of water on a stainless steel surface at elevated temperatures and pressures: In situ characterization and thermodynamic analysis, Journal of colloid and interface science, vol. 561, pp. 870–880, 2020. DOI: 10.1016/j.jcis.2019.11.070.

[193] J. Pátek, M. Součková, and J. Klomfar, Generation of recommendable values for the surface tension of water using a nonparametric regression, Journal of Chemical & Engineering Data, vol. 61, no. 2, pp. 928–935, 2016. DOI: 10.1021/acs.jced.5b00776.

[194] L. Eykens, K. de Sitter, C. Dotremont, L. Pinoy, and B. van der Bruggen, How to optimize the membrane properties for membrane distillation: A review, Industrial & Engineering Chemistry Research, vol. 55, no. 35, pp. 9333–9343, 2016. DOI: 10.1021/acs.iecr.6b02226.

[195] P. Stephan, S. Kabelac, M. Kind, D. Mewes, K. Schaber, and T. Wetzel, VDI-Wärmeatlas. Heidelberg: Springer Verlag Berlin, 2019, ISBN: 978-3-662-52988-1. DOI: 10.1007/978-3-662-52989-8.

[196] V. Karanikola, A. F. Corral, H. Jiang, A. Eduardo Sáez, W. P. Ela, and R. G. Arnold, Sweeping gas membrane distillation: Numerical simulation of mass and heat transfer in a hollow fiber membrane module, Journal of Membrane Science, vol. 483, pp. 15–24, 2015. DOI: 10.1016/j.memsci.2015.02.010.

[197] H. Bissett, J. Zah, and H. M. Krieg, Manufacture and optimization of tubular ceramic membrane supports, Powder Technology, vol. 181, no. 1, pp. 57–66, 2008. DOI: 10.1016/j.powtec.2007.06.005.

[198] C. Falamaki, M. S. Afarani, and A. Aghaie, Initial sintering stage pore growth mechanism applied to the manufacture of ceramic membrane supports, Journal of the European Ceramic Society, vol. 24, no. 8, pp. 2285–2292, 2004. DOI: 10.1016/S0955-2219(03)00643-5.

[199] L. García-Fernández, B. Wang, M. C. Garcıa-Payo, K. Li, and M. Khayet, Morphological design of alumina hollow fiber membranes for desalination by air gap membrane distillation, Desalination, vol. 420, pp. 226–240, 2017. DOI: 10.1016/j.desal.2017.07.021.

[200] P. Uchytil, Gas permeation in ceramic membranes Part I. Theory and testing of ceramic membranes, Journal of Membrane Science, vol. 97, pp. 139–144, 1994. DOI: 10.1016/0376-7388(94)00156-S.

[201] J. C. Lagarias, J. A. Reeds, M. H. Wright, and P. E. Wright, Convergence properties of the Nelder-Mead simplex method in low dimensions, SIAM Journal of Optimization, vol. 9, no. 1, pp. 112–147, 1998.

[202] K. Charfi, M. Khayet, and M. J. Safi, Numerical simulation and experimental studies on heat and mass transfer using sweeping gas membrane distillation, Desalination, vol. 259, no. 1-3, pp. 84–96, 2010. DOI: 10.1016/j.desal.2010.04.028.

[203] S. Zhao, P. H. Feron, Z. Xie, J. Zhang, and M. Hoang, Condensation studies in membrane evaporation and sweeping gas membrane distillation, Journal of Membrane Science, vol. 462, pp. 9–16, 2014. DOI: 10.1016/j.memsci.2014.03.028.

[204] International Electrotechnical Comission, IEC 60584-1:2013. Thermocouples: Part 1: EMF specifications and tolerances. TC 65/SC 65B - Measurement and control devices. 17.200.20 - Temperature-measuring instruments, 2013.

[205] Y. Wibisono, E. R. Cornelissen, A. Kemperman, W. van der Meer, and K. Nijmeijer, Two-phase flow in membrane processes: A technology with a future, Journal of Membrane Science, vol. 453, pp. 566–602, 2014. DOI: 10.1016/j.memsci.2013.10.072.

[206] Z. Ding, L. Liu, J. Yu, R. Ma, and Z. Yang, Concentrating the extract of traditional chinese medicine by direct contact membrane distillation, Journal of Membrane Science, vol. 310, no. 1-2, pp. 539–549, 2008. DOI: 10.1016/j.memsci.2007.11.036.

[207] Z. Ding, L. Liu, Z. Liu, and R. Ma, The use of intermittent gas bubbling to control membrane fouling in concentrating TCM extract by membrane distillation, Journal of Membrane Science, vol. 372, no. 1-2, pp. 172–181, 2011. DOI: 10.1016/j.memsci.2011.01.063.